OpenAIR@RGU

The Open Access Institutional Repository
at Robert Gordon University

http://openair.rgu.ac.uk

Citation Details

Citation for the version of the work held in 'OpenAIR@RGU':

Copyright

Directly Enhancing the Photocatalytic Transformation of CO₂ and Water to Renewable Fuels

Nathan Skillen

A thesis submitted in partial fulfilment of the requirement of the Robert Gordon University, Aberdeen for the award of Doctor of Philosophy

This research programme was carried out in collaboration with The University of St. Andrews and California Institute of Technology

June 2013

Dedication

This thesis is dedicated to the memory of my grandparents, Mary Gracey and James 'Jazzer' Gracey. A source of true inspiration.

Declaration

I hereby declare that no portion of the work referred to in this thesis has been submitted in support for an application for another degree or qualification of this or other university or other institute of learning.

This thesis has been comprised by the author.

Acknowledgment

Abstract

The increases in Greenhouse Gas (GHG) concentrations and depletion of hydrocarbon based fuels have become global concerns. As a result, a number of methods are being developed which aim to restrict GHG and to develop alternative fuels from sustainable sources. Photocatalysis has shown potential to restrict GHG through CO_2 recycling and convert solar energy to alternative fuels through solar H_2 production. This thesis describes the development of photo reactors to reduce CO_2 emissions and to provide a novel method of producing H_2 as a fuel source. A number of photo reactors were developed including three fluidised design concepts and a thin film system. The preliminary evaluation of the reactors was performed using methyl orange (MO) as a model compound and utilising TiO_2 and ZnO. The reduction of CO_2 and H_2 evolution was performed over a range of novel catalysts in the optimised system developed, referred to as the propeller fluidised photo reactor (PFPR). A MO photodegradation efficiency of > 95 % was achieved in all the photo reactors using illumination from a low power 36 W lamp. The reduction of CO_2 was performed in the PFPR under varying illumination sources including UV, simulated and natural solar exposure. CO_2 reduction was not achieved in the unit under any experimental conditions. However, the evolution of H_2 was achieved under both simulated and natural solar irradiation. The results demonstrated that reactor properties such as propeller rotational speed were found to enhance the photo activity of the system through the elimination of mass transport limitations and increasing light penetration. The optimum conditions for H_2 evolution were found to be a propeller rotational speed of 1035 rpm and 144 W of simulated solar irradiation, which produced a rate of 109 $\mu mol\ h^{-1}\ g^{-1}$ over $Pt\text{-}C_3N_4$. Under solar irradiation 8 $\mu mol\ h^{-1}\ g^{-1}$ was evolved over $NaTaO_3.La$. The rate of H_2 evolution over $Pt\text{-}C_3N_4$ increased from 27 to 109 $\mu mol\ h^{-1}\ g^{-1}$, upon increasing the rotational speed of the propeller from 0 to 1035 rpm. Furthermore, the use of the PFPR with solar irradiation displayed the potential for solar photocatalysis applications.

TABLE OF CONTENTS

LIST OF FIGURES

LIST OF TABLES

Glossary

AC   - Activated Carbon

BET   - Brunauer-Emmett-Teller

cm   - Centimetres

cm^2 - Square centimetres

cm^3 - Cubic centimetres

CPC   - Compact Parabolic Concentrator

CR   - Congo Red

DAI   - Dangerous Anthropogenic Interference

dcV   - direct current volts

EDXA - Energy Dispersive X-ray Analysis

Eg   - Band gap energy

eV   - Electron volts

ft   - feet

g   - Gram

g^{-1} - per gram

GB   - Glass beads

GC   - Gas Chromatography

GC-TCD – Gas Chromatography with Thermal Couple Detector

GHG - Green Houses Gases

GJ   - Gigajoules

GPH - gallons per hour

HPLC - High Performance Liquid Chromatography

hr^{-1} - per hour

ID   - Inner Diameter

IUPAC - International Union of Pure and Applied Chemistry

Kg   - Kilogram

KN   - Kilonewtons

L   - Litre

L^{-1} - per litre

LED   - Light-emitting Diode

LMB   - Leuco Methylene Blue

m   - Metres

M   - Moles

m/z   - mass to charge ratio

m^2 - Meters square

m^3 - Meters cubic

MB   - Methylene Blue

MCPR   - Multi Chamber Photo Reactor

mg   - Milligram

min^{-1} - Per minute

μL   - Microlitre

mL   - Millilitre

μm   - Micrometres

μmol   - Micro moles

mM   - Milli moles

mm   - Millimetres

MO   - Methyl Orange

NHE   - Normal Hydrogen Electrode

nm   - Nanometres

N_{RE} - Reynolds number

^oC - Degrees Celsius

OD   - Outer Diameter

PDA   - Photodiode Array

PE   - Photodegradation Efficiency

PEC   - Photoelectrocatalytic

PFPR   - Propeller Fluidised Photo Reactor

PMMA - Poly (methyl methacrylate)

ppm   - Parts per million

PTC   - Parabolic Trough Concentrator

PTFE   - polytetrafluoroethylene

RB   - Rose Bengal

rpm   - rotations per minute

R_t - Retention time

s^{-1} - Per second

SCE   - Standard Hydrogen Electrode

SED   - Sacrificial Electron Donor

SEM   - Scanning Electron Microscope

SFPR   - Sparged Fluidised Photo Reactor

SS   - Stainless Steel

TCE   - Trichloroethylene

TFMTPR – Thin Film Multi Tubular Photo Reactor

TNT   - Titania Nano Tubes

TW   - Terawatts

U_{mf} - Minimum fluidisation velocity

UV   - Ultra-violet

W   - Watts

Wt % - Weight percentage

Publications

The following is a list of publications resulting from the research detailed in this thesis.

Publications

MCCULLAGH, C., **SKILLEN, N**., ADAMS, M., ROBERTSON, P.K.J., 2011. Photocatalytic Reactors for Remediation: A Review. *Journal of Chemical Technology and Biotechnology,* 86(8), pp. 1002-1017

ADAMS, M., **SKILLEN, N.,** MCCULLAGH, C., ROBERTSON, P.K.J., 2013. Development of a doped titania immobilised thin film multi tubular photo reactor. *Applied Catalysis B: Environmental,* 130–131(0), pp. 99-105

Conferences

SKILLEN, N., ADAMS, M., ROBERTSON, P.K.J., 2011 Evaluation of a Novel Fluidised Photo Reactor by Methyl Orange Degradation. The 16th International Conference on TiO2 Photocatalysis: Fundamentals and Applications (TiO2-16) (Poster)

SKILLEN, N., ADAMS, M., MCCULLAGH, C., ROBERTSON, P.K.J., Novel Photocatalytic Reactor Technology for Environmental Applications. The 19th International Conference on the Conversion and Storage of Solar Energy (IPS-19th) (Presentation)

SKILLEN, N., ADAMS, M., MCCULLAGH, C., ROBERTSON, P.K.J., Novel Photocatalytic Reactor Technology for Environmental Applications: An Update. The UK and Ireland Semiconductor Photocatalytic Network Meeting (UKISPC) at University College London. (Presentation)

SKILLEN, N., ADAMS, M., MCCULLAGH, C., ROBERTSON, P.K.J. The Design and Construction of a Novel Propeller Fluidised Photo Reactor for Application in Photocatalytic Processes. Semiconductor Photochemistry 4 (SP4) (Poster)

Conferences Attended

The 3rd International Conference on Semiconductor Photocatalysis (SP3) at Strathclyde University, UK (2010)..

UK and Ireland Semiconductor Photocatalysis Network Meetings (UKISPC) at University of Ulster (2010), University College London (2011 and 2012) and Queens University Belfast (2012).

Chapter 1 Introduction

1.1 The Current Energy Situation

Hydrocarbon based fuels (fossil fuels) are the primary resource for the worlds energy supplies. With increasing demand for global energy, however, there has been rapid growth in the field of energy development, with a view towards the generation of an alternative energy source to provide global sustainability. Extensive focus is now being given to alternative sources such as wind, biomass, tidal, nuclear, solar, H_2 production and CO_2 reduction. Ediger et al. (2007) stated that the aim of energy sustainability development was to 'meet the needs of the present generations without comprising the ability of future generations to meet their own needs'.

While there is both global awareness and agreement over the current unfavourable energy situation, an increase in energy requirement is still expected to occur; in 2001 the energy requirement was 13.5 TW/year, however by 2050 the expected energy requirement will be 27 TW/year (Li *et al.*, 2011). In addition to this, Shafiee and Topal (2009) predicted that oil and gas samples are predicted to increase from 36 million barrels/day in 2006 to 46 and 61 million barrels/day in 2015 and 2030 respectively.

The growth of energy demands, amongst other factors, was previously discussed by Medows *et al.* in 1972 in their publication 'The Limits to Growth'. Meadows and colleagues developed a world model that investigated the exhaustion of non-renewable resources. Their model was built specifically to investigate trends which were of global concern including accelerated industrialisation, rapid population growth, widespread malnutrition, depletion of non-renewable resources and a deteriorating environment. Meadows and colleagues predicted that each of these factors were increasing and following exponential growth. They concluded the limit to growth of the planet being reached within the next 100 years, resulting in a sudden and uncontrollable decline in both population and industrial capacity. Even taken into consideration increased technological advancement, the model still predicted that the world would not be capable of sustaining the rate of growth of the factors stated above for more than a few decades. The report discussed that ecological and economic stability could be

reached if the growth rates of these factors were to be altered, stating 'a concerted attack on all major problems at once can achieve the state of equilibrium necessary to survival'.

There remains growing debate over both the accelerated consumption of fossil fuel energy and the quantity of fossil fuel reserves remaining in the Earth. The continued use of fossil fuel in industrial sectors as a source of energy threatens global stability and sustainability (Midilli and Dincer, 2008). The emission of greenhouse gases (GHG) from the combustion of hydrocarbons has been shown to negatively interfere with the climate system, Figure 1 (Hoel and Kverndokk, 1996). Furthermore the overuse of fossil fuels has resulted in the accelerated rate of hydrocarbon resource depletion. It is noteworthy that hydrocarbons are not solely used for providing energy and have a number of important roles in other industrial applications (chemical feedstock, solvents etc.), which will be significantly affected by their depletion.
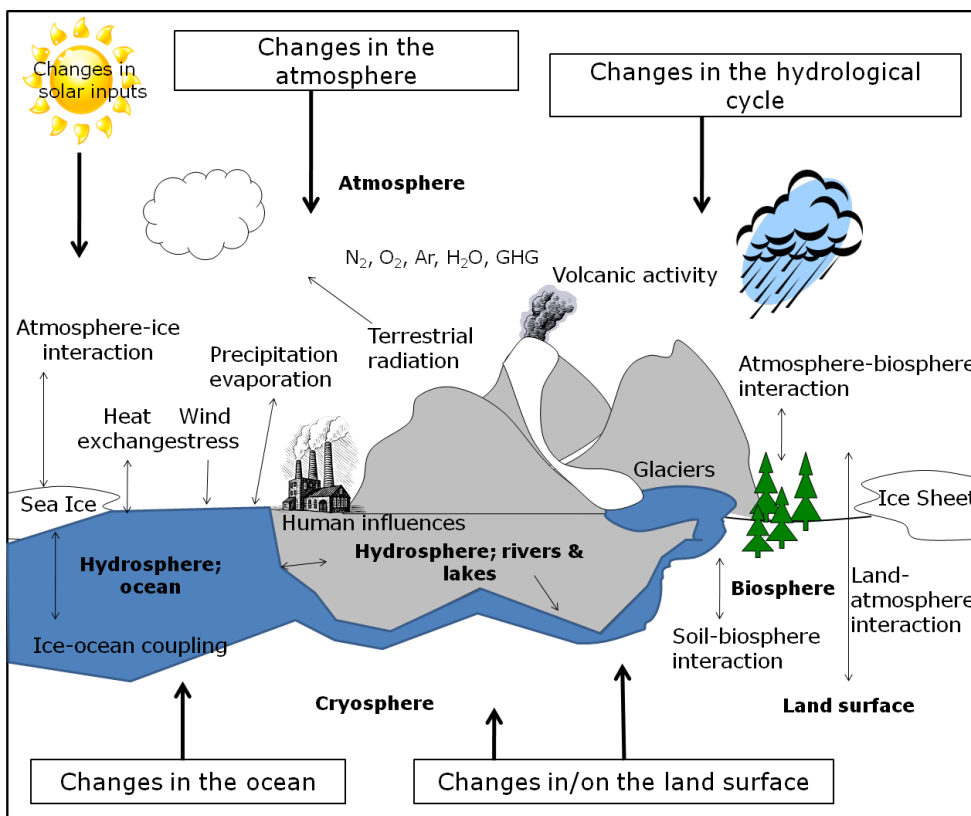
Figure 1; *Schematic of climate system detailing the 5 components of the system (bold), activities/factors involved (thin arrows) and variables which are subject to change (bold)*

Presently, the world energy supply is primarily provided by hydrocarbon based fuel reserves; liquid fuel is used for transportation, oil and gas for heating houses and coal, oil and gas for conversion into electricity. It is a mature and well established global energy supply which has proved efficient. Fossil fuel energy has been developed and improved over a significant time frame to produce the current optimised system. Hydrocarbon based fuels have obvious advantages including easy storage and transportation, an already well established global energy structure and high volumetric energy density of 33 GJ/m^3 (Li *et al.*, 2011).

The remaining quantities of oil, gas and coal reserves are difficult to calculate as is the exact time frame they will become exhausted. This has given rise to the argument between individuals who believe 'fossil fuel peak production' will occur soon and thereafter a rapid decline in supplies will be observed and major oil companies who are of the opinion that the reserves will provide enough fossil fuels for the next 'few' decades. Fossil fuel peak production is the estimated time frame at which fossil fuels reach a maximum point (peak) of production (Leggett *et al.*, 2012), which is likely the point at which all easily accessible reserves are exhausted. Thereafter a rapid decline in resources to the point of depletion will be observed.

While there is much speculation surrounding this topic it can be stated that oil, gas and coal are finite resources and are non-renewable and thus will become depleted over time. Moreover, regardless of when peak fossil fuel production levels are reached the growing global energy demand will increase and with that will increase the rate at which fossil fuels are consumed. Once easily accessible reserves of fossil fuels are exhausted, the production of fossil fuels will decrease and the economic impact of this will be damaging (Shafiee and Topal, 2010). Further to this point with global energy demand increasing, regardless of the volume of fossil fuels remaining in the ground the level of fossil fuels that can be 'commercially exploited' at prices the global economy has become accustomed to is limited and will decline at a significantly rapid rate (Owen *et al.*, 2010). Owen and colleagues went on to state that the result of this will mean that oil may become a 'supply constrained market' as oppose to a 'demand-led' one, resulting in the 'era of plentiful and low cost petroleum' coming to an end.

Therefore with the impact of fossil fuel resources affecting numerous global sectors it is vital to investigate at what stage a 'critical point' is reached. A critical point will be reached when fossil fuel based climate system interference causes dangerous anthropogenic interference (DAI) or the global energy demands cannot be met.

To investigate this, the following points must be addressed:

- The expected time frame for fossil fuel peak production along with fossil fuel reserves depletion
- The impact of fossil fuel consumption on global warming
- The current response to ensure energy sustainability is achieved in the absence or presence of fossil fuels.

Discussed hereafter is firstly the time scale for fossil fuel peak production and fossil fuel reserves. Secondly, the impact the combustion of fossil fuels is having on the Earth's climate system (global warming) along with the potential solution to overcome these issues.

1.2 Fossil Fuel Peak Production and Reserves

Recently Leggett *et al.* (2012) stated that civilisation is faced with two significant threats; global warming from fossil fuel use and secondly fossil fuel peak production levels being reached. Leggett and colleagues reviewed a number of prediction models to determine the peak production levels for oil, gas and coal. The results of this comparison are illustrated in Table 1. The table shows that oil and gas peak production is expected to be reached in the next decade with coal outlasting other fossil fuels.

Fossil Fuel	Peak production year	Standard deviation (yr)	Number of estimates
Conventional oil	2016	12.8	28
Conventional + unconventional oil	2022	18	17
Gas	2022	9.4	9
Coal	2048	25.9	7

Table 1; *Peak production for oil, gas and coal based upon findings of Leggett et al. (2011)*

When discussing peak production levels for fossil fuels it is important to consider the rate at which production occurs. Ward *et al.* (2012) developed a model to investigate the production growth and decline of fossil fuels. They discussed in their model that production 'P(t)' is allowed to grow exponentially according to the specified initial growth rate 'r', but is progressively curtailed as the overall quantity of the extracted resource approaches the recoverable resource quantity 'Q_∞' remaining at time t=0 (Ward *et al.*, 2012). This model is described in Equation 1

$$P(t) = P_o e^{krt}(1 - \frac{Q}{Q_\infty})$$ **Equation 1**

Where 'Q' is the cumulative production at time 't' (Q=0 when t=0), 'P_o' is the production rate at t=0, and 'k' is an exponent scaling factor. k is used to force the model to yield exponential growth conforming to the specified growth rate 'r' for at least the duration of the first step (t_1), and is determined by Equation 2.

$$k \approx \frac{ln[(1+r)^{t_1}/(1 - \left(\left(\frac{P_o(1 + (1+r)^{t_1})t_1)}{2Q_\infty}\right)\right)]}{rt_1}$$ **Equation 2**

This model produced an asymmetrical growth profile which allowed for a varying rate of growth. This model differed from previous ones which produced a symmetrical profile of growth suggesting the growth rate would be equal to the depletion rate. Ward and colleagues showed that with a longer growth phase (10 %) an increased peak of production was achieved with a sharp decline thereafter. At 10 % the peak production was observed within 20 years. At decreasing growth phases of 7.5, 5, 2.5 and 0.01 %, the peak production was lower with less of a decline over a longer period of time.

The investigations into fossil fuel peak production can be coupled with investigations into when oil, gas and coal reserves are predicted to be depleted. In 2009 Shafiee and Topal utilised mathematical models to determine the number of years fossil fuels will remain. Based upon the calculations conducted it was found oil, gas and coal had depletion times of 35, 37 and 107 years respectively. Based upon these findings it is estimated that by 2042 the only fossil fuel remaining will be coal.

1.3 Impact of Fossil Fuel Combustion on Global Warming

The primary cause of long-term anthropogenic global temperature rise is the release of GHG into the atmosphere, predominantly the release of CO_2 from the combustion of hydrocarbon fuels (Hoel and Kverndokk, 1996). It is predicted that the average global mean temperature will increase by 6 $^{\circ}$C by the end of the century (Girod *et al.*, 2009). The impact of this temperature increase is sufficient to switch the Earth's climate from glacial conditions to an 'ice-free' Antarctica (Li *et al.*, 2011). Furthermore Chiari and Zecca (2011) stated that if global warming is to be restricted to +2 $^{\circ}$C (in respect to pre-industrial times) to ensure no DAI occurs, it is essential that CO_2 concentrations are kept at ~400 ppm.

The increase in CO_2 is believed to be a result of an imbalance between anthropogenic carbon emissions and the ability of terrestrial and ocean processes to remove and convert CO_2 (Solomon *et al.*, 2007). This imbalance resulted in global average atmospheric CO_2 rising from ~ 280 ppm at the start of the industrial revolution to ~ 381 ppm in 2006 (Friedlingstein *et al.*, 2010; Mikkelsen *et al.*, 2009). This growth rate is a consequence of 3 factors;

- Global economic activity (generated from the use of fossil fuels and land-use change)
- The carbon intensity of the economy
- The functioning of unmanaged carbon sources and sinks on land and in oceans.

While there is general agreement with the fact that CO_2 levels must be reduced the immediate capping of CO_2 emissions from the burning of fossil fuels is simply not feasible. It is estimated (Li *et al.*, 2011) that in order to supply the worlds energy requirement 1 billion barrels of oil are consumed every 12 days. The impact of which in relation to GHG emission is $\sim$ 1 trillion pounds of CO_2 being released into the atmosphere. As the immediate capping is not possible the reduction of CO_2 must be achieved. Therefore a number of strategies, including scientific technology and government policy, which aim to reduce the emissions of all GHG levels have been developed. Discussed below is the scientific approach to lowering and recycling CO_2.

1.4 Alternative Sources to Fossil Fuel Energy

It is evident that the dangerous climate interference caused by fossil fuel combustion, coupled with the overall depletion of fossil fuel reserves requires an adequate response. The development of, and transition to, a low carbon system is a viable approach. The development of such a system, however, is yet to be fully developed and there is much debate over the transition pathway such a process would take. Therefore, methods into CO_2 remediation have been investigated in an attempt to recycle CO_2 and reduce atmospheric concentrations. Current approaches to both alternative energy sources and CO_2 reduction methods are summarised in Figure 2 (Lee and Lee, 2003; Mounira, 1996; Usui and Ikenouchi, 1997).
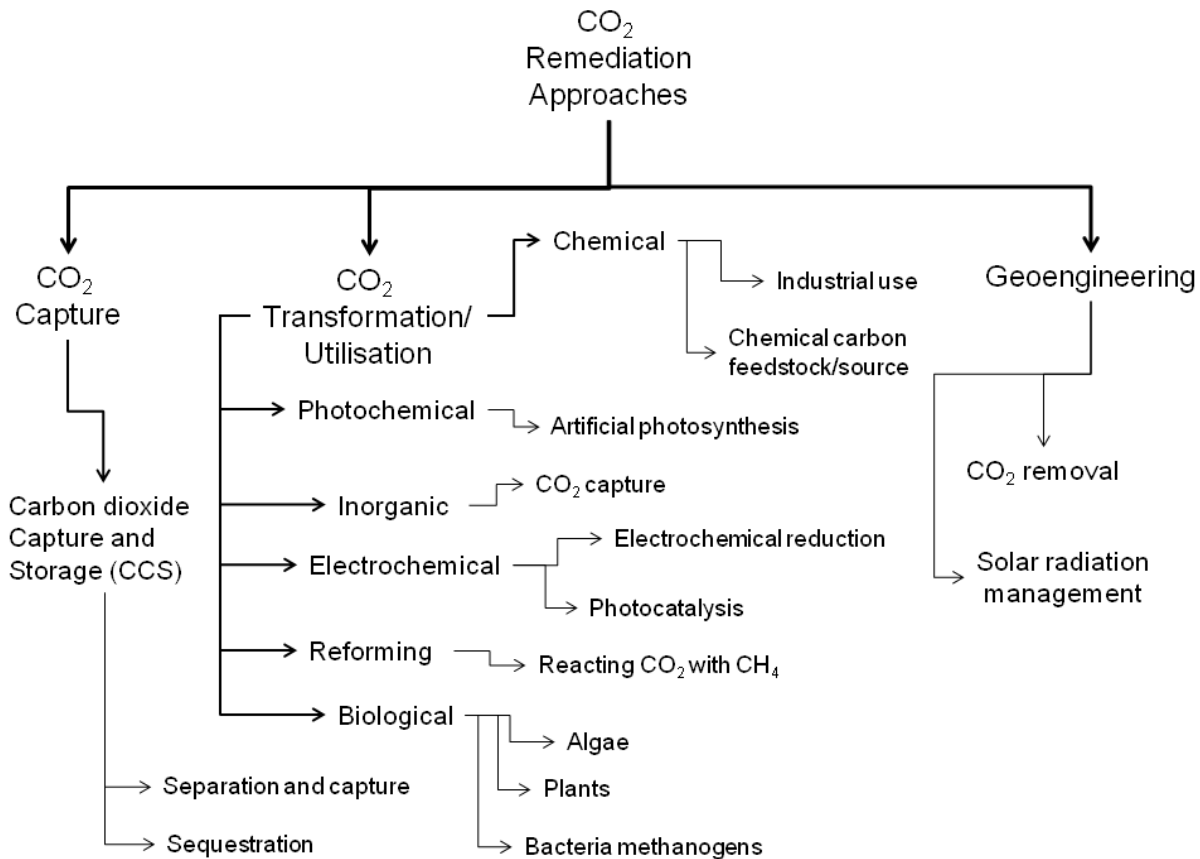
Figure 2*; Summary of CO$_2$ remediation approaches*

The increase in energy requirement on a global scale means that alternative energy sources must be developed to initially match current hydrocarbon usage and secondly replace them. This process is complex and will require a significant time frame to be achieved. Selected literature has stated the current energy system could be replaced by renewable alternatives by 2050 (Deluchhi and Jacobson, 2011).

Presently the main energy source is hydrocarbon based, accounting for 85 % of usage with the remaining 15 % being comprised of alternative energy sources such as solar, tidal, wind, nuclear, biomass and photovoltaics, Figure 3 (Delucchi and Jacobson, 2011). The immediate transition from a hydrocarbon based energy source to one of these current alternatives is not feasible.
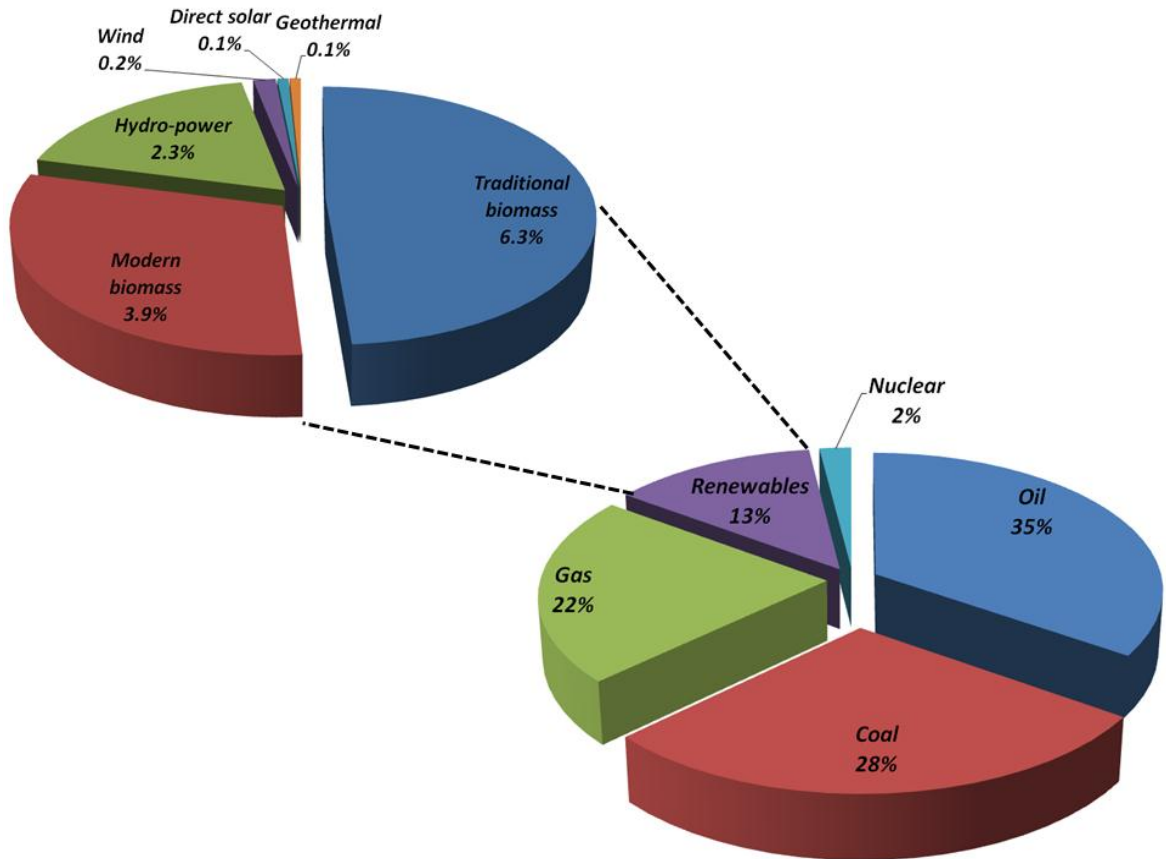
Figure 3; *Distribution of world energy consumption*

The comparison of renewable energy sources shows that the use of solar energy has excellent potential. Solar energy is clean, abundant, non-monopolised, environmentally and economically beneficial and provides the Earth's surface with ~120000 TW/year (Gust, 2009). Solar energy has a significant limitation in the unpredictability of the delivery of photons to the Earth's surface. Solar energy is an intermittent irradiation source and therefore must be successfully collected, converted and stored to allow for utilisation as an alternative fuel.

The use of solar energy as an alternative renewable energy has been shown to be efficient in photosynthesis. The photosynthesis process uses solar light for two systems in plants and algae. Firstly the generation of O_2 via the photolysis of H_2O and secondly the reduction of CO_2 via ribulose bisphosphate (RuBP) in the Calvin cycle. The process of photosynthesis in both systems is schematically shown in Figure 4. The system is efficient but it should be noted that the kinetics of

photosynthesis are slow and are dependent on the species and size of the plant. In larger plants the process is responsible for the growth and reproduction along with internal processes such as transportation of materials. Essentially, the larger the plant grows the greater the demand for energy, thus photosynthesis as a remediation process for CO_2 in large plants is slow. In simpler structured and smaller plant species photosynthesis has a moderately high efficiency.
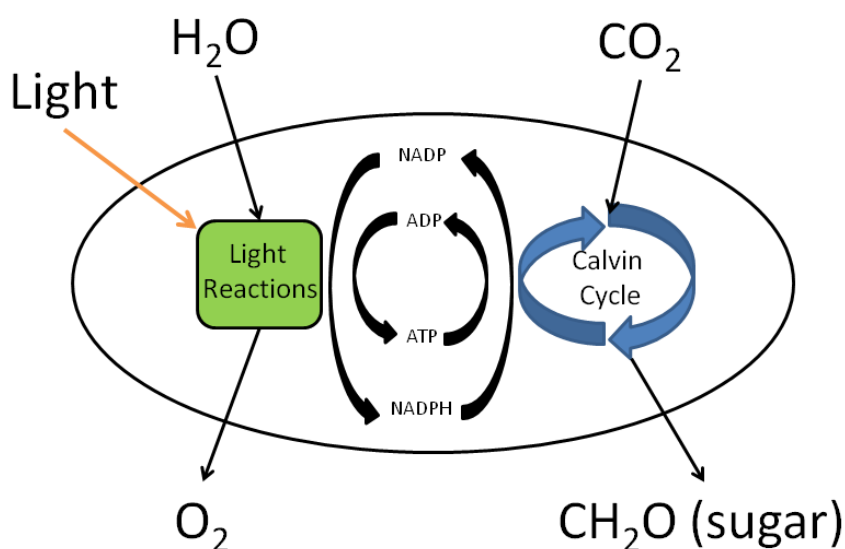
Figure 4; *Schematic of photosynthesis principle*

The mimicking of photosynthesis through artificial photosynthesis and photocatalysis for the generation of H_2 and the reduction of CO_2 has the greatest degree of potential to not only provide an alternative fuel source but to also achieve efficient CO_2 recycling and lower atmospheric emissions (Bian *et al.*, 2012). Furthermore, the generation of H_2 and reduction of CO_2 to fuels is an extremely efficient way of utilising solar energy. The following equations demonstrate the potential pathways for the generation of fuels and reduction of CO_2 by solar energy utilising photocatalysis.

Solar Hydrogen:	Chemical Potential (eV vs NHE)	
$2H_2O + 4h^+ \rightarrow O_2 + 4H^+$	+1.23	**Equation 3**
$2H^+ + 2e^- \rightarrow H_2$	0.00	**Equation 4**
CO$_2$ Conversion:		
$CO_2 + e^- \rightarrow CO_2^-$	-2.21	**Equation 5**
$CO_2 + 2H^+ + 2e^- \rightarrow HCOOH$	-0.19	**Equation 6**
$CO_2 + 2H^+ + 2e^- \rightarrow CO + H_2O$	-0.19	**Equation 7**
$CO_2 + 4H^+ + 4e^- \rightarrow HCHO + H_2O$	-0.06	**Equation 8**
$CO_2 + 6H^+ + 6e^- \rightarrow CH_3OH + H_2O$	+0.03	**Equation 9**
$CO_2 + 8H^+ + 8e^- \rightarrow CH_4 + H_2O$	+0.18	**Equation 10**

1.5 Photocatalysis

Semiconductor photocatalysis is essentially a 'nature-mimicking' act attempting to recreate photosynthesis, in which a catalyst is exposed to light of an appropriate wavelength resulting in excitation of the energy band gap caused by the overlapping of S- and P-orbital's (Robertson, 1996). Upon this excitation, electrons travel from the valence band to the conduction band allowing reduction and oxidation reactions to take place as a result (Hoffmann *et al.*, 1995). The positive hole from the movement of the electron in the valence band acts as a powerful oxidant while the band electrons are excellent reductants (Mills and Le Hunte, 1997).

Photocatalysis has been defined by the IUPAC Commission as 'a change in the rate of chemical reactions or their generation under the action of light in the presence of photocatalysts that absorb light quanta and are involved in the chemical transformation of the reaction participants' (Serpone *et al.*, 2002). In heterogeneous catalysis the activation process is thermal, however photonic activation is utilised for heterogeneous photocatalysis. When considering both

heterogeneous catalysis and photocatalysis the process can be characterised by the following stages (Wood, 2008);

- The movement of the reactant in the fluid phase to the catalyst surface
- Adsorption of at least one of the reactants
- Reaction in the adsorbed phase takes place
- Desorption of the product from the surface
- Removal of the products from the interface region

TiO_2 is a common photocatalyst and can be used as an example to demonstrate the process of photocatalysis. TiO_2 acts as a photocatalyst due to its electronic structure, characterised by an electronically filled valence band and empty conduction band separated by a band gap, Figure 5.
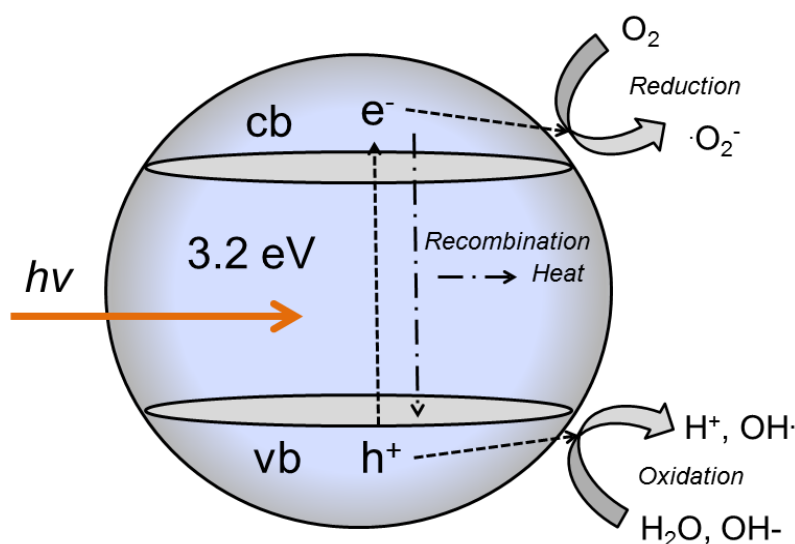
Figure 5; *Schematic representation of TiO_2 photo excitation*

The photocatalytic process can be expressed as shown in Equation 11 to Equation 17. If a photon of energy greater than or equal to the bandgap energy, E_g, is absorbed by TiO_2, an electron is promoted from the valence band to the conduction band. This generates a reducing electron in the conduction band and an oxidising hole in the valence band (Equation 11). The electron and holes formed are highly charged and result in redox reactions, which can ultimately result in the oxidation and reduction of target pollutants. At this stage there are

two pathways which can occur; the excited conduction band electrons may recombine with the valence band holes generating heat energy or alternatively the electron/hole may be trapped in surface states, undergo reactions with electron donating or accepting species that are adsorbed on the TiO_2 surface. Hydroxyl radicals are believed to be generated on the surface of TiO_2 through a reaction of the valence band holes with adsorbed water, hydroxide or surface titanol groups (Equation 12). The hydroxyl radicals are capable of reacting with the reactants and producing oxidised products (Equation 13). The photogenerated conduction band electrons react with electron acceptors such as oxygen which generates superoxide (O_2^-) (Equation 14). The superoxide is then capable of reacting with H^+ to form a hydroperoxyl radical (Equation 15). Thermodynamically the redox potential of the TiO_2 electron/hole pair should enable the production of hydrogen peroxide, primarily via the reduction of adsorbed oxygen (Taqui *et al.*, 1992; Khan *et al.*, 1992) (Equation 16). Hydrogen peroxide formed is then capable of reacting with the conduction band electron to form further hydroxide and hydroxyl radicals

$$TiO_2 + h\nu \rightarrow TiO_2\ (e_{cb}^- +\ h_{vb}^+)$$ **Equation 11**

$$h_{vb}^+ + OH_{ads}^- \rightarrow\ OH_{ads}$$ **Equation 12**

$$OH_{ads}^- +\ Reactants \rightarrow Oxidised\ products$$ **Equation 13**

$$e_{tr}^- +\ O_{2,\ ads} \rightarrow O_2^{\cdot-}$$ **Equation 14**

$$O_2^{\cdot-} + H^+ \rightarrow HO_2^{\cdot}$$ **Equation 15**

$$HO_2^{\cdot} +\ HO_2^{\cdot} \rightarrow H_2O_2 +\ O_2$$ **Equation 16**

$$H_2O_2 + e_{cb}^- \rightarrow OH +\ OH^-$$ **Equation 17**
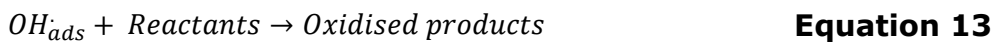
The rate of photocatalysis can be dictated by a number of factors including light intensity, presence of metal dopants, concentration of substrate and catalyst morphology. Catalyst morphology is capable of dictating reaction rate primarily through the catalyst platform and thus surface area. There have been three catalyst platforms frequently reported; pellet, powder and thin film (McCullagh *et*

al., 2011). Powdered catalysts are commonly deployed as they have a high surface area allowing for increased reaction between the catalyst and substrate. Pellet and thin film catalysts have been used as alternatives in an attempt to alleviate catalyst handling issues including separation of catalyst from an aqueous media.

Photocatalysts are typically metal oxides and sulphide complexes and a number have been reported in the literature; TiO_2, CdS, SnO_2, WO_3, SiO_2, ZrO_2, ZnO, Nb_2O_3, Fe_2O_3, $SrTiO_3$, CeO_2, Sb_2O_4 and V_2O_5 (de Richter and Caillol 2011). The bandgap structures of selected semiconductors, in relation to the potential required for water splitting (green section), is shown in Figure 6. TiO_2 is a common benchmark photocatalyst used in the literature due to its low toxicity, low cost, stability and abundance.
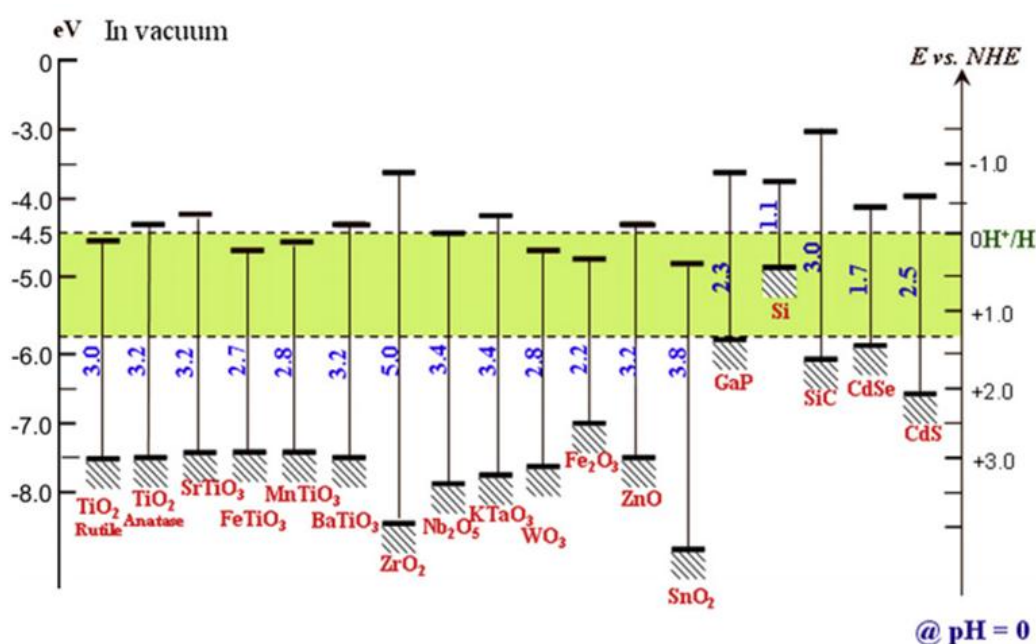
Figure 6; *Bandgap structure of various semiconductors in relation to the redox potential of water (green bar) (Jing et al., 2010)*

Discussed hereafter is a brief overview of CO_2 photo reduction, H_2 production and reactors operated in photocatalysis. An extensive and comprehensive review of the data is shown in Table 2 and Table 3.

1.6 Photo Reduction of CO_2

Photocatalysis is a domain of science still in its infancy, however shows potential to meet the previously mentioned criteria for the reduction of CO_2 based upon the following observations;

- Photocatalyst with a large band gap are capable of solar photonic activation
- Photocatalytic reduction of CO_2 generates products which can be utilised as solar fuels
- Photocatalytic processes are already commercially available
- Reactor design can be modular to allow for incorporation into a variety of industrial sectors

Furthermore, CO_2 reduction by photocatalysis presents an attractive approach to solar energy utilisation for the production of solar fuels, CO_2 recycling and thus reducing global warming (de Ritcher and Caillol, 2011; de Ritcher *et al.*, 2013; Li *et al.*, 2012; Liu *et al.*, 2012; Mao *et al.*, 2012).

1.6.1 CO_2 Photoreduction Catalysts

There has been a range of publications on the photocatalytic reduction of CO_2 (Anpo *et al.*, 1995; Anpo *et al.*, 1998). The first example of simple semiconductor particles being employed to reduce CO_2 was reported by Halmann (1978) where p-type gallium phosphide was used. In the same year Hemminger *et al.* (1978) investigated the reaction of CO_2 and H_2O in gas phase in order to produce CH_4. Reduction of CO_2 over TiO_2 began contemporaneously with Inoue *et al.* (1979) demonstrating reduction via CO_2 being bubbled through water. The reduction of CO_2 in water on the surface of TiO_2 is shown in Figure 7. The early reports published during 1978 and the following years demonstrated the production of HCHO, HCOOH, CH_3OH, C_2H_5OH, CH_3CHO, CH_4 and C_2H_6 as the primary products (Halmann, 1978; Hemminger *et al.*; 1978; Inoue *et al.*, 1979).
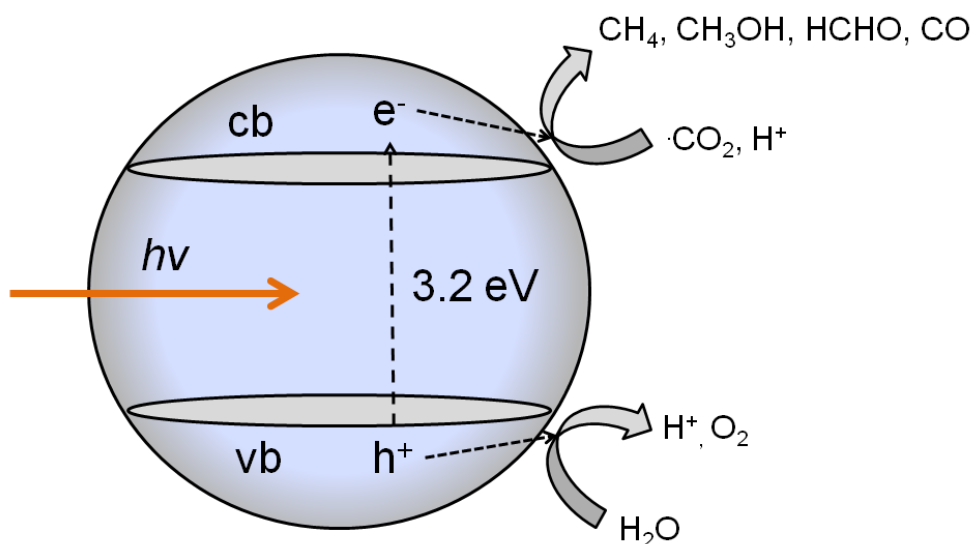
Figure 7; *Processes that occur upon photo-excitation of TiO$_2$ during CO$_2$ reduction*

While Halmann (1978) pioneered the work into CO$_2$ reduction over photocatalysts in a H$_2$O medium the efficiency of the system was low. Mori *et al.* (2012) reported high efficiencies of CH$_4$ and CH$_3$OH in their review of CO$_2$ reduction over various titanium oxide photocatalysts. CO$_2$ reduction was investigated over bulk TiO$_2$, imp-Ti-oxide/Y-zeolite (10 % weight as TiO$_2$), imp-Ti-oxide/Y-zeolite (1 % weight as TiO$_2$), ex-Ti-oxide/Y-zeolite (1 % weight as TiO$_2$) and Pt-loaded ex-Ti-oxide/Y zeolite (1 % weight as TiO$_2$). The yield of CH$_4$ was low over bulk TiO$_2$ < 1.0 µmol h^{-1} g^{-1} however over the Pt-loaded catalyst the yield of CH$_4$ was significantly increased to ~13 µmol h^{-1} g^{-1}. It was over the ex-Ti-oxide/Y-zeolite (1 wt% as TiO$_2$) that the highest yield of CH$_3$OH was observed (~ 5 µmol h^{-1} g^{-1}). The ex-Ti-oxide/Y-zeolite was concluded to be tetrahedral in shape based on the presence of a single pre-edge peak at 4967 eV. In contrast to this the imp-Ti-oxide/Y-zeolite was found to be crystalline in structure based upon the formation weak pre-edge peaks.

Solar conversion of CO$_2$ to hydrocarbons has also been reported in the literature (Varghese *et al.*, 2009). The publication focused on high rate conversion of CO$_2$ to products such as CH$_4$ and H$_2$ over nitrogen-doped titania nanotube arrays. The initial challenge with solar-driven photocatalysis is the development of a catalyst

suitable for solar activation and CO_2 reduction. Varghese and colleagues (2009) employed the high surface area titania nanotubes (NT) loaded with Pt and Cu to achieve the desired reaction. In a stainless steel vessel equipped with a quartz window for solar radiation, the generation of CH_4 was recorded over NT-Pt (annealed at $460^{\circ}C$), NT-Pt-600 (annealed at $600^{\circ}C$) and NT-Cu-600. The highest rate of CH_4 was 70 ppm cm^{-2} hr^{-1} ($\sim$ 0.07 µmol h^{-1}) over NT-Cu-600 with the overall rate of hydrocarbon production recorded at 104 ppm^{-2} hr^{-1} ($\sim$ 0.0319 µmol h^{-1}). An increased rate of H_2 production was observed in the study at $\sim$190 ppm cm^{-1} hr^{-1} ($\sim$ 1.5 µmol h^{-1}) utilising the Pt loaded NT catalyst. The formation of both H_2 and CH_4 under solar illumination is beneficial as both have potential as alternative fuel sources.

1.6.2 CO$_2$ Photoreduction Reactors

Novel photocatalytic reactors reported for the reduction of CO_2 are limited with the focus primarily on catalyst development. There have been publications on recirculating systems (Lo *et al.*, 2007) and fluidised systems (Reilly *et al.*, 2012) which have achieved photoreduction.

Recently Koci *et al.* (2011) published an investigation into the impact of photo reactor geometry on the reduction of CO_2. The paper used two annular batch reactors varying in dimensions along with ZnS nanoparticles deposited onto a substrate. The paper investigated reactor dimensions such as the diameter of the shell tube, the maximum liquid volume of the reactor when the lamp was immersed and the volume of the reactor when the lamp just touched the liquid surface.

Koci and colleagues found that the ratio of liquid and gas phase volumes within the reactors directly influenced the formation of reduction products; in both reactor 1 (R1) and reactor 2 (R2) the highest yield of product (CH_4 and CH_3OH) was found when a liquid phase volume of 100 mL was used. Decreasing the volume of the R1 reactor to below 100 mL resulted in the tip of the illumination source moving away from the surface of the liquid phase. The impact of which was a sharp decline of CH_3OH yield from $\sim$16 µmol g^{-1} at 100 mL to 4 µmol g^{-1} at 50 mL. The positioning and distance of the lamp from target pollutants is also a

key characteristic requiring consideration. Koci found the number of available photons decreased as the lamp distance increased; at a distance of 0, 2 and 5 cm the number of photons were 9.2 x 10^{15}, 4.4 x 10^{15} and 3.7 x 10^{15} respectively. The reactor configuration is shown in Figure 8.
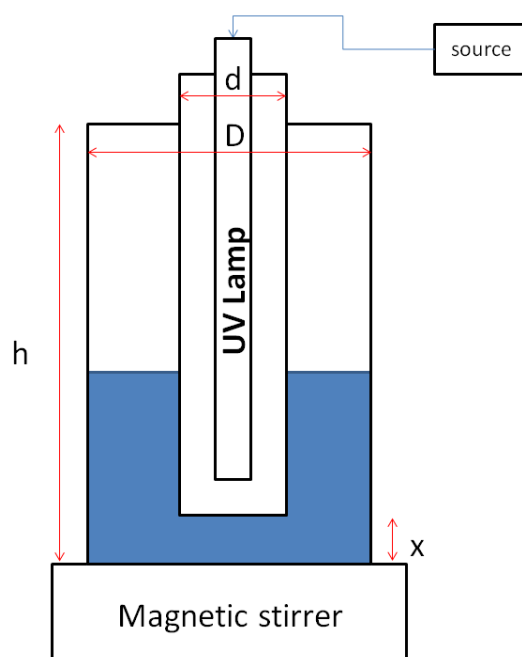
Figure 8; *Reactor configuration by Koci et al. (2011) where h is the height of shell tube, d is the diameter of quartz glass tube, D the diameter of shell tube and X the distance of inner tube from bottom*

Solar reactors have also been reported in the literature for the reduction of CO_2. The optical fibre photo reactor (OFPR) is of particular interest for solar CO_2 conversion due to its intelligent design allowing for increased utilisation of light, Figure 9 (Peill and Hoffmann, 1995). The OFPR is an excellent example of a photo reactor using a thin film coating to eliminate downstream processing techniques. The unit consisted of packed optical fibres which acted as supports for a thin film catalyst. Model pollutants were passed over the coated optical fibres while exposed to irradiation. The unit operated on the principle of incident light being split in two beams when first in contact with the surface of the fibre. Part of the light penetrated the layer of catalyst on the fibre and creates

excitation, while the other beam was reflected off the fibre and is transmitted along the length of the unit. This allowed the light to gradually spread through the length of the reactor.
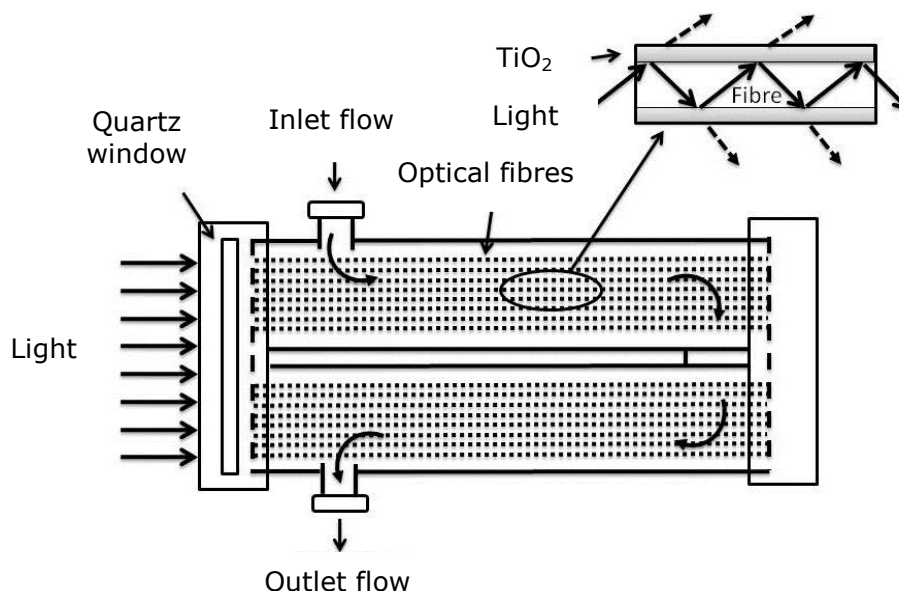
Figure 9; *Schematic illustration of the OFPR, Peill and Hoffmann (1995)*

Optical fibre reactors for a range photocatalytic processes have been reported in the literature (Ji *et al.*, 2011; Danion *et al.*, 2007; Zhang *et al.*, 2012). A number of publications have also reported the use of optical fibre reactors for the photocatalytic reduction of CO_2 including; Wu *et al.* (2005) who reported CO_2 reduction to CH_3OH, Wang *et al.* (2013) who investigated the reduction of CO_2 in a optical fibre monolith reactor and Wang *et al.* (2010) investigated the reduction of CO_2 over $NiO/InTaO_4$.

The OFPR has been utilised in the reduction of CO_2 to fuels under UV and solar light by Nguyen and Wu in 2008. Two photocatalysts were utilised in this investigation; $Cu\text{-}Fe/TiO_2$ along with $Cu\text{-}Fe/TiO_2\text{-}SiO_2$. The products obtained in this study included C_2H_4 and CH_4, along with traces of C_2H_5 and CH_3OH. The product formation under UVA illumination demonstrated selectivity towards the photocatalyst used, with the exception of CH_4 which was evolved with each of the photocatalysts. The highest rate of CH_4 production, 1.860 µmol h^{-1} g^{-1} was found when the catalyst $Cu(0.5 \text{ wt.\%})\text{-}Fe(0.5 \text{ wt.\%})/TiO_2\text{-}SiO_2$ on optical fibres was used. C_2H_5 evolution was selective in production and was only seen over Fe and

Cu containing catalysts; the highest production rate of 0.575 μmol h^{-1} g^{-1} was found when the catalyst Cu(0.5 wt.%)-Fe(0.5 wt.%)/TiO$_2$ on optical fibres was used. In comparison natural sunlight (from a solar concentrator) produced a production rate of 0.279 μmol h^{-1} g^{-1} with the catalyst Cu(0.5 wt.%)-Fe(0.5 wt.%)/TiO$_2$-SiO$_2$ on optical fibres. The solar concentrator utilised continuously tracked the trajectory of the sun throughout the day. The benefits of this system included uniform light distribution throughout the reactor, a feature not seen in traditional packed bed designs and the visible light driven catalyst which the authors concluded enhanced the applicability as a commercial and industrial application.

Recently Liu *et al.* 2012 reviewed the use of TiO$_2$ nanomaterials for CO$_2$ conversion to solar fuels with a degree of focus given to reactor design. A number of reactor designs were investigated including the OFPR, a fluidised bed reactor and photoelectrocatalytic (PEC) cell reactor. The PEC reactor mimics the two photosynthesis systems in plants where CO$_2$ is reduced and H$_2$O is split into H$_2$ and O$_2$. The photoanode of the reactor was constructed on nanstructured TiO$_2$ thin films while the cathode was carbon cloth loaded with Pt or Fe/CNT (Liu *et al.*, 2012). Based upon their investigation, Liu and colleagues proposed a solar reactor suitable for fuel production which is illustrated in Figure 10. The cyclone design utilises Titania Nano Tube (TNT) membranes and ensures sufficient mixing, minimal light loss and controllable contact time between catalyst surface and target species.
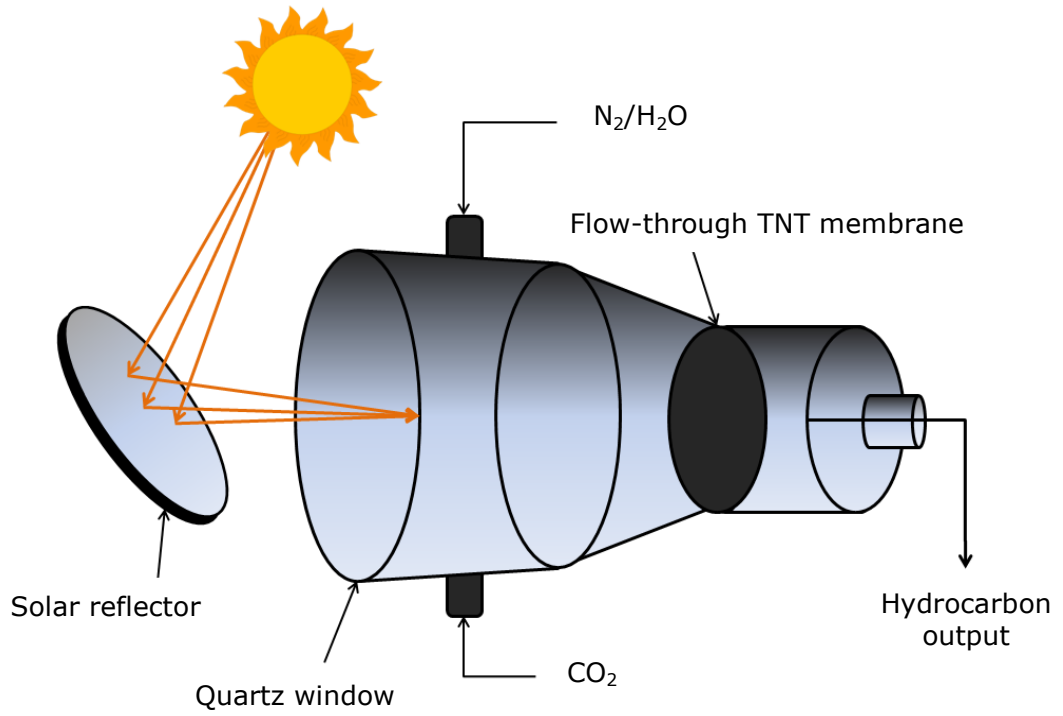
Figure 10*; Schematic illustration of proposed solar reactor by Liu et al. (2012)*

Catalyst	Phase	Reductant	Products formed	Yield of product	Reference
AgBr/TiO$_2$	Liquid-gas	H$_2$O with KHCO$_3$	CH$_4$	128.56 µmol g^{-1}	Abou Asi *et al.* (2011)
			CH$_3$OH	77.87 µmol g^{-1}	
			C$_2$H$_6$O	13.28 µmol g^{-1}	
			CO	32.14 µmol g^{-1}	
TiO$_2$ powder	Liquid-gas	Liquid CO$_2$	HCOOH	8 x 10^{-6} mol(g-cat)$^{-1}$	Kaneco *et al.* (1997)
TiO$_2$ powder	Liquid-gas	Supercritical fluid CO$_2$	HCOOH	9 x 10^{-6} mol(g-cat)$^{-1}$	Kaneco *et al.* (1999)
Kaolinite/TiO$_2$	Liquid-gas	H$_2$O	CH$_4$	7.5 µmol/g-TiO$_2$	Koci *et al.* (2011)
			CH$_3$OH	4.5 µmol/g-TiO$_2$	
Ag-TiO$_2$	Liquid-gas	H$_2$O	CH$_4$	0.08 µmol/g-cat	Koci *et al.* (2010)
			CH$_3$OH	1.8 µmol/g-cat	
ZnS-MMT	Liquid-gas	0.2 M NaOH	CH$_3$OH	160 µmol/g-cat	Koci *et al.* (2011)
			CH$_4$	8 µmol/g-cat	
			CO	1 µmol/g-cat	
			H$_2$	1.4 µmol/g-cat	

Table 2; *Overview of selected photocatalytic CO$_2$ reduction publications*

Catalyst	Phase	Reductant	Products formed	Yield of product	Reference
HNb_3O_8	Liquid-gas	H_2O	CH_4	7 µmol g cat^{-1}	Li *et al.* (2012)
Cu/TiO_2-SiO_2	Gas- Vapour	H_2O	CO	60 µmol g-cat^{-1} h^{-1}	Li *et al.* (2010)
			CH_4	10 µmol g-cat^{-1} h^{-1}	
CdS	Liquid-gas	Various solvents	CO (with acetonitrile)	0.7 µmol	Liu *et al.* (1998)
			Acetone (with acetonitrile)	1.8 µmol	
			HCOOH (with acetonitrile)	0.3 µmol	
$BiVO_4$	Liquid-gas	1.0 M NaOH	CH_3OH	35 µmol	Mao *et al.* (2012)
$CdS(Bi_2S_3)/TiO_2$	Liquid-gas	$NaOH/Na_2SO_3$ in water	CH_3OH	224.6 µmol/g	Li *et al.* (2012)

Table 2 (continued); *Overview of selected photocatalytic CO_2 reduction publications*

1.7 Photocatalytic H_2 Production

Research and development into photocatalytic water splitting technology has become abundant with emphasis on both catalyst and system design (Maeda, 2011; Midilli and Dincer, 2008). The process of H_2O splitting on the surface of a photocatalyst is shown in Figure 11. The splitting of pure H_2O into H_2 and O_2, shown in Equation 3, is described as an 'uphill reaction' where a large positive change in the Gibbs free energy is observed (ΔGo = -238 kJmol-1) (Maeda, 2011). To achieve H_2O splitting the conductance band of the catalyst must be more negative than the reduction potential of H^+ to H_2 (0 V vs NHE at pH 0), Equation 4. The valence band must also be more positive than the oxidation potential of H_2O to O_2 (1.23 V vs NHE) (Maeda, 2011). As the process of pure H_2O splitting is challenging to achieve due to the exergonic nature of the reaction, sacrificial reagents such as methanol, sodium sulphate, triethanolamine (TEA) and oxalic acid are often employed to determine the activity of a selected photocatalytic system.
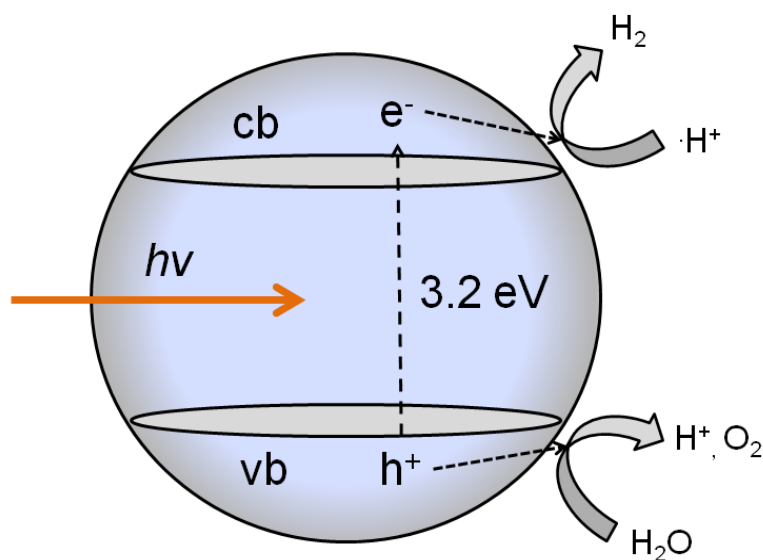
Figure 11; *Processes that occur upon photo-excitation of TiO$_2$ during H$_2$O splitting*

Systematically the concept of clean energy driven large scale photocatalytic H_2O splitting is reliant on two factors; the efficient delivery of natural photons and the transfer of target species to photocatalyst surfaces. This simple concept is illustrated in Figure 12.
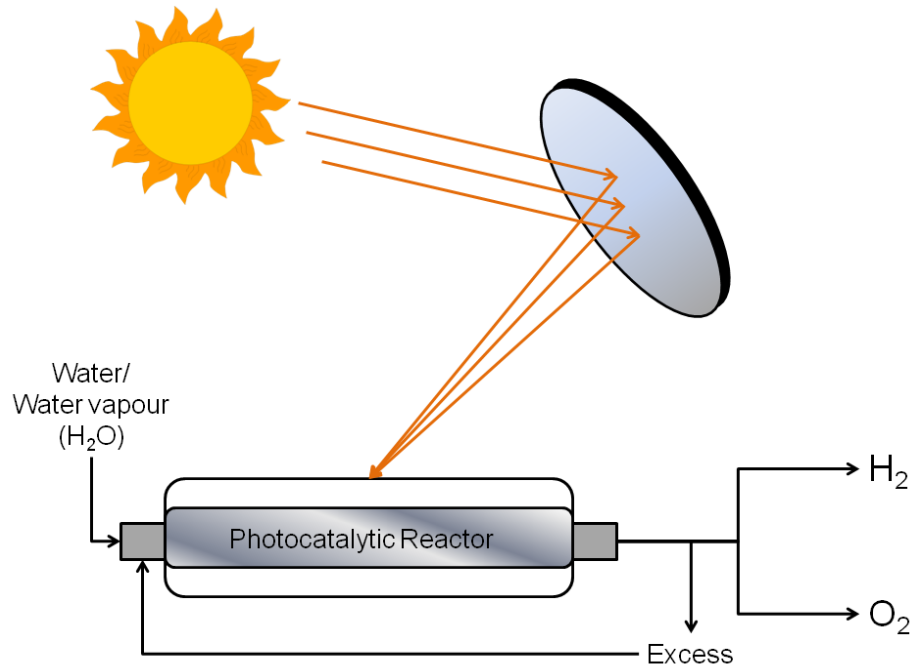
Figure 12*; Systematic illustration of H_2O splitting under natural light*

The efficient delivery of photons and increase of mass transport can be optimised by the choice of photocatalyst platform, reaction medium and reactor configuration. The photocatalyst platform and reactor configuration can dictate the mass transport limitations of the system and the impact of downstream processing costs, while the reaction medium may need to contain sacrificial electron donors (SED) to enhance the efficiency of the process.

1.7.1 H$_2$ Producing Photocatalysts

While the schematic in Figure 12 illustrates the potential simplicity of the system, there are challenges which must be addressed to achieve high quantum efficient photocatalytic systems.

Jing *et al.* (2010) described the challenges faced in order to achieve high quantum efficiencies for catalysts which already have the appropriate band gap for the process as:

- Quick electron/hole recombination in the bulk or on the surface of semiconductor particles
- Rapid back reactions of oxygen and hydrogen to reform H$_2$O on the surface of a catalyst
- Inability to efficiently utilise natural light
- Separation of hydrogen and oxygen gas as they are produced simultaneously

Figure 6 shows a selection of semiconductor catalysts which have a band gap structure suitable for the splitting of H$_2$O. Further examples of catalysts which have generated H$_2$ from the H$_2$O splitting are summarised in Table 3. Of the catalysts illustrated CdS has been extensively used to generate high levels of H$_2$. The use of CdS as catalyst has the drawback of photocorrosion and is therefore often incorporated into mesoporous structures or combined with other photocatalysts including TiO$_2$, ZnO and ZnS in an attempt to lower the risk of, or prevent photocorrosion Liu *et al.* (2012).

Recently Liu and colleagues (2012) investigated the efficiency of CdS incorporated into a mesoporous structure (MCM-41) along with the impact of Ti and Zr doping for the production of H$_2$ from H$_2$O splitting. The experiment was performed in a standard Pyrex glass vessel with illumination provided from a 300 W Xe lamp with a 430 nm cut off filter. The report concluded that the catalysts CdS/Zr$_{(0.005)}$-MCM-41 and CdS/Ti$_{(0.02)}$-MCM-41 with surface areas of 655.6 and 138.4 m^2 g^{-1} respectively showed the highest production of H$_2$ in a triethanolamine solution; ~ 30 µmol and 47.11 µmol of H$_2$ evolution after 5 hrs of illumination for CdS/Zr$_{(0.005)}$-MCM-41 and CdS/Ti$_{(0.02)}$-MCM-41 respectively.

High efficiencies of H_2 production over novel catalysts has been reported in the literature at the laboratory scale; Wei *et al.* (2009) reported 354 cm^3 g^{-1} H_2, Wang *et al.* (2012) reported 188.25 μmol h^{-1} g^{-1}. H_2 while Lin and Chang (2010) achieved 3522 μmol h^{-1} g^{-1}. The optimum conditions of the system illustrated in Figure 12 is the photocatalytic splitting of pure H_2O in the absence of a SED. A NiO-loaded $NaTaO_3$ doped with lanthanum catalyst was employed for the splitting of pure H_2O in the investigation by Kato *et al.* (2003). While the irradiation source was UV the quantum efficiency of the system was 56 %. The particles were found to have a high crystallinity which when coupled with the small particle size (0.1-0.7 μm) encouraged the reaction between the photogenerated electrons/holes with H_2O molecules over that of the recombination process. The presence of lanthanide ions was found to significantly increase the photocatalytic activity with optimum loading being 2 % producing 19.8 μmol h^{-1} of H_2.

1.7.2 Photo Reactors for H_2 Production

Whilst the production of H_2 and reduction of CO_2 are both viable methods as solar fuel generators, the latter is far more challenging than the former. As such catalyst and reactor development in H_2 production has progressed more rapidly than CO_2.

If photocatalytic production of H_2 is to be utilised as an alternative fuel, however, it is essential that the development of photocatalytic reactors focuses towards systems which are capable of converting solar energy. As already discussed in relation to CO_2 solar reduction there are considerations which much be addressed for reactor design. Discussed hereafter are examples of reactors capable of solar H_2 production.

Jing *et al.* (2009) discussed that the conversion of solar energy to storable H_2 for use as a fuel and alternative energy source is an efficient way of harvesting sunlight. In addition they hypothesised that the use of a solar concentrator can ensure full utilisation of solar radiation which arrives at the surface of the Earth.

Contrary to other publicised work in the literature (Liu *et al.* 2012), Jing *et al.* 2009 stated that a solar reactor cannot be designed without first concentrating natural sunlight in an attempt to enhance the intensity. An example of a solar

concentrator can be seen in the review published by Malato *et al.* (2002) which discussed the work carried out at the Plataforma Solar de Almeria focusing on photocatalytic degradation of water contaminants. The review discussed the use of solar concentrators such as on line-focus parabolic trough concentrators (PTCs) and Compact Parabolic Concentrator (CPC) for incorporation into reactor designs for wastewater treatment. An example of a two-axis PTC is shown in Figure 13.
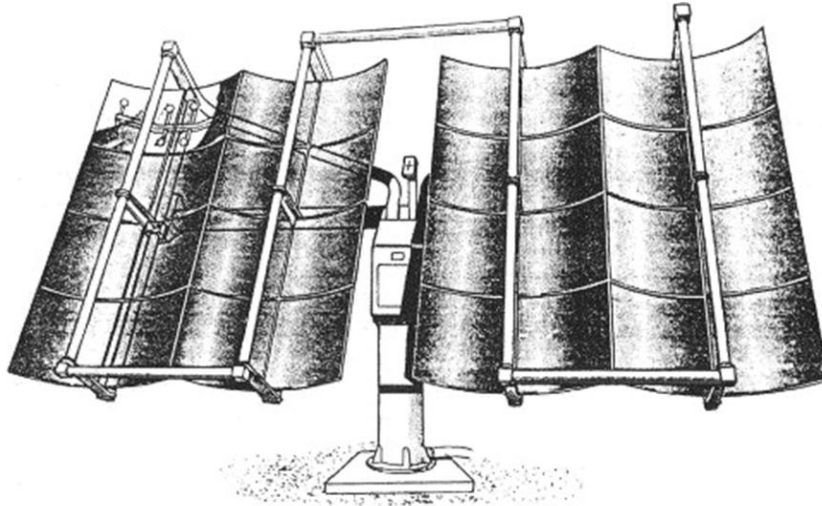
Figure 13*; Illustration of a two-axis PTC (Malato et al., 2002)*

The production of H_2 from water in a solar photocatalytic reactor in the literature is limited with the primary focus generally on photocatalytic detoxification and H_2 production from hydrogen sulphide (Jing *et al.*, 2010). Production of H_2 from hydrogen sulphide over semiconductor particles (platinised CdS) using solar irradiation has previously been reported (Linkous *et al.*, 1994; Linkous *et al.* 1995) along with H_2 from a sulphide/sulphite solution over CdS/ZnS (Koca and Sahin, 2002). While examples of solar photocatalytic reactor development for detoxification can be seen in publications by Minero *et al.* (1993) Gernjak *et al.* (2004), Malato *et al.* (2002) and Goslich *et al.* (1997).

Jing *et al.* (2010) investigated the use of a CPC based unit for the development of a solar photocatalytic system for the production of H_2. The research group developed three H_2 producing reactors which are shown in Figure 14. This series of reactors were constructed to demonstrate the process of reactor development from lab scale to outdoor demonstration scale with Figure 14 (a) demonstrating a

small scale closed circulation system, (b) showing a scaled up hydrogen producing reactor activated by simulated solar light and (c) a large scale CPC-based reactor under direct solar light.
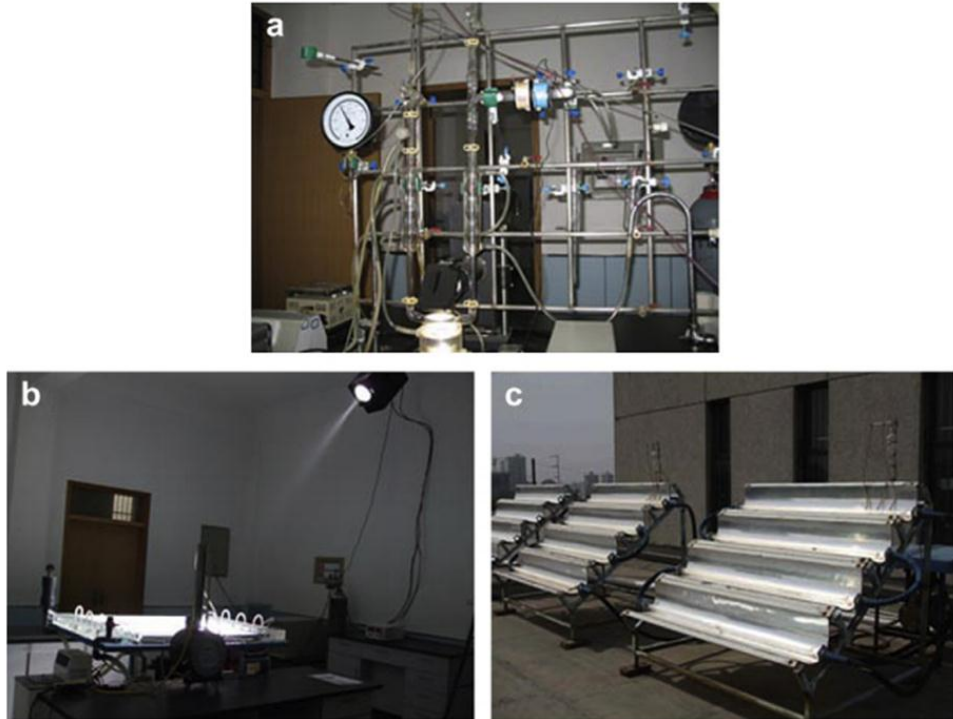
Figure 14; *Images of (a) a small scale closed circulation photocatalytic systems, (b) scaled up SPHR under simulated solar light and (c) SPHR with CPC under direct solar light (Jing et al., 2010)*

The evaluation of the large scale CPC-based reactor under direct solar irradiation was carried out by Jing *et al.* in 2009. The reactor was comprised of CPC and tubular photo reactors for the evolution of H_2 production from non pre-treated H_2O. A schematic of the experimental set up is shown in Figure 15. As can be seen the unit was comprised of fourCPC modules, which were inclined at 38 ^{0} for exposure to solar radiation. Exposure of solar irradiation via the CPC resulted in the evolution of H_2 which was monitored by a GC. The reaction medium was composed of non pre-treated tap water, CdS (photocatalyst) and SED (Na_2SO_3, Na_2S). The results show that H_2 production was achieved in the system with 300 mL of H_2 production recorded after 1 hr. Under optimum conditions a H_2 production rate of 1.88 L/h was recorded.
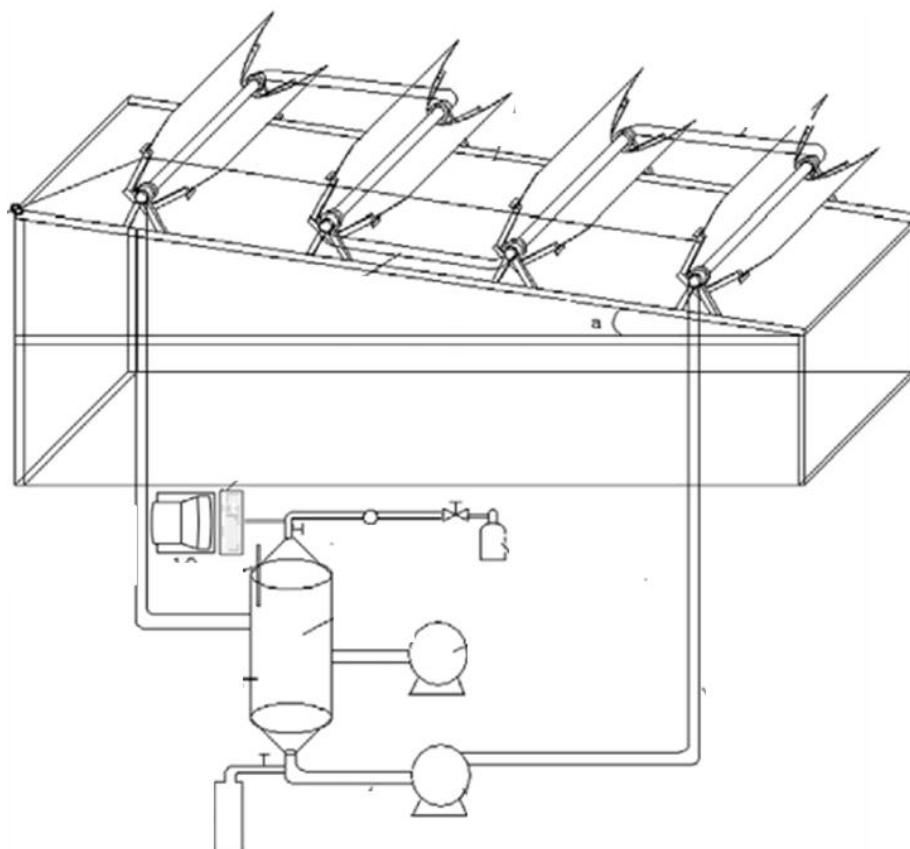
Figure 15*; Schematic of Jing et al. (2009) CPC solar photocatalytic reactor*

Reference	Catalyst	Reductant	Illumination source	Products	Yield of product
Wang *et al.* (2012)	(Pt-loaded) Bi1-xSmVO$_4$	Na$_2$SO$_3$/AgNO$_3$	300/500 W Xe lamp	O$_2$	95.90 µmol h^{-1} g^{-1}
				H$_2$	188.25 µmol h^{-1} g^{-1}
Liu and Syu (2012)	N-doped mesoporous TiO$_2$	CH$_3$OH	450 W Xe lamp with 420 nm cut off	H$_2$	14.9 µmol g^{-1} h^{-1}
Li *et al.* (2009)	H$_{2.33}$Sr$_{0.97}$NbO$_{14.335}$/Pt	CH$_3$OH	100 W mercury lamp	H$_2$	153.1 cm^3 h^{-1} g^{-1}
Khan and Qureshi (2012)	BaZr$_{0.96}$Ta$_{0.04}$O$_3$	Pure H$_2$O	300 W Xe lamp	H$_2$	180 µmol/h
				O$_2$	90 µmol/h
Lin and Chang (2010)	Au/KTiNbO$_5$	CH$_3$OH	400 W medium-pressure halide lamp	H$_2$	3522 µmol g^{-1} h^{-1}

Table 3; *Overview of selected photocatalytic water splitting publications*

Reference	Catalyst	Reductant	Illumination source	Products	Yield of product
Fan *et al.* (2010)	$ZnIn_2S_4$/fluropolymer fibre composites	Na_2SO_3/Na_2S	350 W Xe lamp	H_2	9.1 mL/h
Li *et al.* (2012)	S-doped WO_3	Fe^{3+}	250 W high pressure mercury lamp (UV)	O_2	99.9 mol L^{-1} g^{-1} h^{-1}
			250 W high pressure Xe lamp (vis)	O_2	76.7 mol L^{-1} g^{-1} h^{-1}
Wei *et al.* (2009)	$HLaNbO_2O_7$:In/Pt	CH_3OH	100 W mercury lamp	H_2	354 cm^3 g^{-1}
Jeong *et al.* (2006)	Ni/$Sr_3Ti_2O_7$	Pure H_2O	400 W high pressure Hg lamp	H_2	164 µmol/h
				O_2	~80 µmol/h
Yan *et al.* (2009)	NiO modified $La_{0.02}Na_{0.98}TaO_3$	Pure H_2O	400 W high pressure mercury lamp	H_2	3.57 µmol h^{-1} g^{-1}
				O_2	1.77 µmol h^{-1} g^{-1}

Table 3 (continued); *Overview of selected photocatalytic water splitting publications*

1.8 Summary of Reactors in the Literature

Photocatalysis is dependent on three factors; the distribution of photons, a highly efficient photocatalyst and reactor configuration. The recognition that all three factors are essential for efficient photocatalysis to take place is of high importance. The focus of work presented here is on the evolution of reactor design towards the objective of CO_2 reduction and H_2 production.

A number of reactor designs have been reported in the literature including the annular photo reactor (Imoberdorf *et al.*, 2007), packed bed photo reactor (Mehrvar *et al.*, 2002), photocatalytic Taylor vortex reactor (Sczechowski *et al.*, 1995), fluidised bed reactor (Dibble and Raupp, 1992), OFPR (Peill and Hoffmann, 1995), falling film reactor (Li Puma and Yue, 1999), thin film fixed bed sloping plate reactor (Adams *et al.*, 2008), swirl flow reactor (Ray and Beenackers, 1997) and the corrugated plate reactor (Zhang *et al.*, 2004).

Examples of reactor schematics found in the literature are shown in Figure 16, Figure 17 and Figure 18, which display an annular flow photo reactor, rotating disc reactor and rotating drum reactor respectively. A comprehensive review of reactors in the literature has been summarised in Table 4 and Table 5. Table 4 summarises reactors which have used thin film catalyst coatings on a solid support (immobilisation) to achieve photocatalytic degradation and conversion, while Table 5 details reactors that deployed catalysts in powder form.
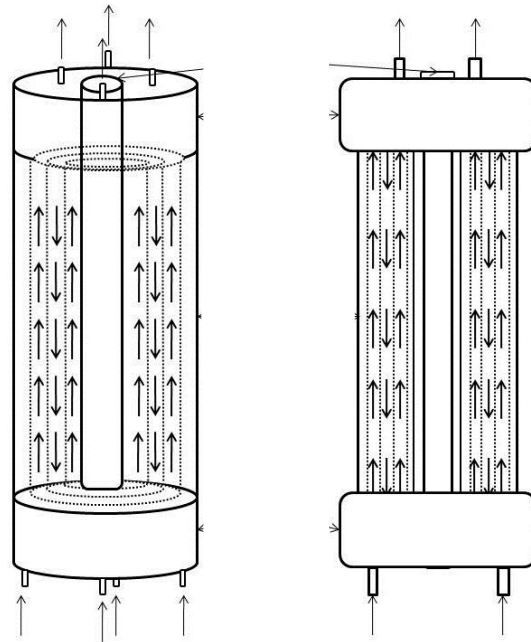
Figure 16; *Schematic of annular flow photo reactor (Imoberdorf et al., 2007)*
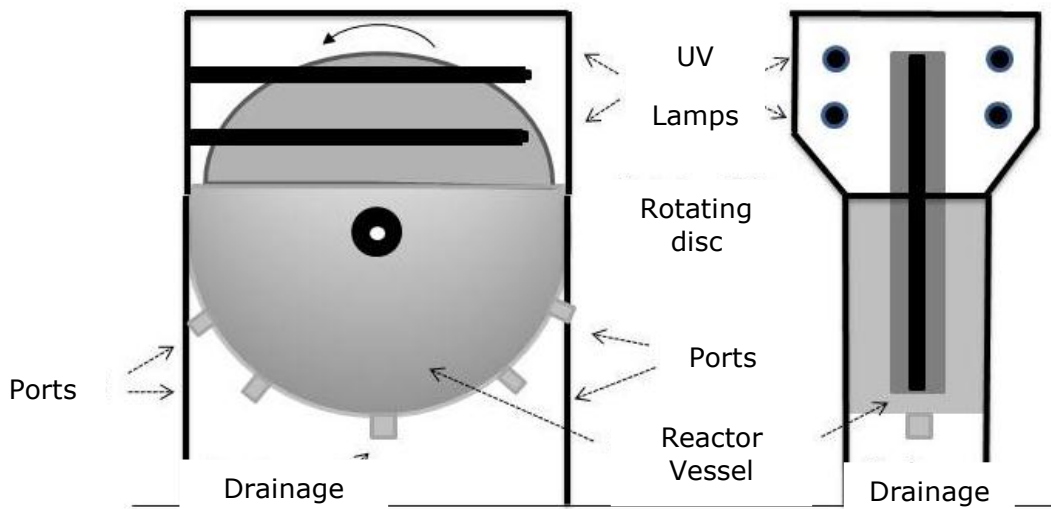
Figure 17; *Schematic of a rotating disc photo reactor (Dionysiou et al., 2000)*
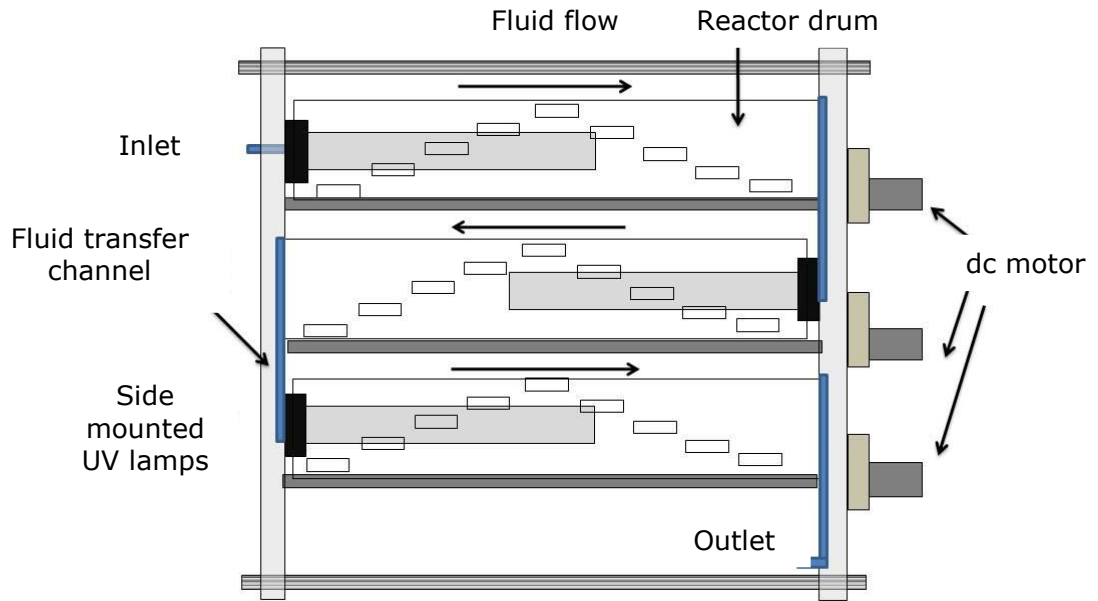
Figure 18; *Schematic of rotating drum photo reactor (Adams et al., 2008)*

Reactant phase	Reactor Name	Evaluation	Catalyst	Reference
Liquid	Optical Fibre Photo Reactor (OFPR)	Degradation of 4-chlorophenol	TiO_2 on quartz fibre cores	Hoffmann and Peill (1995)
	Rotating Disc	4-Chlorobenzoic acid degradation	TiO_2 (coated commercial ceramic and glass balls)	Dionysiou *et al.* (2000)
	Fixed Bed	Waste water treatment	TiO_2	Alexiadis and Mazzarino, (2005)
	Carberry photoreactor	4-chlorophenol degradation	TiO_2 (P25) on sodium glass support.	Cernigoj *et al.* (2007)
	Corrugated plate	4-chlorophenol degradation	TiO_2 (P25)	Zhang *et al.* (2004)
	Spiral photoreactor system (SPS)	4-*tert*-octylphenol	TiO_2 thin film	Wu *et al.*, (2012)
Gas	Circulated system	CO_2 reduction	TiO_2 (P25), ZrO_2	Lo *et al.* (2007)
Vapour	Carbon foam-based photoreactor	Gaseous CH_3OH oxidation	TiO_2 (P25) supported on carbon foam	Hajiesmaili *et al.* (2010)

Table 4; *Tabulated summary of immobilised photo reactors in the literature*

Reactant phase	Reactor Name	Evaluation	Catalyst	Reference
Liquid	Photocatalysis-Ultrafiltration Reactor (PUR)	Fulvic Acid	TiO_2 (P25)	Fu *et al.* (2006)
	Rotating Drum Reactor	Hydrocarbons	TiO_2 (P25)	Adams *et al.* (2008)
	Taylor Vortex	Formate acid	TiO_2 (P25)	Sczechowski *et al.* (1995)
	Fountain	Indigo carmine oxidation	TiO_2	Li Puma and Yue (2001)
	Falling film slurry	Salicylic acid oxidation	TiO_2 (P25)	Li Puma and Yue (1999)
		H_2 production	CdS	Agarwal and Bhaskarwar (2007)
	Internally circulating slurry bubble column reactor	TCE	TiO_2 (P25)	Jeon *et al.* (2005)
	Concurrent downflow contactor reactor (CDCR)	2,4,6-trichlorophenol (2,3,6-TCP)	TiO_2 (VP Aeroperl P25/20)	Ochuma *et al.* (2007)
	Hybrid low-pressure submerged membrane photoreactor	Removal of bisphenol A	TiO_2 (P25)	Chin *et al.* (2007)
	Hybrid photoreactor	Azo dye – reactive blue 69	TiO_2 (P25)	Orozco *et al.* (2009)
	Slurry reactor-immersed membrane	Synthetic wastewater	TiO_2 (P25)	Erdei *et al.* (2008)

Table 5; *Tabulated summary of suspended photo reactors in the literature*

Reactant phase	Reactor Name	Evaluation	Catalyst	Reference
Liquid	Novel labyrinth bubble photocatalytic reactor	Methyl orange degradation	TiO_2 immobilised on quartz glass. (Used in suspension)	Hao *et al.* (2009)
	Fluidised bed photoreactor	Microcystin-LR destruction	TiO_2 coated activated carbon	Lee *et al.* (2004)
	Standard slurry photoreactor	Methylene blue degradation	AgBr/nanoAlMCM-41	Pourahmad *et al.* (2010)
			p-$CaFe_2O_4$/n-Ag_3VO_4	Shifu *et al.* (2009)
		Methyl orange oxidation	$Ag_2Mo_4O_{13\mu}$	Liu *et al.* (2011)
		H_2 production	$Nb_2Zr_6O_{17}-xNx$	Kanade *et al.* (2007)

Table 5 (continued); *Tabulated summary of suspended photo reactors in the literature*

1.9 Summary

The discussion in this introduction chapter has demonstrated the need for an alternative fuel with low carbon content from renewable resources. In addition to this, to ensure global stability global warming must be constrained by the reduction in GHG gas emissions. The lowering of CO_2 emissions can be achieved with the transition from a high carbon system to a low carbon renewable system however, additional measures are still required to aid the reduction of current CO_2 levels.

Photocatalysis is an environmentally friendly alternative for CO_2 reduction and the conversion of solar energy for the production of fuels. The solar photoreduction of CO_2 is still in its infancy and requires further development to be considered a truly viable approach. While the efficiency of catalysts and simple CO_2 photocatalytic reduction systems is increasing there are no examples of large scale photocatalytic reactors being deployed for mass CO_2 reduction.

Alternatively solar H_2 production appears to be a more advanced technology for using solar energy on a larger scale. A number of photocatalysts, both traditional and novel are capable of splitting H_2O for the generation of H_2 and O_2 with increasing efficiencies. In addition to this, there are examples of large scale reactors being deployed for the treatment and splitting of H_2O under natural solar light.

The optimum objective would be the design and construction of a scalable photocatalytic system capable of utilising solar irradiation for the simultaneous reduction of CO_2 and generation of H_2. Intelligent design of the photocatalytic reactor could ensure the system had minimal downstream processing requirements and low maintenance which would encourage the viability of the system on a large scale.

1.10 Research Aims and Objectives

The primary aim of this research was the development of a photocatalytic design concepts, which were capable of reducing CO_2 and generating H_2. The project was conducted in collaboration with The University of St. Andrews and CalTech.

The focus of the collaborative partners was the synthesis of novel catalysts which would be deployed in the reactor concepts developed.

Photocatalytic reactor design development and evolution was an important aspect of this work and was a constant theme discussed in this research. The objective of Chapter 2 was to investigate a number of key reactor parameters including reactor geometry, construction materials, photo delivery systems and methods of increasing mass transport. These parameters would be evaluated through small scale reactor concepts, the results of which would aid the construction of the subsequent reactor design.

The objective of Chapter 3 was to investigate additional parameters including catalyst platform, the use of visible and solar light along with the potential for feasible scale up. This objective would be achieved through the design of a novel thin film reactor concept.

The data obtained from the evaluation of the initial reactor concepts in Chapter 2 and 3, coupled with the requirements put forward by the collaboration partners played an important role in the construction of the final reactor. The objective of Chapter 4 was to analyse the data obtained from the previous chapters in order to develop a reactor concept capable of achieving the primary aim of this research. A fluidised bed configuration was adopted for this design concept. An investigation into the reactor geometry, construction, fluidisation approach and illumination system was discussed.

The objective of Chapter 5 was to evaluate the performance of the fluidised bed design by monitoring the reduction of CO_2 and generation of H_2 over a series of novel catalyst developed by collaborative partners. The operational parameters of the fluidised bed reactor would be investigated in an attempt to enhance the photocatalytic activity of the system. The use of visible and solar illumination would also be investigated to demonstrate the potential of photocatalytic technology for the application of solar fuel generation.

Chapter 2 Design and Evaluation of Sparged Fluidised Photo Reactors

2.1 Introduction

2.1.1 Principle of Fluidisation

The key principles of efficient photocatalysis are the delivery of photons of appropriate wavelength along with increased contact time between reactant and catalyst and increased mass transport of target species to the surface of a catalyst. The process of catalyst fluidisation in a reaction medium can achieve the desired level of interactions, whilst maintaining an increased level of mass transport.

Fluidisation is the process by which a bed of particles are brought from a stationary, solid-like state to a dynamic fluid-like state (de Lasa *et al.*, 2005). This process is achieved by passing either gas or liquid through the bed of stationary particles. The introduction of gas or liquid into the static particle bed forces the flow to travel up through the bed and begin to agitate the particles. At low velocities, fluidisation is not achieved as the aerodynamic drag on particles is low preventing them from leaving a static position.

In order for fluidisation to occur the gravitational force placed on the particles must be counteracted by increasing the aerodynamic drag of the particles. This increase in drag can be achieved by increasing the velocity of gas which passes through the particle bed. Fluidisation is achieved when the gas velocity is increased to the level at which aerodynamic drag is equal to the gravitational force, at which point the particles will have fluidic characteristics. Increasing the gas velocity beyond this point forces the particles to behave erratically and will often result in them being carried away from the desired area of operation. The principle of fluidisation is described by the illustration in Figure 19.
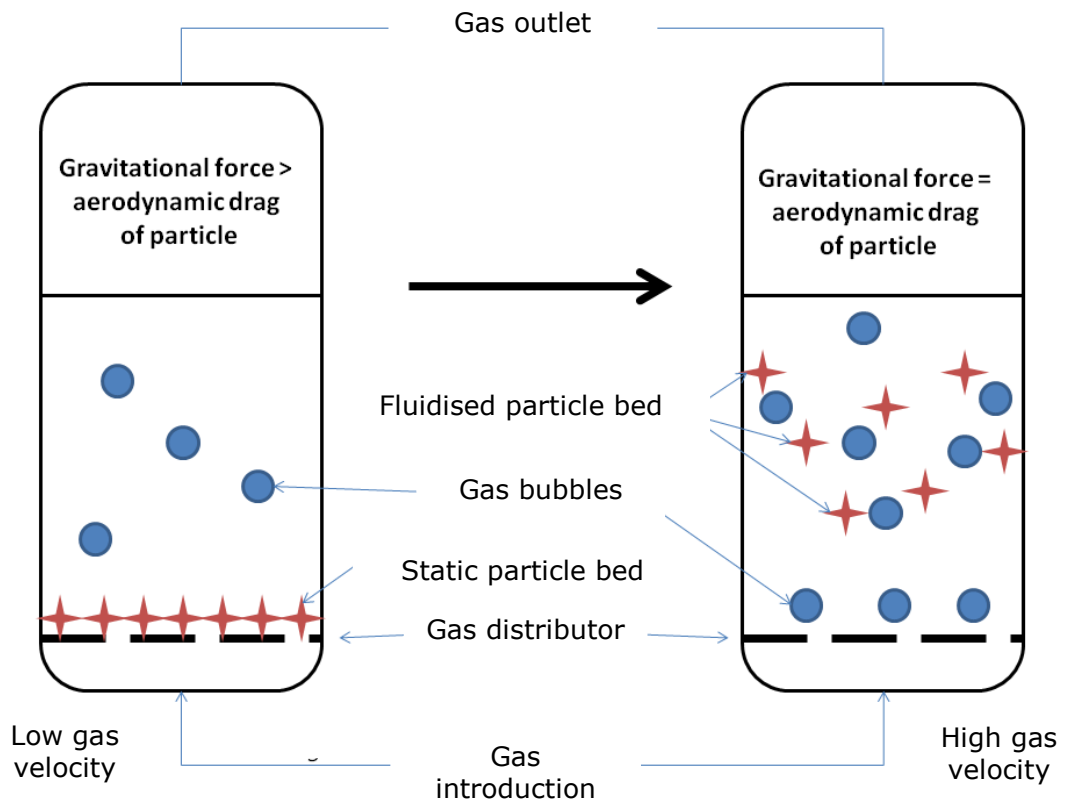
Figure 19*; Schematic illustration of fluidisation process*

Methods to achieve fluidisation in the literature include vibration (Voronstov *et al.,* 2000; Nelson *et al.,* 2007), sound-assistance (Gao *et al.*, 2011) sound-magnetic assistance (Si *et al.,* 2012), magnetic field assistance (Yao *et al.*, 2010) and gas distribution mechanisms (Foster and Bassiti, 2008). The advantages of using a fluidised reactor include a low pressure drop, high throughput and high photocatalyst surface area, allowing for increased catalyst-reactant interaction.

2.1.2 Fluidised Bed Reactors

While considered a relatively new tool in the field of chemical engineering, research has taken advantage of fluidised bed systems with the first applications in the gas and oil industry along with the air purification industry (Paz, 2010). In 1992, Dibble and Raupp used a flat plate fluidised bed reactor to oxidise trichloroethylene (TCE), Figure 20. During their investigation a quantum

efficiency range of 2-13 % was sustained with a reaction rate peaking at 0.8 µmol TCE (g of catalyst)$^{-1}$ min^{-1} [2 µmol/(g of TiO$_2$)$^{-1}$ min^{-1}]. These results are significant in that they were comparable to results produced in a liquid-solid slurry system for the oxidation of TCE, specifically demonstrating a 1 order of magnitude increase.
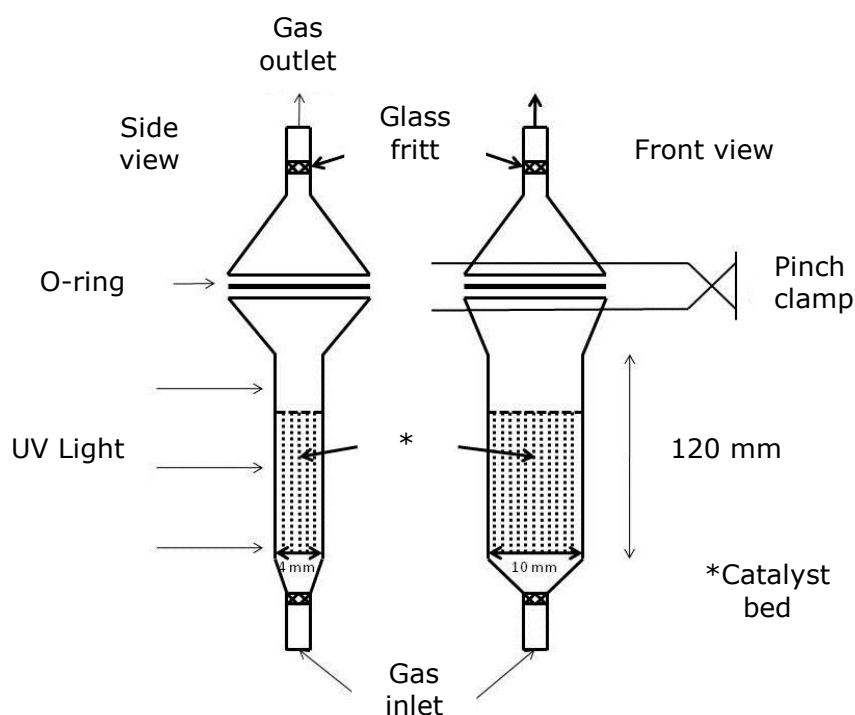
Figure 20; *Schematic of flat plate fluidised bed reactor (Dibble and Raupp, 1992)*

There has been a number of fluidised bed designs utilised for photocatalytic processes, Table 6. Discussed hereafter are selected examples of fluidised bed reactors used in photocatalysis.

Reactor	Phase	Evaluation compound	Catalyst	Reference
Flat plate fluidised reactor	Gas	Trichloro-ethylene (TCE)	TiO_2	Dibble and Raupp (1992)
Two-dimensional fluidised reactor	Gas	Nitric Oxide (NO)	TiO_2	Lim *et al.* (2000)
Circulating fluidised bed (CFB)	Gas	TCE	TiO_2 on silica gel support	Lim *et al.* (2005)
Fluidised bed reactor	Gas	Methanol	TiO_2, TiO_2/Al_2O_3	Nelson *et al.* (2007)
Vibrofluidised bed reactor	Gas	Acetone	TiO_2	Voronstov *et al.* (2000)
Fluidised photocatalytic reactor	Liquid	Azo dye/waste water	TiO_2 pellets	Foster and Bassiti (2008)
Three phase fluidised photocatalytic system	Liquid	Acetic acid and ammonia	$Al-TiO_2$	Son *et al.* (2005)
Sound assisted fluidised bed	Liquid	Formaldehyde	N-doped TiO_2	Gao *et al.* (2011)

Table 6; *Summary of selected fluidised photocatalytic reactors in the literature*

In order to achieve fluidisation the velocity which is introduced into a system must be of a sufficient level. Increasing the gas velocity of a fluidised system has also been reported to increase light transmission, which was demonstrated in a two-dimensional fluidised bed reactor to decompose NO (Lim *et al.,* 2000). Reported in the research was efficient contact between the catalyst (P-25) and reactant gas (NO) which, when coupled with good transmission of UV-light allowed for increased NO decomposition in comparison to an annular flow-type photo reactor. Lim and colleagues observed that increasing the superficial gas velocity increased light transmission, with light intensity significantly increasing at approx. 1.3 U_{mf} (minimum fluidisation velocity), which equated to a sharp increase in NO conversion. Based upon their results, Lim *et al.* concluded the

photocatalysis of NO decomposition requires sufficient residence time and a suitable NO gas velocity to form the proper bubble size allowing good contact between UV light and TiO_2-NO.

Traditionally, fluidisation is achieved by the upward velocity of gas or liquid, however an alternative approach using vibrational agitation of particles has been reported (Voronstov *et al.,* 2000; Nelson *et al.*, 2007). The performance of a series of fixed bed configurations were compared with that of a vibrofluidised bed system for the decomposition of gaseous acetone over granular photocatalysts. The vibrofluidised bed system was shown to be the most effective of the configurations with a quantum efficiency of 8.7 %. The high efficiency of the vibrofluidised bed was attributed to the use of external vibrations coupled with what Voronstov and colleagues called the 'periodic light phenomenon'. This phenomenon was caused by the unconventional movement of catalyst granules in the reactor which in turn allowed for increased absorption of scattered light.

The major limitation to the fluidisation of particles for photocatalytic processes is the potential 'drifting' of particles (Paz, 2010). This is a particular issue often observed when using P25 due to its micrometric size. TiO_2 is classified as belonging to Geldart group C which suggest it is difficult to fluidise (Si *et al.*, 2012). Fluidised bed reactors are often constructed based upon the Geldart grouping of particles which is based upon particle density and size.

In an attempt to ensure continued fluidsation of a particle, an unrequired level of velocity is often used, which can result in particles moving away from the main area of operation and towards areas not illuminated. The following approaches can be utilised to reduce this limitation:

- Reactor geometry to minimise drifting
- Deployment of a catalyst with increased density
- The coupling of small particles to large ones to ensure the particles do not drift

Combining TiO_2 with a larger particle such as Al (Son *et al.*, 2005), activated carbon (AC), glass beads (Kuo *et al.*, 2009) and Fe (Kang, 2003) in an attempt to overcome this drawback has been reported.

Kuo *et al.* (2009) investigated the removal of toluene vapours from a continuous gas stream over activated carbon (AC) and glass beads (GB) with a TiO_2 coating to promote good evenly distributed catalyst. The reactor used in the investigation was a three phase fluidised reactor and is illustrated in Figure 21. The degradation of toluene vapours was accredited to both the use of AC and photocatalysis, however, saturation resulted in certain restrictions when solely using AC. The results displayed that the combination of AC removal of toluene and the photocatalytic removal could significantly extend toluene removal duration. In comparing the effectiveness of the two catalyst types it was found that the GB/TiO_2 was half as effective as AC/TiO_2 for toluene removal. It was observed, however, that coating the catalyst onto the supports of AC and GB allowed sufficient fluidisation of the particles within the reactor without any loss, drifting or trapping of the photocatalysts.

Figure 21; *Image of three phase photocatalytic reactor used by Kuo et al. (2009) for the degradation of toluene*

Presented in this chapter is word conducted on two laboratory scale fluidised reactors. Photocatalytic operating parameters were investigated through the removal of fingerprint compounds. The delivery of illumination was also investigated along with the appropriate selection of lamp power. The results presented in this chapter indicated a suitable evaluation method approach, which could be applied to subsequent photo reactors. The results and observations reported here were also incorporated in the final design discussed in Chapter 4.

2.1.3 Catalyst Strategy and Development

The synthesis and development of novel catalysts in this project was performed by the University of St. Andrews and CalTech. The design strategy for the catalysts was to produce a visible light activated catalyst, which could be deployed in a novel photo reactor system. The catalysts were required to have a band gap energy of < 3.0 eV to ensure visible and solar light excitation. The primary purpose of the catalysts was the reduction of CO_2 and production of H_2. As a result the position of conduction band of the catalysts was a key parameter. A strong reduction potential was required to both reduce CO_2 to hydrocarbon products and to form H_2. The catalysts developed by the University of St. Andrews included:

- Pt-C_3N_4
- C_3N_4
- C_3N_4 (600 ^{o}C)
- TNT-C_3N_4
- $Sr_{0.97}NbO_3$

The catalysts developed by CalTech included:

- Cu-TNT-CdS
- $NaTaO_3$.La

The diffuse reflectance spectra for each of these catalysts are shown in Appendix I. These catalysts were developed to be deployed in units constructed at Robert Gordon University. The nature and form of the catalysts dictated the reactor construct and as such a number of design concepts were investigated, which are

described in the subsequent chapters. Evaluation of the early design concepts allowed the most appropriate unit to be developed for the catalysts to be deployed in. Due to the nature of the catalyst development, which was solely towards CO_2 reduction and H_2 production, they were not evaluated with the early design concepts presented in this chapter. The challenging issue of catalyst immobilisation onto a solid surface also restricted their use with the thin film reactor design discussed in Chapter 3. Therefore, the catalysts were deployed in the PFPR Model I and II units described in Chapter 4, with the results discussed in Chapter 5.

2.2 Experimental

2.2.1 Design Concepts of Small Scale Photo Reactors

2.2.1.1 Sparged Fluidised Photo Reactor (SFPR)

The Sparged Fluidised Photo Reactor (SFPR) was constructed to provide fluidisation of powdered photocatalysts via an open gas distributor. A standard separation funnel was utilised to form the body of the reactor which provided the advantage of a sustainable glass surface for illumination and shape to allow for even gas distribution. The borosilicate glass body allowed light transmittance in the range of 340 to 2000 nm. A narrow gas distributor located at the base of the unit also restricted catalyst trapping.

The SFPR used a sparging rig located at the base of the unit to supply an air supply. Air was introduced into the system by a Jun Aquarium Air Pump, Model ACO-5503. A tee split connector and one way valve were used to allow for a sparging line and sample line to be present. At the base of the reactor a sample tap was located which allowed the required volume of model compound to be extracted for analysis. The maximum capacity of the vessel was 250 mL with an operating capacity of 150 mL. A schematic of the unit is shown in Figure 22.
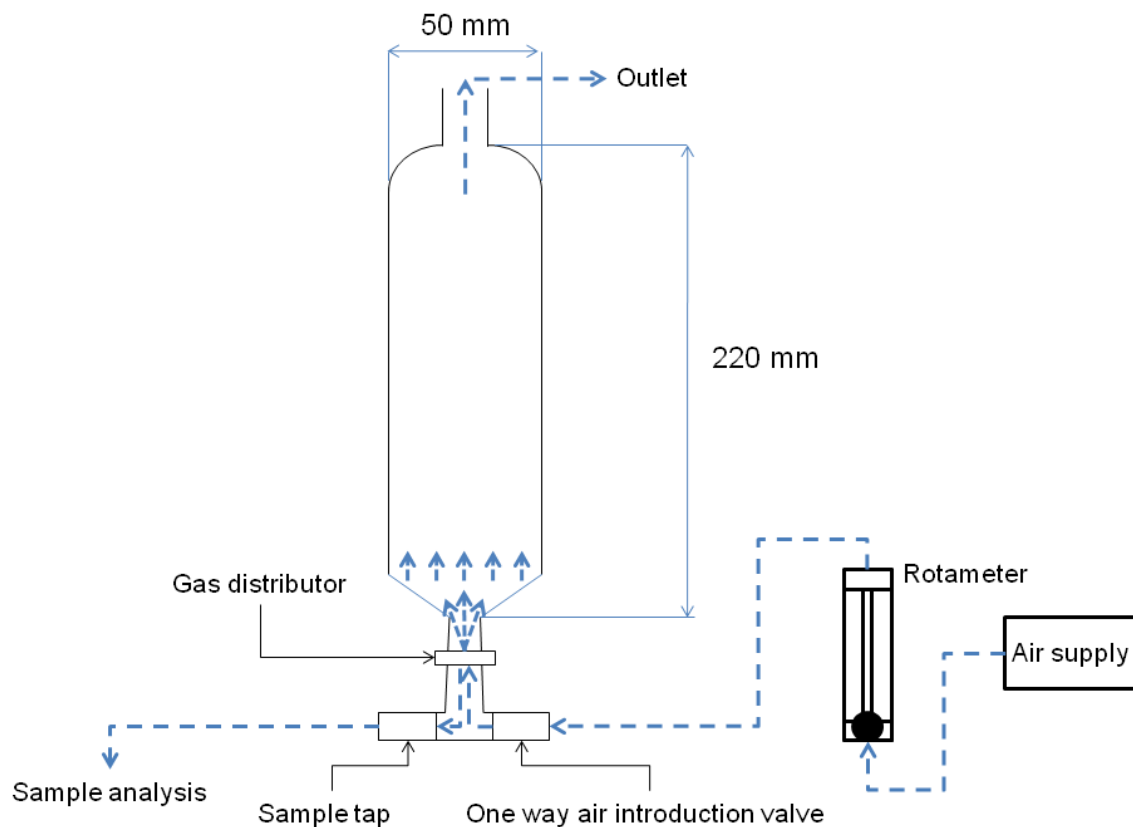
Figure 22; *Schematic representation of SFPR. Dashed arrows represent the direction of air flow*

Illumination was provided by four different UV based systems; a 500 W Dr. Hönle UV lamp, 2 arc structured lamps which each housed 6 individual strip lamps (providing 98 W of illumination), 1 arc lamp and a 36 W UV compact non integrated fluorescent lamp. Figure 23 details the position in which illumination was provided.

a.

b.

500 W UV
Lamp

200 mm

100
mm

c.

d.

Top View

8 W UV black
strip lights

100
mm

100
mm

Top View

8 W UV black
strip lights

100
mm
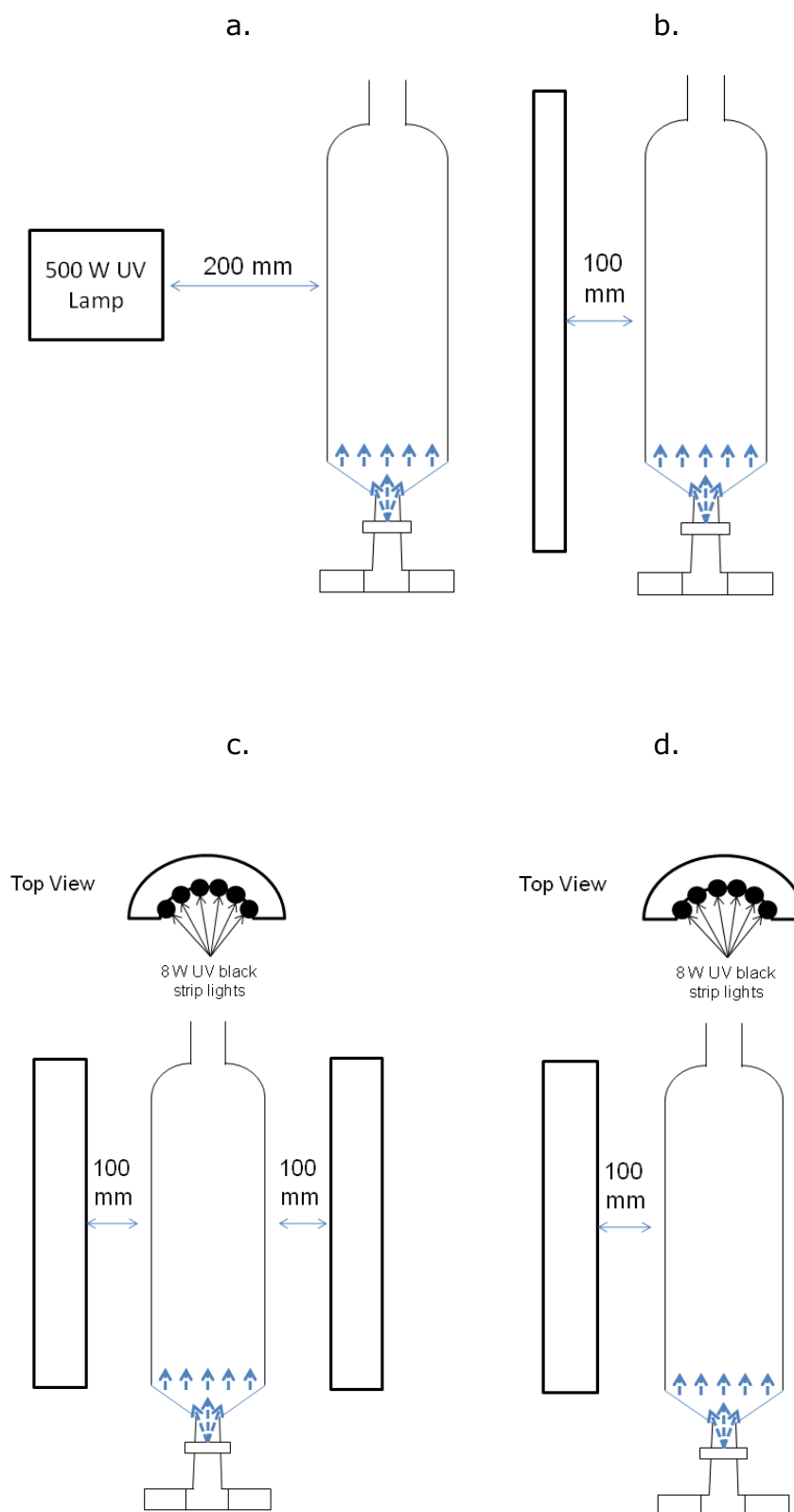
Figure 23; *Schematic representation of lamp position and distance from reactor.*
a. 500 W lamp, b. 36 W compact lamp c. 98 W arc lamps and d. 49 W arc lamps

2.2.1.2 Multi Chamber Photo Reactor (MCPR)

The Multi Chamber Photo Reactor (MCPR) was constructed to provide fluidisation simultaneously to fourreaction chambers, Figure 24. The reaction chambers were constructed of glass and positioned in a light containment box to increase maximum reflectance. Each individual vessel had a maximum capacity of 35 mL and an operational capacity of 15 mL. Sampling was achieved by needle extraction through a port in the lid of each vessel.
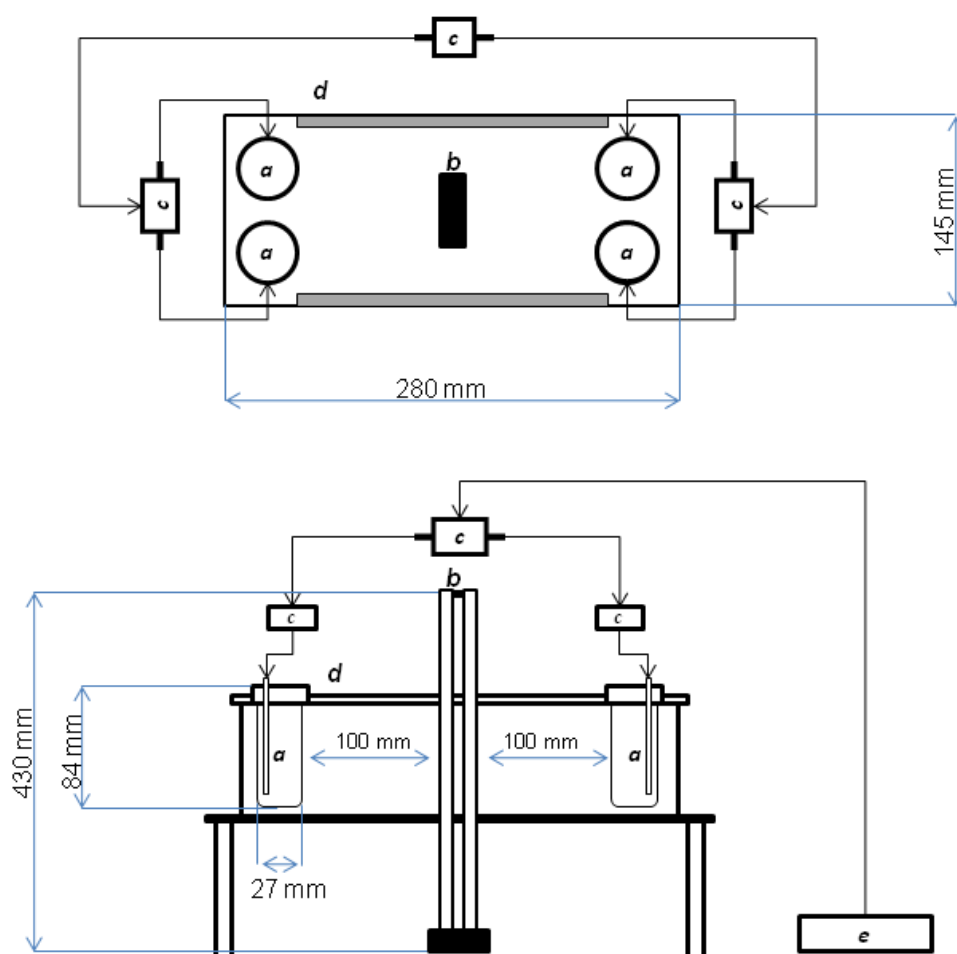
Figure 24; *Schematic representation of MCPR with a. glass reaction vessel, b. 36 W UV compact non-integrated lamp, c. stainless steel Swagelok tee fitting, d. aluminium lined light box with mirrors, e. air pump*

A sparging rig was constructed to allow a single air flow to be equally split to the fourreaction chambers. The sparging rig comprised of analytical tubing and fittings to ensure an equal distribution of air. A Swagelok SS 316 tee fitting initially split the air supply equally into two lines. A second tee fitting further was used to split each air line into two reaction vessel. A central glass rod with an open air distributor was positioned in each reaction vessel that provided fluidisation of the particles. Air was supplied by a Jun Aquarium Air Pump, Model ACO-5503.

The lamp containment box was constructed of wood with a mirrored and thin aluminium lined inner surface. A lamp was positioned centrally in the box with each vessel equally positioned in each corner of the box. Illumination was provided by a single 36 W compact non integrated fluorescent lamp. An image of the reactor is shown in Appendix I.

2.2.2 Evaluation

2.2.2.1 Dye Degradation

Evaluation was carried out using methyl orange (MO), rose bengal (RB) and congo red (CR) all from Sigma-Aldrich. The chemical structures of the dyes are shown in Appendix I. Detailed here is the general method applicable to all dyes discussed.

2.2.2.2 Photocatalytic Procedure

Table 7 details the typical parameters for the photocatalytic unit used. Standard stock solutions of dyes were prepared; 1×10^{-2} M MO (3.27 g in 1000 mL), 1×10^{-2} M RB (10.17 g in 1000 mL) and 1×10^{-2} M CR (6.96 g in 1000 mL). A predetermined volume and concentration of dye based upon the reactor being evaluated was introduced into the vessel; 150 mL for the SFPR, 15 mL for the MCPR; 1×10^{-5} M for MO and CR; 1×10^{-4} M for RB. Commercial catalysts TiO_2 P25 (Sigma Aldrich) and ZnO (Fisher Scientific) were deployed. The diffuse reflectance spectrum of P25 TiO_2 is shown in Appendix I.

Reactor	Dye	Lamp (W)	Irradiation time (min)	Sampling time intervals (min)	λ max (nm)	Catalyst
SFPR (Mark I and II)	MO	500	50	10	464	TiO$_2$
		96	50	10	464	TiO$_2$
		49	50	10	464	TiO$_2$
		36	50	10	464	TiO$_2$, ZnO
MCPR	MO	36	50	10	464	TiO$_2$, ZnO
	RB	36	50	10	548	ZnO
	CR	36	50	10	496	ZnO

Table 7; *Photocatalytic procedure details for the degradation of selected model dye compound*

The pH of CR and RB was adjusted to pH 9.6 using a carbonate-bicarbonate buffer (Sigma Aldrich). The pH of MO was not adjusted and was typically at pH 7.

Samples (1.5 mL) were taken at set time intervals based upon the time frame of the experiment. Separation of the catalyst from the model pollutant was done by syringe filtration using a Millipore 0.22 μm syringe filter and centrifugation by a Technico Mini Microcentrifuge, C1301B-230V (20 min at ~ 6000 rpm).

The PE of samples was calculated utilising the following equation:

$$PE(\%) = \left[\frac{T_O - T_s}{T_O}\right] * 100 \qquad \textbf{Equation 18}$$

Where 'PE' represents photodegradation efficiency, 'T_O' represents the initial concentration of the reaction medium and 'T_s' represents the concentration of the sample being analysed. Each experiment conducted was given a dark equilibrium

period representing $1/5^{th}$ of the entire reaction time frame. A sample was taken before and after the dark period to calculate the level of dark absorbance using Equation 18.

2.2.2.3 Illumination Sources

UV lamps in the range of 36 W - 500 W were used. The lamps used were spectrally analysed using a Stellarnet EPP2000 Spectrometer to determine their exact emissions. The spectral outputs of the lamps are shown in Appendix I. The emission spectra of the 36 W PL-L UV lamp (Philips, Model CLEO) shows a large UV peak at 350 nm and a sharp shoulder peak at 353 nm. The other visible emissions can be seen at 404, 436, 546 and 578 nm. The spectra of the 49/98 W and 500 W lamp show strong UV peaks at 366 and 368 nm respectively, Appendix I.

2.2.2.4 UV-Visible Spectrometry Analysis of Dye Degradation

Analysis was carried out by UV-Visible analysis to monitor the absorbance levels of individual dyes. To identify the absorbance peak of each dye a scan from 300 to 800 nm of known concentration was performed, Appendix I. The scans identified the primary peak of MO at 464 nm, RB at 544 nm and CR at 498 nm. A wave program function was then applied at the specific wavelength, identified by the scan, to measure absorbance of each sample.

Samples were analysed by a Perklin Elmer UV-Vis Spectrophotometer and concentrations of unknown samples were determined by comparison to a standard calibration graph for each individual dye, Appendix I.

2.2.2.5 HPLC Analysis of Dye Degradation

The instrument used for the investigation of the MO degradation pathway was a Waters 2695 Separation Module (Waters, Elstree, UK). High resolution photodiode detection was performed with a Waters 2996 Photodiode Array Detector (PDA) (Waters, Elstree, UK). Separation of analytes was performed with

an Atlantis C18 column 2.1 mm x 150 mm inner diameter, with a 5 μm particle size (Waters, Elstree, UK). The analysis was performed using an isocratic gradient with a mobile phase comprised of 10 mM ammonium acetate and acetonitrile (C_2H_3N) (Rathburn, Walkersburn, UK) (76:24). The flow rate applied was 0.2 mL min^{-1}. The PDA resolution was set to 1.2 nm and data was acquired in the range of 300 to 600 nm. The wavelength used to analyse MO was 462 nm. Column temperature was set to 40 °C. The identification of MO was carried out based upon retention time and UV-Vis absorbance of a standard MO sample shown in Appendix I. A 1 x 10^{-4} M starting concentration was used and photocatalytic degradation was carried out over 1 % ZnO, 40 min illumination from a single 36 W UV lamp with samples taken at 5 min intervals.

2.3 Operational Testing of the SFPR

Evaluation of a photo reactor is of importance to determine the limitations of operation. There are broadly two rate limiting steps in photocatalytic reactors; mass transport limitations and sufficient exposure of catalyst to illumination. Evaluation of a reactor is capable of determining the ability to which the unit overcomes these rate limiting steps.

The SFPR ensured movement of catalyst and model pollutant via sparging fluidisation. An air supply was introduced into the vessel via an open air port distributor, forming bubbles to agitate the photocatalyst. This provided the system with the following advantages; control over the formation of bubbles and velocity of air introduced, increased mass transport and electron hole scavenging through the increased concentration of O_2.

As a result of these advantages the catalyst was kept at an optimum suspended state within the reaction medium allowing for appropriate exposure to illumination. The fluidisation of a catalyst bed is also capable of increasing light penetration. Agitation by fluidisation is described as being 'random' in comparison to more traditional methods which utilised magnetic stirrers and plates. Magnetic stirrers create uniform movement of catalyst within a reaction medium which results in suspension of catalyst particles.

This random movement is capable of utilising the random light phenomenon which has been described in the literature (Voronstov *et al.,* 2000). The phenomenon states the random movement of particles within a reactor are more likely to absorb scattered light than that of particles that move in a uniformed fashion (i.e. stirred reactors).

Discussed here is the investigation into varying operational parameters of the SFPR including; illumination source, catalyst and gas velocity. In addition the degradation pathway of MO in the SFPR is investigated by HPLC.

2.3.1 Effect of Illumination

The results of the effect of illumination upon MO degradation in the SFPR are highlighted in Table 8 and Figure 25. The results of increasing the lamp power are shown in Table 8, detailing removal rates and removal of MO per watt. As indicated by results, the greatest ratio was observed for the 36 W lamp due to the low power output and increased removal level of MO, 0.025 x 10^{-5} M W^{-1}.

Power	PE (%)	Rate (x 10^{-5} M hr^{-1})	MO Removal/W (x 10^{-5} M W^{-1})
36	96.5	1.16	0.025
49	97.5	1.18	0.019
98	99.2	1.19	0.009
500	98.1	1.18	0.002

Table 8; *Summary of MO removal by varying illumination power*

The highest removal of dye recorded was 99.2 % under illumination from two arc structured array lamps (98 W). The removal achieved by additional lamps was 96.5, 99.2 and 98.1 % for 36, 98 and 500 W lamps respectively. The fastest rate

of degradation within the initial 10 min illumination period was achieved under the 500 W lamp at a rate of 0.084 x 10^{-5} M min^{-1}. This is comparable to 0.075 x 10^{-5} M min^{-1} under the 36 W lamp and 0.08 x 10^{-5} M min^{-1} under the 98 W lamp.
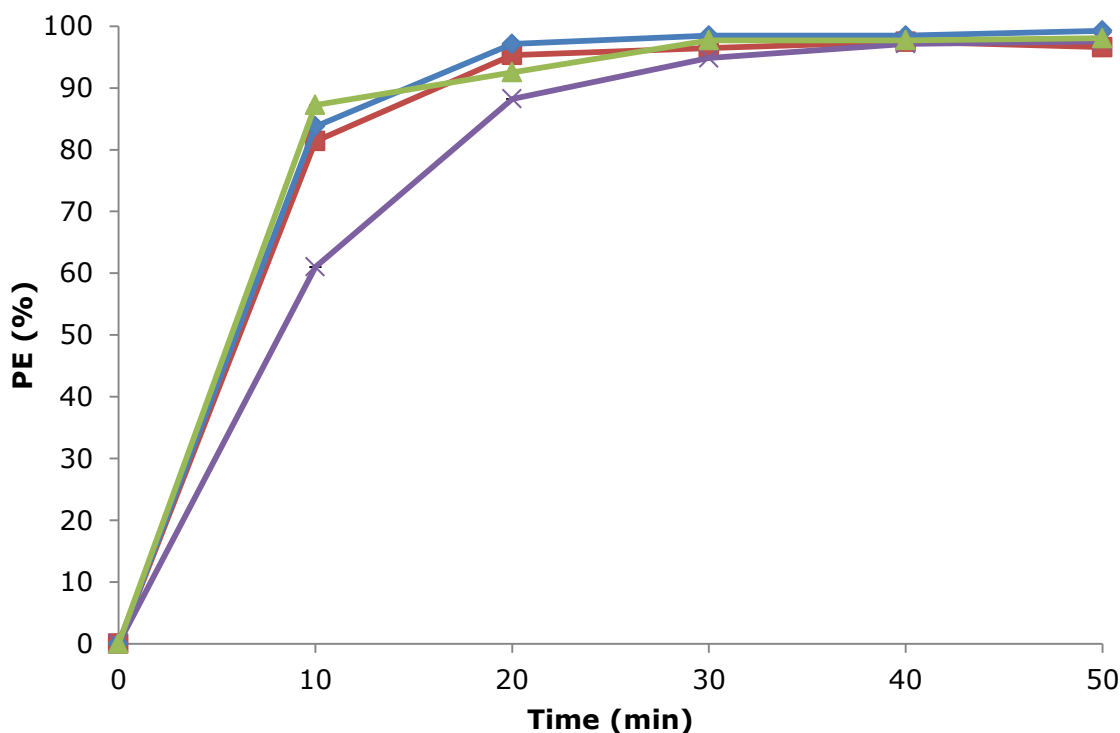
Figure 25; *PE of MO over TiO$_2$ P25 in the SFPR with a 500 W lamp (green Δ), 98 W lamp (blue ◇), 49 W lamp (purple ¤) and 36 W lamp (red □). Conducted under aerobic conditions at pH 7.*

Control tests were performed under photolysis conditions in the absence of a catalyst to show the removal of MO was primarily a result of photocatalysis. The lowest removal of MO under these conditions was 3.7 % under the 36 W lamp. In contrast the 49, 98 and 500 W lamps produced photodegradation efficiencies of 12.19, 20.85 and 19.56 % respectively, suggesting degradation under these illumination sources was not purely photocatalytic. The increased power of the 500 W and 98 W lamp, along with the 360 ^{O} exposure provided by the 98 W lamp, resulted in the increased MO degradation by photolysis. In contrast the low power of the 36 W lamp prevented significant photolysis degradation occurring. Furthermore, the 36 W lamp has low energy consumption, high life time and was

versatile to positioning and inclusion into reactor designs as either a sole illumination source or as part of an illumination array. This level of versatility was not observed when using the 49, 98 and 500 W lamps.

The results showed that increasing lamp power can have a minimal and negative impact in a photocatalytic system. The primary purpose of the lamp was to promote catalyst excitation. In order for this to happen the lamp used was required to provide sufficient energy to allow an electron in the valence band to travel across the energy band gap to the conduction band. As TiO_2 was deployed the energy band gap was 3.2 eV and thus a wavelength of approximately 388 nm was needed. The lamp spectra and rate of recombination could explain the impact of lamp power on PE of MO. The lamp spectra of the lamps used are shown in Appendix I and a narrow peak was recorded for the 49/98 W and 500 W lamp at 366 and 368 nm respectively. In contrast, the 36 W lamps showed a broader peak at 350 nm. TiO_2 is expected to show increased activity when using a shorter wavelength range such as 315-360 nm. Taken into consideration the glass surface transmitted light from 350 nm, the output of the 36 W lamps at 350 nm may have increased catalyst excitation. In relation to the rate of recombination, significantly increasing the power of the lamp could promote an increased number of electros to travel to the conduction band. If the number of electrons promoted are not trapped in the surface nor accepted by O_2 the result will be electron hole recombination.

2.3.2 Effect of Gas Velocity

Two commercial catalysts, P25 and ZnO, were investigated in relation with gas velocity. Figure 26 shows the removal of MO over P25 and ZnO, after 2 mins illumination and 10 mins illumination over a range of gas velocities. Two observations were recorded including the comparable level of PE by P25 and ZnO, along with the impact of increasing gas velocity. After 2 and 10 mins of illumination comparable rates of removal were achieved for P25 and ZnO. After 2 min a PE of 70.38 and 74.37 % was recorded for ZnO and P25 respectively. After 10 min the PE was 99.80 and 99.56 % respectively. The rate of degradation was found to be marginally higher over P25 than over ZnO; 0.0753×10^{-5} M min^{-1}

and 0.0741 x 10^{-5} M min^{-1} during the 2 min period of illumination for P25 and ZnO respectively. The rate of degradation decreased as the irradiation period increased with P25 and ZnO displaying 10 min illumination rates of 0.0179 and 0.0184 x 10^{-5} M min^{-1} respectively. P25 and ZnO were expected to be comparable based upon the same band gap energy of 3.2 eV and positioning of the valence (2.7 eV vs NHE) and conduction band (-0.5 eV vs NHE).
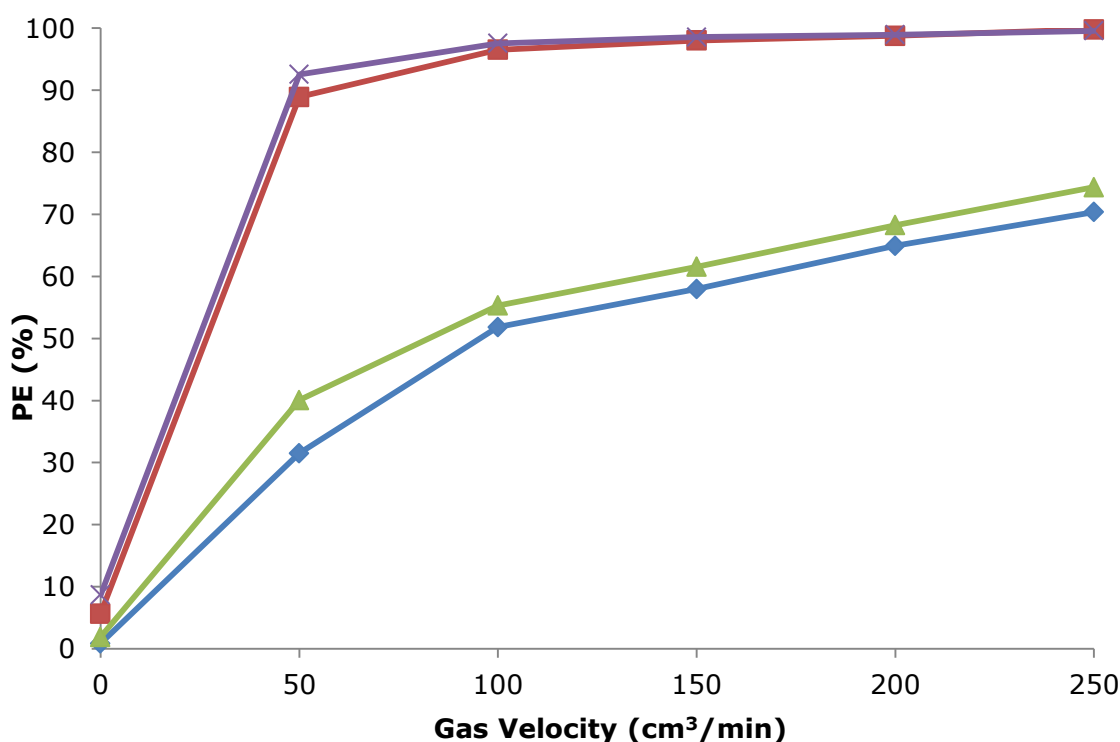
Figure 26; *PE of MO over P25 and ZnO over a range of gas velocities. 2 min PE over P25 (green Δ) and ZnO (blue ◊). 10 min PE over P25 (purple ¤) and ZnO (red □). Conducted under aerobic conditions at pH 7 and irradiation from a 36 W UV lamp*

The degradation of MO was observed to increase while increasing the velocities of gas in the SFPR from 0 to 250 cm^3/min over P25 and ZnO. The profile of MO removal over ZnO and increasing velocities of gas is shown in Figure 27. Increasing the gas velocity improved the mixing conditions, light penetration of the unit and increased concentration of O_2. These factors contributed towards increased degradation of MO. At gas velocities of 50, 100, 150, 200 and 250

cm^3/min the PE was calculated at 88.9, 97.0, 98.0, 98.8 and 99.8 % respectively. Furthermore the degradation rate was found to increase at higher velocities. After the initial 2 min period of irradiation a significant increase from 0.00 to 0.153 x 10^{-5} M MO min^{-1} and 0.153 to 0.2495 x 10^{-5} M MO min^{-1} was seen when increasing the gas velocity from 0 to 50 cm^3/min and 50 to 100 cm^3/min respectively. Thereafter the rate further increased to 0.282, 0.307 and 0.337 x 10^{-5} M MO min^{-1} for 150, 200 and 250 cm^3/min respectively.
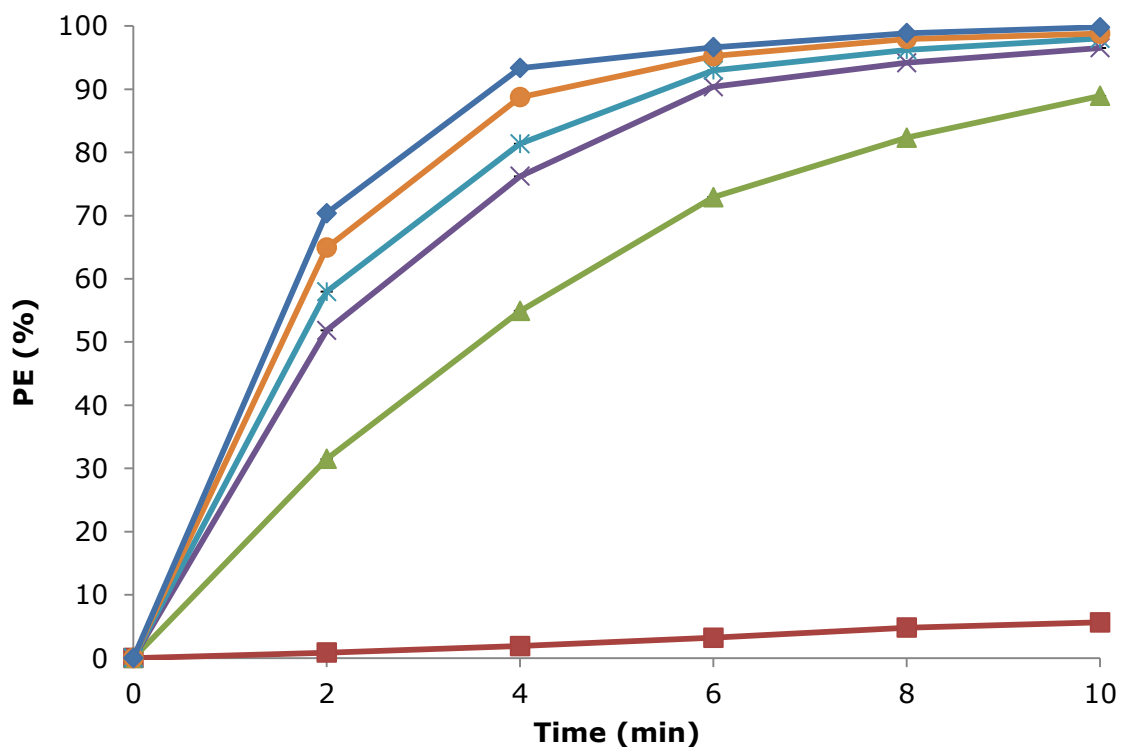
Figure 27; *PE of MO over ZnO in the SPFR over gas velocities 0 cm^3/min (red □), 50 cm^3/ml (green Δ), 100 cm^3/min (purple ¤), 150 cm^3/min (blue ¤), 200 cm^3/min (orange o) and 250 cm^3/min (navy ◇). Conducted under aerobic conditions at pH 7 and irradiation from a 36 W UV lamp*

As the SFPR was fluidised by the introduction of gas via a distributor, the velocity at which the gas was introduced was an important parameter. Gas inlet velocity is capable of dictating the extent to which mass transport affects a photocatalytic reactor (Assadi *et al.*, 2012). At 0 cm^3/min the SFPR is mass transported limited and thus degradation was minimal at 5.6 %. Under these conditions only small

proportions of the model pollutant in close proximity to the catalyst bed at the base of the reactor chamber are degraded. The MO which reached the surface was degraded immediately,. However, to increase the rate of degradation mass transfer would have to be increased. Under these conditions the remaining stock of MO was not circulated to allow for degradation. In addition, as fluidisation is not achieved a dense catalyst bed is formed at the base of the reactor restricting UV light transmission and distribution. This point was discussed by Lim *et al.* (2000) who found a critical fluidisation point must be reached before light transmittance is suitable to allow photocatalytic transformation.

The removal of MO was performed over two commercially available photocatalysts, P25 TiO_2 and ZnO. P25 has been shown to be effective for the degradation of a range of model pollutants (Alonso-Tellez *et al.*, 2012; Dillert *et al.*, 2012; Qin *et al.*, 2009 and Sangchay *et al.*, 2012). There are, however, limitations to its use in relation to handling and downstream processing. The low settling velocity and micrometric particle size of TiO_2 significantly increases the level of difficulty in separating catalyst from pollutant to produce a catalyst free sample. Alternatively, ZnO was investigated to reduce downstream processing whilst maintaining a comparable level of photoactivity to P25.

2.3.3 Analysis of MO Degradation Pathway by HPLC

The mechanism of dye degradation which takes place in a photocatalytic system is often overlooked. Rashed and El-Amin, 2007 described the mechanism of photocatalytic dye degradation through a series of equations shown in Equation 11 and Equation 19 - Equation 23. Upon illumination of a photocatalyst, electrons travel from the valence band to the conduction band forming in the process a reducing electron in the conduction band and an oxidising hole in the valence band, Equation 11. The electrons generated are capable of reducing the dye or alternatively reacting with electron acceptors such as O_2 which is present on the surface of the catalyst or dissolved in H_2O. The result of which is the formation of superoxide radical anions, Equation 21. The superoxide radical anion is capable of reacting with H^+ to form hydroperoxyl radicals (Equation 22). The holes formed are capable of oxidising the dye to form R^+ or alternatively they can react

with OH or H_2O resulting in the formation of OH$^{\cdot}$ radicals, Equation 19 and Equation 20. The formation of $O_2^{\cdot-}$ and OH$^{\cdot}$ along with $HO_2^{\cdot}$, result in the degradation of dyes via photocatalysis. The production of OH$^{\cdot}$ radicals are sufficient to oxidise the majority of MO to it is final mineral products, Equation 23.

$$TiO_2 + hv \rightarrow TiO_2\ (e_{cb}^- + \ h_{vb}^+) \qquad \textbf{Equation 11}$$

$$TiO_2(hVB^+) + H_2O \rightarrow TiO_2 + H^+ + OH^- \qquad \textbf{Equation 19}$$

$$TiO_2(hVB^+) + OH^- \rightarrow TiO_2 + OH^{\cdot} \qquad \textbf{Equation 20}$$

$$TiO_2(eCB^-) + O_2 \rightarrow TiO_2 + O_2^- \qquad \textbf{Equation 21}$$

$$O_2^- + H^+ \rightarrow HO_2^{\cdot} \qquad \textbf{Equation 22}$$

$$Dye + OH^{\cdot} \rightarrow degradation\ products \qquad \textbf{Equation 23}$$

Figure 28 displays the chromatogram of a MO sample exposed to 5 min of illumination. Chromatograms of samples exposed to 10, 20, 30 and 40 mins illumination are shown in Appendix I. The MO peak is still evident, however the peak area was significantly reduced from 7.6×10^6 (at 0 min) to $2.8\ 10^6$. This reduction of peak area and retention of additional peaks indicates that photodegradation of the compound had begun.
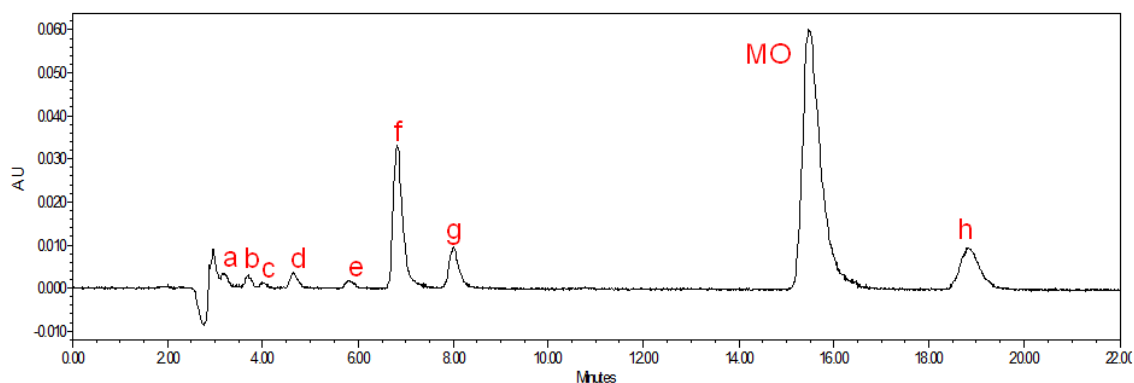
Figure 28; *HPLC chromatogram of sample exposed to 5 min UV illumination displaying MO sample and intermediate samples a,b,c,d,e,f,g and h*

The peaks retained represent intermediates in the pathway and are detailed in Table 9. In addition to the peaks shown in Figure 28 a small peak was retained at 10.7 min after 10 mins of illumination, intermediate *i*. The lambda max of the compounds retained was also recorded and displayed in Table 9.

Intermediate	R_t (min)	Max Peak Area (x10^6)	Lambda max (nm)
a	3.2	0.070	426
b	3.7	0.160	399
c	4.0	0.060	436
d	4.6	0.050	486
e	5.8	0.050	458
f	6.8	1.200	430
g	7.9	0.260	467
h	18.8	0.280	480
i	10.7	0.009	475

Table 9; *R_t, max peak areas and lambda max values of intermediates in the MO degradation pathway*

The peak area of compounds retained after 40 mins irradiation are minimal suggesting complete degradation of MO to mineral products. This can be further illustrated by results shown in Figure 29. The navy plot of the graph shows the degradation of MO over time represented by a decreasing peak area (primary *y* axis). The additional plots (secondary *y* axis) are those of the intermediate products in the pathway. It was observed that each intermediate product reached a peak production level before beginning to undergo degradation. The initial intermediates formed, *f* and *h*, show a peak production at 5 min irradiation thereafter a reduction in peak area is recorded. Intermediates *g, b and a* showed peak production at 10, 15 and 20 mins respectively.
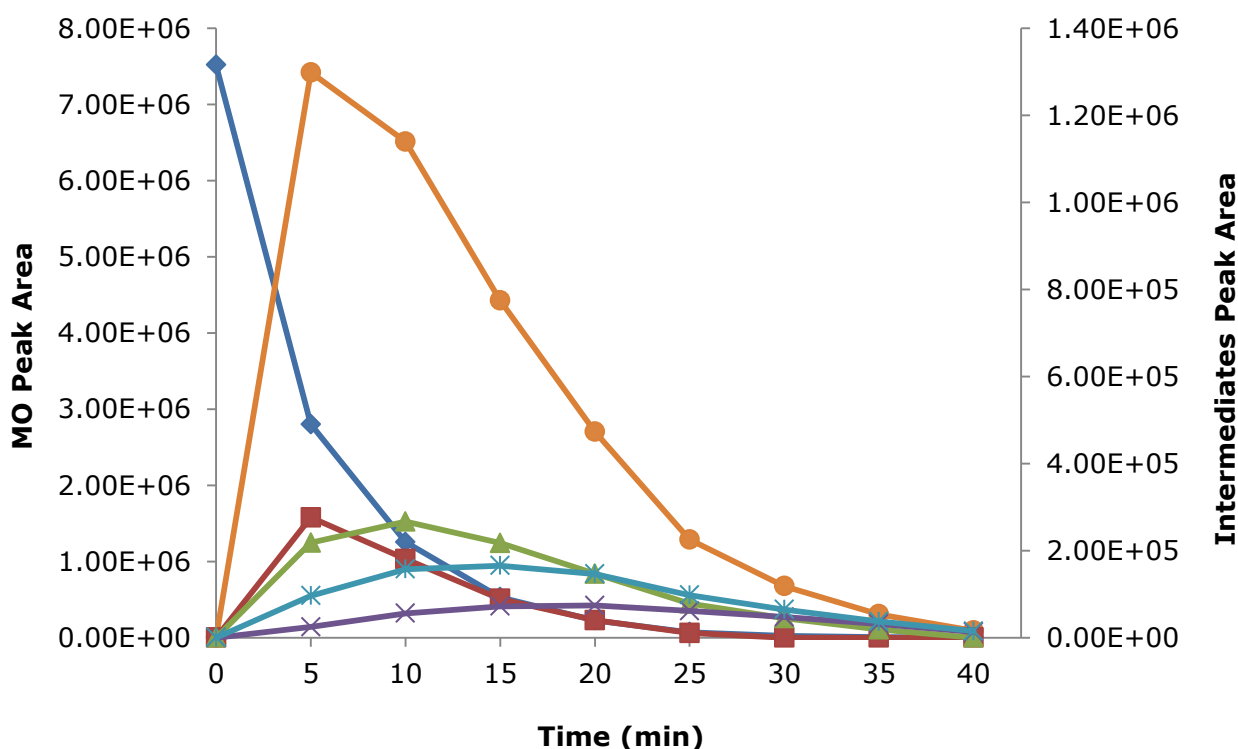
Figure 29; *Degradation of MO as peak area over time (navy ◇, primary axis) and generation of MO degradation pathway intermediates (secondary axis); Intermediates a (purple ¤), b (blue ¤), f (orange o), g (green Δ) and h (red □)*

Kinetic analysis was performed on the intermediate products formed during the breakdown of MO. The ln *C* vs time was plotted, where *C* is the concentration of the sample, to determine the rate constant *k*. The plot showed a linear

relationship, confirming the appearance and disappearance of intermediate products followed first order analysis. The rate constant k was determined using the slope of the line. The rate constants for the intermediates shown in Figure 29 are summarised in Table 10. Where applicable, a rate constant for the appearance (k_{app}) and disappearance (k_{dis}) were calculated. The k_{app} value was not calculated for MO, intermediates f and h as MO was the compound being degraded and intermediates f and h did not show enough points to accurately calculate a rate constant.

Compound	k_{app} (min^{-1})	k_{dis} (min^{-1})
MO	NA	0.1887
Intermediate a	0.0541	0.1103
Intermediate b	0.071	0.1011
Intermediate f	NA	0.1245
Intermediate g	0.0404	0.1216
Intermediate h	NA	0.1567

Table 10; *Rate constants of intermediate products formed in MO breakdown, where k_{app} is the rate constant of the appearance and k_{dis} is the rate constant of the disappearance of the compounds*

A number of the intermediates in the pathway were capable of being identified based upon the lambda max. values recorded. Intermediates *a, b, f, g and h*, shown in Figure 29 had lambda max readings of 426, 399, 430, 467 and 480 nm respectively. These values correspond to intermediates reported in the literature by Chen *et al.* (2008), Chen *et al.* (2005) and Baiocchi *et al.* (2002). Chen *et al.* utilised four 4 W lamps for illumination of a novel Ag/ZnO catalyst to detect four primary intermediates. Further to the Chen *et al.* investigation, Baiocchi *et al.* reported additional products. Baiocchi *et al.* and Chen *et al.* found products in the pathway with lambda max values of 398, 422, 430, 463, and 480 nm. The

intermediates correspond accordingly to the intermediates *a, b, f, g and h*, observed in this investigation. Baiocchi *et al.* and Chen *et al* reported a *m/z* of 276, 290, 306, and 320 for lambda max of 399, 426/431, 462 and 479 nm respectively.

The proposed structures of these intermediates are shown in Figure 30. The demethylation of the CH_3 branch on MO resulted in the formation of intermediate *b*, while the demethylation of a single CH_3 branch of MO formed intermediates *a* and *f*. The monohydroxylation of the benzene ring resulted in the formation of intermediate *h*. The monohydroxylation and demethylation of MO resulted in the formation of intermediate *g*.
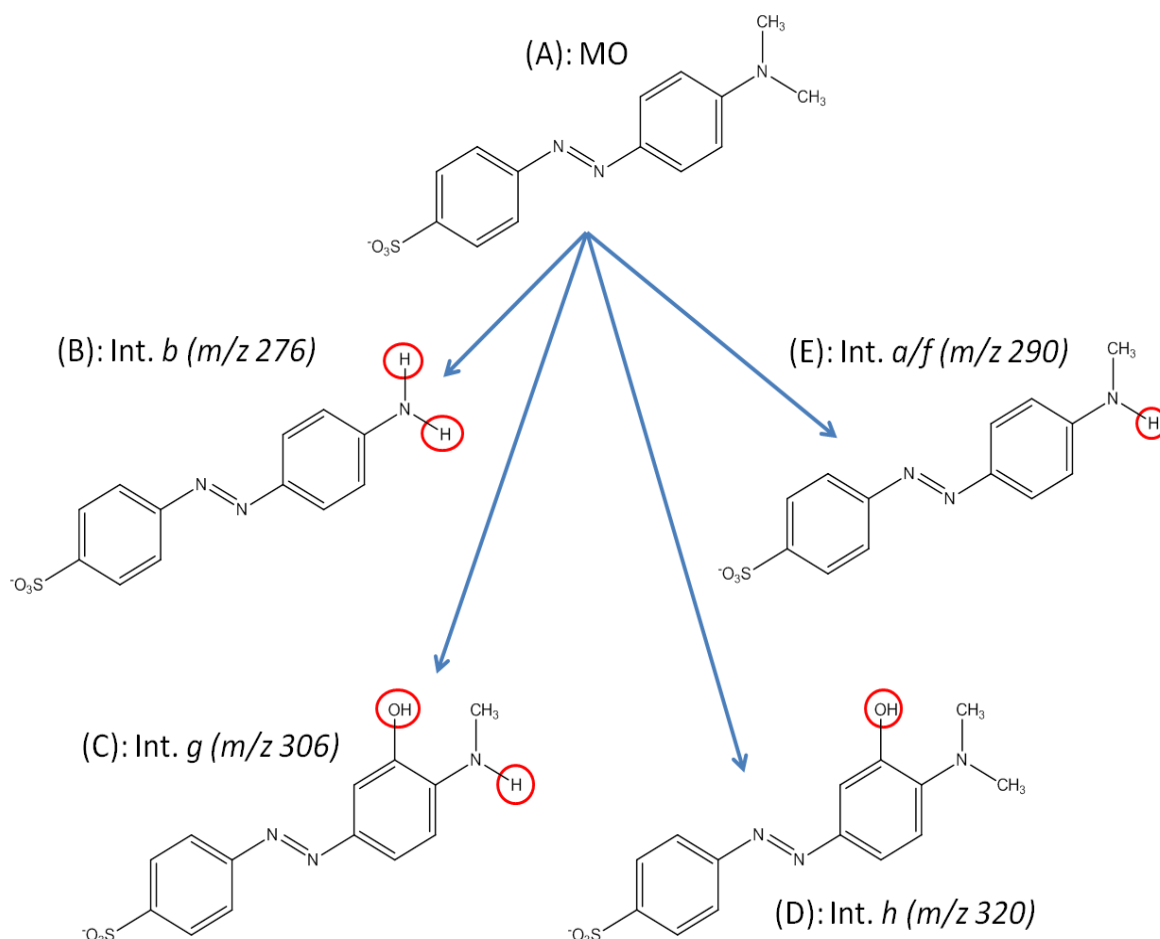
Figure 30; *Predicted degradation products of MO. (A) MO m/z 304 to (B) Int. b m/z 276, (C) Int. g m/z 306, (D) Int. h m/z 320 and (E) Int. a/f m/z 290*

2.4 Operational Testing of the MCPR

At laboratory scale photo reactors are small scale and traditionally in the range of millilitres rather than litres. The MCPR was designed to address this point and to provide a degree of reproducibility in the results. The system was constructed to allow the operation of fourreaction chambers simultaneously. The orginal concept was to allow multiple novel catalysts, synthesised by the collaboration partners, to be evaluated. The multi chamber design concept allowed operational parameters such as initial concentration, mass transport, catalyst and model dye to be investigated.

2.4.1 Simultaneous Operation

The main feature of the MCPR was the operation of multiple reaction chambers. The unit could be operated to allow two parameters to be simultaneously monitored i.e. two reaction chambers could be operated with sparging while the remaining two chambers were operated statically.

The effect of sparging was investigated over P25 and ZnO in the MCPR, Figure 31. At a gas velocity of 250 cm^3/min, 94.63 % MO degradation was recorded for ZnO, which was comparable to P25 at 93.89 %. This was expected based on previous results shown in the SFPR. As the MCPR had a capacity too small to be operated at a gas velocity lower than 250 cm^3/min, the effect of no sparging and prior agitation was monitored. Removing the sparging resulted in the system being mass transport limited and thus removal was significantly reduced to 8.89 and 5.23 % for P25 and ZnO respectively. The increase in removal of P25 under these conditions was a result of the settling velocity of P25 which is slower than that of ZnO, thus was maintained in suspension for a longer period. The effect of removing the sparging rig and agitating the reaction medium prior to irradiation further highlights this point. Under these conditions the system was controlled by mass transport and the settling velocity of the catalyst. The PE of MO over P25 and ZnO was 66.89 and 57.78 % respectively. The results show that continuous catalyst movement through sparging or mechanical agitation would be required to achieve the optimum levels of removal. Under static conditions the light

penetration would decrease and mass transport limitations would increase at the point the catalyst settles out.
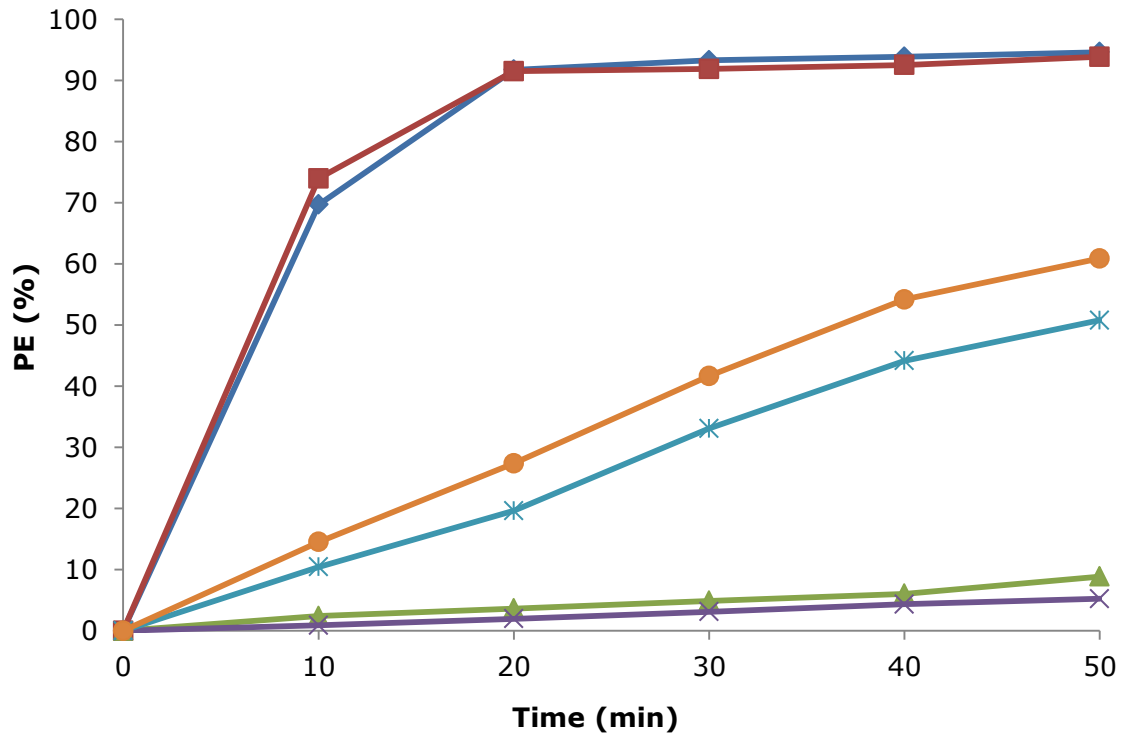
Figure 31; *PE of MO over P25 with sparging (red □), P25 without sparging (green Δ), P25 with prior agitation (orange o), ZnO with sparging (navy ◇), ZnO without sparging (purple ¤) and ZnO with prior agitation (blue ¤). Conducted under aerobic conditions at pH 7 and irradiation from a 36 W UV lamp*

As the MCPR was being operated as a modular system, reproducibility was a key parameter. The reproducibility between reaction chambers was found to be high based upon the standard deviation of samples, Table 11. Table 11 shows the PE of MO achieved in two reaction chambers operating simultaneously along with the standard deviation between the chambers. The highest standard deviation recorded was 0.0057. Replicate experiments performed also showed the results were within the range shown in Table 11. As can be observed, there was minimal difference in PE between the two reaction chambers. This indicated the chambers were both subject to an equal air flow and irradiation exposure.

Time (min)	RC$_1$ PE (%)	RC$_2$ PE (%)	SD
0	0	0	0.0
2	70.47	69.03	0.0057
4	92.13	91.42	0.0021
6	92.52	94.03	0.0021
8	93.31	94.4	0.0014
10	93.7	94.78	0.0014

Table 11; *Comparison of sparged reaction chambers containing ZnO where RC is reaction chamber and SD is standard deviation*

2.4.2 Effect of Initial Concentration

The impact of increasing the MO concentration on the performance of the MCPR for MO degradation is illustrated in Figure 32. Increasing the initial concentration of the MO concentration lowered the photocatalytic degradation from 96.4 % to 75.6 % for concentrations of 1.0 and 10.0 x 10^{-5} M respectively. The decrease is primarily due to the concentration of MO in the system being greater than the catalyst is capable of removing in the given time frame and secondly, the effect increased MO concentration has on light penetration depth. The increase in initial concentration restricts light penetration which reduces the number of photons reaching the surface of the catalyst. This was also shown in work carried out by Chen *et al.* (2006).
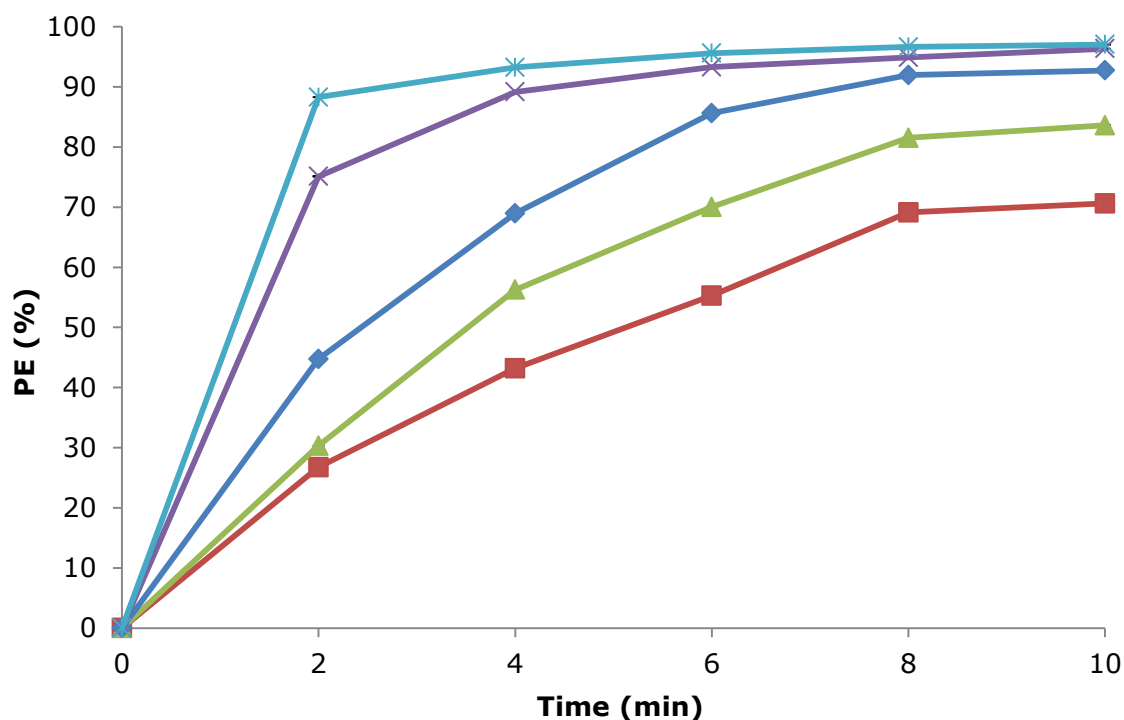
Figure 32; *PE of varying MO concentrations over ZnO in the MCPR; 1 x 10^{-5} M (blue ¤), 2.5 x 10^{-5} M (purple ¤), 5.0 x 10^{-5} M (navy ◇), 7.5 x 10^{-5} M (green Δ) and 10 x 10^{-5} M (red □). Conducted under aerobic conditions at pH 7 and irradiation from a 36 W UV lamp*

The unit was operated as previously described in Section 2.4.1. The standard deviation and PE of reaction chambers were monitored to ensure they were operating within a comparable range. It was found that increasing the starting concentration increased the standard deviation of reaction chambers. The highest recorded standard deviation of 0.0912 was found between samples taken from reaction chambers with an initial starting concentration of 10 x 10^{-5} M after 5 mins of illumination. This level of standard deviation was acceptable for units operating simultaneously.

The initial rate of photocatalytic degradation can be analysed by using the Langmuir-Hinshelwood kinetic rate model. The Langmuir-Hinshelwood law can be expressed as shown in Equation 24 where r_o is the initial rate of disappearance of the substrate, C_o is the initial concentration of the substrate, k is the rate constant of the reaction and K is the Langmuir adsorption constant.

$$r_o = \frac{kKC_o}{1 + KC_o}$$

Equation 24

The values for *k* and *K* can be determined from the plot of $1/r_o$ vs $1/C_o$, Figure 33. A linear plot is shown for Figure 33 and thus the MCPR system for MO degradation did follow the Langmuir-Hinshelwood model. The equation of the line provides the intercept and slope which corresponded to $1/k$ and $1/kK$ respectively. From the graph, k and K were determined as 3.24×10^{-5} M min^{-1} and 3.1×10^{-2} dm^3 µmol^{-1} respectively.
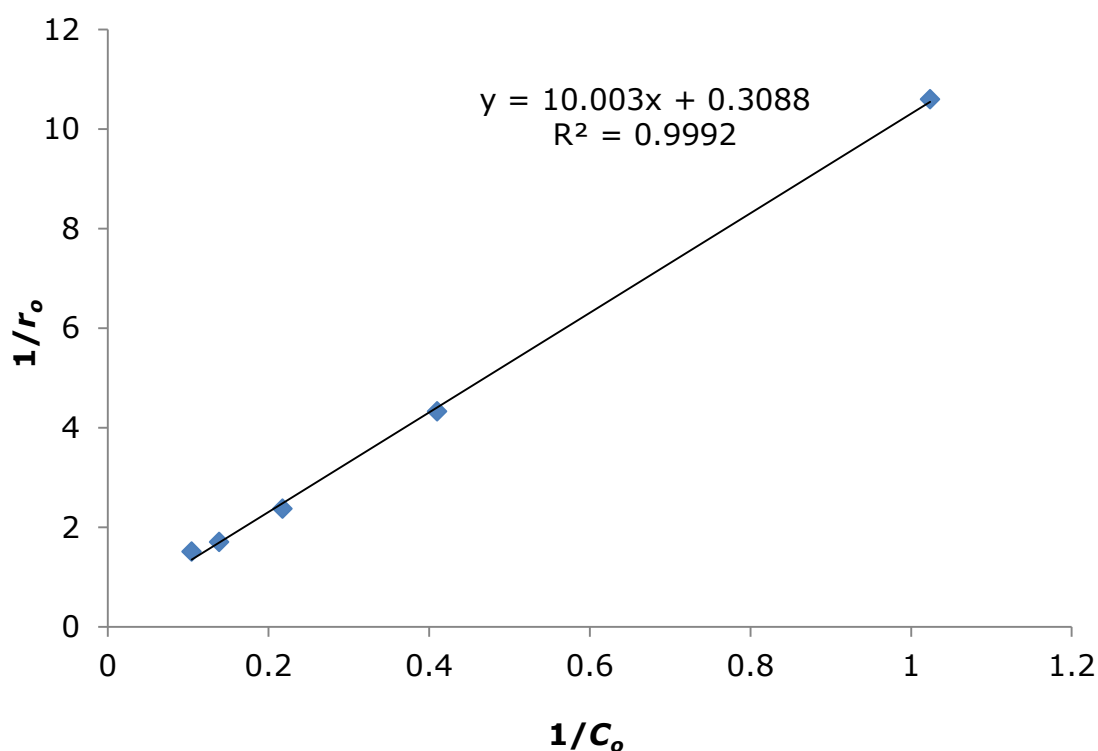
Figure 33; *Plot of the reciprocal of the initial rate ($1/r_o$) vs. the reciprocal of the initial concentration ($1/C_o$)*

2.4.3 Effect of Model Dyes

To further test the capabilities of the reactor system model pollutants of increasing molecular weight were used; CR at 696.66 g/mol and RB 1017.85

g/mol. RB is rarely reported in the literature as a means of photocatalytic evaluation, however, CR has been reported more frequently (Sakkas *et al.*, 2010; Sansiviero *et al.*, 2011; Melghit and Al-Rabaniah, 2006; Melghit *et al.*, 2006, Wahi *et al.*, 2005).

The degradation of RB is shown in Figure 34. The results show the removal of RB occurred as a result of photolysis and photocatalytic degradation in the presence of ZnO. A PE of 96.02 % was recorded for photocatalytic degradation with a PE of 60.6 % for the degradation of RB under light and no catalyst. Degradation of 3.7 % was recorded during the dark control, thereafter saturation of the catalyst was achieved and no significant degradation was recorded.
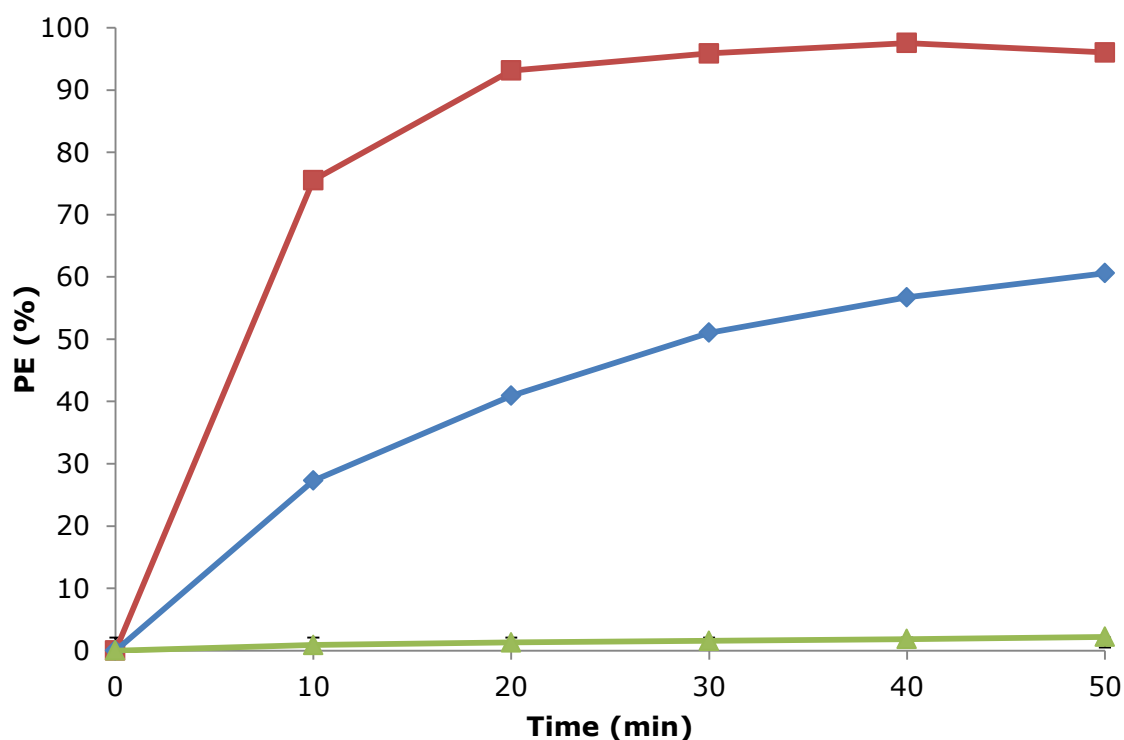
**Figure 34*;* *PE of RB over ZnO in MCMPR. Light control (green Δ), dark control (blue ◇) and ZnO test (red □). Conducted under aerobic conditions at pH 9.6 and irradiation from a 36 W UV lamp*

When CR was deployed as an evaluation compound a PE of 95.5 % was achieved under photocatalytic conditions. Under dark conditions a level of 64.9 % was

recorded. During the dark equilibrium period, however, 56.7 % degradation was noted thereafter limited degradation was recorded. The dark control showed there was a rate of 0.559 x 10^{-6} M min^{-1} during the dark equilibrium period. Thereafter a reduced rate of 0.0162 x 10^{-6} M min^{-1} was recorded for the remaining 50 min. In comparison, the presence of ZnO and illumination, showed a similar degradation rate was observed during the dark equilibrium period, 0.545 x 10^{-6} M MO min^{-1}. Upon illumination the degradation rate was 0.082 x 10^{-6} M min^{-1} which is an 80.2 % increase in PE, demonstrating degradation was still occurring and at a faster rate than if no illumination was present. The degradation of CR under photocatalytic, photolysis and absorption mechanisms is shown in Figure 35.
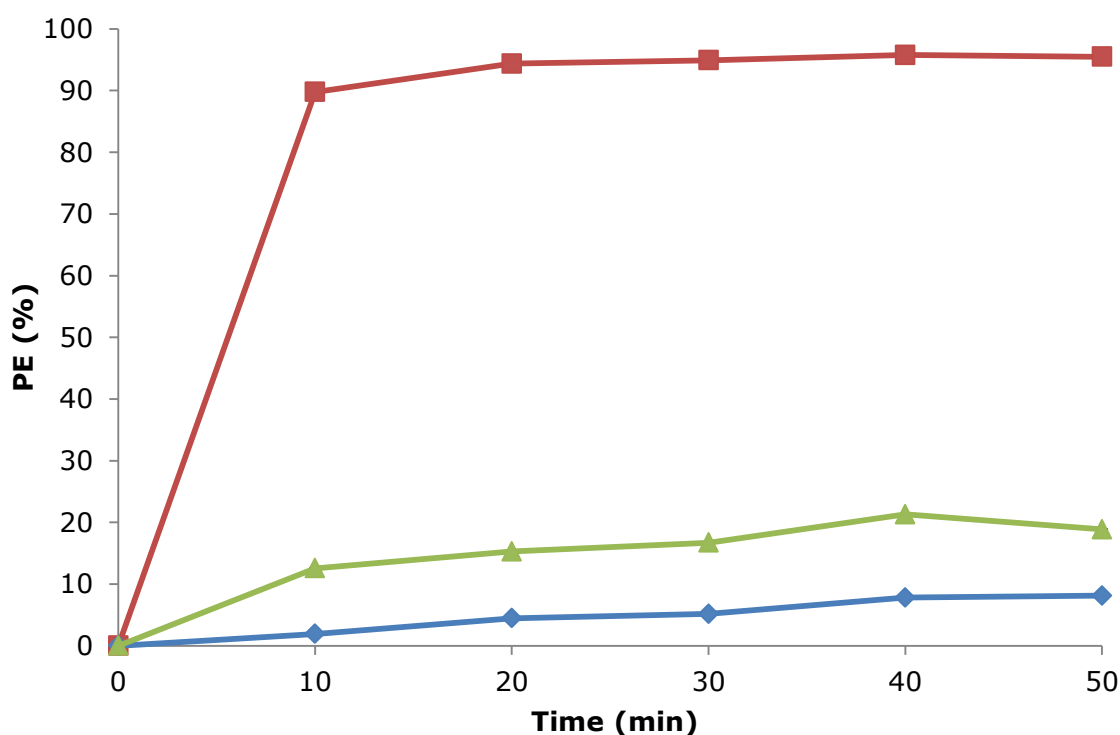
Figure 35; *PE of CR over ZnO in MCMPR. Light control (green Δ), dark control (blue ◇) and ZnO test (red □). Illumination started at 10 min for light control and test. Conducted under aerobic conditions at pH 9.6 and irradiation from a 36 W UV lamp*

The removal of CR and RB are summarised in Table 12. These results indicated the degradation of the dyes was achieved by three mechanisms; photocatalysis, absorption and photolysis.

Degradation Mechanism	Congo Red PE (%)	Rose Bengal PE (%)
Photocatalysis	95.5	96.02
Photolysis	8.12	60.60
Absorption	18.86	2.21

Table 12; *Comparison of removal of RB and CR by photocatalysis, photolysis and absorption*

2.5 Comparison of The SFPR and MCPR

The photocatalytic systems described in this chapter each presented advantages. The SFPR allows for up to 150 mL reaction mediums to be operated along with controlled introduction of air, while the MCPR allows for small scale experimentation with simultaneous operation of reaction vessels. The SFPR was adaptable to use with a number of lamp configurations while the MCPR was designed to utilise a single low power 36 W lamp.

To allow for comparison, MO degradation results achieved in the SFPR and MCPR are shown as hourly degradation rates and PE in Table 13. In both reactors comparable PE were reported with results ranging from 94.4 – 99.1 %. The degradation rates were comparable and were in the range of $1.09 – 1.19 \times 10^{-5}$ M hr^{-1}. These rates are coherent with the level of degradation achieved. The highest rate of 1.19×10^{-5} M hr^{-1} was observed in the 98 W SFPR system, which was a result of the illumination source providing 360 $^{\circ}$ irradiation resulting in increased light penetration and minimal light loss. The rate of the 36 W lamp was comparable at $1.16 \ 10^{-5}$ M hr^{-1}. This slower rate of degradation can be overlooked when the low power, energy efficiency and versatility of the 36 W

lamp is taken into account. This result, along with the rate of the MCPR (1.09 x 10^{-5} M hr^{-1}) demonstrated that the efficiency of a photo reactor system could be increased by using a 360 $^{\circ}$ array structure of 36 W lamps over that of a sole illumination source. Typically a sole illumination source would require to be immersed to maximise light penetration and distribution. This observation was taken into consideration in subsequent reactor designs described in Chapter 3 and 4.

System	Vol. (mL)	Illumination (W)	Irradiation time (min)	PE (%)	Degradation rate (x 10^{-5} M h^{-1})
MCPR	15	36	50	94.4	1.09
SFPR	150	36	50	96.5	1.16
		49	50	97.5	1.18
		98	50	99.2	1.19
		500	50	98.1	1.18

Table 13; *Comparison of MO degradation in the SFPR and MCPR*

2.6 Comparison of Model Dye Degradation

Comparison of the degradation rates of MO, CR and RB in both the SFPR and MCPR systems are shown in Figure 36. Minimal difference in overall degradation efficiency was recorded for all model dyes in both systems. The results showed, however, that under control conditions a variable level of degradation was achieved between the three dyes. CR and RB were subject to removal by the absorption and photolysis along with photocatalysis. The degradation of MO, however, was observed to be primarily photocatalytic driven. This observation would suggest that MO is a stable finger print compound suitable for evaluating

photo reactors. The reliability of CR and RB as evaluation compounds was found to be low. Issues arose when increasing the concentration of RB as the dimer version became prominent, which is indicated by a small shoulder peak at approximately 510 nm (shown in UV-Vis spectra of RB in Appendix I). Previously, methylene blue (MB) has been used as an evaluation compound (Houas *et al.*, 2001; Kasanen *et al.*, 2011; Zhang *et al.*, 2009; Mills, 2012), however, the literature has also reported concern over the use of MB as an evaluation method (Mills and Wang, 1999; Lee and Mills, 2003). Based upon the results shown in this chapter and that reported in the literature it was concluded MO would be used as an evaluation method for subsequent photo reactors.
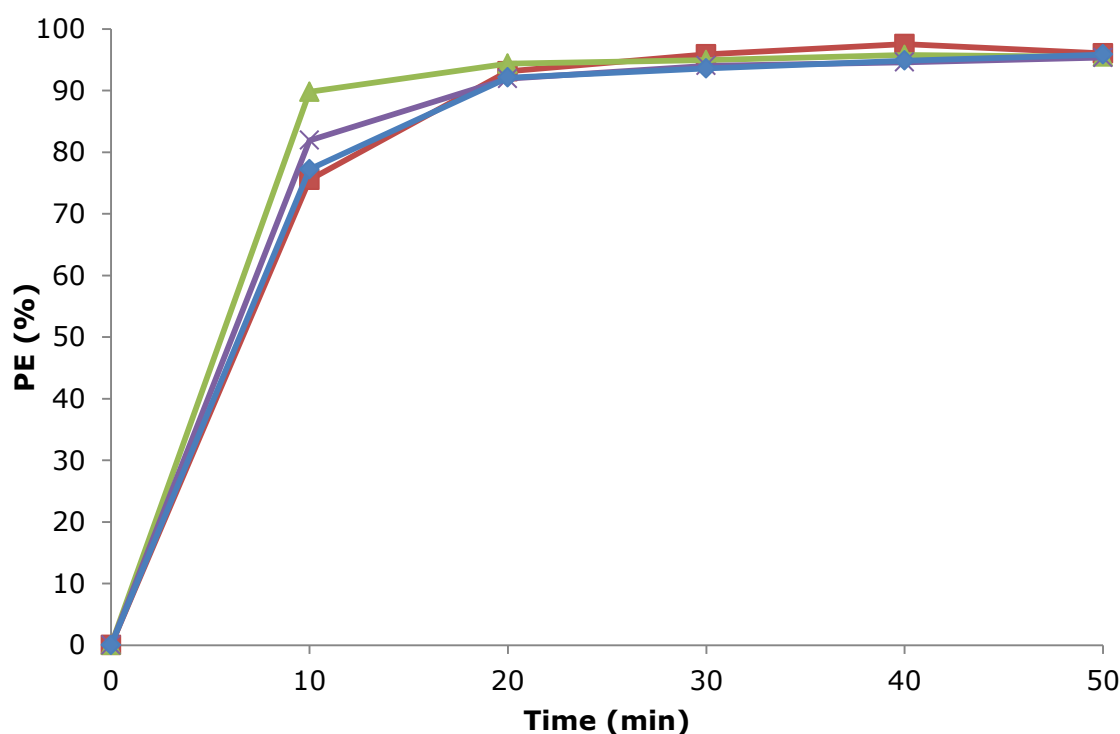
**Figure 36*; PE of RB (red □), CR (green Δ), MO (purple ¤) over ZnO in the MCPR and MO (blue ◇) over ZnO in the SFPR*

The photocatalytic degradation of MO, RB and CR is routinely reported in the literature. A number of literature publications have been summarised in Table 14 that demonstrate the degradation of model dyes. The results discussed in this chapter are in accordance with what has been published. A PE of > 95 % was

achieved for all dyes. Furthermore the level of degradation achieved is in a reduced time frame (50 min illumination) to most reported in the literature.

Reference	Dye	Catalyst	Irradiation source	Time frame (min)	PE (%)
MCPR	RB	ZnO	36 W UV	50	96.0
Ameen *et al.* (2012)	RB	Polyaniline/ graphene NC's	300 W Xe	180	56
Maji *et al.* (2011)	RB	ZnS NC's	200 W Tungsten	220	100
Maji *et al.* (2012)	RB	α-Fe$_2$O$_3$	200 W Tungsten	140	100
MCPR	CR	ZnO	36 W UV	50	95.5
Zhu *et al.* (2009)	CR	Chitoson/nano-CdS	300 W Xe	180	85.9
Chong *et al.* (2009)	CR	Kaolinite/TiO$_2$	11 W UV	240	100
Erdemoglu *et al.* (2008)	CR	P25 TiO$_2$	Natural light	30	~ 98
MCPR	MO	ZnO	36 W UV	50	95.3
SFPR	MO	ZnO	36 W UV	50	95.8
Chen *et al.* (2006)	MO	Pelagite	500 W Mercury	60	100
Wang *et al.* (2011)	MO	TiO$_2$ films on quartz tube	30 W Mercury	480	98.7
Nam *et al.* (2006)	MO	P25 TiO$_2$	15 W UV	120	100

Table 14; *Summary of literature on the degradation of RB, CR and MO*

Table 14 illustrates that a number of publications employ high power lamps (>300 W) for the photocatalytic degradation of dyes (Ameen *et al.*, 2012; Zhu *et al.*, 2009; Chen *et al.*, 2006). Under strong illumination degradation of the model dyes is expected and typically PE of >90 % were achieved. In addition to what was discussed earlier with the SFPR, the incorporation of these lamps into scaled up design can present a complex challenge and is often not energy efficient enough to be viable. Furthermore 300 and 500 W Xe lamps often provide 'spot-light' illumination where only a small area is exposed to irradiation. This is a viable approach for small scale reactors that are irradiated through an illumination window (< 15 cm OD) however for scaled up designs or units which run a series of reaction vessels these lamps do not meet the requirements.

There are examples in the literature of low power lamps being utilised for dye degradation; Nam *et al.* (2006) utilised a 15 W UV lamp to achieve complete degradation of MO, Wang *et al.* employed a 30 W lamp also for the degradation of MO and Chong *et al.* (2009) utilised an 11 W UV lamp for the complete degradation of CR. Furthermore, it was observed during this investigation that utilising a 36 W lamp a PE (96.5 %) of MO, that was comparable to that reported in the literature, was achieved. The 36 W lamp provided a diffuse light output which was capable of illuminating a number of reaction vessels along with being incorporated into an array structure to provide illumination for scaled up designs. It is in the view of the author that high power (> 300 W) lamps are not required in photocatalytic systems. Furthermore, the use of high power lamps is not acceptable in an energy and carbon footprint conscious industry.

2.7 Conclusions

The design, construction and evaluation of two bench top scale fluidised reactors were presented in this chapter. These reactors investigated the basic principles of reactor design and methods of evaluation. Through investigating operational parameters such as catalyst, dye and illumination source along with gas velocity and mass transport limitations, an effective method of evaluation was achieved. This method of evaluation was applied to subsequent photo reactors discussed in Chapter 5.

Illumination sources ranging from 36 to 500 W were used in conjunction with the SFPR. The 36 W lamp produced a PE of 96.5 %, which was found to be comparable to high power lamps that showed a PE of 97.5 % (49 W), 99.2 % (98 W) and 98.1 % (500 W). The 36 W lamp had advantages over that of the alternative lamps including low power consumption, long life time and versatility in the positioning of the lamp. Based upon these results the 36 W lamp was included into additional design concepts discussed in Chapter 3 and 4.

Operational parameters such as catalyst and dye selection provided the basis for an effective evaluation method to be used with additional reactors. The SFPR and MCPR showed that > 95 % MO removal was achieved over ZnO and P25. The handling issues of P25, including catalyst removal and adhesion of the catalyst to the reactor wall, were not observed when ZnO was deployed. The use of three finger print dyes showed MO to be the optimum compound for evaluation of reactor designs. MO was found to be a stable azo dye which was not readily degraded under photolysis or absorption processes.

The investigation of gas velocity and mass transport limitations showed the importance of increased catalyst-reactant interactions. Increasing the gas velocity in the SFPR form 50 to 250 cm^3/min produced an increase in PE of 88.9 % to 99.8 %. Similarly in the MCPR, when no sparging was used the level of removal was significantly lower than when sparging was present. These results indicated that the fluidisation of particles increased the removal of MO through two processes; the interaction of dye with radicals formed on the catalyst surface and by increasing light penetration by the fluidisation of an otherwise dense catalyst bed.

Discussed in this chapter was the investigation into fluidisation of powder catalysts in UV based systems for the removal of model compounds. The degradation pathway of this method was also monitored by HPLC analysis to detect intermediates in the pathway. This method was used as a preliminary evaluation approach, which could be applied to additional reactor designs. In order to obtain the optimum design concept for the subsequent photo reactors in the research, additional factors such as catalyst platform and illumination were also investigated. The following chapter builds upon observations recorded in this chapter. Discussed in the following chapter is the use of a thin film catalyst

immbolised onto a solid support. The design concept described investigates reducing handling issues and visible illumination, using the 36 W lamps, with a view towards solar photocatalysis.

Chapter 3 Design and Evaluation of a Novel Thin Film Multi Tubular Photo Reactor

3.1 Introduction

3.1.1 Principles of Immobilised Thin Film Reactors

Commercialisation of a photocatalytic system can be limited by the separation of catalyst from pollutant stream (Zhang *et al*., 2012; Alexiadis and Mazzarino, 2005). This is a drawback often observed when a fluidised or suspended system is employed. Briefly discussed in Chapter 2 are the methods for overcoming this limitation; reactor geometry (Meng *et al*., 2009) and the coupling of small particles with large ones (Son *et al.*, 2005; Kuo *et al*., 2009; Kang, 2003). In addition to these solutions, the design of the photo reactor itself can present an engineering solution to the problem. The immobilisation of a photocatalyst onto a solid support removes the need for separation of catalyst from pollutant.

The immobilisation of a catalyst onto a surface or incorporated into a thin film presents a host of advantages over the use of suspended systems. This approach however, is often over looked due to the decrease in surface area that comes with the immobilised reactor design (Mascolo *et al.*, 2007). The advantages which are associated with immobilised designs include; simplistic reactor designs suitable for scale up, highly recyclable catalysts and minimal downstream processing procedures such as filtration and separation. In relation to this aspect of design, the question should be asked if a loss in surface area is acceptable in return for a more industrially applicable reactor design.

The principle of immobilisation is to permanently attach or 'coat' a catalyst to a solid surface support. This can be achieved by coating a catalyst onto a large particle such as silica beads or activated carbon. Alternatively, a thin film can be applied onto a larger support such as a glass slide. Literature has demonstrated a number of surfaces have been utilised for thin film coating including steel, titanium, activated carbon, zeolites, glass, quartz, glass fibres, optical fibres and silica (Adams *et al*., 2008; Uzunova *et al.*, 2008; Zhu *et al*., 2012; Zhang *et al*., 2010; Cushnie *et al.*, 2010; Vella *et al.*, 2008; Danion *et al.*, 2006). The ability to

coat a wide variety of materials is an attractive prospect that has allowed photocatalysis to gain industrial implementation. Recent commercial applications include indoor air cleaning, process vent treatment, groundwater treatment, disinfection of hospital rooms, self-cleaning lamp covers. Larger scale examples include self-cleaning paints, self-cleaning glass and self-cleaning coatings (de Ritcher *et al.*, 2013).

When considering the immobilisation of a photocatalyst onto a support alternative parameters to those investigated in Chapter 2 must be addressed. The thickness of the film produced and residual contact time between the catalyst and model compound can directly affect the photo activity of a system (Han and Bai, 2011; Uner and Oymak, 2012). Hand and Bai (2011) concluded that increasing the film thickness of their N-doped TiO_2 thin film increased the removal of MO under visible illumination. The authors hypothesised that an increase in film thickness increased the absorption of photons and thus generated more electron/hole pairs increasing the concentration of active radicals capable of MO degradation.

Nogueira and Jardim (1996) investigated the residual contact time between a catalyst and model compound through monitoring the angle of a glass support with an immobilised photocatalyst film for MB degradation under solar irradiation. A degradation level of 95.8 % was recorded when the angle of the glass platform containing the thin film was set to 22°, with a lower level of degradation of 89 % when the angle was set to 25°. The results of the Nogueira and Jardim publication demonstrated the contact angle between the thin film catalyst and model pollutant was critical to ensure firstly light penetration was not restricted by fluid thickness and secondly, the target species was exposed to sufficient catalyst to allow for degradation to occur. This was further confirmed by work carried out by Adams *et al.* (2008) who found a shallow angle of 15 ^{o} for their reactor plate increased degradation efficiency. They concluded that the shallower plate angle decreased the flow rate and increased the residence time between the effluent and catalyst surface.

Photocatalytic activity can be significantly affected by the surface area of a catalyst (Mascolo *et al.*, 2007). A number of investigations have been reported which aim to increase photocatalytic efficiency by increasing surface area.

Surface areas of photocatalysts in the range of 27.5 m^2 g^{-1} through to 400 m^2 g^{-1} have been reported (Zhang *et al.*, 2008; Liang *et al.*, 2010). The literature generally states that increasing surface area will improve photocatalytic activity, as an increased number of sites for photocatalytic reactions will be present. This was the focus of an investigation by Amano *et al.* (2010), where CO_2 evolution from acetaldehyde decomposition increased with an increasing specific surface area from 10 to ~33 m^2 g^{-1}. Furthermore, investigations have attempted to increase the already high surface area of TiO_2 (50 m^2 g^1) in an attempt to improve photocatalytic transformations. Phonthammachai *et al.* (2006) produced TiO_2 with a high surface area of 163 m^2 g^{-1} for inclusion into a membrane for the degradation of 4-nitrophenol.

Presented in this chapter is an investigation into the development of a novel thin film multi tubular photoreactor with a lanthanide doped titania sol gel coating. The purpose of this aspect of the research was to demonstrate an alternative approach to catalyst platforms and reactor design. The promising results indicate potential for the thin film design to be incorporated into hybrid designs for large scale industrial applications that utilise low power illumination and solar illumination. As discussed in Chapter 2 these results were incorporated into the design concept discussed in Chapter 4.

3.2 Experimental

3.2.1 Design Concepts of Photo Reactor

The Thin Film Multi Tubular Photo Reactor (TFMTPR) was designed as a static photocatalytic system with no downstream processing requirements. A glass sample vessel was utilised as the body of the reactor, to allow the reactor to be sustainable when exposed to prolonged illumination. The reaction vessel was packed with individual glass rods (Figure 37). A photocatalyst sol gel was coated onto the inner surface of the reactor vessel and each glass rod was dip coated to provide a full and even coating of the rod. The reactor had an operating capacity of 20 mL and required no agitation or separation of catalyst.
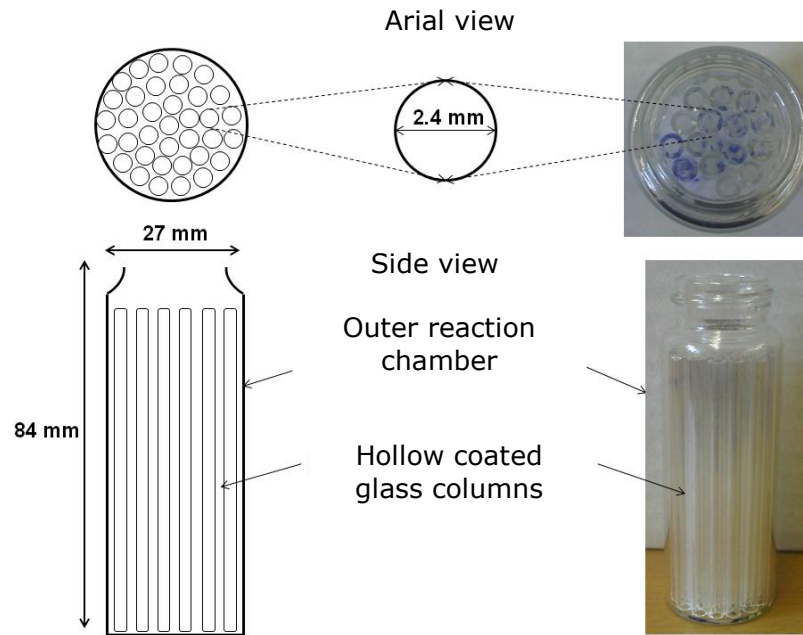
Figure 37; *Schematic representation of Thin Film Multi Tubular Photo Reactor (TFMTPR)*

The multi tubular photo reactors were produced by dip coating glass tubes in the titania sol gel solution. The glass tubes (Fisher Scientific) were cut prior to coating into 65 mm lengths. These tubes were allowed to dry at room temperature before being calcined in a high temperature chamber furnace (Carbolite, UK) at 450 °C for 30 min.

The reactor vessel (Supelco), was coated on the inside with the sol gel solution and allowed to dry at room temperature before calcination at 450 °C for 30 min. 32 glass tubes were placed into the glass reactor vessel producing the unit shown in Figure 37.

The reactor was operated in a light containment box as shown in Figure 38. The box had a 0.008 mm aluminium lining with mirrors positioned to increase light reflectance.
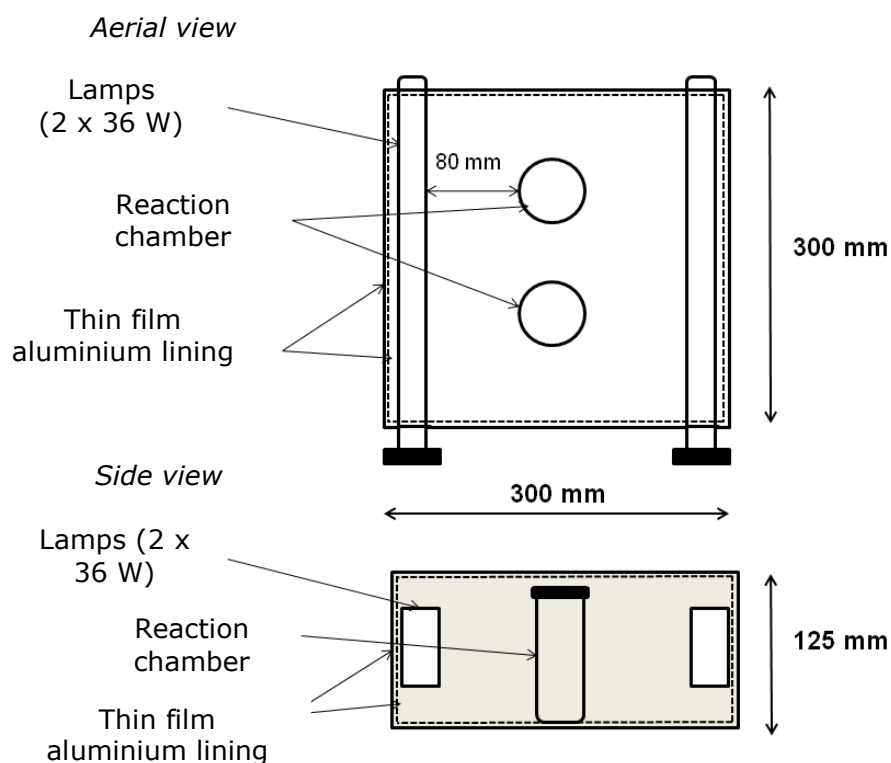
Figure 38*; Configuration of illumination box*

3.2.2 Catalyst Coatings

3.2.2.1 Titania Sol Gel

The sol–gel formulations were produced following a modified method by Mills *et al.* (2003). 4.65 g (4.43 mL) of glacial acetic acid was added to 20 mL of titanium isopropoxide. To this solution 120 mL of 0.1 mol L^{-1} nitric acid was added before heating the mixture at 80 °C for 8 h in a water bath. The resulting opaque solution was then filtered through a 0.45 μm filter to remove any aggregated particles.

3.2.2.2 Doped Titania Sol Gel

To produce the doped titania films, $Nd(NO_3)_3 \cdot 6H_2O$ (Fisher Scientific), was dissolved in the 120 mL of 0.1 mol L^{-1} nitric acid before adding the solution to the titanium isopropoxide and acetic acid. Two concentrations of 0.5 wt% (0.6

g) and 1 wt% (1.6 g) were examined. The sol was completed by heating in a water bath as detailed in Section 3.2.2.1.

3.2.2.3 Coated Silica Particles

Coated silica particles were produced by saturating a beaker of 50 – 100 µm particles with the titania sol. The coated particles were then transferred to a clean flat surface, where they were spread thinly and allowed to dry at room temperature before calcination at 450 $^{\circ}$C for 30 minutes.

The coated and uncoated silica particles were analysed under a scanning electron microscope (SEM) to determine the quality of coating and energy dispersive x-ray analysis (EDXA) was also carried out to determine elemental distribution.

3.2.3 Illumination Sources

3.2.3.1 UV and Visible Illumination

The spectral outputs of the lamps used are shown Appendix I. The Philips CLEO PL-L UV, previously used in the SFPR and MCPR, was used with the TFMTPR. A 36 W visible emitting lamp (RS Electronics, Model General Electric Biax L 830) was also utilised. The spectra of the visible lamp shows a single ultra violet emission of 364nm with the remaining strong emissions in the visible region, 404, 486, 543, 587, 611 nm being the predominant wavelengths.

3.2.3.2 Solar Illumination

Solar irradiation experiments were performed by exposing the TFMTPR to natural photons of light in the laboratory. The photocatalytic unit was placed within a mirrored light box and angled to face the position of the sun. The light box was manually moved to track the position of the sun for the duration of the experiment. The light box containing the TFMTPR was positioned out of a laboratory window allowing it to be exposed to direct sunlight. The experiments were conducted during the summer months (July and August) in Aberdeen,

United Kingdom. The weather conditions on the day of the experiment were clear with minimal to no cloud coverage and full sun coverage.

3.2.4 Photocatalytic Procedure

MO, 1×10^{-5} M was used as a model pollutant to compare the photocatalytic activity of the coated silica beads and the multi-tubular photo reactor. Experiments were also performed using P25 TiO_2 as a base comparison. Reaction volumes of 20 mL were withdrawn from the stock solution for each individual experiment. Each experiment was allowed an equilibrium time of 20 mins in the dark prior to illumination for 90 mins. Samples (1 mL) were taken, by syringe extraction, before and after the equilibrium period to allow the dark absorbance to be calculated. During the 90 min illumination period samples were taken every 30 mins in triplicate. In addition to triplicate samples, experiments were also run in triplicate. A syringe filter (0.45 μm) was utilised to filter samples during P25 experiments. No filtration was required for the silica coated beads and immobilised coated glass columns. Analysis of samples was carried out by UV-Vis spectrometry, monitoring absorbance of MO at 462 nm.

3.3 Results and Discussion

3.3.1 SEM/EDXA of Coated and Uncoated Silica Particles

To investigate the surface coating of the thin film onto the silica particles, SEM and EDXA analysis was conducted. The SEM image of uncoated silica particles is shown in Figure 39 (a). The image shows a smooth textured surface with minimal porosity. Figure 39 (b) shows the particles with a thin film coating present on the surface. The surface of the particle can be observed to have altered to a more porous and fractured surface structure. The surface effects observed are due to variation in sol gel thickness, drying and proximity of particles during furnace annealing. The thicker areas of coating tend to be more fragile and do not bond as well to the surface. The process of manufacture can be greatly improved to eliminate the surface fracturing.

(a)   (b)
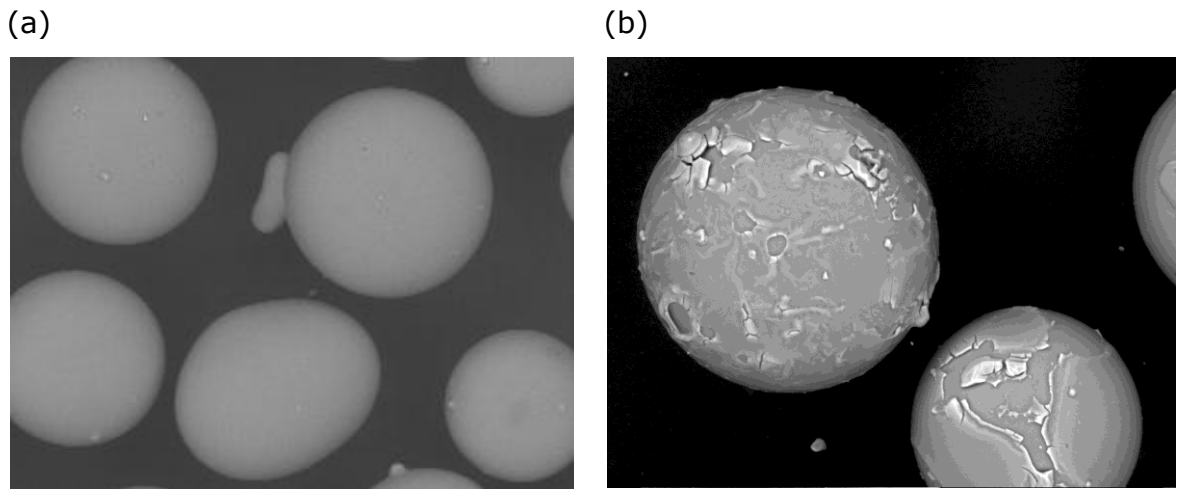
Figure 39; *(a) uncoated silica particles and (b) titania coated silica particles*

The EDXA analysis of the uncoated and coated particles is shown in Figure 40 and Figure 41 respectively. The EDXA spectrum of the uncoated particles shows a standard composition of silica particles.
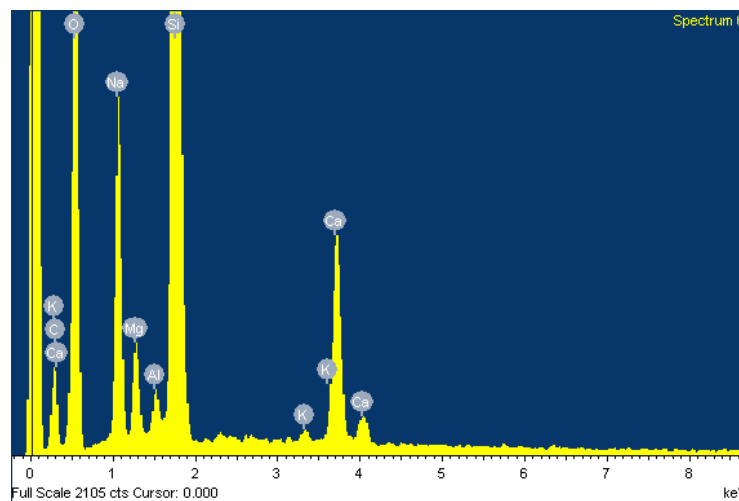
Figure 40; *EDXA spectrum of undoped silica particles*

Figure 41 shows that the coated particle has the same silica glass composition, however, with the addition of Ti which was present due to the sol-gel coating. The EDXA analysis also shows elemental evidence of the Nd doping. This confirms that the Nd did incorporate into the catalyst matrix and was not expelled during the washing stages of the synthesis.
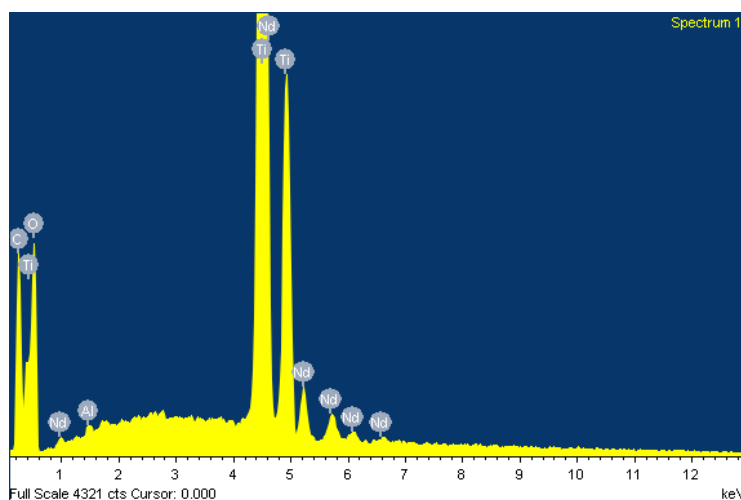
Figure 41*; EDXA spectrum of Nd-TiO$_2$ silica particles*

3.3.2 MO degradation by Photocatalysis under UV irradiation

The degradation of MO by P25, coated silica beads and coated glass tubes is shown in Figure 42. The results showed that near complete degradation was achieved by P25 (97 %), the 1% Nd-TiO$_2$ thin film (95 %) and the 0.5 % Nd-TiO$_2$ thin film. In comparison, the coated silica beads showed minimal activity, achieving a PE of 3.2 %. This value was within the degradation recorded under control conditions. Under photolysis conditions a PE of 10.3 % was recorded, while under dark conditions no degradation was recorded when the coated silica beads and glass tubes were present. As expected, under dark conditions and in the presence of P25 a PE of 5.2 % was recorded. Figure 42 displays a faster rate of degradation was achieved by P25 over that of the 0.5 and 1.0 % Nd-TiO$_2$ thin films in the initial 30 mins of illumination; 0.03 x 10^{-5} M min^{-1}, 0.026 x 10^{-5} M min^{-1} and 0.025 x 10^{-5} M min^{-1} for P25, 0.5 % and 1.0 % coatings respectively. Degradations rates over 90 mins, however, showed the rate of 0.01 x 10^{-5} M min^{-1} was recorded for P25, 0.5 % doped and 1.0 % Nd-TiO$_2$.
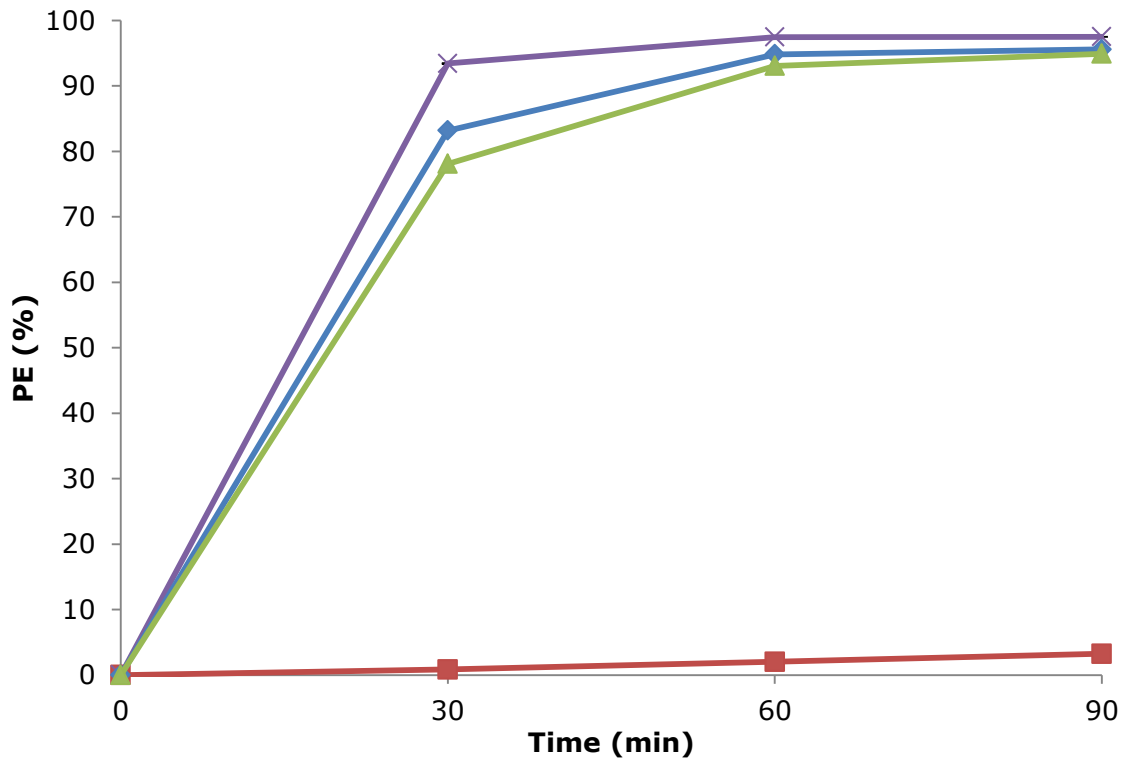
Figure 42; *PE of MO by P25 TiO$_2$ (purple ¤), coated silica beads (red □), coated glass tubes with 0.5 % doping (green Δ) and 1 % doping (blue ◇). Conducted under aerobic conditions at pH 7 and irradiation from two 36 W UV lamps*

The standard P25 stirred reactor was expected to produce a produced a high PE. This was attributed to the high surface area of P25 and increased interaction between MO and catalyst active sites. The comparable PE achieved by the Nd-TiO$_2$ thin films was attributed to the reactor design and light distribution within the reaction vessel. An immbolised reactor system is typically dictated by mass transport of the bulk reactant to the catalyst coated surface. The TFMTPR was designed to alleviate this requirement by using a packed column design to ensure a close proximity between bulk reactant and catalyst surface was achieved. The coated columns also ensured light was well distributed within the reaction system, which resulted in photos reaching central columns and promoting catalyst excitation. The packed column design allowed light to be absorbed and reflected to additional columns, which increased the number of active sites for MO degradation to occur.

The limited degradation achieved by the coated silica particles was unexpected. The TFMTPR displayed the thin coatings were photo active, therefore it is likely

the catalyst platform prevented the degradation. The low PE was potentially the result of a poor and uneven catalyst coating. The previous SEM images (Figure 39) showed the particles to have a cracked and fragile coating on the surface. This was likely due to the coating technique used. During the coating procedure the clumping of particles was observed, which would result in an uneven coating. The agitation of the catalyst by a magnetic stirrer may have also caused the particles to collide and in the process damage or remove parts of the coating. In addition to this the loading weight of the catalyst particles requires further investigation. Due to the increased density and size of the particles, an increased loading weight was deployed. The increased loading weight may have restricted the light penetration in the system. The primary design concept of the coated beads was to improve catalyst handling and reduce downstream processing techniques. The coated silica beads were capable of falling out of suspension when agitation was stopped. This was a result of the high density of the particles. This would also prevent drifting if the particles had been deployed in a fluidised photo reactor. The application of these coated particles, however, is limited and further investigation is required to optimise both the coating procedure and deployment of the beads.

The units were also investigated in respect to catalyst handling and downstream processing techniques. The limitations of P25 have been well documented previously. The micrometric size increases handling issues and difficulty in obtaining catalyst-free sample. The downstream processing of the coated glass column and coated silica bead reactors was minimal in comparison to the time consuming, expensive and unreliable downstream processing associated with P25. Prior to UV-Vis spectrometer analysis of the P25 samples, separation of catalyst and reaction mixture was achieved by syringe filtration. This method cannot provide 100 % separation due to the colloidal-like suspension created by P25. This was shown by the variation observed between standard deviation of replicates, 0.0673. In comparison the standard deviation of the silica beads and TFMTPR was 0.0245 and 0.0157 respectively.

The results presented here are comparable to those published in the literature. Zhang et $al.$ (2010) investigated MO degradation by TiO_2 thin films prepared onto nickel network pieces. The coated pieces (80 x 40 mm) were placed into a 1000 mL capacity reactor equipped with a 28 W UV lamp. The initial starting

concentration was 5 mg/L (1.5×10^{-5} M). The highest level of degradation achieved was 95.5 % after 105 min illumination. This result was comparable to the 95 % degradation rate obtained for the TFMTPR. Furthermore the reaction rates are comparable at 0.01 and 0.0098 min^{-1} for the TFMTPR and Zhang *et al.* investigation respectively. The level of degradation achieved by Zhang *et al.* was high in relation to the volume of MO treated, low power of lamp and the reduced experimental time frame. By comparison, the TFMTPR had a significantly reduced capacity (20 mL), however the level of photodegradation achieved in scaled up models of the TFMTPR was also shown to be >90 % (see section 3.3.6) suggesting the TFMTPR would be capable of treating a volume of 1000 mL with approximately an 90-95 % PE.

Photodegradation by thin films immobilised onto paper in a standard stirred batch reactor was investigated by Barka *et al.* in 2008. The reactor had a capacity of 500 mL and was illuminated by a 125 W UV lamp. The lamp was immersed into the reaction medium to provide maximum delivery of photons. The reactor was agitated by a magnetic stirrer to increase mass transport as the paper coated photocatalyst was located on the inner wall of the reactor wall. Complete degradation was achieved in the vessel within 10 hrs under illumination and in the presence of the photocatalyst. This level of degradation was increased with the use of anions Na_2SO_4, $NaNO_3$ and NaCl to complete degradation within 6 hrs of UV irradiation. While this level of degradation was significantly lower than that recorded for the TFMTPR, there are differences between the systems which must be taken into consideration before directly comparing. The initial starting concentration utilised by Barka *et al.* was ~3.6 x 10^{-5} M (TFMTPR was 1.0×10^{-5} M) and the vessel capacity was 25 times larger than that of the TFMTPR reactor. The difference in capacity could be neglected based upon the relationship between scale up of the TFMTPR and the photodegradation efficiency shown in Table 15. It is also viable to hypothesise that the TFMTPR would achieve similar levels of degradation within a shorter time than the Barka *et al.* vessel at the same starting concentration.

Comparative analysis of the TFMTPR to the standard P25 stirred vessel and units discussed in the literature is summarised in Table 15.

System	Catalyst	Illumination source	Irradiation time (min)	PE (%)
TFMTPR	1 % Nd-doped TiO_2 thin film	2 x 36 W PL-L UV lamps	90	95
Standard P25 stirred	P25 TiO_2	2 x 36 W PL-L UV lamps	90	97
Zhang *et al.* (2010)	TiO_2 thin films on nickel networks	28 W UV lamp	105	95.5
Barka *et al.* (2008)	TiO_2 thin film coated onto paper	124 W UV lamp	360	~>99.0 %
Han and Bai (2011)	TiO_2 thin film	150 W UV-vis Xe lamp	120	~65 %

Table 15; *Summary of MO degradation under UV irradiation*

3.3.3 MO Degradation by Photocatalysis under Visible Irradiation

Figure 43 illustrates MO degradation by P25 and coated glass tubes under visible irradiation. The coated silica beads showed no MO degradation under the visible light conditions and are not shown in Figure 43. As previously stated, the control experiments showed no discernible degradation with a PE of 1.4 % recorded under photolysis conditions. Figure 43 shows unexpected results for the degradation of MO in the presence of P25 under visible irradiation. A PE of 97 % with a 30 min degradation rate of 0.026×10^{-5} M min^{-1} was recorded. Degradation of MO by the TFMTPR under visible was achieved at a level of 53 % and 70 % for the 0.5 % Nd-TiO_2 and 1 % Nd-TiO_2 thin films respectively. The 30 min degradation rate recorded for the 0.5 % Nd-TiO_2 and 1 % Nd-TiO_2 was slower than that of P25 at 0.006 and 0.011×10^{-5} M min^{-1} respectively.
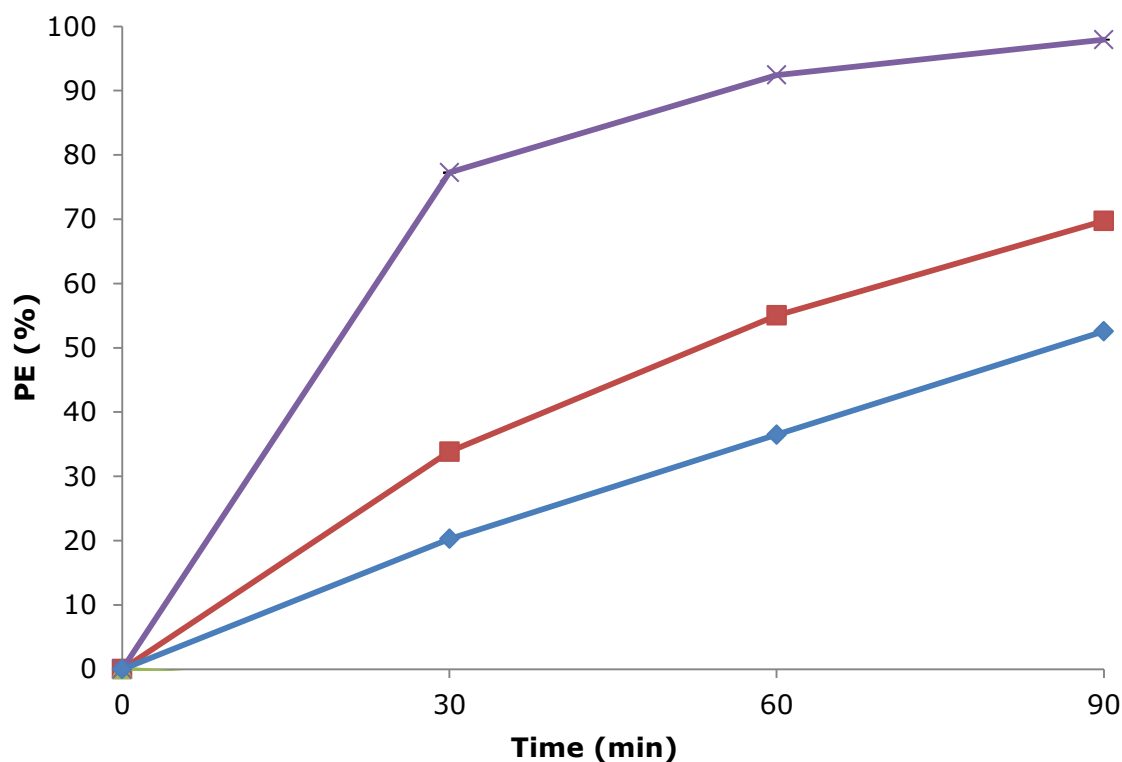
Figure 43; *PE of MO by P25 TiO$_2$ (purple ¤), coated glass tubes with 0.5 %
doping (blue ◊) and 1 % doping (red □). Conducted under aerobic conditions at
pH 7 and irradiation from two 36 W visible lamps*

The unexpected PE of P25 under visible irradiation was due to the presence of UV
emissions from the visible lamps (lamp spectra shown in Appendix I). Literature
reports that electrons will not be transported across the band gap of P25 (3.2
eV) by the energy provided by visible light alone (Robertson, 1997). The spectra
of the visible lamp showed a UV emission peak at 365 nm, which was thought to
be sufficient to promote excitation of P25.

The performance of the TFMTPR was attributed to the presence of Nd in the thin
film catalyst. Increasing the level of dopant from 0.5 to 1 % showed an increase
in PE from 53 to 70 %, along with an increased rate of MO degradation. As Nd
acts as a visible light absorbed, increasing the presence was thought to increase
the promotion of electrons and thus the production of surface radicals for
degradation. A proposed mechanism is detailed in the following section.

3.3.4 MO Degradation by Photocatalysis under Solar Irradiation

Novel catalyst synthesis and development for visible light activated photocatalysis is widely discussed in the literature, with a number of articles focusing on visible light activation of TiO_2 (Taga, 2009; Abe *et al.*, 2004; Wang *et al.*, 2010; Komai *et al.*, 2011; Kim *et al.*, 2011; Sato *et al.*, 2005; Min *et al.*, 2011). Previous results suggest the TFMTPR was active under UV and visible irradiation sources, and thus would be suitable for solar irradiation.

The TFMTPR was exposed to natural solar illumination on a laboratory roof to monitor the degradation of MO, Figure 44. A PE of 79 % and 90 % was recorded for the 0.5 % and 1.0 % coated tubes respectively. These results confirmed confirming that solar irradiation was suitable for the thin film photocatalyst activation. As previously seen, the increase in dopant level from 0.5 % to 1.0 % increased the PE.
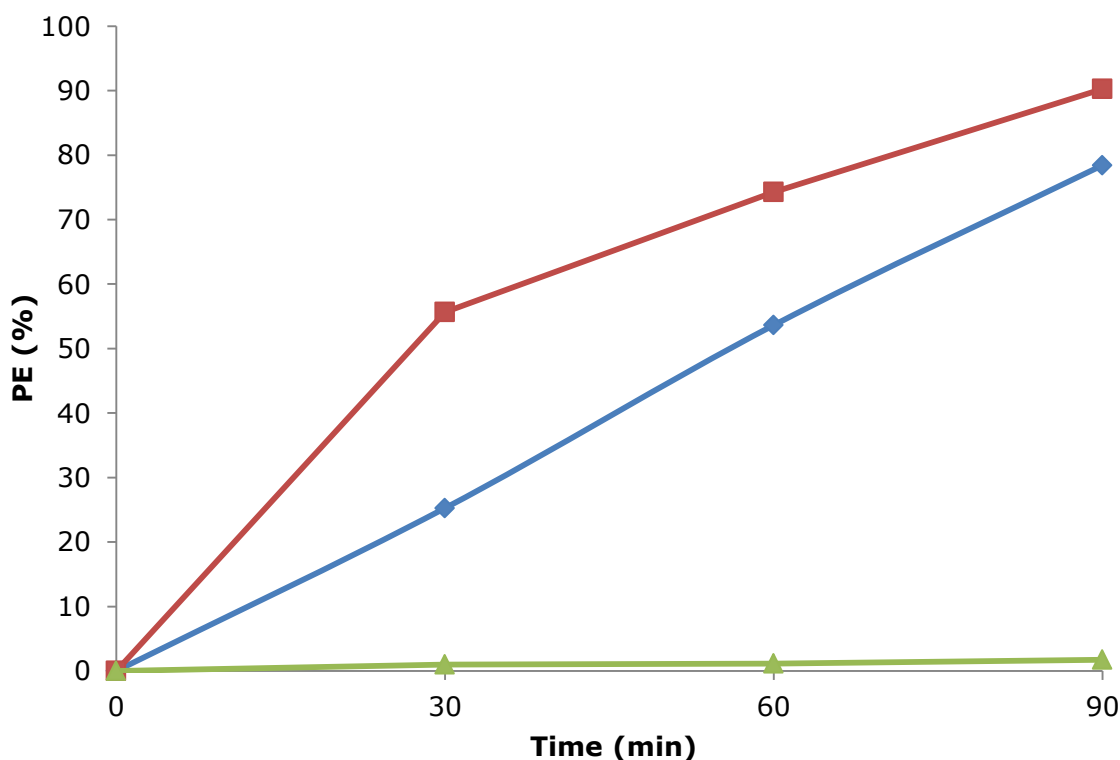
Figure 44; *PE of MO in the TFMTPR under natural illumination with a control (green Δ), 0.5 % dopant (blue ◇) and 1.0 % dopant (red □). Conducted under aerobic conditions at pH 7 and solar irradiation*

The proposed method of degradation by the Nd-TiO$_2$ thin film coating is shown in Figure 45. The incorporation of Nd particles resulted in the presence of sub-band gap levels from the 4f orbital of Nd. These sub-band gap levels were situated below the conduction band of TiO$_2$, lowering the band gap of the catalyst. Thus, valence band electrons would be promoted to the Nd 4f level by absorbing visible light photons. These trapped electrons were then capable of reacting with O$_2$ and to form products such as ·O$_2^-$ and ·OH which were capable of degrading MO. It was also proposed that electrons would be excited to the conduction band of TiO$_2$ along with the Nd 4f levels, which would allow the absorption of UV and visible light. Nd absorbs light at a range of wavelengths including the visible wavelengths of 431, 474, 514, 527, 583, 684, 742, 747, 806, 865 and 878 nm (Gschneidner and Eyring, 1999). Increasing the concentration of Nd increased the absorption of visible light and thus electron excitation and degradation.
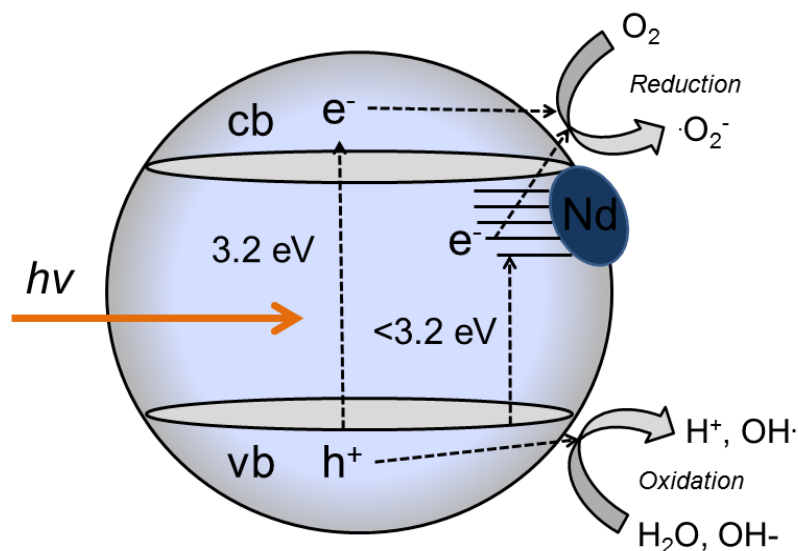
Figure 45; *Schematic representation of proposed mechanism of MO degradation by Nd-TiO$_2$*

The proposed method of MO degradation by the Nd-TiO$_2$ films was based upon Nd acting as a visible light acceptor coupled with the photocatalytic activity of TiO$_2$. Thus, using natural sun light as an illumination source is beneficial for the presence of both UV and visible photons. This was also shown by Chatti *et al.* in 2007 during their investigation into the degradation of MO over TiO$_2$ coated onto

zeolites. Heteropolyacid and TiO_2 were incorporated into a zeolite matrix along with transition metals to shift activation of the catalyst into the visible region. The use of TiO_2 with heteropolyacid allowed for the utilisation of UV and visible photons present in sunlight. Chatti and colleagues found their Ni containing TiO_2/HPA-zeolite photocatalyst degraded ~3.5 mg/g of TiO_2 of MO under natural light (starting concentration of 5 mg/L), with a similar level of 3.4 mg/g of TiO_2 of MO under simulated solar light. As the 5 mg/L (1.5×10^{-5} M) starting concentration was similar to the 1×10^{-5} M used in the TFMTPR, the results of the Chatti *et al.* study can be compared to the TFMTPR results. Under simulated solar illumination approximately 82 % degradation was achieved which was a 12 % increase over the TFMTPR results under the visible PL-L lamps. The significant increase can be accounted for by the increase in illumination source power and time frame; 72 W for 90 min and 400 W for 240 min for the TFMTPR and Chatti *et al.* investigation respectively. Under natural light the 3.5 mg/g of TiO_2 degraded by the Ni/TiO_2/HPA-zeolite catalyst equates to approximately 70 % degradation over a 240 min time frame. The TFMTPR, however, showed an increased level of MO degradation utilising both the 0.5 % (79 %) and 1.0 % (90 %) doped TiO_2 thin film catalyst.

Photodegradation of MO under solar irradiation has been reported in the literature (Chatti *et al.*, 2007; Zhu *et al.*, 2012; Al-Qaradawi and Salaman, 2002; Guo *et al.*, 2011). There are few publications, however, that allow for direct comparisons of results presented here. Recently Zhu *et al.* (2012) selected MO as a model pollutant for the evaluation of TiO_2/ZnO/chitosan nanocomposite thin films under simulated solar irradiation. The irradiation was provided by a high power 300 W Xe lamp that covered a broad spectrum of 300 to 1100 nm, with 5.2 % of the irradiation below 390 nm. After 4 hours illumination, 97 % degradation was achieved utilising the novel catalyst thin films. This was comparable to the 90 % recorded under solar illumination illustrated in Figure 44. The higher degradation rate obtained by Zhu *et al.* could be accounted for by the longer illumination time frame of 4 hrs and the use of an artificial illumination source, which would show minimal variation in intensity over a period of time in comparison to natural light. A point of interest in the Zhu *et al.* publication was the level of dark absorbance recorded. In control experiments conducted with the TFMTPR a dark absorbance of 3.9 % was observed while Zhu and colleagues

recorded 30.8 % degradation during dark controls suggesting that it was both adsorption and photocatalytic mechanisms which produced the degradation rate of 97 %. The low (< 4 %) adsorption level of the TFMTPR would suggest it was primarily a photocatalytic degradation process.

Guo *et al.* (2011) also utilised simulated solar illumination to degrade both MO and rhodamine B over TiO_2 nanostructures, nanotubes and nanowire. The use of TiO_2 nanotubes produced the highest level of degradation of MO at 98.9 % after 60 min of illumination. As was discussed previously this level of degradation was again comparable to the TFMTPR under natural light. While the 98.9 % degradation achieved within 60 mins was higher than that of the 90 % within 90 mins for the TFMTPR, the simulated solar light in the Guo *et al.* publication was provided by an 800 W Xe lamp. The environmental and economic benefits of utilising natural light for the degradation of model pollutants by photocatalysis vastly outweigh those of utilising a high power 800 W Xe lamp.

Table 16 summarises the degradation of MO by solar and simulated solar irradiation presented in the literature in relation to the degradation results obtained for the TFMTPR under visible and solar irradiation.

System	Catalyst	Illumination source	Irradiation time (min)	PE (%)
TFMTPR	1 % Nd-TiO_2	72 W visible lamps	90	70
TFMTPR	1 % Nd-TiO_2	Natural sunlight	90	90
Guo *et al.* (2011)	TiO_2 nanotubes	800 W Xe lamp	60	98.9
Zhu *et al.* (2012)	TiO_2/ZnO/chitosan thin film	300 W Xe lamp	240	97
Chatti *et al.* (2007)	Ni/TiO_2/HPA/Zeolite catalyst	Natural sunlight	240	~70
Chatti *et al.* (2007)	Co/TiO_2/HPA/Zeolite catalyst	2 x 200 W tungsten bulbs	240	~82

Table 16; *Summary of MO degradation under solar and simulated solar irradiation*

It was noteworthy that the investigation into solar activation of the TFMTPR is still in its infancy and requires further consideration. Solar light is a varying illumination source and requires careful analysis to determine the wavelength composition. This point is addressed further in the future work section of this thesis (Chapter 6).

3.3.5 Effect of Surface Area

Surface area is a controlling factor in photocatalysis and can significantly alter the rate kinetics of a reaction. The surface area of immobilised catalysts is often overlooked, as powder provides a greater surface area for catalytic activity. Immobilised reactor configurations which utilise the full catalyst coating and reduce mass transport limitations can, however, be highly photocatalytically active. To achieve photocatalytic efficiency in an immobilised system, mass transport limitations can be reduced through close contact of catalyst and pollutant allowing for increased residence time or via the agitation of the model pollutant, as discussed in Vella *et al.* 2010.

The TFMTPR in this investigation showed mass transport limitations can be reduced by the use of closely packed coated columns. The configuration ensures the model pollutant was constantly in close contact with a coated surface. This increased the ease of transport and reaction between catalyst and pollutant.

Figure 46 shows the level of degradation achieved by P25 (97 %) and the TFMTPR (95 %) under UV light in relation to the calculated surface area. The calculated surface area of the TFMTPR refers to the physical surface area available for photocatalytic activity and was not based upon a surface area assigned by BET (Brunauer-Emmett-Teller) analysis. Despite a significantly reduced surface area, in comparison to the suspended system, the immobilised catalyst performed within ~3 % of the P25 suspended system. For industrial applications, the TFMTPR can be considered to have outperformed the suspended system as no agitation or downstream processing of samples was required, which reduced the overall energy consumption, cost and time frame of the reaction.
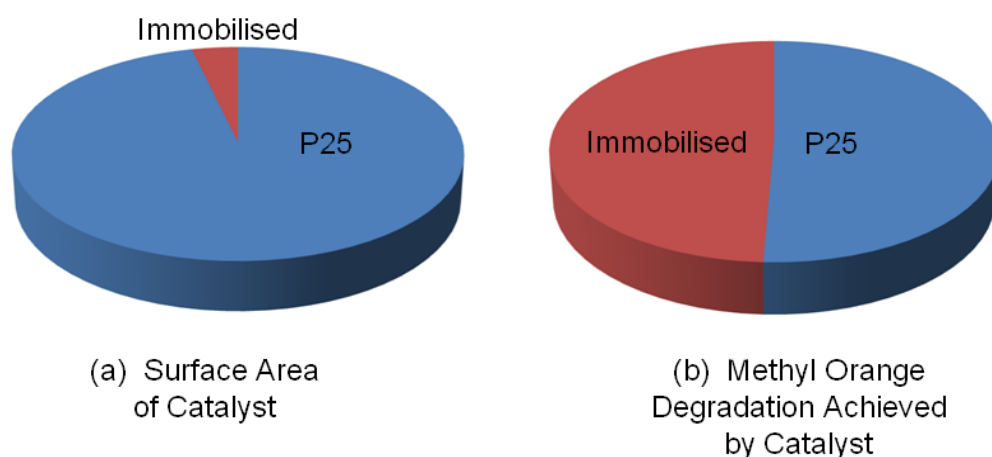
Figure 46; *Comparison of MO degradation and catalyst surface area*

Comparison of suspended and immobilised systems has previously been discussed in the literature (Mascolo *et al.*, 2007). The evaluation of the Mascolo *et al.* systems was carried out by monitoring the degradation of methyl red (MR) over a P25 suspended system and TiO_2 nanoparticles immobilised onto the inner wall of the reactor. The reactor vessels utilised were identical in construction with the only difference being the dispersal of P25 in one, while the other contained the photocatalyst coating on the inner wall. As expected P25 showed a higher level of photo activity in relation to MR degradation; degradation rates of 0.010 and 0.0198 k (min^{-1}) were recorded for the immobilised and suspended systems respectively.

The comparable results of the TFMTPR to a P25 suspended system obtained were not replicated in the Mascolo *et al.* paper. The authors stated that the supported catalyst coating had low porosity, concluding 'an overall reduction of active surface area available for target molecule adsorption' was observed which produced the low level of photodegradation. It should be noted that from a reactor design view point the reactor configuration in the paper did not utilise the coated catalyst to its maximum potential. The coating of the catalyst on the inner surface would require significant agitation of the reaction medium to ensure mass transport of model pollutant to active sites on the catalyst surface. This was not achieved and thus the photodegradation was significantly lower than that of the P25 suspended system.

Catalysts immobilised onto a solid support will rarely have a surface area greater than that of a powdered catalyst, and thus must look to reactor design and construct to ensure the appropriate level of catalyst-reactant interaction was achieved. This was shown by Ling *et al.* (2004) who achieved comparable phenol degradation in an immobilised system to a P25 system. The system was comprised of coated glass columns coiled round a central illumination source, which had the aqueous reaction medium pumped through. The immobilised system achieved 95 % degradation in 3.5 hrs illumination which was comparable to 95 % achieved in 3 hrs by a P25 slurry system. The authors concluded that the increased rate of degradation achieved in the P25 system could be overlooked as the coated design concept had no downstream processing requirements and thus would be capable of treating water at a low cost whilst maintaining comparable photocatalytic efficiencies to that of slurry systems.

3.3.6 Mark I, II and III Multi Tubular Scale Up

Scale up is traditionally feasible via two approaches; mathematical modelling using small scale experimentation or physical scale up of reactors from laboratory to pilot and then industrial scale. During physical scale up of reactors, modularisation can be used to run units as parallel, in series or as batch. Physical scale up involves careful consideration of enlarging the unit to a scale suitable of treating large industrial scale pollutants. The latter is challenging from an engineering perspective as the final product may not be economically or environmentally acceptable to be used in commercial applications. Literature has identified the issues relating to increasing catalyst loading, volume and energy required for agitation (Adams *et al.*, 2008; McCullagh *et al.,* 2010; Robertson 1996; Salu *et al.*, 2010; McCullagh *et al.,* 2011). Thus, scale up of a reactor requires intelligent design which allows for a degree of enlargement and incorporation into modular systems.

The TFMTPR was a simple design concept that has been shown to be effective at small scale. The design also allows enlargement of the unit as the unit was comprised of minimal components. Moreover, the unit was a static reactor and requires no mechanical agitation thus the enlargement process involves only the scale up of the reactor body and coated columns. It can be seen from the

literature that photocatalytic immobilised reactor configurations often involve a means of agitation via stirring or aeration in an attempt to overcome the limited mass transport of the system. While this may increase the degradation rate it increases the complexity of the system in relation to the scale up. Gunlazuardi and Lindu (2005) used a magnetic stirrer to agitate their aqueous solution of pentachlorophenol to encourage contact with TiO_2 thin films supported on a titanium metal. Han and Bai (2011) utilised an air distributing device to both introduce oxygen into the system and transport their reaction medium of MO to the surface of a thin film coating. Similarly Mahmoodi and colleagues (2006) utilised an air pump to bring their solution of Reactive Red 198 into contact with their coated reactor walls.

To examine the feasibility and ease of scale up for processing increased volumes of dye, two larger multi tubular photo reactors were created. A 200 mm tube reactor was created using a 250 ml measuring cylinder as the reactor vessel and a 260 mm tube reactor was created using a 350 ml hydrometer jar as a reactor vessel. Due to the large size of the scaled up reactors it was not possible to coat the inside of these vessels. The 260 mm tube size was the maximum permissible size which could be processed in the furnace. Table 17 shows a summary of all three TFMTPR including their dimensions and recorded PE. Discussed later in this thesis (Chapter 5) are the results for degradation of MO in the Propeller Fluidised Photo Reactor (PFPR) Model I and II in which it was observed the experimental time frame for achieving a high level (>90 %) PE increased as the capacity of the reactor increased. Shown here are three reactors of increasing capacity producing comparable PE within the same time frame (90 min illumination). The decrease in photodegradation efficiency recorded from Mark I to Mark II ($\sim$ 3.2 %) and III ($\sim$ 3.4 %) can be accounted for by the lack of coating on the reactor body.

Reactor	Volume (mL)	Number of Tubes	Tubular length (mm)	PE (%)
Mark I	20	32	65	94.97
Mark II	120	61	200	91.78
Mark III	250	92	260	91.62

Table 17; *Mark I, II and III reactor degradation rates, volume and tubes*

3.4 Conclusion

The performance of the TFMTPR was discussed in this chapter. The reactor was designed as an alternative approach to the fluidised system presented in Chapter 2. The reactor showed a comparable level of MO removal to that of a standard P25 slurry system. The Nd-TiO$_2$ catalyst structure, which increased visible light absorption, and closely packed column design, which reduced mass transport limitations, ensured a high level of degradation. Under UV illumination degradation was within 3 % for the two systems. The TFMTPR required no mechanical agitation or downstream processing techniques, which typically are a necessity with a P25 slurry system. The application of a powder catalyst in any reactor design generates sample handling issues, an inability to accurately monitor online degradation and the need to filter processed effluent streams. Also the environmental impact of increased energy consumption to run a suspended powder reactor unit increases the carbon footprint. These issues were removed completely by the use of the TFMTPR. There was no limitation on sample monitoring, risk of suspended material discharge or unnecessary power wastage.

The immobilisation of Nd doped TiO$_2$ catalysts onto two supports was investigated. The results demonstrated that the immobilisation onto silica particles showed minimal photocatalytic activity. This was thought to be due to low catalyst surface area coupled with reduced residual contact time between pollutant and catalyst surface. Coating the catalyst onto glass tubes in a closely packed column design was shown to overcome these limitations. The coated tubes allowed for maximum light penetration into the reactor system along with

ensuring sufficient light distribution amongst the packed columns. The arrangement of the packed tubes allowed for increased residual contact time between the catalyst and pollutant, without the need for mechanical agitation.

The TFMTPR was shown to be active under UV, visible and solar irradiation. The presence of Nd^{3+} particles in the thin films increased the ability of the coatings to absorb visible light. The incorporation of Nd particles resulted in the presence of sub-band gap levels from the 4f orbital of Nd. These sub-band gap levels lowered the band gap of the catalyst and allowed valence band electrons to be promoted to the Nd 4f level by absorbing visible light photons. Increasing the concentration of Nd increased the absorption of visible light and thus electron excitation and degradation. Under visible illumination MO degradation rates of 53 % and 70 % were obtained for 0.5 % and 1.0 % dopant levels respectively. Under natural sunlight a 20 % improvement in degradation rate was observed from 70 % to 90 % for 0.5 % and 1.0 % dopant concentrations respectively.

The viability of scale up was demonstrated with the construction of the Mark II and Mark III reactors, which showed comparable levels of degradation despite an increase in column length, number of columns and vessel capacity; photodegradation efficiencies of 95 %, 92 % and 92 % PE were recorded for the Mark I, Mark II and Mark III reactors respectively. These results showed the TFMTPR could be scaled up towards industrial application via modularisation whilst maintaining a high level of photocatalytic activity.

The results presented in Chapter 2 and Chapter 3 provided the scope for reactor design and presented a number of key parameters, which were considered for subsequent designs. The SFPR, MCPR and TFMTPR all showed the potential of low power 36 W lamps. The method of catalyst platform and deployment however, required the consideration of additional factors. The focus of the collaborative partners was the synthesis of novel powder photocatalyst. Whilst the TFMTPR was an applicable engineering concept, a challenging issue was faced in producing a liquid precursor which incorporated novel photocatalyst synthesised by the University of St. Andrews and CalTech for use as a thin film coating. Thus, to maximise the potential of the powder catalyst a fluidised bed design concept was produced based upon observations and results previously obtained in

Chapter 2 and 3. The design and construction of the fluidised bed system is described in Chapter 4, with the operation of the unit described in Chapter 5.

Chapter 4 Design Concept of a Novel Fluidised Bed Reactor for CO_2 Reduction and H_2 Production

4.1 Introduction

It has been stated in the literature that the 'design of highly efficient photocatalytic systems is of vital interest and one of the most desirable yet challenging goals in the research of environmentally friendly catalysts' (de Lasa *et al.*, 2005). In the design and construction of a photocatalytic reactor, Bouchy and Zahraa (2003) stated there are four basic considerations which must first be taken into account; the photocatalytic process, rate of photocatalytic degradation, specific rate and general system. Based upon these considerations, the design of a reactor should be conducted in order to achieve a set of parameters. The requirements of a photocatalytic unit are detailed below:

- Capable of operating under aerobic and anaerobic conditions
- Robust
- Applicability for scale up and modularisation
- Versatility to operate in multi-phase reactions
- High mass transport
- Maximum utilisation of an irradiation source
- Minimal downstream processing techniques
- Cost effective with a low carbon footprint
- Versatility for utilisation with a range of illumination sources
- Effective light distribution within the reactor

4.1.1 Photocatalytic Reactor Development

The design and development of conventional chemical reactors has been well established, with a number scaled up to industrial scale (Bonvin, 1998; de Lasa *et al.*, 2005). The development of photocatalytic units, however, requires consideration of additional factors to that considered for traditional chemical ones, specifically relating to reactor fabrication material, methods of catalyst deployment and delivery of illumination (Bouchy and Zahraa, 2003; McCullagh *et*

al., 2011). Currently it is these parameters, which have limited their applicability to scale up.

4.1.2 Illumination source consideration

The need for catalyst activation by irradiation is the key difference between conventional chemical reactors and photocatalytic systems. The photo activity of a catalyst and thus a reactor requires the presence of photons. Illumination is a critical factor of photocatalysis and the source of radiation is a controlling issue for both the design of the photo reactor and its potential for large-scale implementation. Cassano and Alfano (2000) discussed these factors and stated the following parameters must be considered in reactor design:

- Illumination source selection including the efficiency, spectral distribution, general geometry and parameters of operation
- The design of the reactor in relation to the illumination source
- Design of the reactor illumination source including mirrors, reflectors, windows and the materials for construction and the applicable cleaning procedures

Further to this, the material through which light is transmitted must be of a high grade. The obstruction and scattering of light from the use of Pyrex glass or particles which do not participate in the photocatalytic process should be avoided (Bickley *et al.,* 2005). In particular the grade of glass employed in externally illuminated photo reactor is a critical consideration and must provide the following characteristics:

- High transmittance of light
- High temperature resistance
- High purity
- Thermal shock resistance
- Chemical inertness
- Durability

A key consideration for photo reactor design in relation to illumination is firstly the source of irradiation and secondly the distribution within the photocatalytic

unit. Furthermore the successful scaling up of a photo reactor requires that the number of photons absorbed per unit time and per unit volume is increased with increasing reactor capacity (Curco *et al.*, 1996).

Scaling up a laboratory based illumination source is extremely challenging. To ensure efficiency at industrial level the spectral output of the lamps used must match that of the laboratory lamp and provide enough energy to ensure excitation of the photocatalyst. The volume of catalyst deployment must also be considered at this point, especially in the case of powdered catalyst. At laboratory scale powdered catalyst, such as P25, is typically deployed in a system in the 0-5 g range, however, at industrial scale the volume of catalyst used would be in the range of 1 – 100 kg. The illumination source selected must have sufficient distribution and light penetration capabilities to ensure adequate delivery of photons to allow catalyst excitation on this large scale. The controlling factors in this aspect of reactor design are the type and position of illumination source (de Lasa *et al.*, 2005).

Photocatalytic illumination types can be broadly divided into UV, visible and solar. While UV driven photocatalysis coupled with TiO_2 has produced a high level of efficiencies across a broad range of processes (Nakata and Fuijishima, 2012), its potential for scale up is limited. Visible light and solar photocatalysis is of particular interest as the use of an entirely sustainable illumination source is the optimum operational conditions and would further aid the commercialisation of photocatalysis. The challenge remains, however, that a highly efficient photocatalyst is required to utilise solar illumination. It is worth remembering solar illumination covers the entire spectral range and from an industrial view point there is less demand for a purely visible light activated catalyst.

Assuming a photocatalyst capable of solar activation is deployed the second challenge involves the positioning of the illumination source. Typically illumination can be internal (immersed lamp), external or via a distributed light source. If solely considering solar activation an immersed lamp is not required and it is rather the positioning of the reactor, not the source, which is critical. The use of mirrors and reflectors to ensure a constant stream of photons is delivered to the photocatalytic unit is a viable option (Jing *et al.*, 2009; Liu *et al.* 2012; Malato *et al.*, 2002). While the use of mirrors and reflector increase the

engineering complexity of the overall system for large scale design it is a beneficial comprise as solar irradiation intensity is increased.

4.1.3 Reactor Fabrication Material

The material utilised for photocatalytic reactor development is required to meet a number of factors. The materials used in reactor construction should provide the optimum reaction environment without playing a role in the chemical conversion. It should be recognised, however, that no material is capable of providing the ideal characteristics required for optimal reactor design and construction. Therefore, it is essential the correct and most efficient material is chosen based on the parameters of both the desired photo conversion and the overall photo system configuration. The following factors were considered during the construction of the reactors:

- Chemically inert
- Thermodynamically stable
- Low expansion
- Simple maintenance and cleaning procedures
- Cost effective
- High light transmittance in relation to illumination exposure
- Where necessary, efficient distribution of light

4.1.3.1 Poly (methyl methacrylate) (PMMA)

PMMA, with a $C_5H_8O_2$ repeating unit, is a good choice of material for both a reactor construct, catalyst support and illumination window. The optical properties of PMMA are favourable for photo reactor construction with a high transparency of ~92 % in the range of 380 to 780 nm (Adams *et al.*, 2008). PMMA is often selected as the material of choice for prototype designs due to its versatility. The material can be easily manipulated which allows for a large degree of flexibility during fabrication, particularly with the positioning of sample ports and gas valves. Despite PMMA having a low maximum operating temperature of ~80 ^{o}C the material has good mechanical strength. At higher

temperatures, however, the Perspex will begin to degrade and light transmission will be significantly reduced as a result. Perspex is also vulnerable to UV degradation over time, which presents a significant problem in its use as a material for construction.

PMMA is routinely employed in the literature for photocatalytic reactor construction (McCullagh *et al.*, 2011). The Double Skin Sheet Reactor investigated in publications by Benz *et al.* (1996), Dillert *et al.* (1999) and van Well *et al.* (1997) had a framework constructed of Plexiglass®. The unit was comprised of a number of channels through which a reaction medium containing a suspended catalyst was passed under solar illumination. The reactor was used in pilot scale studies for waste water treatment and was found to remove 50 % of organic pollutants in an 11 hr time frame. As PMMA is a readily available material and is cost effective it is an ideal material for pilot scale studies.

PMMA was the construction material utilised for the development of novel photocatalytic reactors discussed by Adams *et al.* (2008). Adams and colleagues discussed the development of a multiplate thin film reactor and a rotating drum reactor. In this instance, PMMA was investigated as both a support material for the immobilisation of a thin film catalyst in the multiplate design and as a material for the construction of the rotating drums. The paper by Adams *et al.* investigated two substrate materials to be used for the immobilisation of a thin film catalyst; PMMA and titanium. It was found that PMMA outperformed titanium as a solid support over a number of reactor plate angles.

PMMA was also used as a support structure for a thin film photocatalyst in a publication by Rizzo *et al.* (2006). TiO_2 produced by a sol-gel method was coated onto PMMA stacked rings which were assembled to allow the flow of MB through the stacked structure resulting in photodegradation. The UV transparency of PMMA and ease of manipulation made it an excellent choice for incorporation into this reactor design. The unit was capable of degrading 80 % MB with 10 min of UV irradiation.

4.1.3.2 Stainless Steel (SS)

The properties of SS are favourable for use in the construction of reactor units. While SS is not as easily manipulated as PMMA, it is a more robust material and can withstand extreme operational conditions. As a result a number of SS grades have been developed for multiple purposes in industrial applications. The chemical and physical properties along with the elemental configuration of the steel vary dependant on the grade (Peckner and Bernstein, 1977).

Table 18 summarises the grades currently used in industrial and commercial processes. Austenitic grade SS, in particular grade 316, has a number of characteristics which make it an attractive material for incorporation into photo reactor design. SS 316 has an elemental arrangement of <0.08 % C, <0.1 % N, 16-18 % Cr, 10-14 % Ni and 2-3 % Mo (Leffler, no date).

Steel Category	Elemental Composition (wt %)					Ferro-magnetism
	C	Cr	Ni	Mo	Other	
Martensitic	>0.10	11-14	0-1	-	V	Magnetic
Martensitic-austenitic	<0.10	12-18	4-6	1-2	-	Magnetic
Precipitation hardening	-	15-17	7-8	0-2	-	Magnetic
Ferritic	<0.08	12-19	0-5	<5	Ti	Magnetic
Ferritic-austenitic	<0.05	18-27	4-7	1-4	N,W	Magnetic
Austenitic	<0.08	16-30	8-35	0-7	N,Cu,Ti,Nb	Non-magnetic

Table 18; *Summary of steel categories with elemental composition*

The increased presence of Cr (in comparison to other grades) increases its suitability for incorporation into photocatalytic reactor technology. Cr content in

the alloy increases resistance to corrosion along with oxidation resistance at high temperature. Further increasing the Cr content will decrease the rate of corrosion; a 95.6 % decrease in corrosion rate (mm/year) was observed from 0 to 10 % Cr content (Leffler, no date).

The Ni content of SS provides 316 with its austenitic structure, the result of which increases its durability and strength. The addition of Ni changes the structure of SS from ferrite to austenite by altering the structure from body centred cubic to a face centred cubic structure, Figure 47.
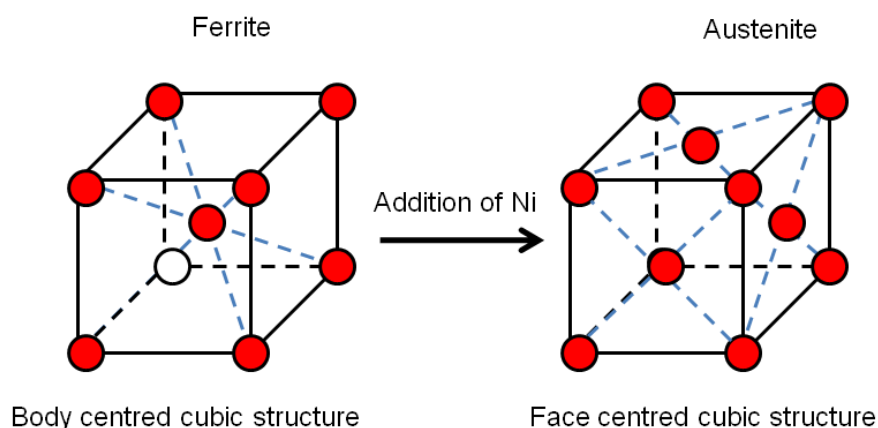
Figure 47; *Schematic representation of Ferrite to Austenite structure of stainless steel by the addition of Ni*

As with PMMA, SS has been employed in photocatalytic reactor design as both a construction material and support for thin film immobilised catalysts (Shang *et al.*, 2003; Chen and Dionysiou, 2006; Chen and Dionysiou, 2006; Rosas-Barrera *et al.*, 2011). Chan *et al.* (2003) employed SS 316 plates as solid supports for the immobilisation of a thin film catalyst for the treatment of wastewater under solar irradiation. The reactor configuration used a step-like structure of SS plates to allow the flow of wastewater (containing benzoic acid) to pass over the thin film catalyst, Figure 48. The SS plates provided a robust structure for coating and no corrosion of the plates were reported in the publication. The investigation concluded 83 % removal of benzoic acid was achieved with a number of intermediates being identified by HPLC analysis.

Figure 48; *Image of step-like SS structure used by Chan et al. (2003)*

4.1.3.3 Quartz

In order to achieve all required optical properties, quartz glass is commonly used in photocatalytic reactor technology. Quartz has excellent thermal, physical, optical and mechanical properties, Table 19 (Richet *et al.*, 1982). Quartz glass offers a robust and stable alternative to Pyrex glass and PMMA materials based upon the thermal and physical properties. Quartz has a continuous operating temperature of 1000 ^{o}C and tensile strength of 70 x 103 KN/m^2. The purity of quartz is high at 99.9 %, which allows a broad range of light transmittance (180 – 2000 nm).

Thermal Properties	
Softening point	1683 ^{o}C
Annealing point	1215 ^{o}C
Strain point	1120 ^{o}C
Continuous operating temperature	1000 ^{o}C
Physical Properties	
SiO_2 purity	99.99 %
Typical metallic impurities	< 10 ppm
Optical Properties	
Light transparency	180-2000 nm
Mechanical Properties	
Density	2.20 x 103 Kg/m^3
Tensile strength	70 x 103 KN/m^2

Table 19; *Thermal, physical, optical and mechanical properties of quartz glass*

An example of quartz glass used for reactor design purposes is seen in a recent publication by Natarajan *et al.* (2011), in which a quartz LED reactor was utilised for the degradation of dyes. The photocatalytic reactor consisted of quartz tubes on which a thin film coating was on the inner wall of the reactor. The reactor was surrounded by an LED illumination jacket. In a 5 hr irradiation time frame dyes Malachite Green, Rhodamine B and MB were degraded to levels of 99, 62 and 61 % respectively. The properties of quartz glass allowed for a high level of light transmittance capable of penetrating the thin film coating on the inside wall and thus degrading the dyes which came into contact.

Quartz has also been shown to be used as a support structure for the immobilisation of catalysts. Vella *et al.* (2010) coated TiO_2 onto quartz wool for

incorporation into a packed bed system. The design concept of this system allowed for intimate contact among reactants, photons and the photocatalytic surface (Vella *et al.*, 2010) for the degradation of formic acid in wastewater streams.

4.1.4 Catalyst Deployment

The method of catalyst platform and distribution within a photo reactor is a key consideration. The method of catalyst deployment is dictated by the catalyst platform. The previous thin design concept (TFMTPR) displayed a significant level of activity towards degradation of MO. The TFMTPR was developed utilising a standard method of thin film synthesis and one which is widely applicable. A range of powder catalysts were developed by CalTech and the University of St. Andrews which could not be deployed as a thin catalyst, thus restricting the further use of the TFMTPR.

As powder catalysts were to be deployed in the system, the primary focus of the design concept was to achieve increased mass transport and maximum light penetration and distribution. Mass transport can be achieved via two processes; convection and diffusion. Convection is the movement of particles by exertion of an external force such as stirring or sparging. Fluidisation achieves mass transport by convection. Diffusion is the transport of particles as a result of a concentration gradient.

Total mass transport can be expressed as shown in Equation 25, where $J_{i(x)}$ is the flux of species to the catalyst surface, D is the diffusion coefficient, $\delta C_{i(x)}/\delta x$ is the concentration gradient, C is the concentration of species and $v_{(x)}$ is the velocity of solution movement.

$$J_{i(x)} = -D\frac{\delta C_{i(x)}}{\delta x} + C_i v_{(x)}$$

Equation 25

Further to this, the mass flux of reactant to catalyst surface which is defined as *Jp* can be expressed as shown in Equation 26, where J_p is mass flux ($gm^{-2} s^{-1}$), k_f

is the mass transfer coefficient (m s^{-1}), C_b is the concentration of reactant in bulk (gm^{-3}), C_s is the concentration of pollutant at the catalyst surface, A_{cat} is the catalyst surface area and V_{liq} is the liquid volume present in the reactor.

$$J_p = k_f(C_b - C_s)\frac{A_{cat}}{V_{liquid}}$$

Equation 26

The rate of pollutant or target species conversion is controlled by the rate of mass transfer. If mass transfer is fast, pollutant concentration at the catalyst surface is equal to that in the bulk. Therefore the mass transfer of a reactor is capable of supplying target species to the catalyst surface to replace those that are consumed by the reaction. Under these conditions the rate of destruction is the limiting factor. Alternatively, if mass transfer is low the target species concentration at the catalysts surface is less than that in the bulk. Mass transfer is the limiting factor under these conditions as target species are immediately destroyed when they reach the catalyst surface. The determination of a mass transport controlled reactor and a non-mass transport controlled reactor can be determined by observing the impact of agitation on the rate of reaction. In a mass transfer controlled reactor increasing the agitation will increase the rate of the reaction. In a non-mass transfer controlled reactor the rate of reaction is unaffected by an increase in agitation.

4.2 Design Concept of the Propeller Fluidised Photo Reactor (PFPR)

The design concept of the PFPR was to construct a unit capable of providing a controllable air tight environment in which novel photocatalysts would be agitated to facilitate desired photocatalytic transformations in gas, solid, liquid and vapour phases. The primary purpose of the unit was the photo reduction of CO_2 and H_2 production from H_2O splitting.

The design properties of the SFPR, MCPR and TFMTPR, which were evaluated in Chapter 2 and 3, were taken into consideration for the development of the PFPR units along with the requirements put forward by collaborative partners. Properties such as photo delivery system, method of fluidisation, catalyst

platform and reactor geometry were based upon previous designs (Section 2.3, 2.4 and 3.3). The design concept of the PFPR focused on the following characteristics:

- Suspension of catalyst particles by mechanical agitation
- Non pressurised unit
- Gas tight
- Versatility in operation - applicable in liquid, vapour and gas phase
- Inclusion of an appropriate irradiation system
- Low maintenance
- Modular

The construction of two PFPR units is discussed in the following chapter, hereafter referred to as PFPR Model I and II.

4.3 PPFR Model I

The key observations made from the results in Chapter 2 relating to reactor performance, evolution and illumination source selection were considered in the design and construction of the PFPR Model I. Discussed here is the reactor geometry, fluidisation approach and illumination source selected.

4.3.1 Reactor Geometry

The unit, constructed primarily of PMMA (Plexiglass XT$^®$), was an annular reactor consisting of a tubular body with a top and base plate.

The PMMA tubular body had a height of 500 mm with an OD, ID and wall thickness of 100, 94 and 3 mm respectively. A schematic illustration and photograph of the unit is shown in Figure 49. To increase the stability of the reactor body and to prevent any obstruction of illumination no sample ports or gas valves were positioned on the outer surface of the PMMA body. This provided the unit with an increased area for irradiation exposure.
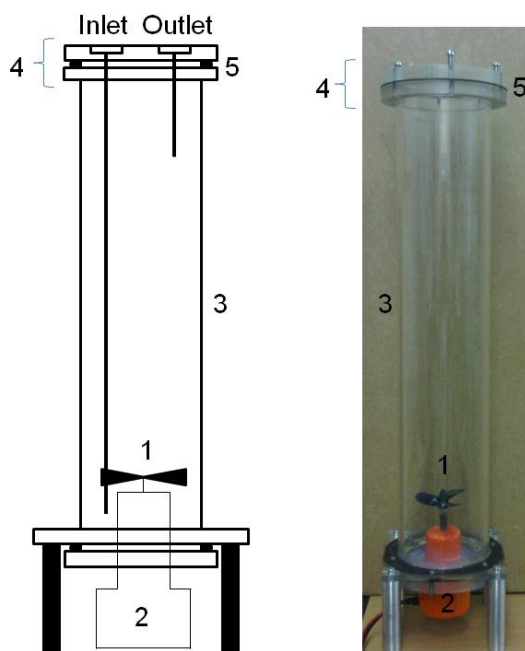
Figure 49; *Schematic of PFPR Model I design with 1. propeller, 2. bilge pump propeller motor, 3. PMMA reactor body, 4. PMMA flange and cap and 5. O-ring seal*

The unit had a calculated volume of ~3600 mL, with an operating capacity range in the liquid phase of 500 to 2000 mL which provided a 3100 to 1600 mL gas headspace volume.

4.3.2 Reactor Top and Base Plates

The top and base plates, also constructed of PMMA, consisted of a flange piece which was sealed to the vessel body, and a cap piece. As the top and base cap posed no obstruction to the illumination path they housed the sample, inlet and outlet valves, along with the propeller motor in the base cap. A static torodial (O-ring) seal and rubber gasket was placed between the flange and caps to ensure an air-tight seal was created. The flange, O-ring seal (Barnwell Ltd.), rubber gasket seal and cap were held in place by 6 M4 bolts, positioned in a circular formation to ensure an even distortion of the O-ring. SS 316 needle bonnet valves (Swagelok, Model SS-ORS2) were used to control the gas flow in the reactor and also as a sample valve from which gas headspace samples could be taken. A cross section schematic of the top and base caps is shown in Figure 50 and Figure 51.
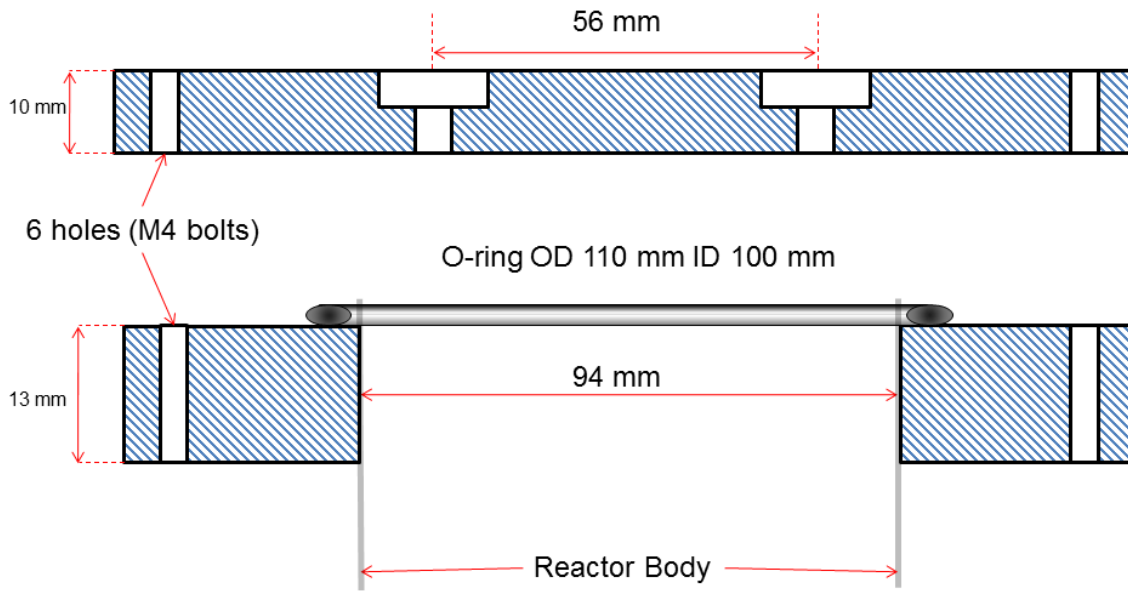
Figure 50; *Cross schematic of the top cap and flange*
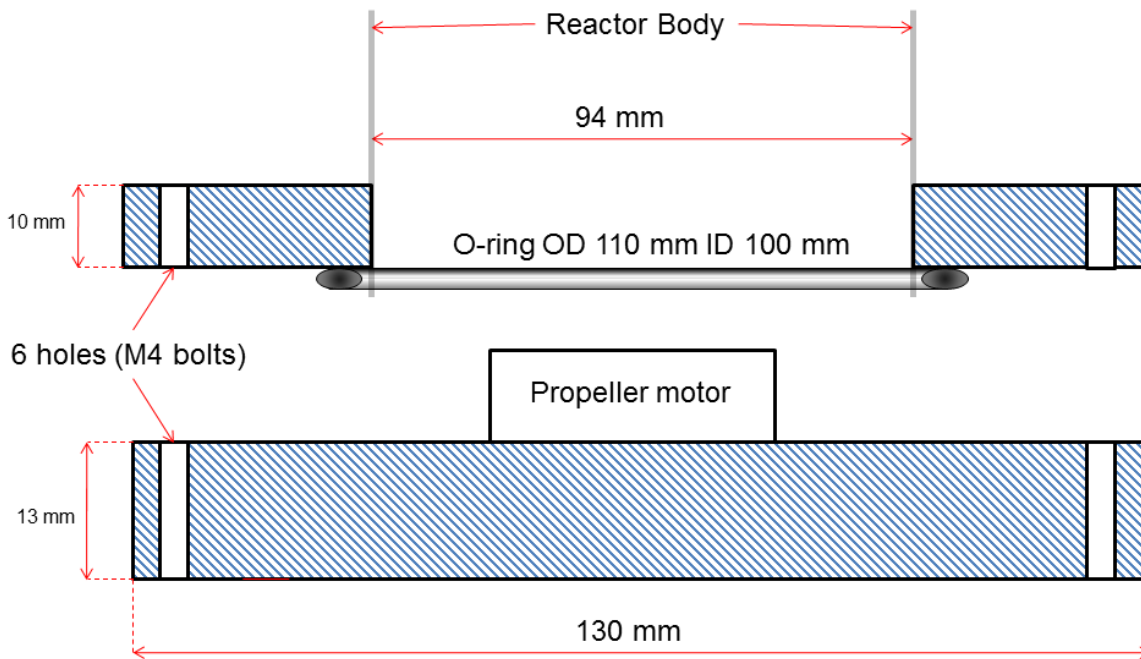
Figure 51; *Cross section schematic of base cap and flange*

4.3.3 Method of Fluidisation

Whilst the SFPR and MCPR showed the introduction of gas at a required velocity is suitable for fluidisation, it was noted that under anaerobic conditions the injection of a gas is not beneficial. Alternatively the TFMTPR relied on the catalyst being fixed to a solid support, thus requiring no fluidisation. The catalyst developed by the University of St. Andrews and CalTech were predominantly in a powder form and not suitable for immobilisation to a solid substrate. Thus, an alternative method of fluidisation was developed.

Fluidisation in the PFPR Model I was achieved by a 60 mm 3 blade nylon propeller with a M4 shaft (Riverside Models) located at the base of the reactor, Figure 52. The rotational speed of the propeller was controlled by a modified 1100 GPH Submersible Bilge pump motor (Secure Fix Direct, Model SFBP011). The motor had a voltage range of 0 - 12 dcV with an optimum operating range of approximately 3 - 7 dcV. This optimum range allowed the propeller to rotate at speeds of 543 to 1267 rpm. This range of rotational speed gave a high level of control over both the mixing capabilities of the propeller and increased aerodynamic drag which brought stationary particles to a fluidised state in the gas, liquid and vapour phase. The propeller geometry was capable of dictating the style of fluidisation. In gas and vapour phase, the angle and shape of blades can increase the thrust created to fluidise the catalyst. In liquid phase, a shallower angle and elongated propeller blade creates increased fluidisation and mixing of a catalyst.

(a)   (b)
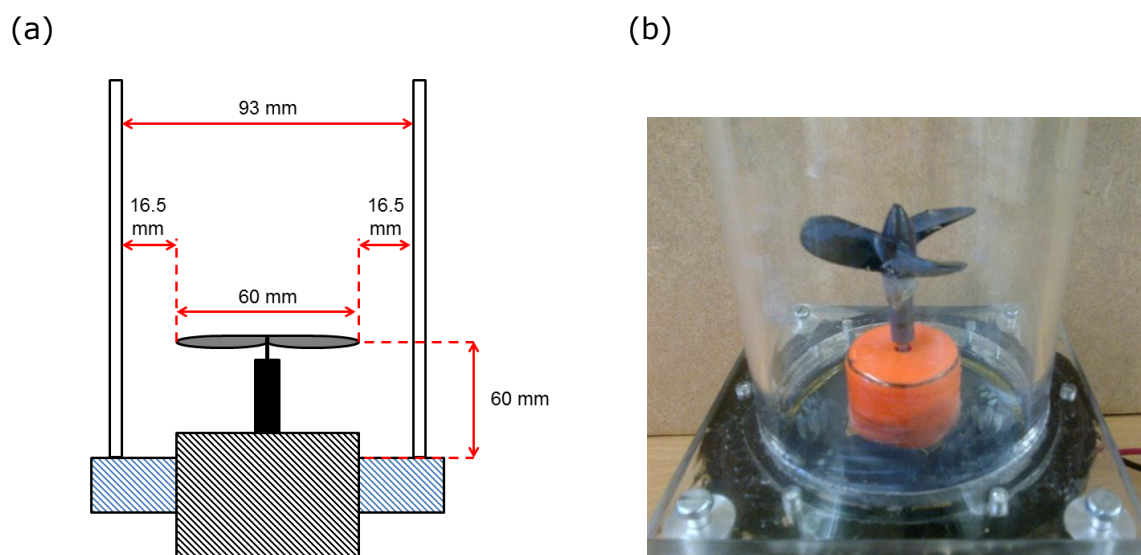
Figure 52*; (a) cross section schematic of propeller positioning in the PFPR Model I and (b) image of 3 blade nylon propeller*

4.3.4 Illumination Source

The design of a photocatalytic unit must achieve the utilisation of the radiant energy as effectively as possible in order to achieve the highest rates of reaction (Camera-Roda *et al.*, 2005). Therefore, the PFPR Model I was designed to be operated with external illumination, which meant an increased area of photocatalyst per unit reaction volume ratio, along with increased mixing capabilities and maximum direct exposure to illumination. This was a key characteristic as a reported limitation of annular reactors is the low area of photocatalyst per unit reaction volume, which is due to a reduced area of annular space as a result of having a centrally positioned immersed illumination source (Josset *et al.,* 2009).

The PFPR Model I was suitable for use with a number of illumination sources however, was limited to short exposure times with high power lamps. Illumination sources investigated included a 500 W high power lamp, 2 48 W arc structured lamps and an array of four36 W compact lamps. Due to the power and heat generated by the 500 W and 2 48 W lamps the rate of degradation of the unit was increased. Exposure from four36 W lamps in a 360 $^{\circ}$ surrounding array

with cooling fans in a thin aluminium lined light box was found to slow the degradation rate of the PMMA, Figure 53.

(a)   (b)
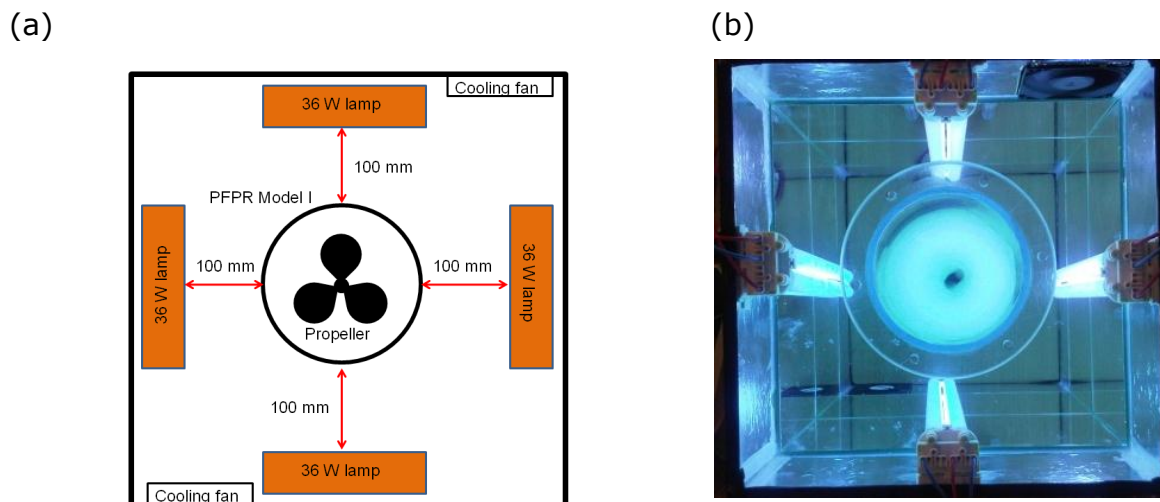
Figure 53; *(a) aerial schematic of illumination system and positioning of PFPR Model I and (b) image of PFPR Model illuminated by four36 W lamps*

4.4 PFPR Model II

The PFPR Model I was an efficient prototype, however, a number of limitations prevented its full utilisation for CO_2 reduction and H_2 production. These limitations included:

- Restricted light transmittance of PMMA
- Degradation of PMMA from prolonged irradiation exposure
- Robustness of general PMMA structure
- The durability of the static O-ring and rubber gasket seal

In an attempt to overcome these limitations the PFPR Model II was constructed based upon a reviewed design. Discussed here is the reviewed design focusing on the reactor geometry including construction materials, fluidisation approach and illumination system.

4.4.1 Reactor Geometry

While the general principle of Model II remained similar to Model I the second unit was downscaled from the prototype. In addition the construction material was changed in an attempt to produce a more robust and reproducible unit. In replace of PMMA, quartz glass (Robson Scientific) and SS 316 (Aalco) were used as construction materials. The annular unit consisted of a quartz glass body with SS 316 flange and caps, Figure 54.
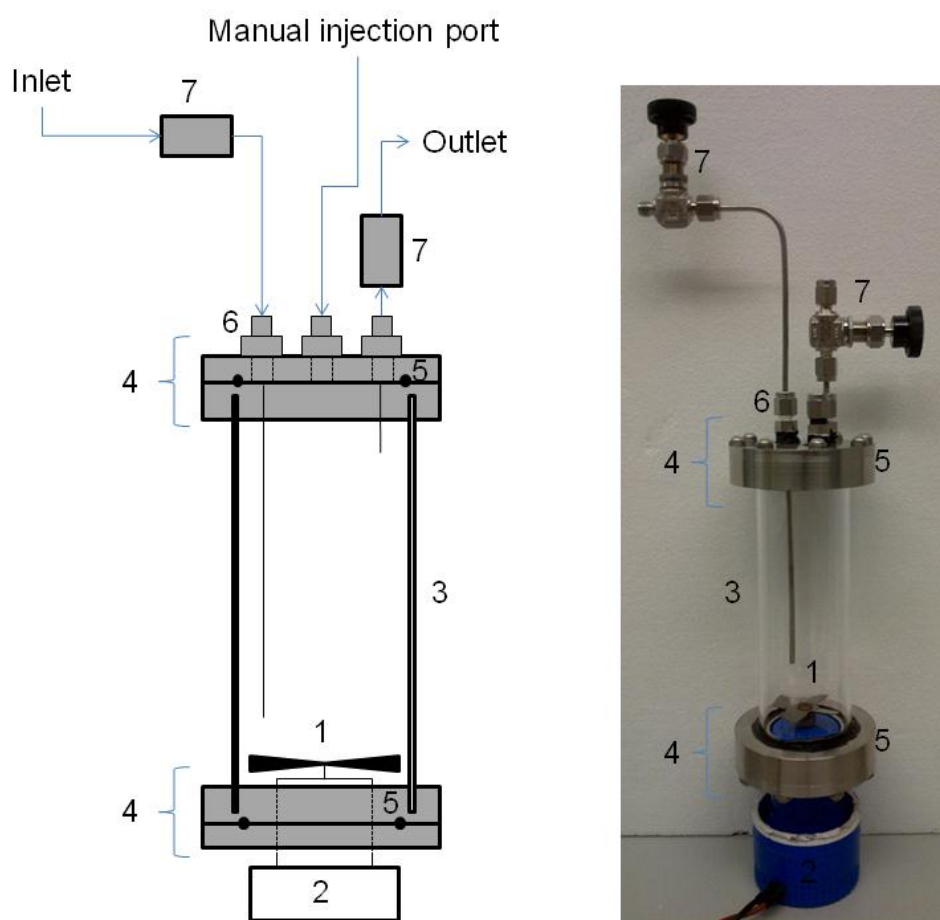

Figure 54; *Schematic of PFPR Model II design with 1. propeller, 2. bilge pump propeller motor, 3. Quartz glass reactor body, 4. SS flange and cap, 5. O-ring seal, 6. SS nipple fitting and 7. Needle bonnet valves*

The quartz glass tubular body had a height of 150 mm with 9 mm at each end embedded into a SS flange piece. The OD, ID and wall thickness of the reactor

body was 50, 46 and 2 mm respectively. As previously discussed, the unobstructed reactor body provided a large surface area for irradiation exposure. The use of quartz glass over PMMA meant the light transmittance was significantly increased. Furthermore, the durability was also increased as quartz glass is capable of withstanding prolonged periods of exposure from low and high power lamps. The unit had a calculated capacity of ~210 mL with a typical operating capacity of 150 mL allowing a 60 mL gas headspace volume. The minimum and maximum operating capacities were 60 mL and 180 mL respectively giving a 150 mL and 30 mL gas headspace volume.

4.4.2 Reactor Top and Base Plates

The design concept illustrated in the PFPR Model I schematics for the top and base plates were adopted, with changes in the PFPR Model II to ensure a durable gas tight seal was maintained. The top and base plates were constructed of two SS assemblies; the flange and cap. An aerial schematic of the top plate assembly is shown in Figure 55. An image of the top plate cap and flange can is shown in Appendix I.
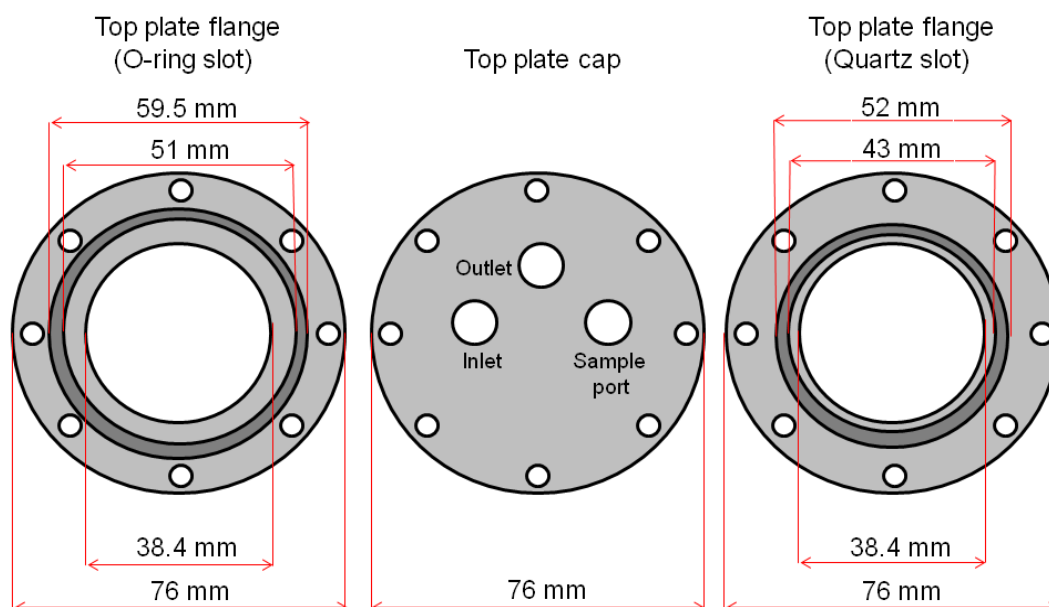
Figure 55; *Aerial schematic of top plate flange and cap*

The flange pieces had a thickness of 13 mm to allow for two grooves on the upper and lower side. On the lower side a slot was drilled 9 mm deep and 4.5 mm wide in which the quartz glass tube was sealed. On the upper side a 4.4 mm slot was drilled to allow for an O-ring seal, Figure 56.
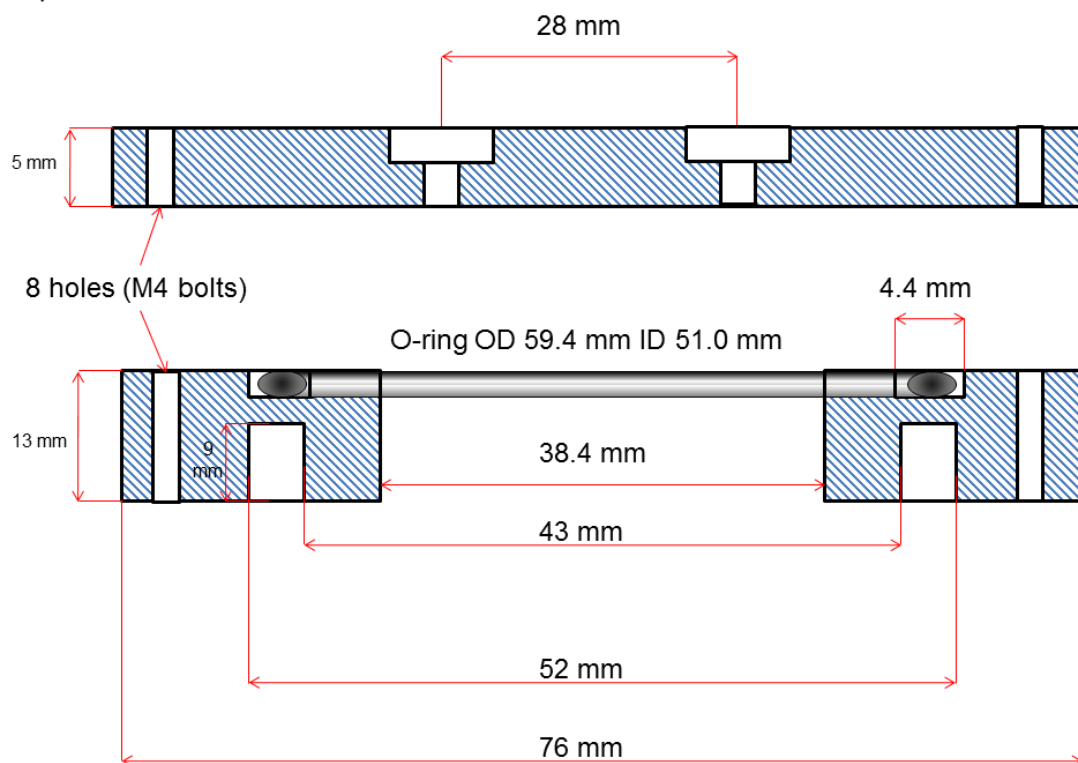
Figure 56; *Cross section schematic of top plate flange and cap.*

The top place construct contained the sample port along with the inlet and outlet valves. Located on the top plate cap were 3 Swagelok SS nipple fittings (Swagelok, Model SS-2-HN 1/8 NPT) for gas inlet, outlet and sampling (Figure 57). Swagelok needle bonnet valves controlled the gas flow through the reactor. The sample port was custom made for the specific parameters of the unit. A high heat resistant silicone based sealant was used on the outer surface of each fitting to enhance the seal.
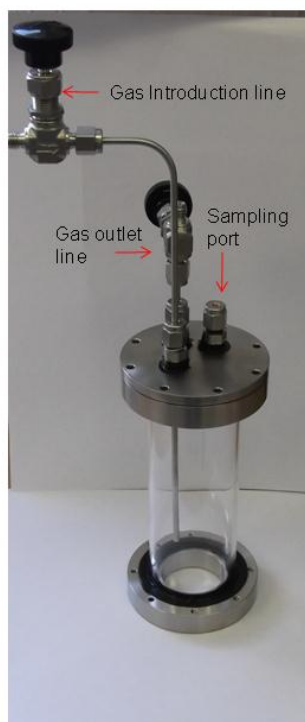
(a)   (b)
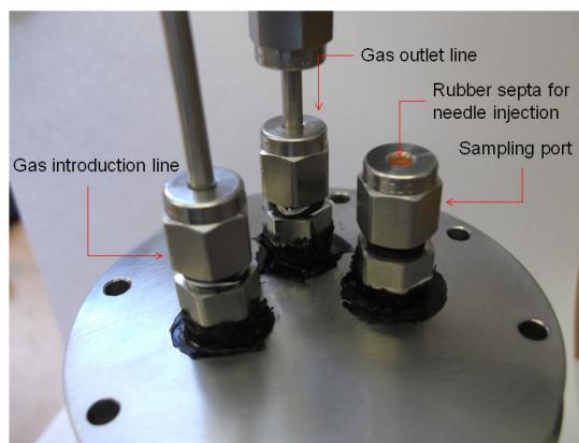
Figure 57; *(a) Image of top plate cap with gas valves and ports and (b) close up image of gas valves and sample port with rubber septa*

In order to operate the PFPR unit with the GC system at the University of St. Andrews the needle valves, which controlled air flow, were also used to draw samples from the headspace for online analysis. A requirement of operating the PFPR Model II with CalTech was the construction of needle extraction port for manual GC injection, Figure 58. The assembly consisted of a Swagelok nipple fitting containing a 60 mm OD Viton 75 O-ring (Barnwell) and septa (Fisher Scientific). The septa (OD 6 mm) were of GC grade, ultra low bleed and stable up to a temperature of 400 $^{\circ}$C. The durability of GC septa was tested with a Thermo Scientific GC Leak Detector. The average number of injections that could be performed before septa failure was 25.
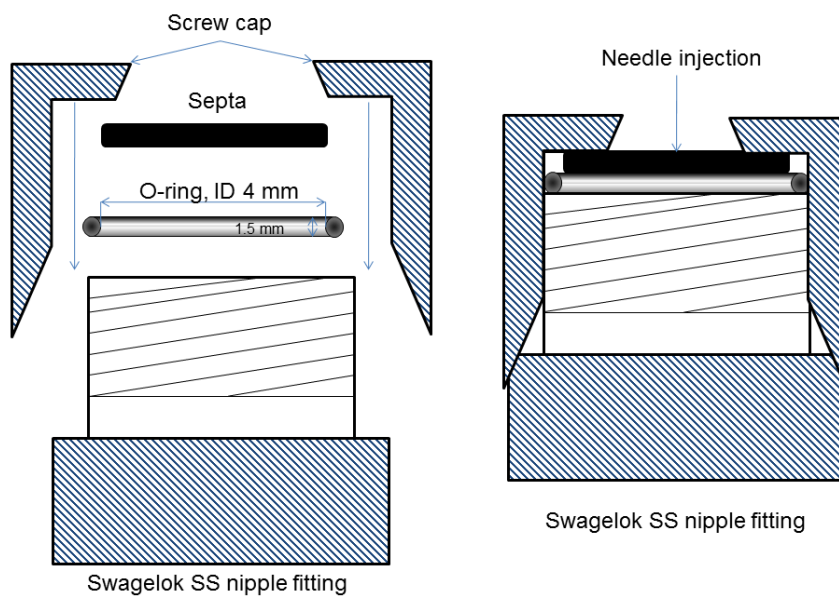
Figure 58; *Cross section schematic of needle injection sample port assembly*

The base flange and cap were constructed in a similar way to the top with minor adjustments, Figure 59. An image of the base plate cap and flange is shown in Appendix I. The design concept for the base cap was to hold the propeller motor, ensuring the base cap and motor were an independent unit and only the top and base flange were fixed to the quartz glass. This alleviated any unnecessary pressure being applied to the glass body of the reactor.
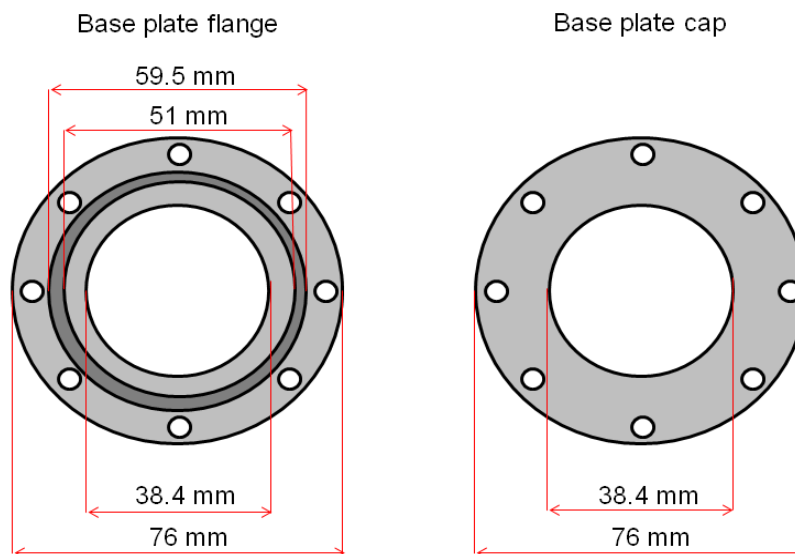
Figure 59; *Aerial schematic of base plate flange and cap*

4.4.3 Reactor Seals

The static O-ring seal and rubber gasket in the PFPR Model I provided an air tight seal however, the durability of the seal was low. This limitation was addressed in the reviewed design. The design concept was to conduct H_2O splitting and CO_2 reduction. Thus, to ensure neither H_2 nor CO_2 reduction products are lost and the reactor was kept under optimum environmental conditions the seals must be gas tight, chemical and high heat resistant and have a low level of expansion.

As previously discussed an O-ring was required between the flange and cap pieces to ensure they were sealed. While the approach discussed above provided the primary seal for the unit, careful consideration was given to the O-ring material and distortion space to ensure when assembled the unit was sealed.

The O-ring material must be appropriate for use with the desired chemical process and should not react with any compounds present in the reactor. Materials utilised for the O-rings included a copolymer of acetonitrile and butadiene (Nitrile NBR) (Barnwell) and fluorocarbon based polymer Viton 75 (Barnwell). Both Viton 75 and Nitrile NBR provide satisfactory seals against H_2, CO_2, CO, CH_4 and N_2, with Viton 75 also providing a satisfactory seal against O_2.

Nitrile and Viton O-rings have a good temperature range at -30 to 120 $^{\circ}$C and -20 to 200 $^{\circ}$C respectively under continuous temperature.

The efficiency of the O-ring in this style of design was reliant on the expansion and distortion created when the seal was fixed between the flange and cap. If not given sufficient space to expand and distort, the O-ring seal will fail. An O-ring seal is reliant on equal pressure and subsequent distortion occurring. In the previous prototype design the O-ring seal was not given a designated space for distortion, and thus expansion of the O-ring was uneven and a gas tight seal was not guaranteed. Therefore, careful consideration was given to the positioning of the O-ring seal in the PFPR Model II. The O-ring had an OD of ~60 mm with a thickness of ~3 mm. A 4.4 mm wide O-ring slot was drilled providing a distortion width of 1.4 mm, as recommended by the O-ring suppliers. Thus, when the reactor was fully sealed the pressure exerted by the top cap forced the O-ring to expand and distort into the slot provided resulting in an air tight seal, Figure 60.
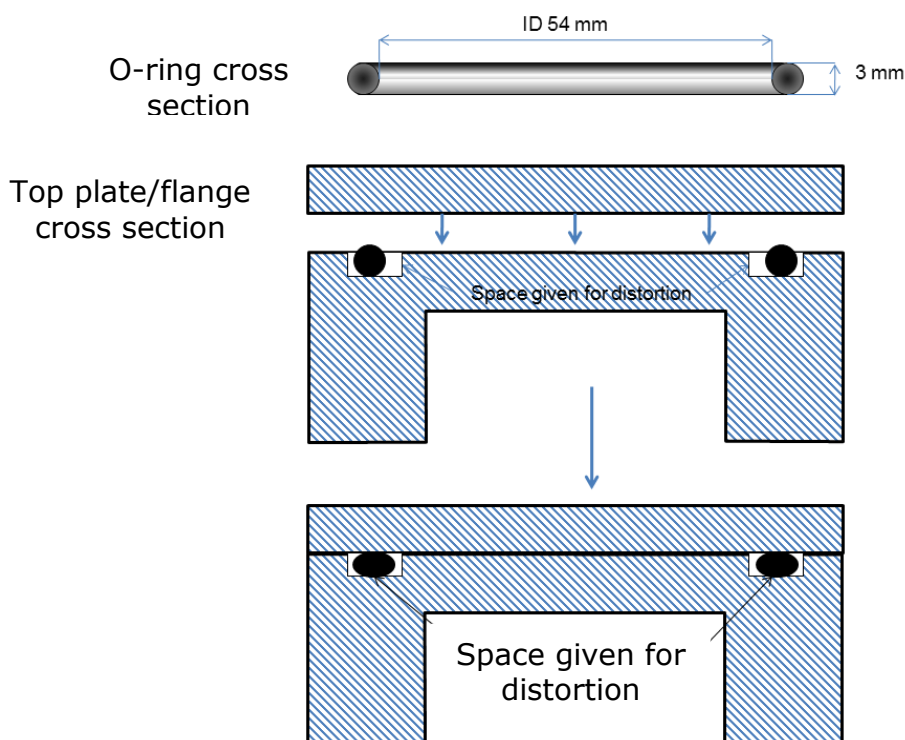
Figure 60; *Cross schematic of O-ring cross section and positioning within flange allowing for distortion*

The seal between the quartz body and SS flange pieces was a key aspect of the unit. The preliminary seal approaches investigated are shown schematically in Figure 61. Figure 61 depicts a single (b) and double (a) O-ring seal approach to securing the glass and flange. This process involved a carefully machined slot being cut into the inner wall of the SS flange in which one or two O-ring seals would be placed. The quartz glass tubular body would then be pushed fitted into the flange piece. While this approach carries the advantage of allowing the reactor to be fully disassembled it relies on external force being applied to ensure an air tight seal. The external force may be generated either manually or through the use of supporting columns, which would be tightened to hold the flange in place. The drawback to this approach was the external illumination source used would be partially restricted due to the external support columns. Furthermore the use of external force results in pressure being applied to the seal and quartz glass which would threaten the structural integrity of the unit.
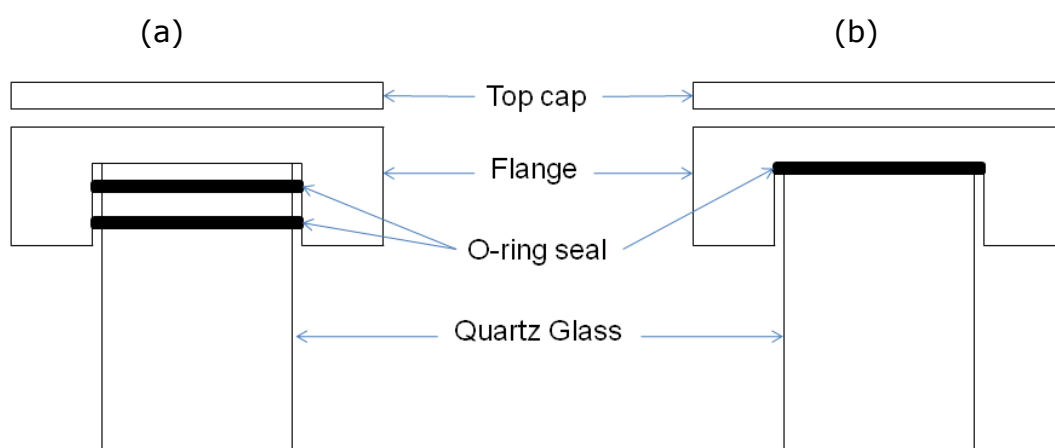
Figure 61; *Schematic of double O-ring (a) and single O-ring (b) seal designs*

An alternative process was taken to seal the flange and quartz body. The process is illustrated in Figure 62. This simple, yet effective approach used a high heat resistant silicone based sealant, which provides an excellent chemical inert seal. The sealant was placed in the machined slot to fill the groove to approx. 5 mm, Figure 62 (a). The glass tube was then accurately placed into the sealant filled

slot ensuring a distance of approx. 1.25 mm was between the outer diameter of the slot and glass tube, Figure 62 (b). This process produced a 'U-shaped' seal between the glass and flange which when set was highly robust and showed minimal shrinkage or expansion, Figure 62 (c). This approach required no application of external force, thus minimising pressure on the reactor body. Once cured for 24 hr, the seal was sufficient to sustain the SS flange pieces.

(a)   (b)

(c)
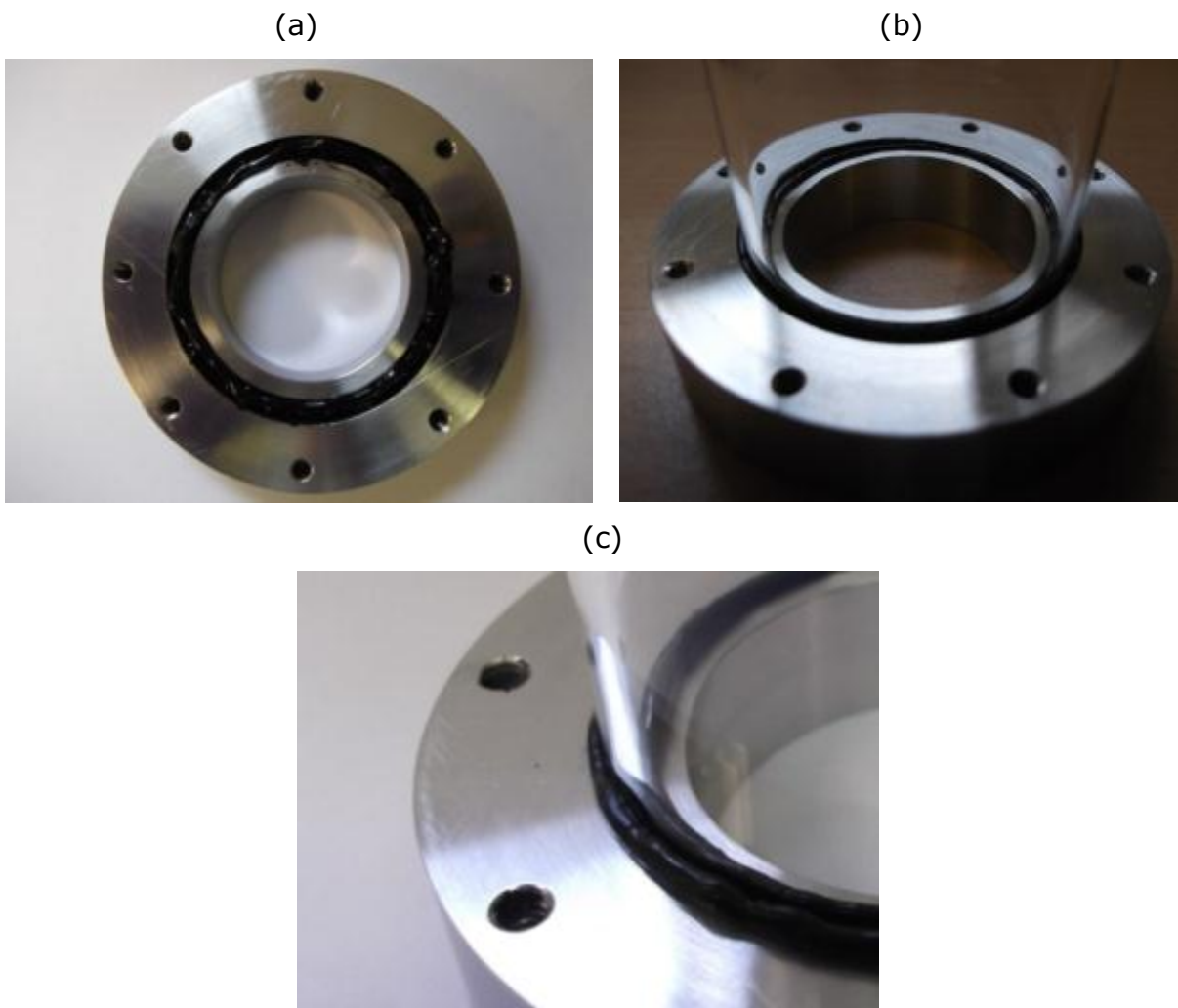
Figure 62; *Images depicting the process utilised to seal the quartz glass tube to stainless steel flange*

4.4.4 Method of Fluidisation

Fluidisation in the PFPR Model II was achieved utilising a 38 mm four blade SS 316 propeller (Fisher Scientific) located at the base of the reactor. The rotational speed of the propeller was controlled by a modified 350 GPH Submersible Bilge Pump motor (Secure Fix Direct, Model SFBPO3) which was sealed into the cap of the base plate, Figure 63.

Figure 63; *Images of Bilge pump motor sealed into base plate cap*

The Bilge pump was adapted to provide a shaft upon which the propeller was mounted. The motor had a voltage range of 0 - 12 dcV with an optimum operating range of approximately 3 - 7 dcV. This optimum range allowed the propeller to rotate at speeds of 519 to 1211 rpm. This range of rotational speed gave a high level of control over both the mixing capabilities of the propeller and upward thrust required to bring stationary particles to a fluidised state in gas, vapour and liquid phases.

In the previous Model I, the propeller was at a height of 60 mm from the reactor base which resulted in the trapping of catalyst particles under the propeller during fluidisation. The height of the propeller in Model II was kept at a close proximity to the base of the reactor (9 mm) which reduced the area under the propeller and prevented the trapping of catalyst particles, Figure 64.

(a)

(b)
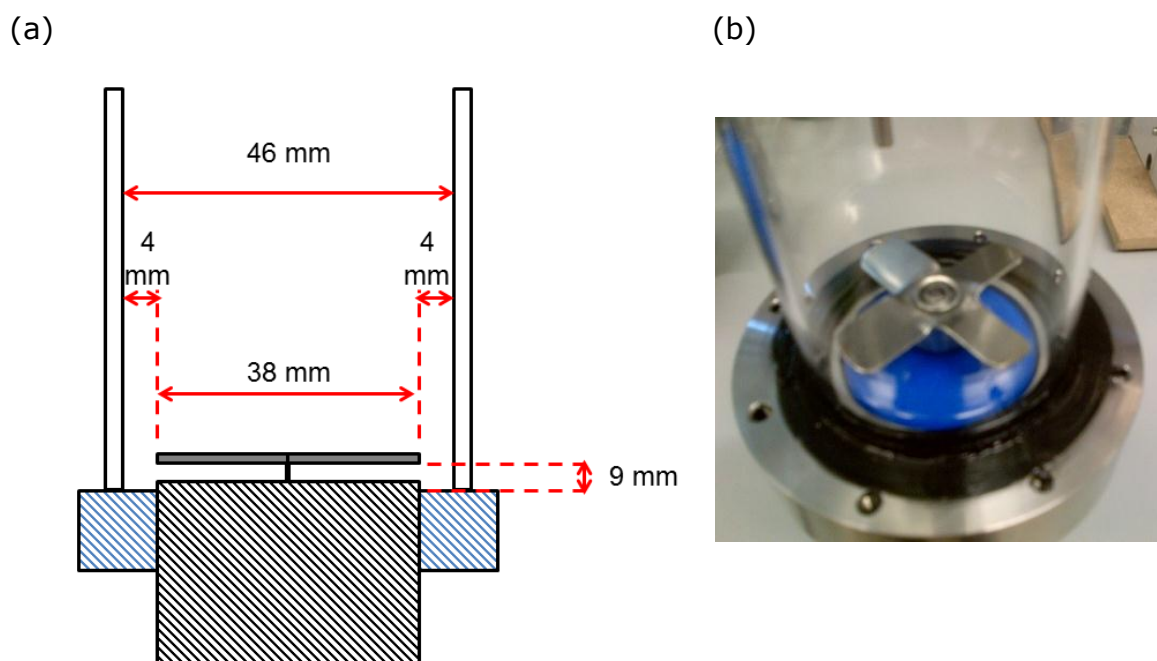
Figure 64; *(a) cross section schematic of propeller positioning in the PFPR Model II and (b) image of four blade SS propeller*

4.4.5 Illumination System

The volume of model pollutant capable of being treated is dictated by catalyst activation by exposure to an irradiation source. The method in which illumination is delivered to a reactor and the source of illumination is significant in photocatalytic studies and can greatly limit the design of a unit. As previously discussed a number of photocatalytic systems adopt medium to high pressure lamps which typically have a range of 300-600 nm. While these lamps are more energy intensive than low power lamps they generate a significant degree of heat, with a significant proportion of the lamp energy being lost as radiated heat (Bickley *et al.*, 2005). Therefore, as with Model I low power 36 W lamps were selected for use with Model II.

The photocatalytic activity of the PFPR II was dependant on the illumination provided along with the illumination source, coverage, distribution and reflectance. In order to control these parameters a light box was constructed. The mirrored Perspex box was designed to house four 36 W compact non integrated fluorescent lamps along with nine air flow control fans, Figure 65.

(a)
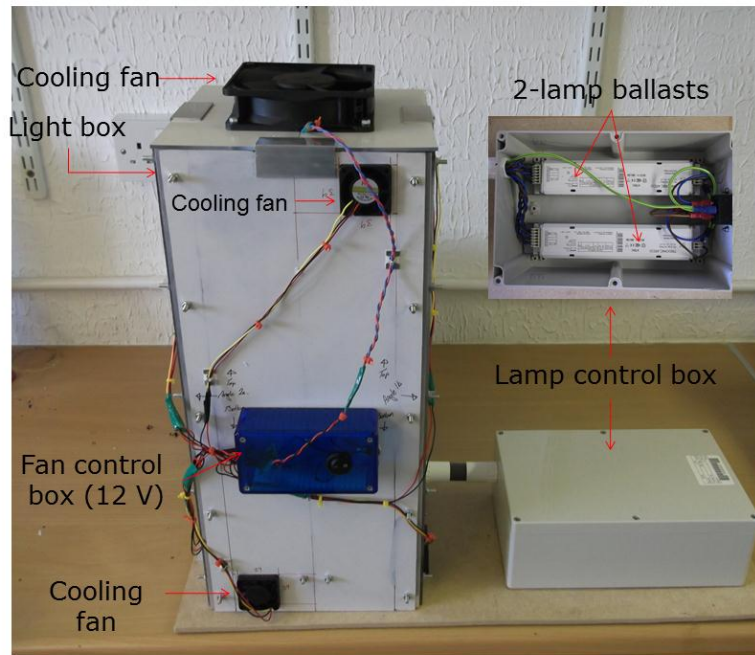
(b)
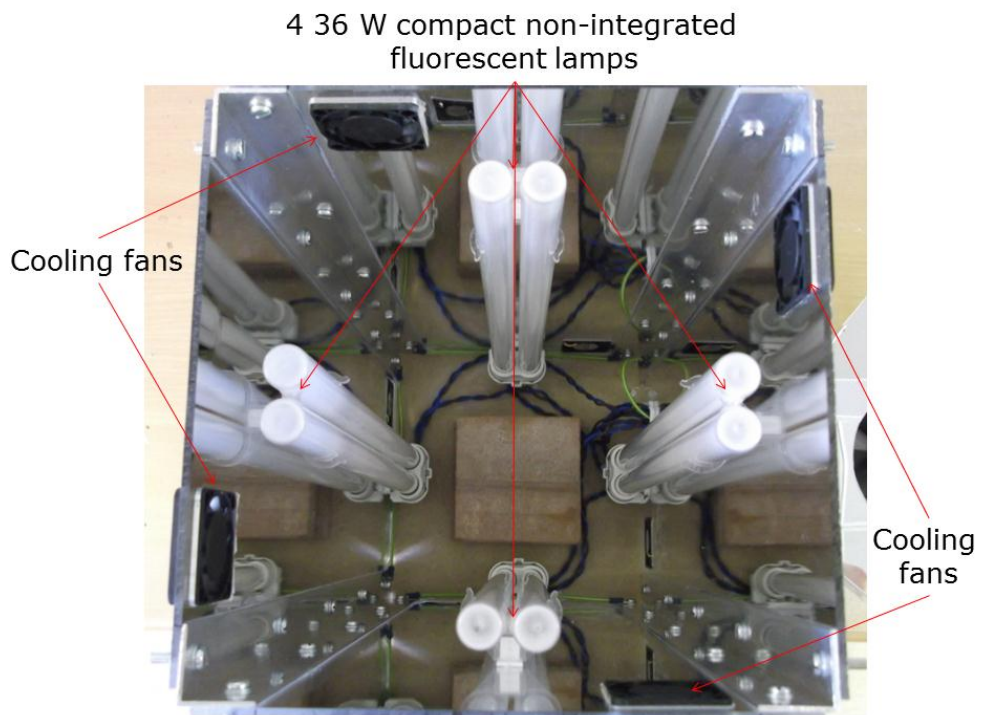
Figure 65; *(a) Image of light box with fan and lamp control boxes present and (b) internal aerial image of light box*

The PFPR was positioned centrally in the light box unit to allow for full illumination coverage. The generation of heat from the lamps can have a negative impact on the operation of a system and thus suitable cooling is required. It is essential that the cooling method does not interfere with the delivery of illumination to the reaction medium. It is also important that the lamp is operated without any obstacles which prevent it from providing full and direct exposure to the desired area of operation.

Cooling fans were positioned to allow for controlled air flow through the unit, Figure 66. Located near the base of the unit were four 30 x 30 mm (Rhino Cables) cooling fans which allowed for an external to internal air flow, while at the top of unit four fans with an internal to external air flow were positioned. In addition to this a single 120 x 120 mm fan was incorporated into the lid of the unit with an external to internal air flow. This air flow ensured the heat generated from the lamps was removed from the unit and the temperature was controlled.
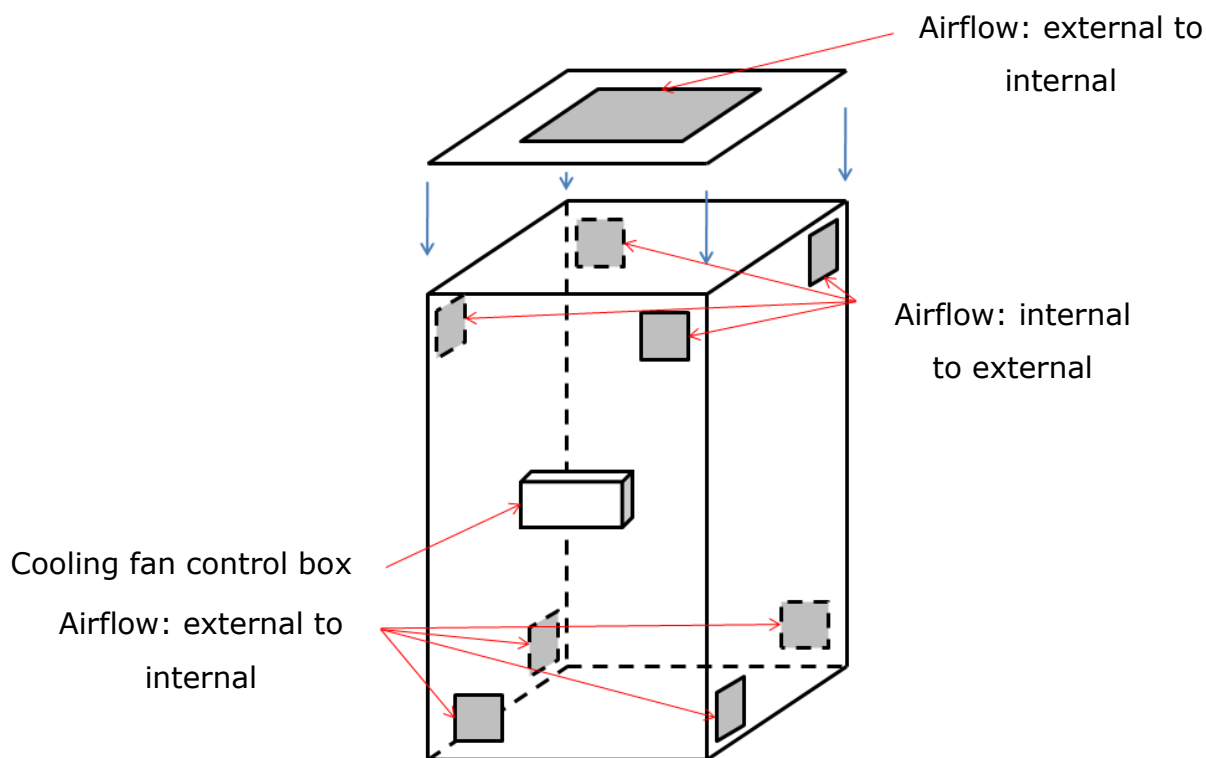
Figure 66; Schematic of cooling fan positioning on PFPR light box

4.5 Operation of the PFPR

4.5.1 Liquid-Solid Phase Operation

The unit was operated in the liquid-solid phase, through the suspension of a photocatalyst in a liquid media. The rotational speed of the propeller impacted the liquid-solid phase by increasing the cavitation and height of the reaction medium. When static the reaction medium was observed to be at a height of 165 mm and 62 mm for Model I and II respectively. At increasing propeller rotational speeds the height of the reaction medium was observed to increase, Figure 67. This trend was observed up to 8 dcV for Model I (1384 rpm) and Model II (1448 rpm) thereafter the height of the reaction medium began to plateau.
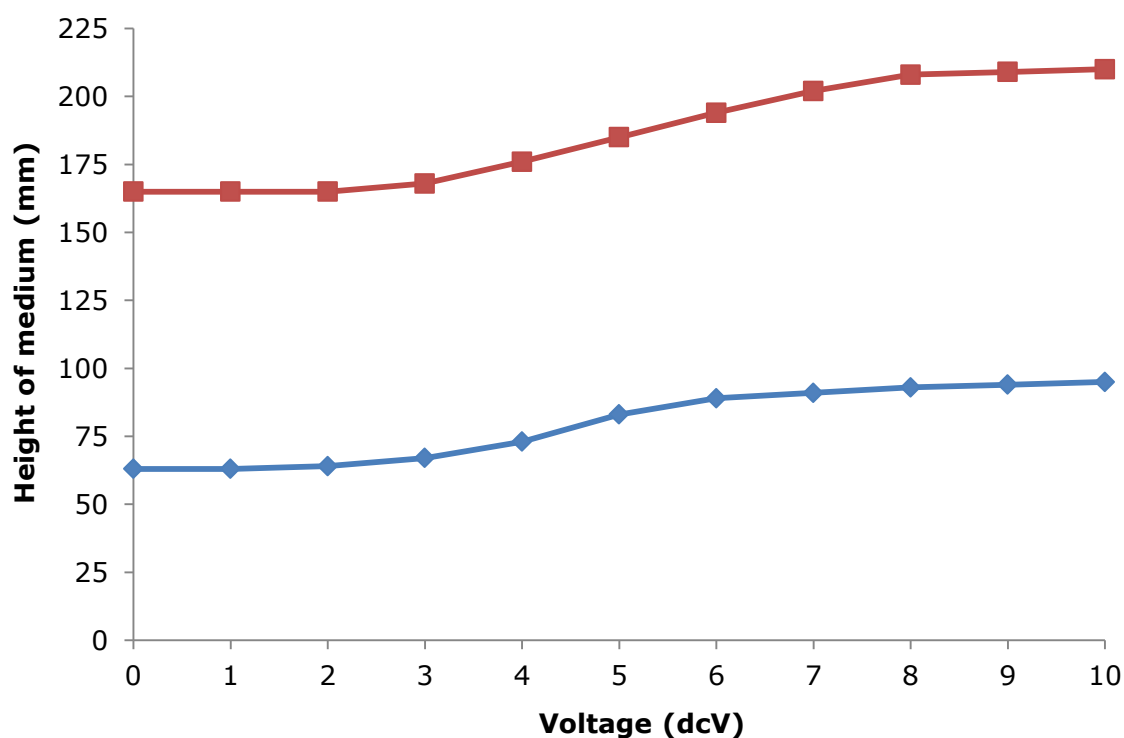
Figure 67; *Relationship between propeller rotation and height of reaction medium in PFPR Model I (blue ◇) and Model II (red □)*

The increase in reaction medium was thought to aid the delivery of photons to the surface of the catalysts. As the 36 W lamps had a length of 420 mm, they were capable of illuminating the full quartz body of the Model II unit and a

significant portion of the Model I unit. Increasing the height of the reaction medium ensures an increased proportion of the exposed area of illumination was utilised. The impact of increasing the rotational speed on the structure of the reaction medium resulted in the generation of cavitations. In the Model II, initial cavitation was recorded at a rotational speed of 289 rpm (2 dcV) and was shown to increase through to 1384 rpm (8 dcV). It was observed that the formation of cavitations reached a critical point (1211 rpm) thereafter the fluidisation of particles in the reaction medium became isolated to particular areas. The process of cavitation formation over increasing propeller speed is shown in Figure 68.
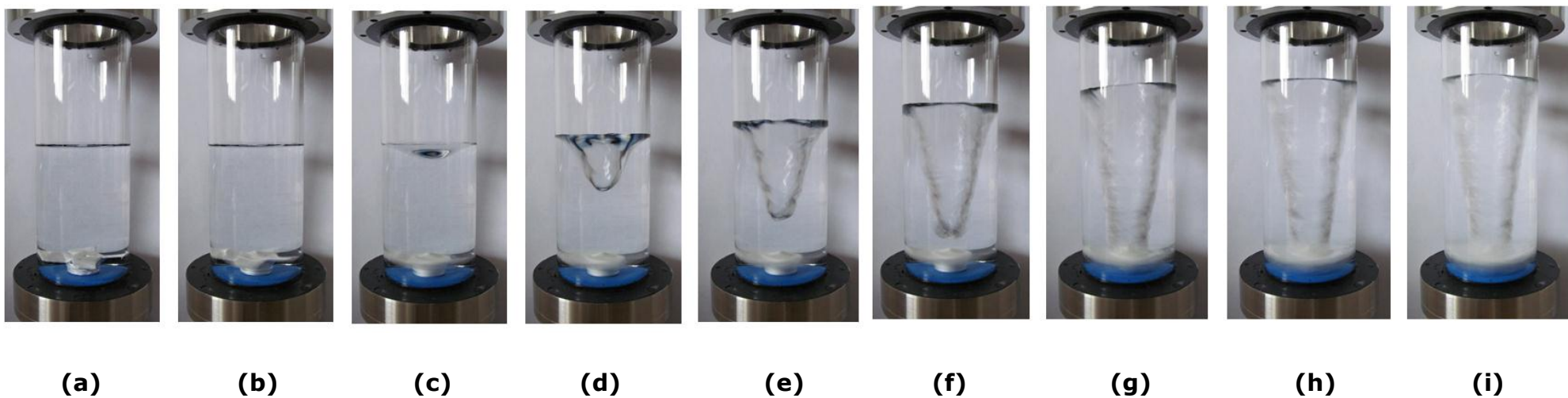
Figure 68; *Images of PFPR at; (a) 0 rpm (0 dcV), (b) 173 rpm (1 dcV), (c) 289 rpm (2 dcV), (d) 519 rpm (3 dcV), (e) 692 rpm (4 dcV), (f) 865 rpm (5 dcV), (g) 1035 rpm (6 dcV), (h) 1211rpm (7 dcV), (i) 1384 rpm (8 dcV)*

The increase in cavitation also aids the efficiency in which illumination was distributed. The cavitation of the reaction medium is highlighted in Figure 69, along with the required area of illumination. It can be seen when the unit was static no cavitation was formed, resulting in decreased light penetration. At 692 rpm (4 dcV), however, it was noted that cavitation was formed and the shape of the medium was altered. The cavitation was cone shaped, the height of which was 52 mm which gave an approximate cone volume of 28.79 cm^3. This volume was void of any reaction medium and thus required no illumination. The result of which was an increase in the light depth penetration, as the medium had been forced towards the inside wall of the unit and thus in the direction of the external illumination.

Static, 0 V   Rotation, 4 V
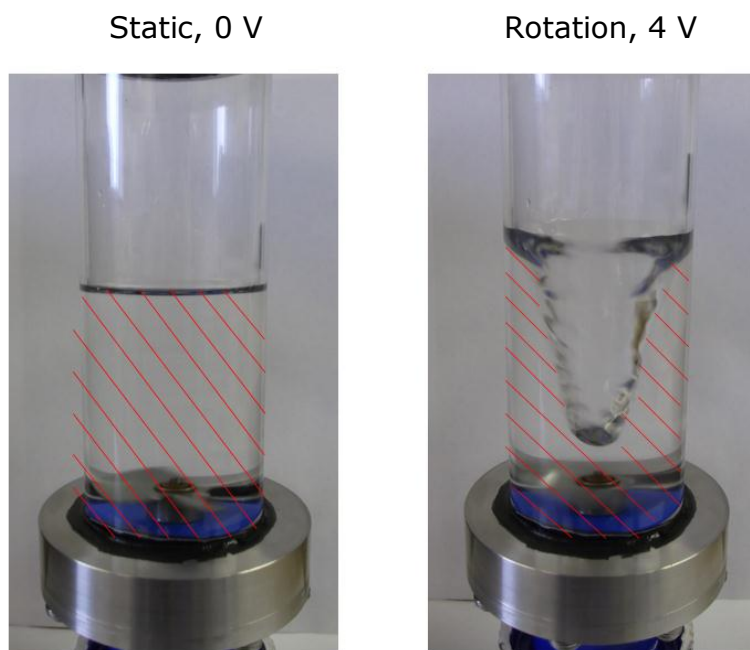
Figure 69; *Images of PFPR displaying the formation of cavitation with required area of illumination highlighted (red)*

Photocatalytic activity was further increased via increased mass transport and catalyst-reactant interactions. Observed during experimentation was the crossing of catalyst particles over the reaction medium cavitation, Figure 70. This was likely a result of cavitation towards the top 'bursting' and as result realising

catalyst particles in the process. This resulted in the movement of catalyst particles being random rather than uniformed. Furthermore this allows for the random light phenomenon to take place, allowing the catalyst moving in a random style to absorb scattered and reflected light (Voronstov *et al.*, 2000).
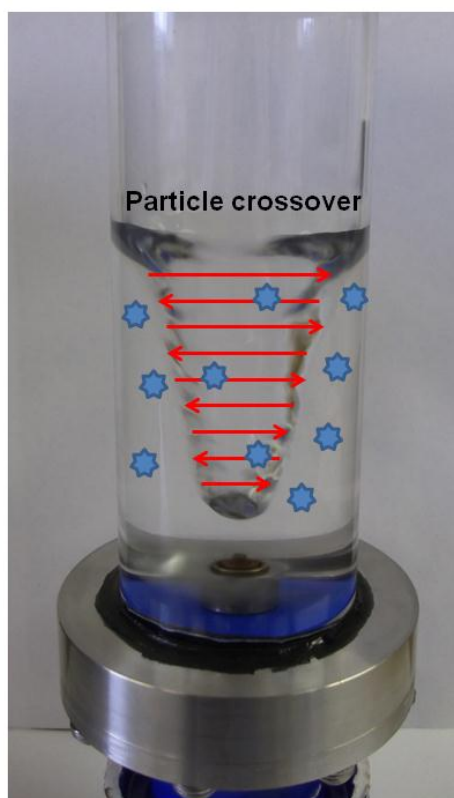
Figure 70; *Illustration of catalyst particles crossing over the cavitation*

4.5.2 Liquid-Solid-Gas Phase Operation

The reduction of CO_2 can be performed in both solid-gas and liquid-solid-gas phase. The literature shows the majority of CO_2 reduction work was performed in the liquid-gas-solid phase, where CO_2 is purged into an aqueous phase. The formation of gaseous products such as CH_4 and CO is measured through analysis of samples taken from the gas headspace. There are limitations with this approach including the solubility of CO_2, mass transport of CO_2 to catalyst surface in liquid phase, and dependence on the liquid-gas interface.

The engineering solution approach to these limitations is the operation of a pure gas phase reactor in which the contact time between reactant and catalyst is significantly increased, which increases mass transport and aids photocatalytic transformation. Gas phase CO_2 reduction in the presence of H_2 gas has been reported over catalysts such as Ga_2O_3 (Teramura *et al.* 2008) $ATaO_3$ (A=Li, Na, K) (Teramura *et al.* 2010) TiO_2 and ZrO_2 (Lo *et al.*, 2007), Rh/TiO_2 (Kohno *et al.*, 1999) and ZnCu-M (III) (M=Al, Ga) (Ahmed *et al.*, 2011). Furthermore, if the H_2 used as a reductant was generated from the solar photocatalytic splitting of water a highly energy efficient system could be established.

Table 2 and Table show that CO_2 reduction is primarily conducted in the liquid-gas phase (Mao *et al.*, 2012; Liu *et al.*, 1998; Koci *et al.*, 2010; Kaneco *et al.*, 1997; Li *et al.*, 2012). Additionally, the novel catalyst developed by The University of St. Andrews and CalTech were for use with H_2O, and thus consideration is required to be given to mass transport of the catalyst and CO_2 along with the liquid-gas phase interface.

Koci *et al.* (2011) stated in their investigation that 'photocatalytic reactions in which both the gas phase and the liquid phase participate are more complex than reaction proceeding in only one phase'. In addition to this, Mukherjee and Ray (1999) stated that scaling up a multi-phase reactor is also challenging and more complex than that of scaling up conventional chemical reactors (due to the absence of an irradiation source) or homogenous photo reactors.

The presence of the gas phase and the liquid phase in the PFPR Model II resulted in the interface between the two phases being of importance. Koci and colleagues discussed the methods in which reaction rate and product selectivity can be influenced suggesting the following:

- A mass transport from the bulk gas phase to the gas-liquid interface
- By dissolved gas diffusion through the liquid to an external catalyst surface
- By an internal mass transfer in the catalyst pores or agglomerates
- By a phase equilibrium
- By the transfer of light radiation

The use of the propeller as a mechanical agitator allowed the suspension of catalyst particles, which increased mass transport and increased the gas-liquid phase interface area. Thus, mass transport from the bulk gas phase to the gas-liquid interface, along with internal mass transfer in the catalyst pores or agglomerates, was achieved. This was primarily achieved by increasing the gas-liquid interface area. The gas-liquid phase interface was directly controlled by the rotational speed of the propeller. Cavitation of the reaction medium occurs as a result of increasing propeller speed which changes the shape of the interface from circular to cone shaped. When static, the circular interface has a calculated surface area of ~16.68 cm^3. At a rotational speed of 692 rpm, however, the surface area of the resulting cone was ~40.44 cm^3, which was a 58.9 % increase over the static interface area. This increase in interface surface area could allow for the increased transport rate of products from the liquid to gas phase.

4.5.3 Reynolds Number Calculations

Dimensionless numbers such as the Reynolds number can be used to characterise the design and performance of a reactor. It is important in reactor design and operation that the Reynolds number of a particular unit is calculated in order to determine the flow. As the PFPR unit was primarily operated in the liquid-gas phase it could essentially be considered as a stirred reactor and thus the Reynolds numbers can be applied.

The Reynolds number can be calculated to determine if the flow of a reactor was laminar or turbulent based on the following equation:

$$N_{RE} = \frac{\rho N D^2}{\mu} \qquad \textbf{Equation 27}$$

Where 'N$_{RE}$' is the Reynolds number, '$\boldsymbol{\rho}$' is liquid density, 'N' is the rotational speed of the propeller, 'D' is the diameter of the propeller and 'μ' is the viscosity of the liquid. Utilising Equation 27, the Reynolds numbers of the PFPR Model I and II were calculated and are shown in Table 20.

Motor (dcV)	Model I speed (rpm)	Model II speed (rpm)	Model I N_{RE}	Model II N_{RE}
0	0	0	0.00	0.00
1	181	173	10838.32	4155.22
2	362	289	21676.65	6941.38
3	543	519	32514.97	12465.67
4	724	692	43353.29	16620.89
5	905	865	54191.62	20776.11
6	1086	1035	65029.94	24859.28
7	1267	1211	75868.26	29086.56
8	1448	1384	86706.59	33241.78

Table 20; *Calculated N_{RE} of PFPR Model I and II*

At N_{RE} values greater than 10000 the flow of a stirred reactor is turbulent with laminar flow present at N_{RE} values lower than 10000. Based upon the N_{RE} calculated in Table 20 the PFPR Model I was considered to have turbulent flow at speeds of 173 to 1448 rpm and the Model II was considered to have turbulent flow at speeds of 519 to 1384 rpm. Turbulent flow was the preferred movement of the aqueous media as mass transport limitations become nonexistent under these conditions (Ballari *et al.*, 2008).

4.6 Conclusion

Presented in this chapter was the design and construction of two novel fluidised photocatalytic reactors. The design concept of the units was to allow for multi-phase reaction operation in order to reduce CO_2 and generate H_2. The construction of the units adhered to a specific set of parameters in an attempt to design a highly efficient photocatalytic system.

The PFPR Model I was produced as a prototype unit to investigate the design concept. The unit was constructed from PMMA, and used a novel method of fluidisation by the rotation of a 3 blade nylon propeller. This approach to fluidisation achieved the suspension of particles in gas, vapour and liquid phase. The unit had an annular geometric design to allow for maximum distribution of light. A low power diffuse irradiation source was used to deliver photons to the unit. The illumination system was constructed of an array of 36 W lamps positioned to emit 360° irradiation.

The PFPR Model I presented a number of potential limitation which restricted the use of the system with CO_2 reduction and H_2 production. These limitations included PMMA degradation, generation of heat from the lamps, inability to maintain an air-tight reaction environment and durability. These limitations were addressed in order to construct the second unit, PFPR Model II.

The PFPR Model II was an optimised system constructed from SS and quartz glass. The design concept remained the same for the second unit, however, the use of SS and quartz produced a highly robust and durable system. The unit was predicted to enhance photocatalytic activity by increasing mass transport through the formation of reaction medium cavitation and an increase in the surface area of the liquid-gas phase interface.

The N_{RE} calculations showed the units had turbulent flow at propeller speeds greater than 173 and 519 for Model I and II respectively. The turbulent flow of the aqueous media was the required condition to reduce mass transport limitations of the system and increase photocatalytic activity.

The PFPR Model I and II were developed as fluidised bed reactors based upon the results of previous designs SFPR and MCPR along with requirements put forward by the collaboration partners. The reactor evaluation was performed by the standard method described in Chapter 2 and by CO_2 reduction and H_2O splitting for H_2 production. The key parameters of the PFPR units were the controlled rotation of the propeller and low power irradiation system. These parameters were capable of enhancing the efficiency of the novel powder catalysts deployed. The evaluation of the reactors is discussed in the following chapter.

Chapter 5 Operational Testing of the Propeller Fluidised Photo Reactor

5.1 Introduction

The aim of this research was to design and develop a photocatalytic unit capable of CO_2 reduction and H_2 production. To achieve the desired photocatalytic reaction the unit constructed would deploy novel photocatalysts synthesised by The University of St. Andrews, and CalTech under irradiation from low power lamps and solar light.

The photo reduction of CO_2 is a challenge in the field of photocatalysis and currently active systems have a low efficiency (<5 %) (Indrakanti *et al.*, 2008). The stability of the compound presents an initial challenge, with the reduction product selectivity presenting an additional one. To overcome these challenges, systems with a highly active catalyst must be deployed in a photo reactor with high mass transport capabilities. Overcoming these challenges would be seen as significantly beneficial as it would allow not only the removal but also the recycling of atmospheric CO_2 to hydrocarbon products for fuel.

The primary reduction product of interest was CH_4 with additional products in the pathway expected to be CO, HCOOH, HCHO and CH_3OH. Although CH_4 is labelled as a GHG, there is interest in it as a chemical feed stock (Taylor and Noceti, 2000; Taylor, 2003) along with as a precursor to further hydrocarbon production via photocatalysis (Yuliati and Yoshida, 2008). Literature has suggested the reaction of C radicals and H atoms lead to the formation of CH_4 (Anpo and Chiba, 1992). The initial reduction of CO_2 leads to the formation of radicals and CO, followed by further reduction to C radicals. Under acidic condition the C radicals are capable of reacting with H^+ to eventually form CH_4. Under base conditions, the C radicals react with hydroxyl groups to eventually form CH_3OH. An alternative pathway for the reduction of CO_2 to CH_4 was described by Nada *et al.* (2011), Figure 71.

$$CO_2 \xrightarrow[+2e_{CB}^-]{+2H^+} HCOOH \xrightarrow[+2e_{CB}^-]{+2H^+} HCHO \xrightarrow[+2e_{CB}^-]{+2H^+} CH_3OH \xrightarrow[+2e_{CB}^-]{+2H^+} CH_4$$

$$\hookrightarrow H_2O \qquad\qquad\qquad\qquad \hookrightarrow H_2O$$
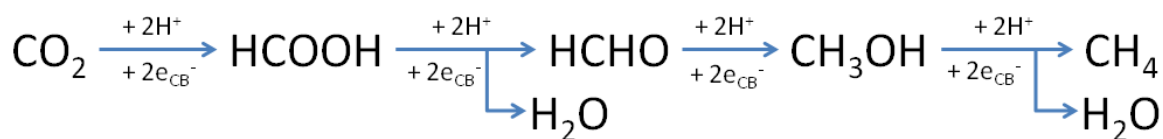
Figure 71; *Pathway of CO$_2$ reduction to CH$_4$*

To achieve energy efficient photocatalytic production of fuels from CO$_2$ along with H$_2$ production, the catalyst deployed must be capable of excitation by solar light, Figure 72. The electromagnetic spectrum of solar light encompasses a number of regions over a broad range of wavelengths, (Skoog *et al.*, 2007). The length of the UV and visible regions of the spectrum are ~10 to 400 nm and ~380 to 780 nm respectively. Approximately 10 % of natural light is comprised of UV wavelengths, while 40 % is comprised of visible wavelengths (Skoog *et al.*, 2007).
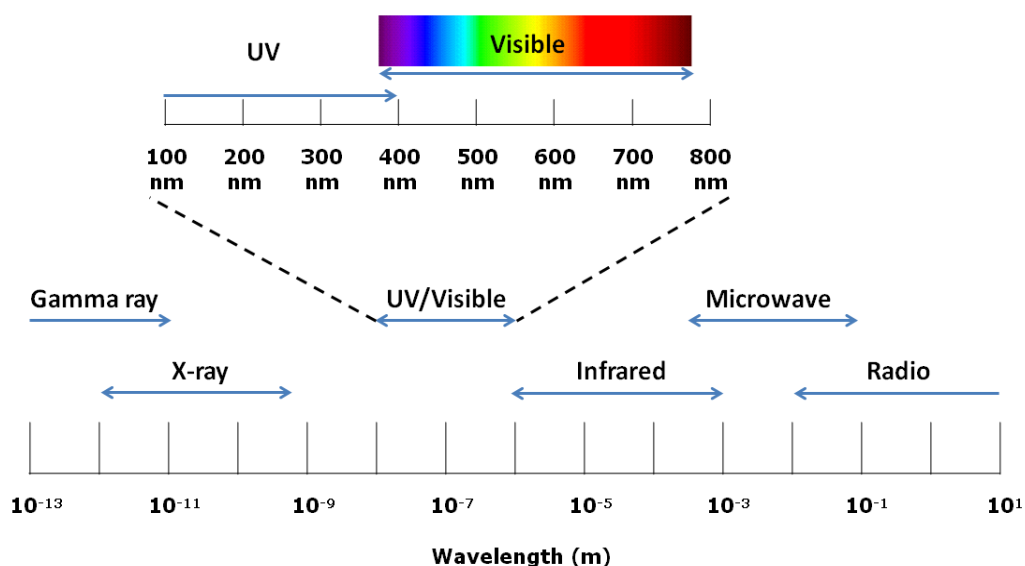
Figure 72; *Electromagnetic spectrum of solar illumination*

This chapter discusses the evaluation of the previously described PFPR Model I and II. Evaluation was conducted through the monitoring of dye degradation,

CO_2 reduction and H_2 generation over novel catalysts Pt-C_3N_4, C_3N_4, C_3N_4 (600 ^oC), TNT-C_3N_4, $Sr_{0.97}NbO_3$, $NaTaO_3$.La and Cu-TNT-CdS. This evaluation processes demonstrated the capability of the key features of the PFPR to enhance photocatalytic efficiency through increasing mass transport and maximising light penetration and distribution. The evaluation method described here also demonstrated the potential application of solar photocatalysis towards fuel production.

5.2 Experimental

The procedure for dye degradation, reduction of CO_2 and H_2O splitting are described below along with illumination sources and analysis methods. The reduction of CO_2 and H_2 production was performed at the University of St. Andrews and CalTech.

5.2.1 Dye Degradation

5.2.1.1 Photocatalytic Procedure

The photocatalytic procedure and analysis was carried out as described in Section 2.3.2 using a 1 x 10^{-5} M concentration of MO along with a 1 % loading weight of ZnO (Fisher Scientific). A volume of 1000 mL and 100 mL aqueous medium was introduced into the PFPR Model I and II respectively. The propeller rotational speed of the PFPR Model I and II was operated in the range of 0 – 905 rpm and 0 – 1730 rpm respectively.

5.2.1.2 Illumination Sources

Illumination was provided by the irradiation box described in Section 4.3.4 and 4.4.5. The irradiation box housed four 36 W PL-L UV lamps (Philips, Model CLEO) which have been described previously in Section 2.2.2.3. The spectral outputs of the lamps are shown in Appendix I.

5.2.2 Photo Reduction of CO_2

5.2.2.1 Photocatalytic Procedure

The photo reduction of CO_2 was performed in the PFPR Model II. In a typical experiment a 100 mL reaction medium consisting of Milli-Q and 1 M isopropanol dissolved in Milli-Q was used. Photocatalysts Cu-TNT-CdS (CalTech), $NaTaO_3$.La (CalTech), $Sr_{0.97}NbO_3$ (St. Andrews) and Pt-C_3N_4 (St. Andrews) were deployed with a loading weight of 1%.

The Model II unit was sealed and purged with CO_2 for 60 min to eliminate the presence of air in the unit. The propeller was operated at a rotational speed of 289 rpm (2 dcV) during purging to prevent photocatalyst settling. Upon completion of purging the inlet and outlet valves were closed, the propeller rotational speed was increased to the required level and illumination was initiated. The propeller rotational speed of the PFPR Model II was operated in the range of 0 – 1730 rpm (0 – 10 dcV).

5.2.2.2 Illumination Sources

Illumination was provided by a 144 W irradiation box, 450 W Xe Arc lamp and solar illumination. The irradiation box was used as described in Section 5.2.1.2 with the addition of 36 W visible emitting lamps (RS Electronics, Model General Electric Biax L 830). The spectral output of the lamps is shown in Appendix I.

The 450 W Xe arc lamp (450 – 1000 W Oriel Research Arc Lamp, Model 66924) was used during a collaboration period at CalTech. A 420 nm cut-off filter was used to remove UV wavelengths. The PFPR Model II was positioned 100 mm from the lamp, Figure 73.
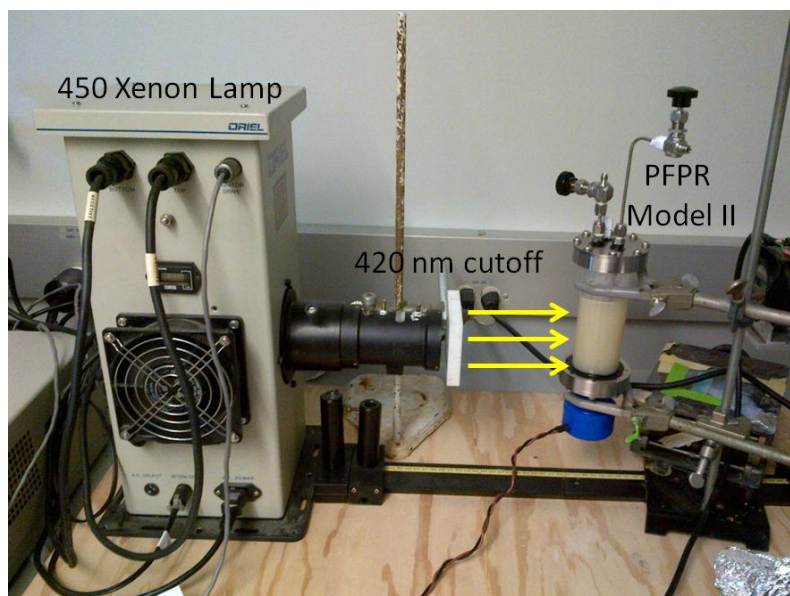
Figure 73; *Experimental set up of 450 W Xe lamp with PFPR Model II*

Solar illumination was collected by The George Ellery Hale Solar Telescope, positioned on the Linde and Robinson building of CalTech, Pasadena. The solar telescope was operated during the period of 24th July to the 14th August 2012. The telescope was capable of continuously monitoring and tracking the sun. Illumination was collected by two mirrors at the top of the structure which guided light through an illumination shaft. The light was then reflected through a second illumination shaft by three gold coated mirrors through three glass windows. A schematic illustration of the solar telescope structure is shown in Figure 74. Images of the George Ellery Hale telescope are shown in Appendix I. The irradiation exposure provided by the solar telescope illuminated the full length of the PFPR Model II tubular body.
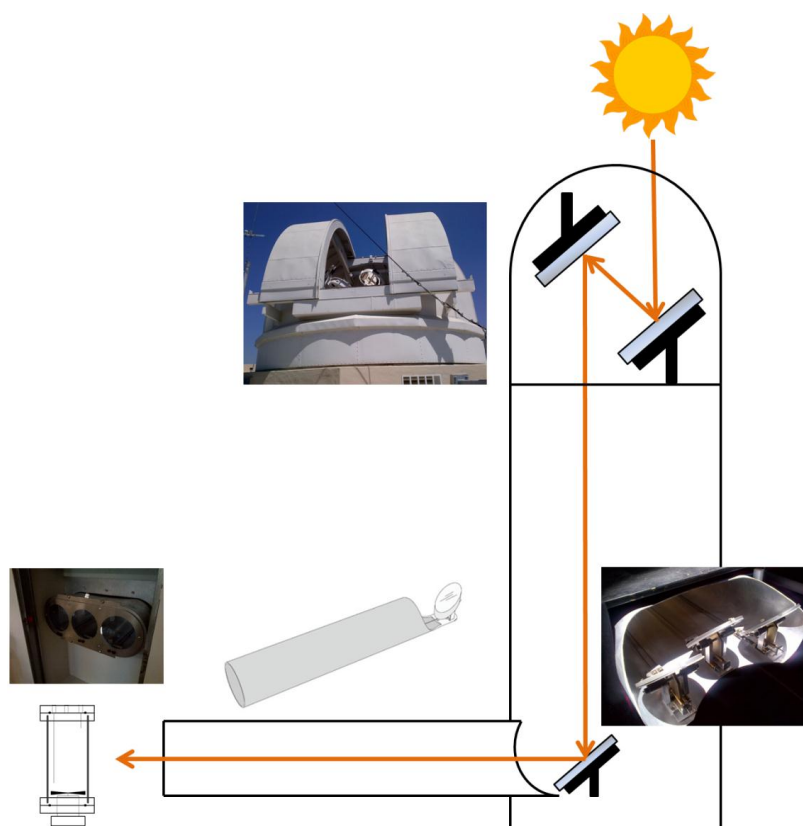
Figure 74*; Schematic illustration of George Ellery Solar Telescope*

5.2.2.3 CO$_2$ Analysis

Gas headspace analysis was performed used samples taken from the unit at dedicated time intervals. A gas tight needle (SGE Analytical Science, 100 µL gastight needle) was used to extract gas samples via the manual injection port located on the PFPR Model II.

The headspace gas composition was monitored using a HP GC equipped with a TCD detector with a molecular sieve column (HP 5890 Series Ⅱ). The carrier gas was He for the quantitative determination of CO$_2$, O$_2$, N$_2$, CH$_4$ and CO. The injection volume of sample was 100 µL. The GC method run time was 18 min, with CO$_2$ being retained at approx. 13 min. CO$_2$ was determined based upon comparison to a standard injection of CO$_2$. A standard injection of CO$_2$ is shown in Appendix I.

5.2.3 Photocatalytic H$_2$O Splitting

5.2.3.1 Photocatalytic Procedure

The production of H$_2$ was performed in the PFPR Model II. In a typical experiment a 100 mL reaction medium consisting of 0.025 M oxalic acid dissolved in Milli-Q was used. Photocatalysts NaTaO$_3$.La (CalTech), Sr$_{0.97}$NbO$_3$ (St. Andrews), Pt-C$_3$N$_4$ (St. Andrews), C$_3$N$_4$ (St. Andrews), C$_3$N$_4$ (600 ^{o}C) (St. Andrews) and TNT-C$_3$N$_4$ (St. Andrews) were deployed with a loading weight of 1 %.

The Model II unit was operated as described Section 5.2.2.1, using Ar to purge the system. The propeller rotational speed of the PFPR Model II was operated in the range of 0 – 1730 rpm.

5.2.3.2 Illumination Sources

The illumination sources used during the H$_2$O splitting experiments were as described in Section 5.2.2.2.

5.2.3.3 H$_2$ Analysis

H$_2$ analysis was performed in collaboration with the University of St. Andrews and CalTech. Gas headspace analysis at CalTech was performed using samples taken from the unit at dedicated time intervals. A gas tight needle (SGE Analytical Science, 100 µL gastight needle) was used to extract gas samples via the manual injection port located on the PFPR Model II.

The headspace gas composition was monitored using GC-TCD that was equipped with a molecular sieve column (HP 5890 Series Ⅱ). N$_2$ gas was used as a carrier gas for H$_2$ determination. A typical injection volume of 100 µL was used. H$_2$ was determined based upon comparison to a standard injection of H$_2$. A standard injection of H$_2$ is shown in Appendix I.

H$_2$ analysis at the University of St. Andrews was performed with an Agilent 3000 Micro Gas Chromatograph. Gas headspace analysis was performed using samples taken from the unit at dedicated time intervals. The sample was drawn from the

outlet of the PFPR Model II to the inlet of the GC by the internal GC pump. The headspace gas composition was monitored using GC-TCD that was equipped with a molecular sieve column (HP 5890 Series Ⅱ). The GC used a dual carrier gas system with Ar and He.

5.3 Operational Testing of the PFPR

5.3.1 Methyl Orange Degradation

The importance of reactor evaluation was previously discussed in Chapter 2. The results of that chapter also allowed a simple reactor evaluation method to be developed. This evaluation method was applied to the PFPR Model I and II, which allowed the PFPR to be compared to the SFPR and MCPR. In addition, this method allowed the performance of the PFPR to be assessed prior to collaboration periods at the University of St. Andrews and CalTech. As the reduction of CO_2 and H_2O experiments were complex, it was important to ensure the PFPR was performing as expected. The use of this evaluation method demonstrated two key points. Firstly, the propeller speed can efficiently control mass transport. Secondly, the illumination system coupled with the annular quartz body of the reactor increase light penetration and distribution ensuring the delivery of photons to a catalyst surface.

5.3.1.1 Effect of Propeller Rotational Speed

The key feature of the PFPR unit to be investigated was the propeller, which controlled the mass transport of reactants and catalyst particles in the system. The rotational speed of the propeller can significantly and directly impact the photocatalytic activity of a unit. Figure 75 shows the relationship between propeller speed, height of reaction medium and photocatalytic degradation of MO in the PFPR Model I.
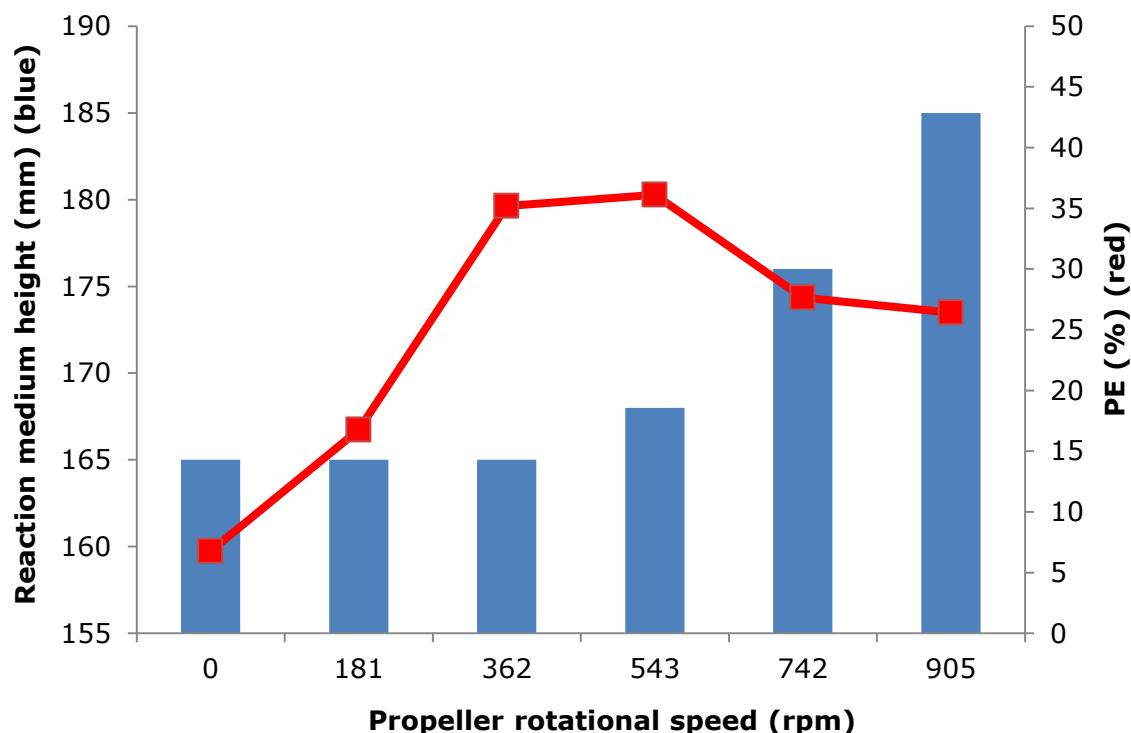
Figure 75; *Relationship between height of reaction medium (blue bars) and PE of MO over ZnO (red □) at selected propeller rotational speeds in the PFPR Model I. Conducted under aerobic conditions at pH 7 and irradiation from four 36 W UV lamps*

The motor was operated in the range of 0 (0 dcV) to 905 rpm (5 dcV) as the volume of liquid being treated prevented operation at higher revolutions. It was found that the volume of the aqueous media reduced the stability of the motor at high propeller rotational speeds.

At 0 rpm (0 dcV) the system was mass transport limited and as such degradation was slow. Under these conditions the degradation rate was initially dictated by the settling velocity of the photocatalyst and the light penetration of the catalyst bed at the base of the unit. At 181 rpm (1 dcV) a 10 % increase in efficiency was observed due to the minimal movement of the photocatalyst in the liquid medium. At 362 rpm (2 dcV) a significant increase (~20 %) was seen which was accredited to the generation of cavitation in the reaction medium. Furthermore this trend continued at 543 rpm (3 dcV) which produced a degradation efficiency of 36.11 % within 150 mins of 144 W illumination. The rate of degradation was

dictated by the rate at which the bulk of MO reached the catalyst bed. At rotational speeds of 724 and 905 rpm (4 and 5 dcV) a decrease in PE was recorded; 27.64 % and 26.41 % for 724 and 905 rpm respectively.

At higher propeller rotational speeds the reduction in the removal of MO was primarily due to the trapping of photocatalyst particles, which limits the mixing efficiency of the reactor. Localised trapping of particles around the propeller at speeds of 724 and 905 rpm was observed. As a result the transportation of MO to the surface of ZnO was reduced, thus preventing the degradation of the dye molecules. At this point mass transport limitations were exceeded to a state that they no longer increase the rate of dye removal.

The trend observed in Model I was reproduced in Model II over a broader range of speeds from 0 (0 dcV) to 1384 rpm (8 dcV), Figure 76. As previously seen at 0 rpm the system was mass transport limited and thus produced minimal degradation. At 289 rpm cavitation of the liquid medium was created and the photocatalyst particles were suspended to a degree that allows significant light penetration, catalyst excitation and thus photocatalytic degradation. Increasing the rotational speed to 692 rpm further increased the cavitation of the reaction medium extending it towards the top of the propeller. At this speed PE was further enhanced from 73 % to 88 % within 2.5 min of illumination. At higher rotational speeds of 1035 and 1384 rpm no significant increase in degradation was recorded. In contrast to Model I results the efficiency of MO removal did not decrease at higher speeds, however was observed to plateau at ~90 %. Therefore, it could be concluded that in the Model I and II mass transport limitations no longer predominate at speeds greater than 543 rpm and 692 rpm respectively.
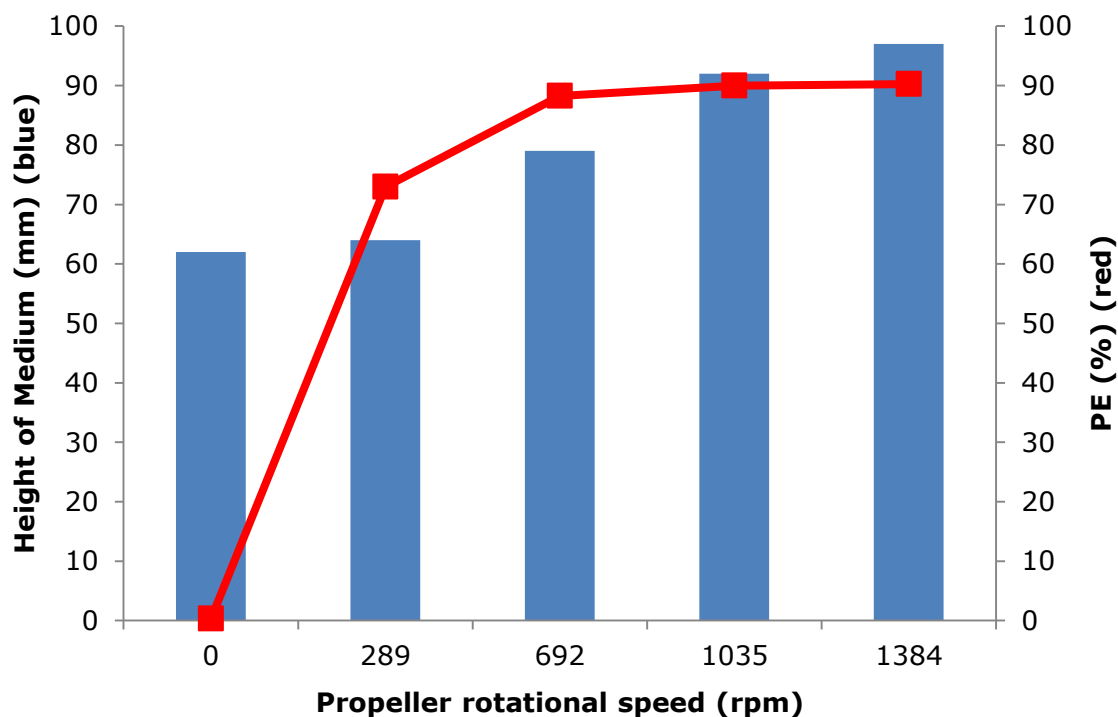
Figure 76; *Relationship between height of reaction medium (blue bars) and PE of MO over ZnO (red □) at selected propeller rotational speeds in the PFPR Model II. Conducted under aerobic conditions at pH 7 and irradiation from four 36 W UV lamps*

As was shown in Chapter 2 the use of 1×10^{-5} M MO and ZnO were a suitable approach to reactor evaluation. Evaluation of the PFPR units by this approach allowed the comparison to the MCPR and SFPR designs described in Chapter 2. The units are compared based upon degradation efficiencies and should be noted that illumination sources varied between systems. Previous results, however, show that illumination power does not significantly impact the removal of MO. The results display PE achieved were > 90 % for all the systems developed. The lowest efficiency and rate recorded was with the PFPR Model I with 91.49 % and 0.18×10^{-5} M h^{-1} respectively. Based upon the reactor construction materials, which restricted light transmittance, and large treatment capacity of this system the low efficiency and rate was expected.

The highest rate of dye removal, 5.65×10^{-5} M h^{-1}, was achieved in the PFPR Model II unit. The high rate of removal can be accredited to the increased optimisation of the reactor parameters including propeller speed, reaction

volume, illumination source, gas velocity and mass transport. Moreover, the PFPR Model II can be considered the most advanced of the units in relation to construction, operation and propeller rotational speed and thus was reflected in the high degradation rate. The design concept and construction of the PFPR Model II was based upon a number of prototypes thus producing a final system which was highly optimised.

5.3.2 Photo Reduction of CO_2

The reduction of CO_2 was performed in the PFPR Model II over a range of novel catalysts and varying illumination sources. The following catalysts were deployed in the PFPR for CO_2 reduction; Cu-TNT-CdS, $NaTaO_3$.La, $Sr_{0.97}NbO_3$ and Pt-C_3N_4. The effects of catalyst and illumination source were investigated and are discussed here.

5.3.2.1 Effect of Illumination

The illumination source is a critical consideration as the primary function of the irradiation is to provide the activation energy for the catalyst. Discussed here is the reduction of CO_2 over novel synthesised catalysts in the PFPR Model II under irradiation from 144 W low power lamps, 450 W medium pressure Xe Arc lamp and solar illumination.

Cu-TNT-CdS was deployed as the principal catalyst for the reduction of CO_2 (based upon results obtained by colleagues at CalTech). Under irradiation from the 144 W low power lamps no reduction of CO_2 was recorded as indicated by Figure 77. Figure 77 displays the chromatogram of a sample exposed to 6 hrs irradiation. The retention of three compounds at R_t of 2.29, 2.73 and 12.90 min was evident. These compounds were identified as O_2, N_2 and CO_2 respectively. CO_2 was identified based upon comparison to a standard injection while the O_2 and N_2 peaks were present in all samples and were thought to be present due to a small amount of air in the GC system.
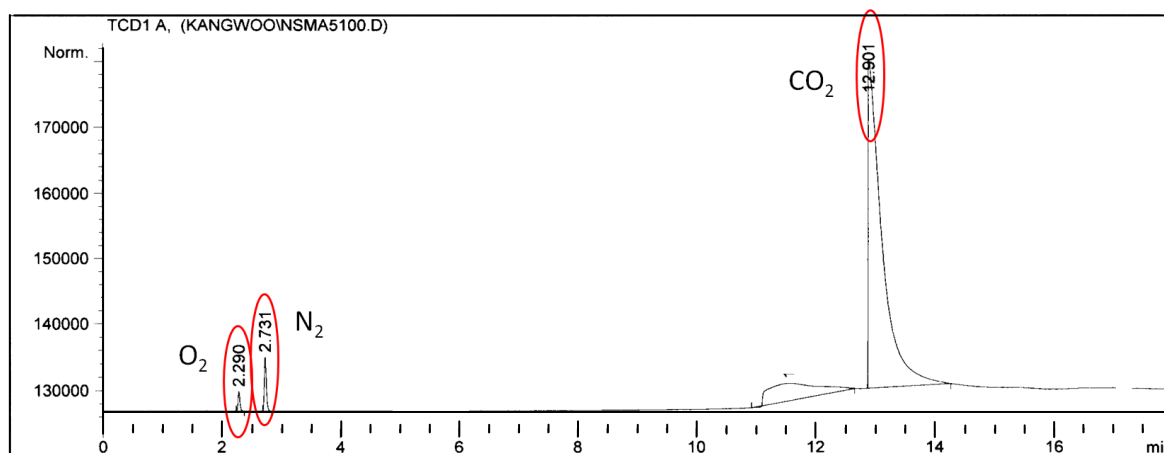
Figure 77; *Chromatogram of CO$_2$ reduction over Cu-TNT-CdS after 6 hrs 144 W irradiation under anaerobic conditions*

During the 6 hr illumination period no discernible variation in the peak area, height or R$_t$ of either O$_2$, N$_2$ or CO$_2$ was reported. These results indicated that the reduction of CO$_2$ had not occurred.

The formation of H$_2$ was also monitored, as the splitting of H$_2$O was expected to occur as a precursor stage to CO$_2$ reduction. The resulted showed that no H$_2$ production occurred during any stage of the experiment. The generation of H$_2$ from H$_2$O splitting combined with CO$_2$ in the system was expected to result in the formation of CH$_4$.

The light intensity was increased through the use of a 450 W Xe arc lamp, Figure 78. In contrast to the diffuse 144 W illumination system the Xe Arc lamp provided a single spot of illumination upon the PFPR tubular body. The arc lamp was operated with and without a 420 nm cut off filter to determine if UV wavelengths were required to promote catalyst excitation.

Figure 78; *PFPR Model II unit under irradiation from the 450 W Xe lamp*

The chromatogram displayed in Figure 79 shows the analysis of a sample exposed to 6 hour illumination without the 420 nm cut off filter. As was previously observed the chromatogram shows the retention of compounds at 2.30, 2.75 and 12.97 min, which represent O_2, N_2 and CO_2 respectively. The operation of the system with the 420 nm cut off filter generated a comparable series of data. These results indicated that the reduction of CO_2 had not occurred under a broad UV-visible range and under visible illumination. As was previously discussed peak area, height and R_t along with H_2 production was also monitored however, no significant data was observed to suggest photo activity of the system.
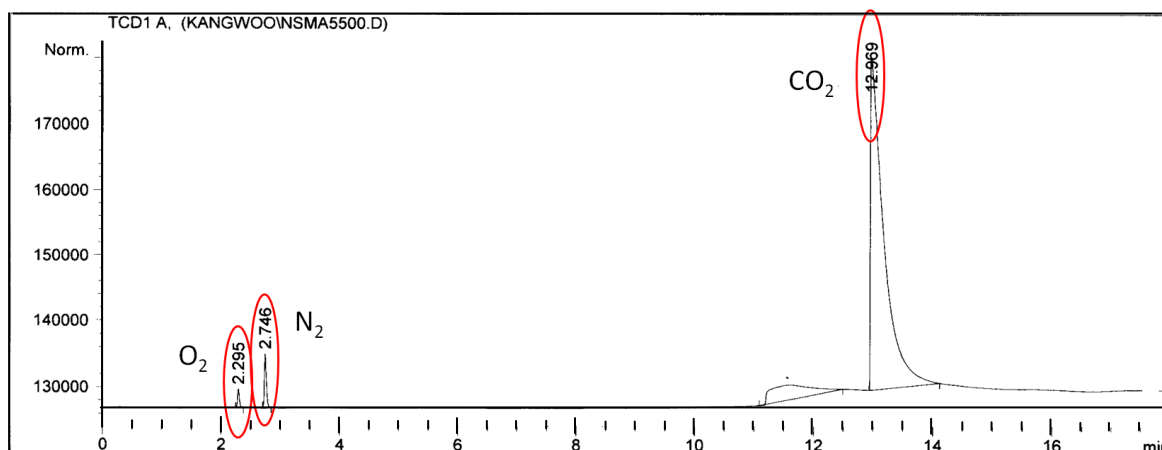
Figure 79; *Chromatogram of CO_2 reduction over Cu-TNT-CdS after 6 hrs 450 W Xe irradiation under anaerobic conditions*

The final illumination source used was solar irradiation collected and delivered by the George Ellery Hale Telescope. As was observed with the previous results, no discernible reduction of CO_2 or H_2 production was achieved under natural illumination, Figure 80. The chromatogram in Figure 80 displays the retention of O_2, N_2 and CO_2 as was previously shown.
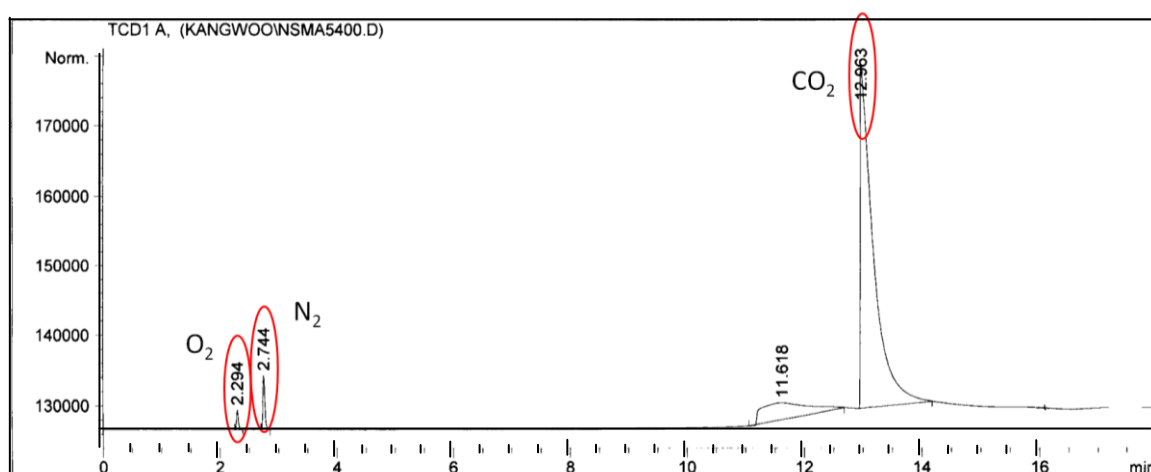
Figure 80; *Chromatogram of CO_2 reduction over Cu-TNT-CdS after 6 hrs solar irradiation under anaerobic conditions*

It was concluded from the results displayed in Figure 77, Figure 79 and Figure 80 that the Cu-TNT-CdS PFPR Model II system was not photocatalytically active. Further to this, additional novel catalysts (Pt-C_3N_4, $Sr_{0.97}NbO_3$ and $NaTaO_3$.La) produced comparable results to those already displayed. As a result investigating the impact of propeller rotational speed on the reduction of CO_2 was no applicable and thus was not conducted.

5.3.2.2 Evaluation of Cu-TNT-CdS at CalTech

In contrast to the results shown in Section 5.3.2.1, promising results had previously been obtained by colleagues at CalTech using a CdS-modified TiO_2 catalyst. The reduction of CO_2 has also been achieved over similar CdS-TNT catalysts in the literature (Li *et al.*, 2012). The results discussed in this section were obtained from colleagues at CalTech as part of paper in preparation.

Over CdS-TiO_2 the detection of CH_4 from the reduction of CO_2 was reported in the presence of different sacrificial electron donors. Additional products formed included C_2H_4, C_2H_6, C_3H_6, C_3H_8 and C_4H_{10} in the presence of isopropanol, sodium formate and water. The product yield was greatest for CH_4 and C_2H_6 in the presence of isopropanol. After 5 hrs irradiation a product yield of ~1.8 µL and ~2.1 µL were recorded for CH_4 and C_2H_6 respectively. Interestingly, peak product yields for all hydrocarbon products were recorded when in the presence of water with CH_4 showing the greatest yield at ~1.6 µL after 3 hrs irradiation.

The unit used for the reduction of CO_2 in the CalTech investigation was a Pyrex glass vessel with a small quartz window for illumination. The unit was sealed by a rubber stopper to provide an air tight seal. Agitation of the aqueous reaction medium was created by the rotation of a magnetic stirring bar, Figure 81.
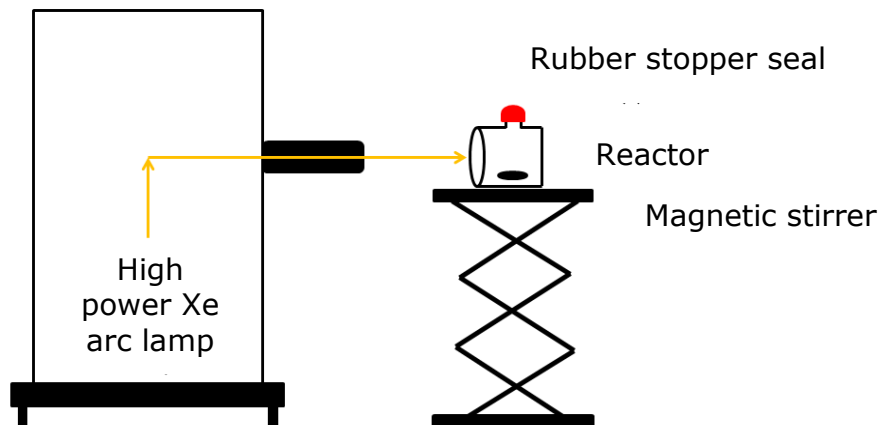
Figure 81; *Schematic of CalTech photocatalytic system*

The reactor construct was a simple design, thus it was feasible to assume the PFPR Model II would be suitable for CO_2 reduction to occur. The Model II provided an airtight environment using high heat resistant sealants, O-rings and SS tapered threads. The rubber stopper used in the CalTech experiments was effective over a short period, however, was not durable for prolonged use. In addition the large quartz surface of the Model II tubular body provided excellent transmittance of light and the rotation of a SS propeller provided significantly increased mixing over that of a magnetic stirrer bar.

The preliminary investigation conducted at CalTech, which reduced CO_2 to a number of hydrocarbon products, used a high power 450 W Xe Arc lamp. This lamp was also used in conjunction with the PFPR Model II in an attempt to reduce CO_2. Thus, based upon the observations discussed in this section the CdS-TNT-Cu PFPR Model II system was a feasible approach to achieve was CO_2 reduction to CH_4. The apparent inactivity of the system is discussed in the following section.

5.3.3 Lack of CO_2 Reduction Activity

The results showed that no CO_2 reduction was reported over Cu-TNT-CdS under illumination from three varying irradiation sources. The catalysts $NaTaO_3.La$, $Sr_{0.97}NbO_3$ and $Pt-C_3N_4$ were also deployed in the PFPR unit and showed no discernible reduction in CO_2 or generation of C_1-C_4 products.

The reduction efficiency of CO_2 and product selectivity primarily depends on two key factors; the photocatalyst properties and reaction conditions. As previously stated, to obtain optimal results the deployment of a highly efficient catalyst within a unit capable of delivering a high rate of mass transport is essential. Therefore to analyse the lack of activity, the following catalyst and reactor specific points are discussed:

- Mass transport limitations
- Transport of products from liquid to gas phase
- Insufficient supply of CO_2 to catalyst surface
- Illumination sources
- Inactivity of the catalysts
- Insufficient redox potential of the catalysts
- Reaction kinetics

5.3.3.1 Mass Transport

The mixing capabilities of the Model II unit were sufficient to reduce mass transport limitations. The fluidisation of the catalyst particles was directly controlled by the rotational speed of the propeller and thus could be maintained in continuous suspension in the reaction medium. In addition, minimal catalyst drifting or trapping was observed, which resulted in the catalyst particles being exposed to illumination and increasing residual contact time between catalyst and reactant. This was evident from the level of MO removal observed in Figure 75 and Figure 76.Previous results also showed the PFPR Model II was capable of operating under turbulent flow as indicated by a Reynolds number of 12466 at 519 rpm.

The transport of products from the liquid to gas phase could significantly restrict the activity of the photocatalyst. In the PFPR the production of products firstly requires the delivery of CO_2 into a liquid phase, where upon it interacts with the catalyst surface. Thereafter, any potential hydrocarbon products are required to travel from the liquid phase to the gas head space of the unit with the aid of the propeller rotation. Therefore, this system was primarily dependent on the solubility of CO_2 in the liquid phase and the volume of CO_2 available for interactions at the catalyst surface. This observation indicates a potential

limitation of the PFPR. Upon sealing, the PFPR was saturated with CO_2 and operated in batch as a closed system. The result of a closed system is the limited supply of carbon available for photocatalytic transformation. It could be stated that the level of the carbon source available in the sealed PFPR was not sufficient to allow for reduction to occur. This point was also addressed by Mao *et al.* (2012) who discussed the selectivity of their CO_2-$BiVO_4$ system towards CH_3OH production to be a result of a limited carbon source in a closed gas reactor.

Alternatively, this was not a limitation reported by Lee *et al.* (2012) in their NiO/Co_3O_4-$InNbO_4$ system or by Lo *et al.* (2007) in their TiO_2 and ZrO_2 recirculating system. The Lee *et al.* investigation used a continuous flow Pyrex reactor which purged CO_2 into a solution $KHCO_3$. The use of $KHCO_3$ and the continuous flow of CO_2 overcame the limitation of CO_2 solubility while maintaining a suitable level of carbon availability for the reduction reaction to take place. Upon visible light illumination (500 W halogen lamp) for 20 hr the optimum yield of methanol was 1.577 $\mu mol\ h^{-1}\ g^{-1}$.

5.3.3.2 Illumination Sources

The illumination source selected for the PFPR system was a key factor. The excitation of a catalyst by the promotion of electrons from the valence to the conduction band is essential for any photocatalytic unit and occurs only as a result of appropriate irradiation. In order for CO_2 reduction to occur a large potential energy barrier must be overcome. The initial one-electron reduction step of CO_2 to $CO_2^{-\cdot}$ requires a potential of -2.21 V vs SCE. The steps in CO_2 reduction are reliant on the redox potential of the catalyst and should the illumination source not be sufficient for the excitation of the desired catalyst, the reduction process will not occur. Thus the band gap of the catalyst dictates the amount of photons that are available for quantum conversion (Koci *et al.*, 2009).

The composition of the catalyst was taken into consideration to ensure appropriate irradiation was delivered. The presence of CdS with TNT resulted in the catalyst being visible light-responsive. Colleagues reported the catalyst to show absorption bands in the UV and visible proportions with visible band edges from 530 to 650 nm, Figure 82. The band gap energy was also reported to be

2.07 to 2.35 eV which was sufficient for visible light activation. The presence of Cu in the catalyst reduced recombination of electrons and holes.
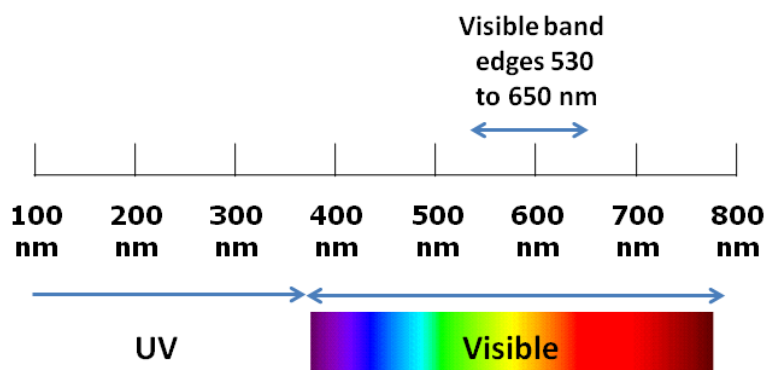
Figure 82; *UV-Vis Spectrum displaying visible band edges*

Based upon this information the use of the 144 W irradiation box, 450 W arc lamp and solar telescope were sufficient to promote catalyst excitation. Further to this, the controlled fluidisation of the catalyst ensured maximum light penetration and distribution within the PFPR unit, thus increasing the absorption of photons by the catalyst. The high power arc lamp was also used in previous work carried out by CalTech to achieve photoreduction of CO_2.

As the reduction of CO_2 to CH_4 is a multi-electron process the rate kinetics play, and thus the length of time a catalyst is exposed to illumination is a key factor. As shown earlier in Equation 5 to Equation 10, the multi-electron steps are far more thermodynamically favourable than the one step approach. A potential issue with the multi-electron process, however, is the decreased rate kinetics. Therefore, an increased irradiation time would be required to observe an increase in CO_2 reduction product yield. CH_4 production has been reported to be negligible within initial illumination periods (0 – 5 hrs) (Koci *et al.*, 2009; Koci *et al.*, 2010; de Ritcher *et al.*, 2013). Koci and colleagues suggested that CH_4 formed as a result of CO_2 with H_2, which formed from the initial splitting of H_2O. Koci *et al.* (2010) also reported the highest yield of products was in the order of H_2 (130 µmol g^{-1})>CH_4 (6 µmol g^{-1})>CH_3OH (1.4 µmol g^{-1})>CO. The PFPR Model II was exposed to illumination for 6 hrs, during which no CO_2 reduction was reported. Furthermore, the production of H_2 was not achieved suggesting H_2O splitting had

not occurred. These results provided further evidence that the catalyst was not photo active in the PFPR unit.

Based upon the above discussion and the results shown in Section 5.3.2.1 it can be stated that the inactivity of the novel catalyst-PFPR system could be ascribed to a combination of the following parameters; the batch operation of the reactor resulting in the limited carbon source availability, the slow rate kinetics of CO_2 reduction and the inactivity of the catalyst.

Addressing the limitations of any CO_2 photo reduction system is done so with a view towards achieving the goal of limiting GHG emissions, whilst using the CO_2 as a feedstock for fuel production (Wu, 2009; Usubharatana *et al.*, 2006). In order to fully assess a system, which may be capable of achieving this objective, alternative and comparable methods of fuel production must also be assessed i.e. solar H_2 production (Indrakanti *et al.*, 2008). Investigations into the comparison of solar H_2 production and CO_2 photo reduction systems is rarely reported, despite both being the main photosynthetic processes for solar fuel generation. Therefore, as the reduction of CO_2 was not achieved in the PFPR Model II, further evaluation was required to both investigate the performance of the system and to determine if alternative methods of solar energy conversion and fuel production are more viable approaches. Thus, further evaluation was performed by monitoring the production of H_2 from H_2O splitting using a range of visible lights and solar illumination.

5.3.4 Photocatalytic H_2O Splitting

In order to achieve a highly effective photocatalytic system these parameters must be achieved in a design. Ascertaining these parameters in a design will not solely achieve the desired system however, as the deployment of an active catalyst is still required. The evaluation of a photo system is dependent on the catalyst initially displaying activity towards the desired photo reaction. At this point the parameters of the reactor can be investigated to understand the level they are capable of enhancing the aforementioned catalyst activity.

The lack of activity observed for the reduction of CO_2 prevented the true evaluation of the PFPR unit. Thus, the generation of H_2 from water splitting was

monitored as a method of catalyst and reactor evaluation and to demonstrate the capacity of novel photocatalytic technology to produce an alternative source of energy.

5.3.4.1 Effect of Propeller Rotational Speed

The effect of propeller speed on the photocatalytic evolution of H_2 is shown in Figure 83. The mass transport limitations were reduced as the propeller rotational speed was increased from 0 rpm to 1035 rpm thus allowing for an increased level of H_2 evolution. The rate of H_2 evolution increased from 27 µmol h^{-1} g^{-1} at 0 rpm to 109 µmol h^{-1} g^{-1} at 1035 rpm. Increasing the propeller speed further to 1384 and 1730 rpm reduced the evolution rate of H_2 to 109 and 103 µmol h^{-1} g^{-1} respectively. The 5.50 % reduction at 1730 rpm was a result of the motor operating at its maximum capacity and thus the stability of the motor voltage and propeller speed were low.
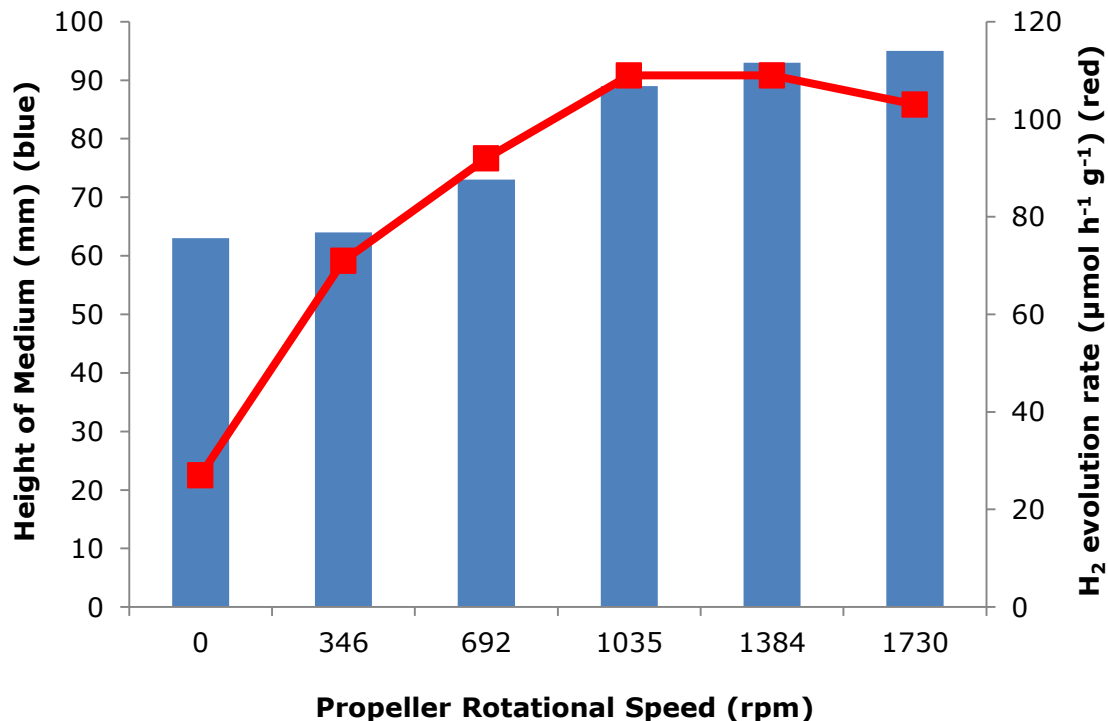
Figure 83; *Relationship between height of reaction medium (blue bars) and H_2 evolution over Pt-C_3N_4 (red □). Conducted under anaerobic conditions and 144 W visible irradiation at selected propeller rotational speeds in the PFPR Model II*

The profile of H_2 production over rotational speeds of 0 to 1384 rpm is shown in Figure 84. The profile of H_2 production in Figure 84 demonstrates the ability of the reactor to enhance the performance of the catalyst Pt-C_3N_4. As previously discussed, increasing the propeller speed results in the cavitation of the reaction medium. In the PFPR Model II the cavitation of the reaction medium begins at 346 rpm which was indicated by the significant increase of 62.5 % in H_2 production from 0 to 346 rpm. It was seen that as cavitation increased the rate of production increased. An increase of 23.19 % from 346 to 692 rpm and 15.98 % from 692 to 1035 rpm was recorded. At the point which full cavitation was achieved, however, production rates begin to decrease. A reduction of 0.76 % from 1035 to 1384 rpm and 5.06 % from 1384 to 1730 rpm was noted. The apparent plateauing of the results indicated the exhaustion of the SED. In order to achieve continued H_2 evolution the oxalic acid would need to be replenished. In the absence of a SED, recombination rates increased and prevented H_2 evolution.
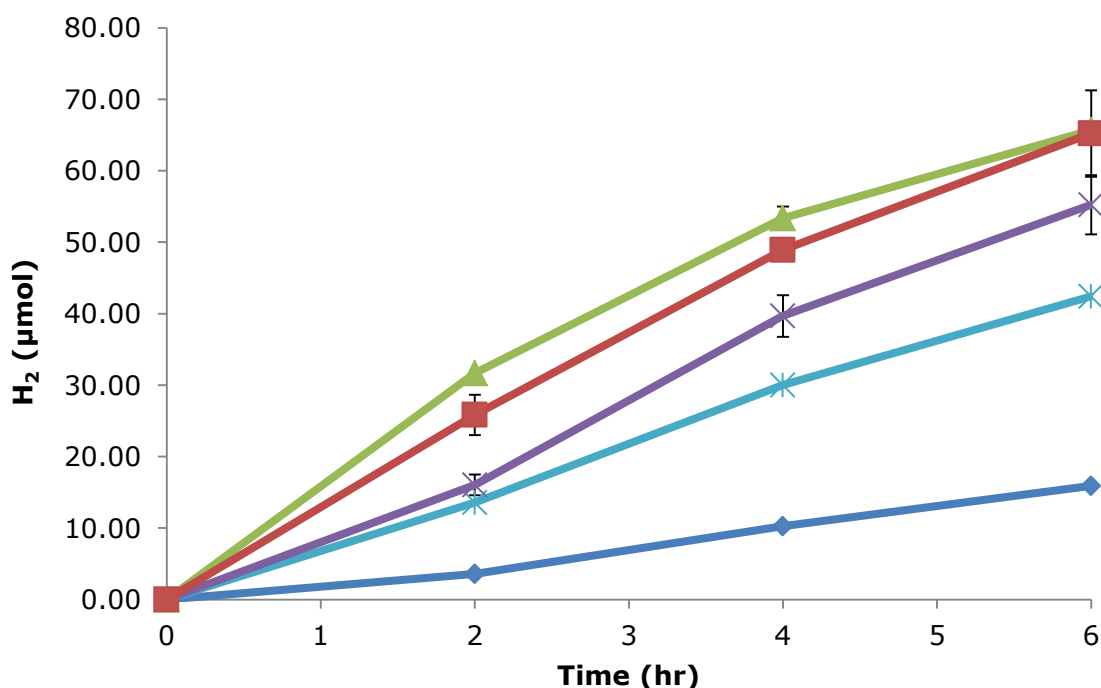
Figure 84; *Evolution of H_2 over Pt-C_3N_4 and varying propeller rotational speeds; 0 rpm (navy ◇), 346 rpm (blue ✾), 692 rpm (purple ✾), 1035 rpm (green Δ) and 1384 rpm (red □). Conducted under anaerobic conditions and 144 W visible irradiation in the PFPR Model II*

Figure 84 also shows the impact of further rotational speed on photocatalytic activity. At increased propeller rotational speeds mass transport limitations are exceeded. At a rotational speed of 1384 rpm the rate of H_2 evolution did not increase from the level reached at 1035 rpm. The rate of H_2 evolution over the 6 hr time frame was calculated to be 109 µmol h^{-1} g^{-1} at both 1035 and 1384 rpm. Photocatalytic activity was not expected to continuously increase with increased propeller rotational speed. In contrast, at higher rotational speeds ($\geq$ 1384 rpm) the trapping and agglomeration of powder occurs, the result of which was reduced surface area of catalyst available for excitation and catalyst-target species interactions.

Furthermore the motor which controls the speed of the propeller becomes variable at increased speeds, which explains the high standard deviation of 6.0335 between replicate samples taken during the 1384 rpm experiments. In comparison the lowest standard deviation recorded after 6 hrs illumination was 0.3057 for replicates of experiments conducted at 1035 rpm.

5.3.4.2 H$_2$ Evolution from The Corrosion of Stainless Steel

The evaluation of a photocatalytic reactor requires the identification and where possible the minimisation and control of limitations. The evaluation of the PFPR showed the major limitation of the unit to be the formation of Fe^{2+} on the propeller surface as a result of stainless steel (SS) corrosion by oxalic acid. The corrosion process generated H_2 as a result.

The reaction between the sacrificial electron donor, oxalic acid, and SS has been reported to generate H_2 (Equation 28 and Equation 29) (Wiersma, 2004; Wiersma *et al.*, 2004; Sekine and Okano, 1989). It has been suggested that the extent to which corrosion is promoted is dependent upon the content of carbon in the steel and the concentration of Fe^{2+} (Abdel *et al.*, 1995).

$$Fe \rightarrow Fe^{2+} + 2e^-$$ **Equation 28**

$$2H^+ + 2e^- \rightarrow H_2$$ **Equation 29**

While the reactor was constructed from materials that were chemically inert, the physical corrosion of the SS 316 four blade propeller was observed. SS grade 316 has increased resistance to corrosion and was selected to prevent corrosion and thus H_2 production. Corrosion resistance under acidic conditions has previously been reported in the literature (Chan *et al.*, 2003). The results indicated, however, that corrosion of the propeller resulted in the production of H_2 in the absence of a catalyst; 58.1 µmol H_2 produced in the absence of a catalyst after 2 hrs illumination.

The results indicated H_2 production in the control study increased as corrosion occurred. Thereafter, the formation of Fe^{2+} products generates a temporary protective barrier which prevents further H_2 production. This protective barrier, however, breaks down as a result of prolonged contact with oxalic acid and corrosion continues generating H_2 (Wiersma, 2004).

In order to reduce the H_2 evolution from the corrosion of the SS, control experiments were conducted using a PTFE lining on the propeller. These results are summarised in Table 21. The table shows with no PTFE lining present H_2 evolution was 58.1 µmol after 2 hrs illumination, which was significantly higher than the 33.1 µmol H_2 produced in the presence of Pt-C_3N_4. The lower level of H_2 produced when Pt-C_3N was present was likely due to the 'turbidity effect', which can occur when a catalyst is dispersed in a liquid medium. The agitation of the catalyst restricts the penetration of light and reduces the number of photons which reach the SS propeller.

Placing an initial PTFE lining on the propeller decreased the H_2 produced by 76.94 % from 58.1 to 13.4 µmol. Increasing the lining on the propeller further decreased the corrosion of the propeller to 4.8 µmol after 2 hours illumination. To demonstrate it was the corrosion of SS resulting in H_2 evolution, experiments in the absence of light, catalyst and oxalic acid were conducted. It was shown in Table 21 that no H_2 evolution was recorded in the absence of oxalic acid and a catalyst, however, H_2 was recorded when there was oxalic present with and without illumination.

Experiment Condition	Illumination	Reaction Medium	H$_2$ (μmol)
No PTFE lining	144 W simulated	0.025 M oxalic acid	58.1
No PTFE lining	Dark	0.025 M oxalic acid	1.5
No PTFE lining	144 W simulated	Distilled H$_2$O	0
Initial PTFE lining	144 W simulated	0.025 M oxalic acid	13.4
Increased PTFE lining	144 W simulated	0.025 M oxalic acid	4.8

Table 21; *Evolution of H$_2$ over oxalic control experiments with no PTFE lining, with an initial PTFE lining, with an increased PTFE lining, with no PTFE and no illumination and with no oxalic and no PTFE lining (purple ¤). Conducted under anaerobic conditions in the PFPR Model II*

The production of H$_2$ from the corrosion of SS was monitored in experiments to ensure the photocatalytic activity could be accurately measured. Figure 85 shows the evolution of H$_2$ with and without Pt-C$_3$N$_4$ over a range of rotational speeds. Interestingly, the largest volume of H$_2$ produced during the control experiments was at a rotational speed of 692 rpm and not 1035 rpm as was seen when Pt-C$_3$N$_4$ was present. At increased rotational speeds (1035 and 1384 rpm) the corrosion of SS and thus the production of H$_2$ was observed to decrease and plateau. This was thought to occur due to cavitation of the reaction medium as a result of increased propeller speed. At speeds of 1035 and 1384 rpm the propeller was no longer in full contact with the reaction medium. Alternatively, at lower speeds full cavitation of the liquid medium had not occurred and thus the oxalic acid has increased contact with the propeller, allowing for corrosion and thus H$_2$ production to occur.
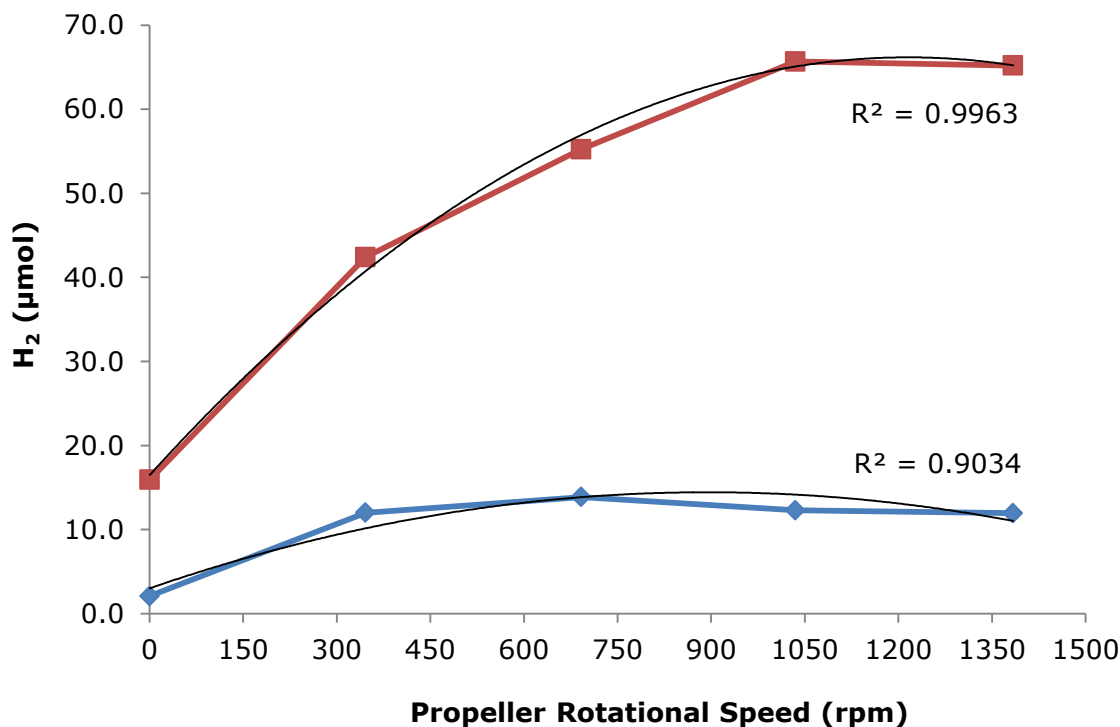
Figure 85; *Relationship between propeller rotational speed and H₂ evolution in the presence (red □) and absence (blue ◇) of a catalyst. Conducted under anaerobic conditions and 144 W visible irradiation in the PFPR Model II*

Figure 85 also indicates the optimum rotational speed of the propeller to be 1035 rpm based upon levels of H_2 produced under the experimental conditions. At 1035 rpm the greatest difference in H_2 production when $Pt-C_3N_4$ was present and absent was recorded at 53.4 µmol. The remaining propeller speeds were in the order 1384 rpm (53.3 µmol) > 692 rpm (41.3 µmol) > 346 rpm (30.4 µmol) > 0 rpm (13.8 µmol).

The production of H_2 from the corrosion of SS was a significant limitation of the PFPR and one which must be addressed in additional PFPR designs. To overcome this issue, more robust linings could be used to coat the propeller and this point is addressed further in Chapter 6. It is worth noting, however, that the oxalic acid was required as a SED by the novel catalysts to generate a high yield of H_2. Work was conducted by colleagues at the University of St. Andrews which used alternative SED such as Na_2SO_3 and TEA. The results of this investigation, however, showed that the production of H_2 was reduced when an alternative SED

was used. A 96.5 % and 78.1 % reduction in H_2 production rates ($\mu mol\ h^{-1}\ g^{-1}$) was recorded for Na_2SO_3 and TEA respectively in comparison to oxalic acid.

5.3.4.3 Effect of Catalyst

The increased performance of Pt-C_3N_4 over that of the control experiments allowed the photocatalytic activity of the catalyst and unit to be observed. The H_2 produced from the control experiments, however, masked the activity of alternative catalyst tested.

Figure 86 shows the activity of C_3N_4, C_3N_4 calcined at 600 ^oC and the composite catalyst TNT-C_3N_4. As can be seen, the non platinised C_3N_4 catalyst displayed lower activity than that of Pt-C_3N_4 for the production of H_2. In addition to this, the profile of the data series of each catalyst suggests the production of H_2 was beginning to plateau and was not increasing. As discussed previously, this was likely a result of SED exhaustion.
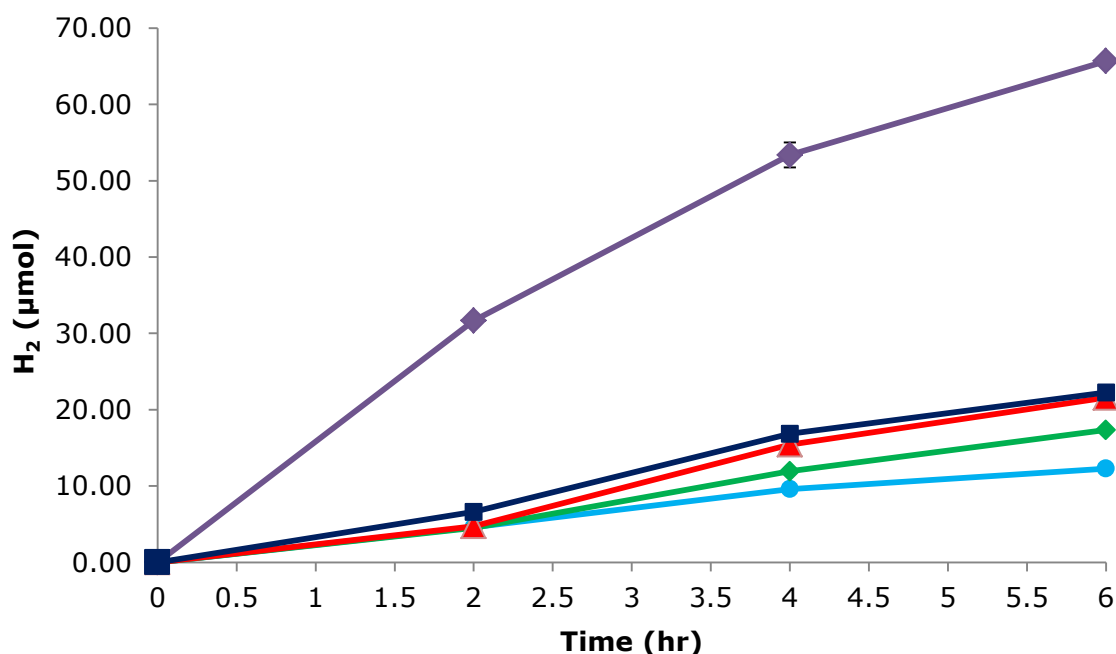
Figure 86; *Evolution of H_2 in the presence of Pt-C_3N_4 (purple ◇), TNT-C_3N_4 (navy □), C_3N_4 600 ^oC (red Δ), C_3N_4 (green ◇) and no catalyst (blue o). Conducted under anaerobic conditions and 144 W visible irradiation at a speed of 1035 rpm in the PFPR Model II*

The enhanced activity of 1 % $Pt\text{-}C_3N_4$ over that of non Pt loaded C_3N_4 was due to the ability of Pt to restrict the recombination of electrons and holes and catalyse proton reduction (Zheng *et al.*, 2009; Yang *et al.*, 2012; Mizukoshi *et al.,* 2007). Pt has improved electron acceptor properties as a result of a larger work function (5.65 eV), as described by Mizukoshi *et al.* (2007), which prevents the recombination of photo generated electrons and holes.

Yang *et al.* (2012) investigated the behaviour of Pt, PdS and Pt-PdS/CdS catalysts through in situ photoelectrochemical measurements in their study, in an attempt to characterise the role cocatalyst play in photocatalytic H_2 evolution. Thin film catalysts were deployed onto fluorine-doped tin oxide conducting glass to measure the current densities. The study showed an increase in cathodic current density of the Pt-CdS catalyst on FTO which they stated as an indication of the ability of Pt to catalyse proton reduction such as H_2 production.

Studies by Zheng *et al.* (2009) have shown that increasing the Pt content to 1 % loading on TiO_2 increases photoactivity. Their study found that with an increase from 0.2 wt. % to 1.0 wt. %, the production of H_2 increased from 55 to 142 mL. Increasing the Pt content further to 3.0 wt. %, however, was shown to decrease H_2 production from 142 to 84 mL. The reduction of photocatalytic activity at high Pt loading weights has been reported elsewhere (Ohtani *et al.* 1997; Sreenthawong and Yoshikawa 2006) and can be a result of Pt particles reducing the number of available active sites on the catalyst for photon absorption and electron donors. Thus inactivity of the catalyst at > 1 % wt. loadings was a result of insufficient excitation. Furthermore, Zheng and colleagues stated that excessive Pt particles may act as recombination centres for photogenerated electrons and holes.

While the presence of Pt has been shown to dictate photoactivity, it is also worth reviewing the practical implications of industrial scale production of a Pt loaded catalyst. At laboratory scale Pt is readily available and is cost effective for small scale experiments which typically produce catalysts in the range of 1-10 g. If industrial scale production of a catalyst was to occur, however, the quantity of catalyst produced would be far greater and in the range of 1-100 kg. Therefore, cost analysis would be required to ensure that the enhanced performance with Pt present outweighed the increased cost of production.

Additional catalysts, $Sr_{0.97}NbO_3$ and $NaTaO_3.La$, were also deployed in the PFPR. The production of H_2 over these catalysts along with the control for comparison is shown in Figure 87. While $Sr_{0.97}NbO_3$ showed an increased rate of production during the first 4 hr period of the experiment, the rate decreased thereafter as the production began to plateau. The rate of production at 2, 4 and 6 hours decreased from 3.96 to 3.61 and to 2.09 µmol h^{-1} respectively. $NaTaO_3.La$ however showed an increasing rate of production over the time frame, suggesting over an extended illumination period the rate of H_2 production would continue to increase. The rate of production increased from 1.55 to 4.24 and 4.50 µmol h^{-1} at 2, 4 and 6 hrs respectively.

Figure 87; *Evolution of H_2 in the presence of $Sr_{0.97}NbO_3$ (green Δ), $NaTaO_3.La$ (orange o) and no catalyst (blue ¤). Conducted under anaerobic conditions and 144 W visible irradiation at a speed of 1035 rpm in the PFPR Model II*
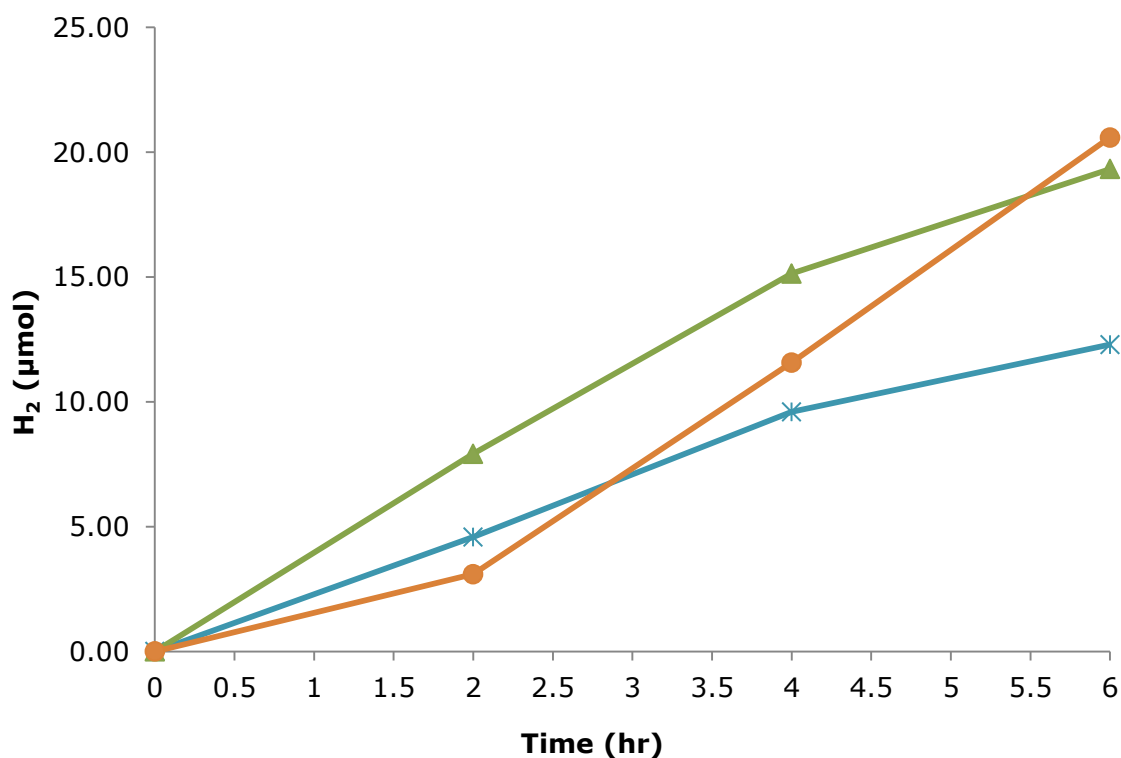
Figure 87 also shows a positive (Equation 30; $y=0.3695x^2 + 1.294x - 0.2425$) and negative (Equation 31; $y=-0.1184x^2 + 2.8048x - 0.1374$) polynomial trendline which indicates the increase and plateau in performance of $NaTaO_3.La$

and $Sr_{0.97}NbO_3$ respectively. Good correlation of data was also observed over all catalyst indicated by the R_2 values, Table 22

Catalyst	R_2 Value
$Pt-C_3N_4$	1
$TNT-C_3N_4$	0.9878
C_3N_4 600 °C	0.981
C_3N_4	0.992
$Sr_{0.97}NbO_3$	0.9992
$NaTaO_3.La$	0.9954
no catalyst	0.9958

Table 22; *R_2 values of data series' shown in Figure 86 and Figure 87*

The volume of H_2 produced and evolution rates along with the normalised values are summarised for comparison in Table 23. The normalised values in Table 23 were calculated to remove the H_2 production which was a result of SS corrosion by oxalic acid, Equation 32.

$$Total\ H_2\ evolution - H_2\ from\ control\ experiments\ = Normalised\ H_2\ evolution$$

Equation 32

Catalyst	H_2 Evolution (μmol)	H_2 Evolution rate (μmol h^{-1} g^{-1})	Normalised H_2 Evolution (μmol)	Normalised H_2 Evolution rate (μmol h^{-1} g^{-1})
C_3N_4	17.3	29	5	8
C_3N_4 600 ^{o}C	21.6	36	9.3	15
TNT-C_3N_4	22.3	37	9.9	17
Pt-C_3N_4	65.7	109	53.4	89
$Sr_{0.97}NbO_3$	19.3	18	7	12
$NaTaO_3.La$	20.6	19	8.3	14

Table 23; *H_2 Evolution and rate over a series of novel catalyst and normalised values to account for H_2 evolved from control experiments*

Positive normalised values are shown for all catalysts indicating that there was H_2 evolution beyond that of the control values. Pt-C_3N_4 was shown to produce the largest volume of H_2 at 53.4 μmol with an evolution rate of 89 μmol h^{-1} g^{-1}, which was a 91.01 % increase over the next best catalyst, TNT-C_3N_4. The photocatalytic activities are in the order Pt-C_3N_4 > TNT-C_3N_4 > C_3N_4 600 ^{o}C > $NaTaO_3.La$ > $Sr_{0.97}NbO_3$ > C_3N_4.

5.3.4.4 Loss of H_2 Through Sampling Procedures

A point of interest in the evaluation of the reactor was the noted pressure drop recorded during the sampling procedure. The PFPR Model II was run in conjunction with an Agilent Micro GC, which through an internal pump drew a sample from the reactor head space. During this process the pressure decreased by 88.52 %, from 0.575 bar to 0.066 bar.

The sample extracted by the GC was dependent on a positive pressure inside the unit to ensure the sample was drawn through the GC inlet. Alternatively if the PFPR was at a low pressure (< 0.15 bar), the GC would draw the sample from

the open outlet which resulted in the presence of increased O_2 and N_2 in the column.

To ensure the pressure was maintained at a level which allowed the GC to draw a sample from the inlet, the PFPR was purged with Ar post sampling. This method adequately increased the pressure, however, also removed a proportion of the H_2 from the unit. Therefore, the concentration of H_2 analysed by the GC was lower than the true value of H_2 produced by the PFPR. This can also be stated for the production of H_2 from the corrosion of SS by oxalic acid.

To demonstrate this point further Figure 88 shows the evolution of H_2 over Pt-C_3N_4 as analysed by the GC (solid line) and the predicted evolution (dashed line), which corrects for the loss of H_2 as a result of Ar purging along with values under photolysis conditions. It was observed when purging the system with Ar post sampling the mean loss of H_2 was 11.82 %. The dotted data series' in Figure 88 corrects for this loss and shows the predicted true value of H_2 produced in the PFPR. Under these conditions the rate of H_2 produced when Pt-C_3N_4 was deployed increased from 109 to 122 µmol h^{-1} g^{-1} (89 to 99 µmol h^{-1} g^{-1} under normalised conditions), while the rate when no catalyst was present increased from 20 to 23 µmol h^{-1} g^{-1}. The values of the predicted H_2 profile also showed good correlation indicated by the R_2 values of 0.9983 and 9905 for the presence and absence of a catalyst respectively.
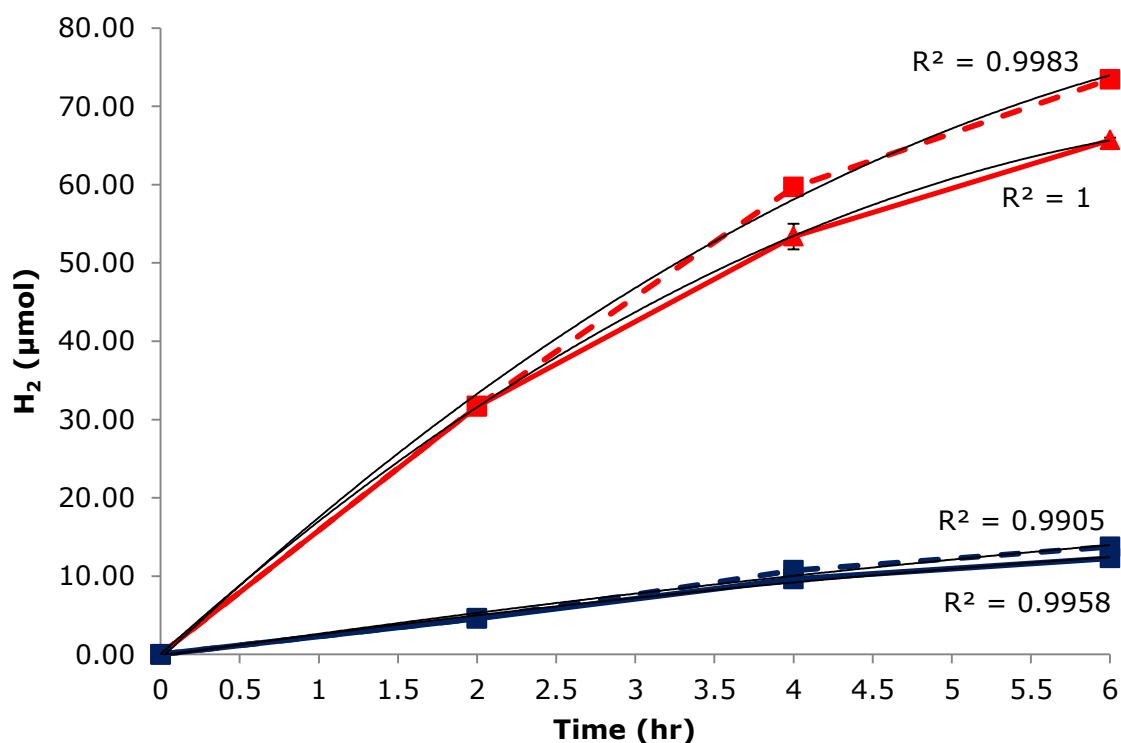
Figure 88; *H_2 evolution in the presence of Pt-C_3N_4 (red Δ), in the presence of Pt-C_3N_4 corrected for the loss of H_2 from purging (dashed red □) and in the absence of a catalyst (navy □) and corrected for loss of H_2 from purging (dashed navy □). Conducted under anaerobic conditions and 144 W visible irradiation at a speed of 1035 rpm in the PFPR Model II*

5.3.4.5 Effect of Illumination

The results which have been displayed in this chapter were performed under illumination from 36 W lamps, providing a total of 144 W and 360 ^{O} irradiation coverage. During a collaboration period with CalTech different illumination sources were used in conjunction with the PFPR Model II, including a 450 W Xe Arc lamp and solar illumination from the George Ellery Hale Telescope (Section 5.2.3.2). The analysis procedure during this collaboration period (described in Section 5.2.3.3) required needle extraction and manual injection into a GC. This allowed the evaluation of the PFPR Model II needle port to be conducted. It should be noted that due to the difference in sampling and analysis procedures, the results obtained at CalTech differed from those obtained when at the University of St. Andrews.

The effect of illumination on the evolution of H_2 is shown in Table 24. H_2 production over $Sr_{0.97}NbO_3$ was shown to be comparable between 144 and 450 W illumination sources. Furthermore, the production of H_2 and evolution rate increased under irradiation from the lower powered lamps. The marginal difference in H_2 can be accounted for by the delivery of photons from the respected illumination sources. The 144 W lamp was composed of four 36 W lamps, which provided diffuse irradiation and full 360 $^\circ$ coverage. The lamps were also positioned in a mirrored light house to increase the reflectance of light and minimise light loss. In contrast the 450 W lamp provided a single spot of illumination upon the PFPR quartz tubular body (Figure 78). The lamp was also not used in conjunction with mirrors or reflectors and thus light loss was expected.

Catalyst	Lamp (W)	H_2 Evolution (μmol)	H_2 Evolution rate (μmol g^{-1} h^{-1})	Normalised H_2 Evolution (μmol)	Normalised H_2 Evolution rate (μmol g^{-1} h^{-1})
$Sr_{0.97}NbO_3$	144	14.6	24	10.5	17
	450 Xe	14	23	6.8	11
$Pt-C_3N_4$	144	9.4	16	5.3	9
	450 Xe	18.1	30	10.9	18

Table 24; *H_2 evolution and rate over $Sr_{0.97}NbO_3$ and $Pt-C_3N_4$ under 144 and 450 W illumination. Conducted under anaerobic conditions at a speed of 1035 rpm in the PFPR Model II*

These results indicate that the scale up of the reactor system would require the incorporation of an array of 36 W lamps, as the fragility and complexity of the 450 W Xe lamp makes it unsuitable for scale up. In addition, the normalised results, which takes into account the H_2 produced from the corrosion of SS, displays a significant difference between the 144 and 450 W lamps. The normalised H_2 values under 144 W irradiation decreased from 14.6 to 10.5 μmol

and 9.4 to 5.3 µmol for $Sr_{0.97}NbO_3$ and $Pt-C_3N_4$ respectively. In contrast, however, a greater decrease was seen under irradiation from the 450 W lamp. A reduction from 14 to 6.8 µmol and 18.1 to 10.9 µmol was observed for $Sr_{0.97}NbO_3$ and $Pt-C_3N_4$ respectively.

Contrasting results were obtained under the same experimental conditions with $Pt-C_3N_4$ deployed as the catalyst. Increasing the illumination source power increased the normalised evolution rate of H_2 from 9 to 18 µmol g^{-1} h^{-1}. The increase was primarily due to the level of H_2 produced during the final period of illumination.

5.3.4.6 George Ellery Hale Telescope

The experimental set up of the PFPR with the solar telescope is shown in Figure 89. Figure 89 shows the illumination of 2 PFPR units operating in parallel with a catalyst present in one unit and absent in the other.

Figure 89; *PFPR under solar irradiation by the George Ellery Hale Solar Telescope*

Table 25 shows the effect of illumination source on the evolution of H_2 over novel catalyst $Sr_{0.97}NbO_3$ from 144 W and 450 W visible illumination and natural illumination provided by the solar telescope. The results show the normalised rate of H_2 production was reduced under natural illumination in comparison to

the 144 and 450 W lamps. A reduction of 88.24 % and 81.82 % was observed from the 144 and 450 W lamps respectively.

Lamp (W)	H_2 Evolution (μmol)	H_2 Evolution rate (μmol g^{-1} h^{-1})	Normalised H_2 Evolution (μmol)	Normalised H_2 Evolution rate (μmol g^{-1} h^{-1})
144	14.6	24	10.5	17
450 Xe	14	23	6.8	11
Solar	2.8	5	1.1	2

Table 25; *H_2 Evolution and rate over Sr$_{0.97}$NbO$_3$ under the illumination from 144 W light box, 450 W Xe lamp and solar illumination. Conducted under anaerobic condition at a speed of 1035 rpm in the PFPR Model II*

The efficiency of solar generated H_2 production was increased over NaTaO$_3$.La, Table 26. The normalised rate of H_2 evolution rose from 2 μmol g^{-1} h^{-1} over Sr$_{0.97}$NbO$_3$ to 5 μmol g^{-1} h^{-1} over NaTaO$_3$.La, which was a 60 % increase. The H_2 evolution profile also shows that over NaTaO$_3$.La the rate at which H_2 was produced was continuous at 5 μmol g^{-1} h^{-1}, suggesting increasing the experiment time frame would further increase the level of H_2.

Catalyst	H_2 Evolution (μmol)	H_2 Evolution rate (μmol g^{-1} h^{-1})	Normalised H_2 Evolution (μmol)	Normalised H_2 Evolution rate (μmol g^{-1} h^{-1})
Sr$_{0.97}$NbO$_3$	2.8	5	1.1	2
NaTaO$_3$.La	4.6	8	2.9	5

Table 26; *H_2 evolution and rate over Sr$_{0.97}$NbO$_3$ and NaTaO$_3$.La under natural illumination. Conducted under anaerobic conditions at a speed of 1035 rpm in the PFPR Model II*

While an increased rate of production would be expected due to the broad spectrum of natural light, which was sufficient to promote excitation of the catalyst, there are a number of factors which first must be discussed when analysing the data including delivery of photons, unpredictability of exposure and intermittent nature of illumination source.

Natural illumination was provided by the George Ellery Hale telescope, which uses a number of angled mirrors to collect and deliver illumination through a quartz window. During the collection and delivery of the light from the source to the sample, a number of potential issues could affect light transmittance. The length of the illumination path from the initial mirror to the window in the laboratory is ~ 40 ft (Oliwinstein, 2011). As the illumination shafts of the telescope are open to the environment, the mirrors and windows which guide the light are subject to contaminants and thus can result in the delivery of photons becoming intermittent. The presence of contaminants on the surface of the mirrors can impede the delivery of photons and thus significantly impact the photo activity of a system (Bickely *et al.*, 2005).

The illumination delivered was also subject to weather conditions on the day of experiment. Cloud coverage and unexpected weather can reduce and restrict the delivery of light through the telescope. The result of which can be dark periods, which reduce the photocatalytic efficiency.

The solar telescope may not be the ideal source of illumination for incorporation into an environmentally efficient photocatalytic system, however, it did demonstrate the ability of photocatalysis to harness solar power for the generation of alternative fuels. Alternative approaches to the solar telescope are discussed in Chapter 6.

5.3.4.7 Comparison to the Literature

Table 27 gives a summary of the optimal rates of H_2 production in the PFPR Model II along with a brief review of H_2 production over novel catalysts in the literature. As the results show, the H_2 production in the PFPR was within the range reported in the literature. Under optimum conditions the PFPR Model II achieved a rate of 109 µmol h^{-1} g^{-1}. This rate was greater than that reported by

Liu and Syu (2012) at 14.9 µmol h^{-1} g^{-1}, Yan *et al.* (2009) at 3.57 µmol h^{-1} g^{-1} and Cui *et al.* (2012) at 20.21 µmol h^{-1} g^{-1}. In addition, this rate was also achieved under low power illumination and not the typical high power Xe arc lamp.

Of particular interest for comparison was the work done by Yan *et al.* (2009), which used a NiO modified $La_{0.02}Na_{0.98}TaO_3$ catalyst similar to that of $NaTaO_3$.La. Under artificial visible illumination comparable rates of H_2 were recorded. A rate of 7 and 3.57 µmol h^{-1} g^{-1} H_2 production was recorded in the PFPR and Yan *et al.* system respectively. The lower level reported by Yan and colleagues was a result of the 2 hour time frame and the use of no reductant. While increased production in the PFPR unit was achieved under low power and natural illumination, it required the presence of oxalic acid. The production of H_2 in pure water in the PFPR was minimal at 1 µmol h^{-1} g^{-1}. This low rate was thought to be due to recombination occurring after photo excitation.

Comparison of H_2 evolution results with the literature is difficult to ascertain, due to the varying nature in which the experiments are conducted. In order to compare the current work presented here to that published in the literature a number of reaction conditions must be taken into account. These include:

- Reactor configuration
- Illumination source
- Experiment time frame

System/Ref	Catalyst	SED	Illumination	Volume (mL)	Time (min)	H_2 ($\mu mol\ h^{-1}\ g^{-1}$)
PFPR Model II	Pt-C_3N_4	Oxalic acid	144 W Light Box	100	360	109
	NaTaO$_3$.La	Oxalic acid	144 W Light Box	100	360	19
	NaTaO$_3$.La	Oxalic acid	Natural	100	360	8
	Sr$_{0.97}$NbO$_3$	Oxalic acid	144 W Light Box	100	360	18
	Sr$_{0.97}$NbO$_3$	Oxalic acid	Natural	100	360	5
Liu and Syu (2012)	N-doped mesoporous TiO$_2$	CH$_3$OH	450 W Xe lamp	155	360	14.9
Khan and Qureshi (2012)	BaZr$_{0.96}$Ta$_{0.04}$O$_3$	Pure H$_2$O	300 W Xe lamp	*	*	900
Jeong *et al.* (2006)	Ni/Sr$_3$Ti$_2$O$_7$	Pure H$_2$O	400 W Hg lamp	475	600	164
Yan *et al.* (2009)	NiO modified La$_{0.02}$Na$_{0.98}$TaO$_3$	Pure H$_2$O	400 W Hg lamp	390	120	3.57
Wang *et al.* (2012)	(Pt-loaded) Bi$_{1-x}$SmVO$_4$	Na$_2$SO$_3$/ AgNO$_3$	300/500 W Xe lamp	80	720	188.25
Lin and Chang (2010)	Au/KTiNbO$_5$	CH$_3$OH	400 W halide lamp	550	300	3522
Cui *et al.* (2012)	CdS/K$_2$La$_2$Ti$_3$O$_{10}$	Na$_2$S	500 W Xe lamp	100	300	20.21

Table 27; *Summary of H$_2$ production in literature and in the PFPR Model II. *information not disclosed*

Reactor configuration including capacity and geometry are important factors when comparing the performance of systems. A number of publications provide limited information on the photocatalytic reactors and systems used. A common approach used in the literature, however, involves high power lamps providing aerial illumination through a quartz window typically with an area of ~15 cm^2, Figure 90 (Liu and Syu, 2012; Sreethawong and Yoshikawa 2006; Yang *et al.*. 2012).
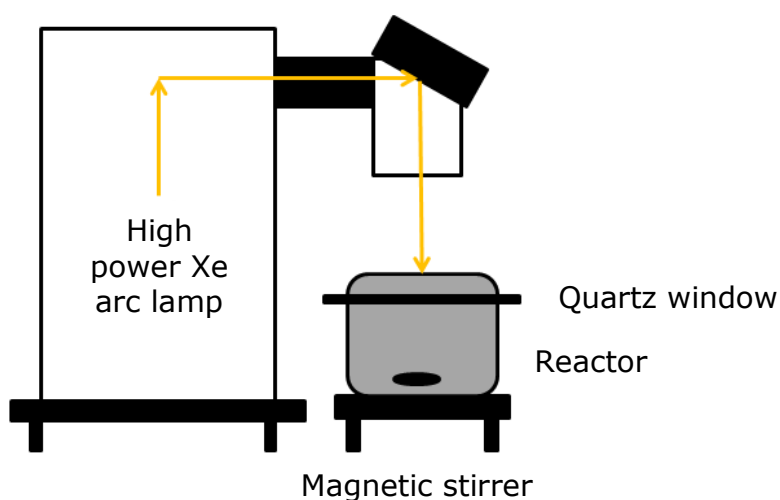
Figure 90; *Block schematic of standard photocatalytic gas reactor used in the literature*

This style of system utilise medium and high power lamps with a power of 300 to 450 W (Khan and Qureshi 2012; Jeong *et al.* 2006; Yan *et al.* 2009; Fan *et al.*, 2010 and Liu and Syu, 2012). These lamps have been used in conjunction with novel catalysts to produce a range of yields of H_2 production. Liu and Syu in 2012 showed a production rate of 14.9 µmol g^{-1} h^{-1} under irradiation from a 450 W Xe lamp, which was significantly lower than that of 89 µmol g^{-1} h^{-1} achieved over Pt-C_3N_4 in the PFPR.

Increased rates of H_2, however, have also been shown by Khan and Qureshi (2012) and Jeong *et al.* (2006). Khan and Qureshi (2012) produced H_2 at a rate of 180 µmol h^{-1} over $BaZr_{0.96}Ta_{0.04}O_3$ under irradiation from 300 W Xe lamp. Furthermore, the level of H_2 achieved was done over 0.2 g of catalyst, therefore

the h^{-1} g^{-1} production rate was 900 µmol h^{-1} g^{-1}. This high level of photocatalytic activity was described by the authors as a result of increased surface area (36 m^2/g) and the increased number of photons absorbed by the catalyst. Interestingly Khan and Qureshi discuss that the increased number of absorbed photons was a result of catalyst development rather than the use of a high power lamp. The development of the catalyst produced a more 'suitable band-gap in terms of source excitation' (Khan and Qureshi, 2012), which allowed for increased photon absorption on the surface of the catalyst. In the view of the author, an interesting comparison would be the deployment of a catalyst capable of producing a high yield of H$_2$ in a unit with low power lamps.

The yield of H$_2$ produced in the literature is primarily dictated by the catalyst deployed. Novel reactor development for H$_2$ production reported in the literature is limited. The majority of novel designs for H$_2$ production are based upon dual systems, which attempts to mimic the photosynthetic system found in plant cells (Liao *et al.*, 2012; Lo *et al.*, 2010; Tsydenov *et al.*, 2012 and Yu *et al.*, 2011).

Recently, however, Reilly and colleagues (2012) reported the construction of a UV-irradiated fluidised bed for H$_2$ production. The design concept of the reactor employed a low power internal illumination source (50 W) in a recirculating annular style fluidised system. The catalyst deployed in the system was Pt loaded TiO$_2$. Similarities can be drawn between this fluidised system and the PFPR as both units adopted an annular geometric design with low power illumination, along with a simple design concept to ensure the unit was not overly complex. The method of fluidisation and delivery of illumination, however, differ between the two systems. Reilly *et al.* adopted a centrally positioned internal illumination source along with a more traditional style of fluidisation through the recirculation of the liquid media, which resulted in agitation of the catalyst bed. The Reilly *et al.* fluidised system produced an optimum H$_2$ rate of 198 µmol/h which was significantly higher than the hourly rate of H$_2$ produced in the PFPR Model II (~ 8.9 µmol/h). To accurately compare these systems however, the following reaction conditions must be considered; catalyst loading, illumination time frame and source. The fluidised system described by Reilly *et al.* used a high catalyst loading weight of 80 g, along with UV light and 24 hr illumination time frame to achieve the optimum rate of H$_2$ production. These reaction conditions adopted by

Reilly *et al.* account for the high production rate of H_2 recorded. Interestingly, if the rate of H_2 production was to be displayed as µmol h^{-1} g^{-1}, as it often is, the rate would be $\sim$ 2.475 µmol h^{-1} g^{-1}, which was significantly lower than that of 89 µmol h^{-1} g^{-1} produced in the PFPR Model II. Furthermore, the catalysts deployed in PFPR Model II were novel synthesised for excitation under natural illumination, while the Pt-loaded TiO_2 catalyst developed by Reilly *et al.* was restricted to UV light.

5.4 Performance of the Reactor

The function of any photocatalytic unit is to provide the optimum environment for the desired conversion to take place, and where possible to facilitate and enhance the performance of the photocatalyst. The conversion efficiency and product selectivity, however, relies on the properties of the catalyst and reaction conditions. While the reactor design can enhance the properties and conditions of the reaction, it is not capable of directly initiating conversion. Therefore, the preliminary reduction process of CO_2 and H_2 production is dependent on the activity of the catalyst. Thereafter, reactor design properties are capable of increasing the conversion rate through increased mass transport and increased delivery of photons.

As the conversion of CO_2 to CO and C_1 to C_4 hydrocarbon products was not recorded, the efficiency of the unit was difficult to determine. The primary properties of the PFPR unit allowed for control over the mixing capabilities, transport of products from the liquid to gas phase and an increased area of irradiation exposure through the quartz tubular vessel body.

The splitting of H_2O for the production of H_2 presents less of a physical and chemical challenge than the reduction of CO_2. H_2 was generated over a number of catalysts investigated and a number of irradiation sources, which provided data to evaluate the performance of the unit. Figure 83 shows the significant impact of propeller rotational speed on the evolution of H_2. The efficiency of the catalyst was shown by the rate of H_2 evolution produced when the unit was operated statically at 0 rpm (27 µmol h^{-1} g^{-1}). Upon increasing the rotational speed, the PFPR enhanced the photocatalytic performance, which was evident by the increased production rate of 109 µmol h^{-1} g^{-1} at 1035 rpm. These results also

correlate with those obtained for dye degradation in the PFPR Model II, Figure 76.

The production of H_2 under illumination from the 144 W visible lamps and 450 W Xe lamp demonstrated the optimum conditions for the PPFR. Moreover, the results demonstrated the versatility of the PFPR unit in operation with varying sources of illumination. The comparative results obtained under different illumination sources also shows that high power illumination sources are not essential for photocatalytic systems.

As previously stated, few comparative studies between CO_2 photo reduction and solar H_2 production are reported. Based upon results published (Indrakanti *et al.*, 2008) and results displayed here the more favourable and feasible approach is that of solar H_2 production. No photo reduction of CO_2 was achieved in this investigation and currently low yields of products are achieved. Abou Asi *et al.* (2011) has reported relatively high yields of products (shown in Chapter 1) however, was done so under artificial not natural light. In any CO_2 photo reduction system it is critical that the units are converting more CO_2 than is being emitted i.e. production of CO_2 from the use of artificial lamps.

Alternatively, H_2 production shows potential as a viable photosynthetic approach with high production rates being reported (3522 μmol h^{-1} g^{-1}) (shown in Chapter 1; Lin and Chang, 2010). In addition, the results reported here show H_2 to be a more viable approach as a significant production rate of 109 μmol h^{-1} g^{-1} was achieved. Furthermore, the production of H_2 achieved under solar illumination was also reported.

Currently there is no standardised reactor used for gas and multi phase photocatalysis. Furthermore, there are few examples of novel gas phase reactors used in the literature. The work presented here demonstrates the applicability of a novel reactor for gas and multi phase photocatalysis. While the reduction of CO_2 was not recorded, the results of H_2 evolution demonstrate the efficiency of the PFPR system to enhance photocatalytic activity. In addition, as the unit was modular it presents initial potential for scale up towards commercialisation processes.

5.5 Conclusion

A series of reactor evaluation methods were conducted to monitor the performance of the novel photo reaction. The operational testing of the PFPR Models included the removal of MO, reduction of CO_2 and the generation of H_2. The degradation of MO displayed the impact of rotational speed on photocatalytic activity. The results indicate the optimum propeller speeds for the Model I and II were 543 and 692 rpm respectively. The degradation efficiencies at these speeds were 36.11 and 88 % for Model I and II respectively. While mass transport was increased at these speeds, the results indicated that the removal of dye did not increase further as the rotational speed of the propeller increased. Therefore, at rotational speeds beyond that of the optimum conditions mass transport limitations no longer predominant. The comparison of the PFPR Models to the previous units (SFPR and MCPR), showed the PFPR Model II achieved the greatest removal rate of MO, 5.65 x 10^{-5} M h^{-1}. This increased removal rate of MO was accredited to the optimisation of the key reactor characteristics such as geometry, construction material, air-tight seals, method of fluidisation and delivery and distribution of illumination.

The second stage of the reactor evaluation was the reduction of CO_2 to hydrocarbon products such as CO and CH_4. The primary purpose to this stage was to evaluate the photo reactor using a challenging multi-phase reaction and also to discuss the application of solar photocatalysis for the generation of clean energy. The reduction of CO_2 was conducted with illumination from 144 W low power lamps, a high power 450 W Xe lamp and natural light delivered by a solar telescope. No reduction of CO_2 was recorded under the operational conditions adopted nor was the detection of CO, CH_4 or additional hydrocarbon products achieved. Furthermore, the analysis of samples taken from the PFPR Model II showed no reduction of CO_2 occurred over novel catalyst CdS-TNT-Cu, $Sr_{0.97}NbO_3$, Pt-C_3N_4 and $NaTaO_3$.La. The lack of CO_2 activity was accredited to inactivity of the catalyst coupled with an insufficient supply of carbon to allow the desired reaction to occur. The batch operation of the PFPR Model II resulted in a low level of carbon available for the conversion of CO_2 to CO and CH_4. The literature has suggested a continuous carbon source stream is required to ensure the reaction takes place (Mao *et al.*, 2012). The inactivity of the catalyst was an ambiguous factor to address. The increase in illumination power from 144 to 450

W ensured sufficient energy was supplied to promote the excitation of electrons across the energy band gap of the catalysts. The use of solar illumination also ensured a broad spectrum of irradiation was provided to promote catalyst activation. The development of a novel visible light activated catalyst for CO_2 reduction is currently one of the most challenging aspects in this domain of work and thus shall be the focus of future work.

The final stage of the reactor evaluation was the production of H_2 from the splitting of H_2O. The primary objectives for this stage where as stated previously for CO_2 reduction. The production of H_2 was achieved in the PFPR Model II under artificial and natural illumination with a number of novel catalysts. The operational parameters of the photo reactor were found to enhance the photo activity of the catalysts. $Pt-C_3N_4$ achieved the highest rate of H_2 production (109 $\mu mol\ h^{-1}\ g^{-1}$) under optimum conditions in the unit, primarily as a result of the 1 % Pt content. As was observed with the removal of MO, the effect of rotational speed was found to increase the activity of the catalyst. The optimum rotational speed of the propeller was 1035 rpm, thereafter increasing the rotational speed decreased the rate of H_2 production displaying again mass transport limitations were no longer the predominant factor in the reaction.

The final stage of the reactor evaluation was also successful by addressing potential limitations. The production of H_2 from the corrosion of SS by oxalic acid resulted in true photocatalytic activity being masked under certain experimental conditions. The addition of a PTFE thin lining to the surface of the propeller, however, reduced this limitation.

It has previously been stated that the ultimate objective for photocatalytic H_2 production is the use of pure water (containing no SED) and natural illumination. Under these conditions in the PFPR Model II the yield of product was low, 1 μmol $h^{-1}\ g^{-1}$. The recombination of electron and holes after photo excitation, which occurred when pure water was used, resulted in oxalic acid being used as an SED.

Chapter 6 Conclusions and Future Work

6.1 Conclusions

This project has provided the scope for increased development in relation to photocatalysts and photo reactor systems. The objective of this project was the development of a photo reactor which could facilitate the conversion of CO_2 to hydrocarbon products and the splitting of H_2O for H_2 production over novel catalysts. The view of this objective was toward the potential of using sustainable energy sources for the production of fuels.

The development of systems, which are capable of providing clean energy through an entirely sustainable source, has become a global aim. Photocatalysis is a suitable process for generating clean energy and for utilising solar energy through CO_2 reduction and H_2 production. In order to achieve these systems the development of a visible light activated catalyst and highly efficient photo reactor system is required.

In 2005 de Lasa *et al.* stated that the challenge in this field is the development of the highly efficient photo reactor system. The development process of a novel photo reactor system has been discussed in this thesis, beginning with early design concepts to address key principles of both photocatalysis and reactor configuration. The SFPR, MCPR and TFMTPR were constructed to evaluate a set of reactor parameters.

The construction of the SFPR and MCPR investigated reactor geometry, methods of fluidisation, UV based photon delivery and intensity along with general operational parameters for the removal of a number of fingerprint dye compounds (MO, MB, CR and RB). The results found intensity of illumination did not significantly increase the removal of dye with the optimum illumination delivery being from a low power 36 W lamp. Using the 36 W lamp the removal of all dyes to > 95 % was achieved over commercial catalyst P25 and ZnO. The removal of the dyes was accredited to photocatalytic, photolysis and absorption mechanisms. These results provided a method of simple reactor evaluation which was applied to subsequent reactor designs. The standard method included; the use of catalyst ZnO as it presented fewer handling issues than that of P25, the

36 W lamp as the illumination source and MO as model pollutant as it was found to be stable and not readily removed by photolysis and absorption.

 The TFMTPR described an alternative approach to catalyst deployment. The TFMTPR was a scalable reactor configuration, which required no mechanical agitation and was suitable for use with visible and solar irradiation. The results showed that despite a low physical surface area the TFMTPR was capable of performing with 3 % of a standard P25 slurry system. In addition the investigation into reactor scale showed the configuration could be scaled up from 20 mL to 250 mL without compromising the photocatalytic efficiency of the system. Despite showing significant potential, the immobilisation of novel catalysts developed by collaborative partners was challenging and thus, the TFMTPR concept was not adopted in the subsequent reactor design. The future application of this reactor concept is discussed in Section 6.2.1.

The results and observations from the early reactor designs were applied to the design and construction of a novel fluidised bed reactor concept. The construction of two units was achieved, PFPR Model I and II. The PFPR Model I was constructed as a prototype to aid the optimisation of the final Model II unit. The performance of the PFPR was evaluated by monitoring dye removal, CO_2 reduction and H_2 production.

The results indicated two key observations. Firstly, the design of the PFPR was successful and capable of enhancing photocatalytic performance, as shown by the near complete removal of MO (~88 % after 2.5 illumination) and generation of H_2. Under optimum operational conditions a rate of 109 µmol h^{-1} g^{-1} H_2 over Pt-C_3N_4 and 6 hrs visible illumination was achieved. This rate was increased to 122 µmol h^{-1} g^{-1} when the loss of H_2, as a result of the pressure drop during sampling, was taken into account (Section 5.3.3.4). The system was also shown to be effective under low power (36 W) and natural illumination for the production of H_2, displaying the potential of the system for application in fuel production from solar energy.

Secondly, the role of the reactor and catalyst are equally important in the design of a photocatalytic system, as shown by the results for CO_2 reduction. Over a broad range of illumination sources and number of novel catalysts the reduction of CO_2 was not achieved, nor was the formation of any hydrocarbon products.

The inactivation of the catalyst and low carbon source level in the reactor as result of batch operation could account for these results. Further development in catalyst synthesis and photo reactor operation is required to overcome these issues.

Whilst one of the target objectives of CO_2 reduction was not achieved in the work presented here, a significant step has been taken from an engineering view point. The PFPR Model II concept has provided a platform for the reduction of CO_2 and production of H_2 to be further investigated towards the objective of solar fuel generation.

6.2 Future Work

The focus of this work can be considered in three regions; reactor development, reactor scale up and clean energy production. Future work is discussed under these headings in this chapter.

6.2.1 Reactor development

The operational testing has shown the potential of the PFPR Model II for the removal of dye, reduction of CO_2 and splitting of H_2O. There are, however, areas of this research which would benefit from additional investigation.

- Fluidisation was created by the rotation of a propeller to create a cavitation of the aqueous medium. The effect of propeller rotational speed was also shown to impact photocatalytic activity. The next stage would be to further investigate the creation of the cavitation and mixing properties through computer based modelling.
- The production of next generation PFPR Models. The operational testing of the PFPR identified the limitations of the systems including corrosion of SS and pressure loss through sampling procedures. Next generation models would investigate alternative propeller materials and surface coatings to prevent corrosion.
- The use of solar light is essential for clean driven photocatalytic technology to progress. Experiments conducted with the George Ellery Hale Telescope

showed the feasibility of using concentrated solar energy for catalyst excitation. Further work on solar irradiation of the PFPR Model II would be beneficial, investigating alternative methods of natural light illumination such as solar furnaces.

- A proportion of the work conducted focused on alternative reactor platform designs in which an Nd-doped TiO_2 sol gel was immobilised on to glass columns. The results showed comparable degradation rates to that of a P25 slurry system. The development of a hybrid system utilising the reactor geometry of the PFPR and coated glass columns of the TFMTPR could produce a highly efficient system with no downstream processing requirements. Furthermore the system would have a wide range of potential applications including environmental remediation, air treatment and clean energy production.

6.2.2 Reactor scale up

The literature has shown the production of visible light activated catalysts is now being routinely reported. Therefore, the forthcoming challenge faced in photocatalysis is the transition from laboratory to industrial scale, while maintaining the same level of efficiency. The scaling up of a photocatalytic system requires the considerations of additional factors, which are associated with the engineering rather than the scientific aspect of photocatalysis.

A realistic approach to scale up is the multiplication of unit rather than the enlargement. The PFPR Model II design concept was to produce a unit which can be incorporated into modular designs, thus allowing a number of units to be run in parallel, in series or as a continuous system. The focus of future scaled up work shall be the reproduction of additional PFPR Model II units for incorporation into a modular system. The system would use an array of compact low power 36 W lamps to provide irradiation in a construct which would maximise light reflectance. The construction of a modular system would significantly increase the capacity of the system. Furthermore the construction of a hybrid system would eliminate the need for mechanical agitation, thus reducing the complex transition of scaling up. Eliminating the mechanical agitation devices will also relieve the requirement of horizontal operation. It is proposed with a hybrid

system the unit can be operated in a vertical positioning. This would allow for light to run parallel with coated glass column up to 1 m in length.

Also to be conducted is the cost analysis of scaling up the PFPR Model II or Hybrid unit for incorporation into industrial applications. Photocatalysis is suitable for use with a broad range of environmental and energy based processes as either a sole method or as an additional polishing stage. The feasibility of this, however, can be dictated by the cost of designing, constructing, and implementing the technology into an already well established construct. The cost analysis would be applicable to not only the photo reactor but also the synthesis of catalyst. Catalyst production would be required in the kilogram range as opposed to the current gram range.

6.2.3 CO_2 reduction and H_2 production

The investigation into CO_2 reduction and H_2 production has provided an insight into the potential for clean energy generating photocatalytic systems. The future work will focus on catalyst and reactor development in an attempt to achieve reduction of CO_2 and the formation of hydrocarbon products. Taking an engineering standpoint the objective of the work will be to reproduce the PFPR Model II in order to create a modular system which operates in a continuous process. A constant flow of CO_2 shall be passed through the system to ensure the carbon source level is sufficient to promote the conversion of CO_2 to CO and CH_4.

The results have also shown the efficiency of the PFPR Model II for the generation of H_2. This potential could be used in a dual gas phase modular system in which H_2 produced from the splitting of H_2O is used as a reductant for the reduction of CO_2. The use of H_2 as a reductant is favourable over H_2O, as the band energy of the H-H bond (436 kJ/ mol) in H_2 is lower than that of O-H bond (464 kJ/mol) in H_2O (Yang *et al.*, 2011). The development of a parallel operating system for the efficient use of solar energy is a realistic and attractive approach. Furthermore, as the two primary photosynthetic processes the development of a combined system would be highly beneficial in limiting GHG emissions and converting solar energy to alternative fuels.

The photocatalytic generation of solar H_2 has been shown in this research while the activity of CO_2 was reported to still be a challenging aspect of photocatalysis evolution. Should an active and efficient catalyst for CO_2 reduction be deployed then a dual system which utilises solar H_2 is a feasible prospect. H_2 has been shown to be an efficient reductant for CO_2 reduction. The design of the PFPR units were to produce a modular system and one which can incorporate a series of units to run in parallel and as such would be ideally suited to a H_2 generation/CO_2 reduction dual system.

This future would also allow the PFPR to be operated as gas phase unit. The PFPR Model II is capable of reducing the aerodynamic drag on stationary particles in a bed formation through the rotation of a propeller to the point at which the particles are brought to a fluidised state. The operational testing conducted in this projected was done so in the liquid-solid-gas phase and thus the unit was not operated in the solid-gas phase. Operating the system in a gas-solid phase would increase the contact time between the catalyst and reactant, thus reducing mass transport limitations. Moreover the penetration and distribution of light in a solid-gas phase unit is increased over that of a liquid-solid-gas phase unit primarily as a result of eliminating the turbidity of an aqueous medium.

Chapter 7 References

ABDEL AAL, M.S., WAHDAN, M.H., GOMMA, G.K., 1995. Influence of Fe^{2+} ion on the corrosion of carbon steel. *Materials Chemistry and Physics,* 39(4), pp. 290-297

ABE, R., SAYAMA, K., ARAKAWA, H., 2004. Dye-sensitized photocatalysts for efficient hydrogen production from aqueous I− solution under visible light irradiation. *Journal of Photochemistry and Photobiology A: Chemistry,* 166(1−3), pp. 115-122

ABOU ASI, M., HE, C., SU, M., XIA, D., LIN, L., DENG, H., XIONG, Y., QIU, R., LI, X., 2011. Photocatalytic reduction of CO_2 to hydrocarbons using $AgBr/TiO_2$ nanocomposites under visible light. *Catalysis Today,* 175(1), pp. 256-263

ADAMS, M., CAMPBELL, I., ROBERTSON, P.K.J., 2008. Novel photocatalytic reactor development for removal of hydrocarbons from water. *International Journal of Photoenergy*

ADAMS, M., SKILLEN, N., MCCULLAGH, C., ROBERTSON, P.K.J., 2013. Development of a doped titania immobilised thin film multi tubular photoreactor. *Applied Catalysis B: Environmental,* 130−131(0), pp. 99-105.

AGARWAL, A., BHASKARWAR, A.N., 2007. Comparative simulation of falling-film and parallel-film reactors for photocatalytic production of hydrogen. *International Journal of Hydrogen Energy,* 32, pp. 2764-2775

AHMED, N., SHIBATA, Y., TANIGUCHI, T., IZUMI, Y., 2011. Photocatalytic conversion of carbon dioxide into methanol using zinc−copper−M (III) (M = aluminum, gallium) layered double hydroxides. *Journal of Catalysis,* 279(1), pp. 123-135.

ALEXIADIS, A., MAZZARINO, I., 2005. Design guidelines for fixed-bed photocatalytic reactors. *Chemical Engineering and Processing: Process Intensification,* 44(4), pp. 453-459

ALONSO-TELLEZ, A., MASSON, R., ROBERT, D., KELLER, N., KELLER, V., 2012. Comparison of Hombikat UV100 and P25 TiO_2 performance in gas-phase photocatalytic oxidation reactions. *Journal of Photochemistry and Photobiology A: Chemistry,* 250(0), pp. 58-65

AL-QARADAWI, S., SALMAN, S.R., 2002. Photocatalytic degradation of methyl orange as a model compound. *Journal of Photochemistry and Photobiology A: Chemistry,* 148(1−3), pp. 161-168

AMANO, F., NOGAMI, K., OHTANI, B., 2010. Correlation between Surface Area and Photocatalytic Activity for Acetaldehyde Decomposition over Bismuth Tungstate Particles with a Hierarchical Structure. *Langmuir,* 26, pp. 7174-7180

AMEEN, S., SEO, H., SHAHEER AKHTAR, M., SHIN, H.S., 2012. Novel graphene/polyaniline nanocomposites and its photocatalytic activity toward the degradation of rose Bengal dye. *Chemical Engineering Journal,* 210(0), pp. 220-228.

ANPO, M., CHIBA, K., 1992. Photocatalytic reduction of CO2 on anchored titanium oxide catalysts. *Journal of Molecular Catalysis,* 74(1-3), pp. 207-212

ANPO, M., YAMASHITA, H., ICHIHASHI, Y., EHARA, S., 1995. Photocatalytic reduction of CO2 with H2O on various titanium oxide catalysts. *Journal of Electroanalytical Chemistry,* 396(1–2), pp. 21-26.

ANPO, M., YAMASHITA, H., IKEUE, K., FUJII, Y., ZHANG, S.G., ICHIHASHI, Y., PARK, D.R., SUZUKI, Y., KOYANO, K., TATSUMI, T., 1998. Photocatalytic reduction of CO2 with H2O on Ti-MCM-41 and Ti-MCM-48 mesoporous zeolite catalysts. *Catalysis Today,* 44(1–4), pp. 327-332.

ASSADI, A.A., BOUZAZA, A., WOLBERT, D., 2012. Photocatalytic oxidation of trimethylamine and isovaleraldehyde in an annular reactor: Influence of the mass transfer and the relative humidity. *Journal of Photochemistry and Photobiology A: Chemistry,* 236(0), pp. 61-69.

BAIOCCHI, C., BRUSSINO, M.C., PRAMAURO, E., PREVOT, A.B., PALMISANO, L., MARCI, G., 2002. Characterization of methyl orange and its photocatalytic degradation products by HPLC/UV–VIS diode array and atmospheric pressure ionization quadruple ion trap mass spectrometry. *International Journal of Mass Spectrometry,* 214, pp. 247-256.

BALLARI, M.D.L.M., BRANDI, R., ALFANO, O., CASSANO, A., 2008. Mass transfer limitations in photocatalytic reactors employing titanium dioxide suspensions: I. Concentration profiles in the bulk. *Chemical Engineering Journal,* 136(1), pp. 50-65.

BARKA, N., ASSABBANE, A., NOUNAH, A., ICHOU, Y.A., 2008. Photocatalytic degradation of indigo carmine in aqueous solution by TiO2 coated non-woven fibres. *Journal of hazardous materials,* 152(3), pp. 1054-1059.

BENZ, V., MÜLLER, M., BAHNEMANN, D.W., WEICHGREBE, D., BREHM, M., 1996. Reaktoren für die photokatalytische Abwasserreinigung mit Stegmehrfachplatten als Solarelemente. *Deutsche Offenlegungsschrift (DE),* 195(14), pp. 372.

BIAN, Z., WANG, H., FU, W., LI, L., DING, A., 2012. Two bifunctional RuII/ReI photocatalysts for CO2 reduction: A spectroscopic, photocatalytic, and computational study. *Polyhedron,* 32(1), pp. 78-85.

BICKLEY, R.I., SLATER, M.J., WANG, W.-. 2005. Engineering Development of a Photocatalytic Reactor for Waste Water Treatment. *Process Safety and Environmental Protection,* 83(3), pp. 205-216

BONVIN, D., 1998. Optimal operation of batch reactors—a personal view. *Journal of Process Control,* 8(5–6), pp. 355-368

BOUCHY, A., ZAHRAA, O., 2003. Photocatalytic Reactors. *International Journal of Photoenergy,* 05, pp. 191-7

CAMERA-RODA, G., SANTARELLI, F., MARTIN, C.A., 2005. Design of photocatalytic reactors made easy by considering the photons as immaterial reactants. *Solar Energy,* 79(4), pp. 343-352

CASSANO, A.E., ALFANO, O.M., 2000. Reaction engineering of suspended solid heterogeneous photocatalytic reactors. *Catalysis Today,* 58(2–3), pp. 167-197

ČERNIGOJ, U., ŠTANGAR, U.L., TREBŠE, P., 2007. Evaluation of a novel Carberry type photoreactor for the degradation of organic pollutants in water. *Journal of Photochemistry and Photobiology A: Chemistry,* 188(2-3), pp. 169-176

CHAN, A.H.C., CHAN, C.K., BARFORD, J.P., PORTER, J.F., 2003. Solar photocatalytic thin film cascade reactor for treatment of benzoic acid containing wastewater. *Water research,* 37(5), pp. 1125-1135.

CHATTI, R., RAYALU, S.S., DUBEY, N., LABHSETWAR, N., DEVOTTA, S., 2007. Solar-based photoreduction of methyl orange using zeolite supported photocatalytic materials. *Solar Energy Materials and Solar Cells,* 91(2–3), pp. 180-190.

CHEN, J., WANG, D., ZHU, M., GAO, C., 2006. Study on degradation of methyl orange using pelagite as photocatalyst. *Journal of hazardous materials,* 138(1), pp. 182-186.

CHEN, L., TSAI, F., HUANG, C., 2005. Photocatalytic decolorization of methyl orange in aqueous medium of TiO2 and Ag–TiO2 immobilized on γ-Al2O3. *Journal of Photochemistry and Photobiology A: Chemistry,* 170(1), pp. 7-14

CHEN, T., ZHENG, Y., LIN, J., CHEN, G., 2008. Study on the Photocatalytic Degradation of Methyl Orange in Water Using Ag/ZnO as Catalyst by Liquid Chromatography Electrospray Ionization Ion-Trap Mass Spectrometry. *Journal of the American Society for Mass Spectrometry,* 19(7), pp. 997-1003.

CHEN, Y., DIONYSIOU, D.D., 2006. Correlation of structural properties and film thickness to photocatalytic activity of thick TiO2 films coated on stainless steel. *Applied Catalysis B: Environmental,* 69(1–2), pp. 24-33

CHEN, Y., DIONYSIOU, D.D., 2006. TiO2 photocatalytic films on stainless steel: The role of Degussa P-25 in modified sol–gel methods. *Applied Catalysis B: Environmental,* 62(3–4), pp. 255-264

CHIARI, L., ZECCA, A., 2011. Constraints of fossil fuels depletion on global warming projections. *Energy Policy,* 39(9), pp. 5026-5034

CHIN, S.S., LIM, T.M., CHIANG, K., FANE, A.G., 2007. Hybrid low-pressure submerged membrane photoreactor for the removal of bisphenol. *Desalination,* 202, pp. 253-261.

CHONG, M.N., LEI, S., JIN, B., SAINT, C., CHOW, C.W.K., 2009. Optimisation of an annular photoreactor process for degradation of Congo Red using a newly synthesized titania impregnated kaolinite nano-photocatalyst. *Separation and Purification Technology,* 67(3), pp. 355-363.

CUI, W., LIU, L., MA, S., LIANG, Y., ZHANG, Z., 2012. CdS-sensitized K2La2Ti3O10 composite: A new photocatalyst for hydrogen evolution under visible light irradiation. *Catalysis Today,* (0).

CURCÓ, D., MALATO, S., BLANCO, J., GIMÉNEZ, J., 1996. Photocatalysis and radiation absorption in a solar plant. *Solar Energy Materials and Solar Cells,* 44(2), pp. 199-217.

CUSHNIE, T.P.T., ROBERTSON, P.K.J., OFFICER, S., POLLARD, P.M., MCCULLAGH, C., ROBERTSON, J.M.C., 2010. Photobactericidal effects of TiO2 thin films at low temperatures -a preliminary study. *Journal of Photochemistry and Photobiology A: Chemistry,* 216, pp. 290-294.

DANION, A., DISDIER, J., GUILLARD, C., JAFFREZIC-RENAULT, N., 2007. Malic acid photocatalytic degradation using a TiO2-coated optical fiber reactor. *Journal of Photochemistry and Photobiology A: Chemistry,* 190(1), pp. 135-140.

DANION, A., DISDIER, J., GUILLARD, C., PAISSE, O., JAFFREZIC-RENAULT, N., 2006. Photocatalytic degradation of imidazolinone fungicide in TiO2-coated optical fibre reactor. *Applied Catalysis B: Environmental,* 62(3-4), pp. 274-281.

DE LASA, H.I., SERRANO, B., SALAICES, M., 2005. *Photocatalytic Reaction Engineering.* 1st ed. New York, USA: Springer.

MEADOWS, D.H., MEADOWS, D.L., RANDERS, J., BEHRENS III, W.W., 1972. *The Limits to Growth*. 1st ed. London, UK. Universe Books (New York) and Earth Island Limited (London)

DE_RICHTER, R., CAILLOL, S., 2011. Fighting global warming: The potential of photocatalysis against CO2, CH4, N2O, CFCs, tropospheric O3, BC and other major contributors to climate change. *Journal of Photochemistry and Photobiology C: Photochemistry Reviews,* 12(1), pp. 1-19.

DE_RICHTER, R.K., MING, T., CAILLOL, S., 2013. Fighting global warming by photocatalytic reduction of CO2 using giant photocatalytic reactors. *Renewable and Sustainable Energy Reviews,* 19(0), pp. 82-106.

DELUCCHI, M.A., JACOBSON, M.Z., 2011. Providing all global energy with wind, water, and solar power, Part II: Reliability, system and transmission costs, and policies. *Energy Policy,* 39(3), pp. 1170-1190.

DIBBLE, L.A., RAUPP, G.B., 1992. Fluidized-bed photocatalytic oxidation of trichloroethylene in contaminated air streams. *Environmental Science and Technology,* 26, pp. 492-495.

DIJKSTRA, M.F.J., BUWALDA, H., DE JONG, A.W.F., MICHORIUS, A., WINKELMAN, J.G.M., BEENACKERS, A.A.C.M., 2001. Experimental comparison of three reactor designs for photocatalytic water purification. *Chemical Engineering Science,* 56(2), pp. 547-555.

DILLERT, R., CASSANO, A.E., GOSLICH, R., BAHNEMANN, D.W., 1999. Large scale studies in solar catalytic wastewater treatment. *Catalysis Today,* 54, pp. 367-282.

DILLERT, R., STÖTZNER, J., ENGEL, A., BAHNEMANN, D.W., 2012. Influence of inlet concentration and light intensity on the photocatalytic oxidation of nitrogen(II) oxide at the surface of Aeroxide® TiO2 P25. *Journal of hazardous materials,* 211–212(0), pp. 240-246.

EDIGER, V.Ş., HOŞGÖR, E., SÜRMELI, A.N., TATLIDIL, H., 2007. Fossil fuel sustainability index: An application of resource management. *Energy Policy,* 35(5), pp. 2969-2977.

ERDEI, L., ARECRACHAKUL, N., VIGNESWARAN, S., 2008. A combined photocatalytic slurry reactor-immersed membrane module system for advanced wastewater treatment. *Separation and Purification Technology,* 62, pp. 382-388.

ERDEMOĞLU, S., AKSU, S.K., SAYILKAN, F., İZGI, B., ASILTÜRK, M., SAYILKAN, H., FRIMMEL, F., GÜÇER, Ş., 2008. Photocatalytic degradation of Congo Red by hydrothermally synthesized nanocrystalline TiO2 and identification of degradation products by LC–MS. *Journal of hazardous materials,* 155(3), pp. 469-476.

FAN, W., ZHOU, Z., XU, W., SHI, Z., REN, F., MA, H., HUANG, S., 2010. Preparation of ZnIn2S4/fluoropolymer fiber composites and its photocatalytic H2 evolution from splitting of water using Xe lamp irradiation. *International Journal of Hydrogen Energy,* 35(13), pp. 6525-6530.

FOSTER, N.R., BASSITI, K., 2008. Photocatalytic reactor European Patent. *World Patent,* .

FRIEDLINGSTEIN, P., HOUGHTON, R.A., MARLAND, G., HACKLER, J., BODEN, T.A., CONWAY, T.J., CANADELL, J.G., RAUPACH, M.R., CIAIS, P., LE QUERE, C., 2010. Corresponce: Update on CO2 emissions. *Nature Geoscience,* 3, pp. 811-812.

FU, J., JI, M., ZHAO, Y., WANG, L., 2006. Kinetics of aqueous photocatalytic oxidation of fulvic acids in a photocatalysis-ultrafiltration reactor (PUR). *Separation and Purification Technology,* 50, pp. 107-113.

GAO, H., SI, C., ZHOU, J., LIU, G., 2011. Sound assisted photocatalytic degradation of formaldehyde in fluidized bed reactor. *Journal of the Taiwan Institute of Chemical Engineers,* 42(1), pp. 108-113.

GERNJAK, W., MALDONADO, M.I., MALATO, S., CÁCERES, J., KRUTZLER, T., GLASER, A., BAUER, R., 2004. Pilot-plant treatment of olive mill wastewater

(OMW) by solar TiO2 photocatalysis and solar photo-Fenton. *Solar Energy,* 77(5), pp. 567-572.

GIROD, B., WIEK, A., MIEG, H., HULME, M., 2009. The evolution of the IPCC's emissions scenarios. *Environmental Science & Policy,* 12(2), pp. 103-118.

GOSLICH, R., DILLERT, R., BAHNEMANN, D., 1997. Solar water treatment: Principles and reactors. *Water Science and Technology,* 35(4), pp. 137-148

GSCHNEIDNER, K.,A., EYRING, L., eds, 1999. *Handbook on the Physics and Chemistry of Rare Earths, Volume 26.* Holland: Elsevier.

GUNLAZUARDI, J., LINDU, W.A., 2005. Photocatalytic degradation of pentachlorophenol in aqueous solution employing immobilized TiO2 supported on titanium metal. *Journal of Photochemistry and Photobiology A: Chemistry,* 173(1), pp. 51-55

GUO, C., XU, J., HE, Y., ZHANG, Y., WANG, Y., 2011. Photodegradation of rhodamine B and methyl orange over one-dimensional TiO2 catalysts under simulated solar irradiation. *Applied Surface Science,* 257(8), pp. 3798-3803.

GUST, D.E.A., 2009. *Solar Fuels via Artificial Photosynthesis.* American Chemical Society.

HAJIESMAILI, S., JOSSET, S., BÉGIN, D., PHAM-HUU, C., KELLER, N., KELLER, V., 2010. 3D solid carbon foam-based photocatalytic materials for vapor phase flow-through structured photoreactors. *Applied Catalysis A: General,* 382(1), pp. 122-130.

HALMANN, M., 1978. Photoelectrochemical reduction of aqueous carbon dioxide on p-type gallium phosphide in liquid junction solar cells. *Nature,* 275, pp. 115-116.

HAN, H., BAI, R., 2011. The effect of thickness of photocatalyst film immbolised on a buoyant substrate on the degradation of methyl orange dye in aqueous solutions under different light irradiations. *Industrial and Engineering Chemistry Research,*

HAO, X., LI, H., ZHANG, Z., FAN, C., LIU, S., SUN, Y., 2009. Modeling and experimentation of a novel labyrinth bubble photoreactor for degradation of organic pollutant. *Chemical Engineering Research and Design,* 87(12), pp. 1604-1611.

HEMMINGER, J.C., CARR, R., SOMORJAI, G.A., 1978. The photoassisted reaction of gaseous water and carbon dioxide adsorbed on the SrTiO3 (III) crystal face to form methane. *Chemical Physics Letters,* 57, pp. 100-104.

HOEL, M., KVERNDOKK, S., 1996. Depletion of fossil fuels and the impacts of global warming. *Resource and Energy Economics,* 18(2), pp. 115-136

HOFFMANN, M.R., MARTIN, S.T., CHOI, W., BAHNERMANN, D.W., 1995. Environemental Applications of Semiconductor Photocatalysis. *Chemical Reviews,* 95(1), pp. 69-96.

HOUAS, A., LACHHEB, H., KSIBI, M., ELALOUI, E., GUILLARD, C., HERRMANN, J., 2001. Photocatalytic degradation pathway of methylene blue in water. *Applied Catalysis B: Environmental,* 31(2), pp. 145-157.

IMOBERDORF, G.E., CASSANO, A.E., IRAZOQUI, H.A., ALFANO, O.M., 2007. Optimal design and modeling of annular photocatalytic wall reactors. *Catalysis Today,* 129(1–2), pp. 118-126.

INDRAKANTI, V.P., KUBOCKI, J.D., SCHOBERT, H.H., 2009. Photoinduced activation of CO2 on Ti-based heterogenous catalysts: Current state, chemical physics-based insights and outlook. *Energy and Environmental Science,* 2, pp. 745-758

INOUE, T., FUJISHIMA, A., KONISHI, S., HONDA, K., 1979. Photoelectrocatalytic reduction of carbon dioxide in aqueous suspensions of semiconductor powders. *Nature,* 277, pp. 637-638.

JEON, J., KIM, S., LIM, T., LEE, D., 2005. Degradation of trichloroethylene by photocatalysis in an internally circulating slurry bubble column reactor. *Chemosphere,* 60, pp. 1162-1168.

JEONG, H., KIM, T., KIM, D., KIM, K., 2006. Hydrogen production by the photocatalytic overall water splitting on : Effect of preparation method. *International Journal of Hydrogen Energy,* 31(9), pp. 1142-1146.

JI, Z., CALLAHAN JR., D.M., ISMAIL, M.N., WARZYWODA, J., SACCO JR., A., 2011. Development and characterization of a titanosilicate ETS-10-coated optical fiber reactor towards the photodegradation of methylene blue. *Journal of Photochemistry and Photobiology A: Chemistry,* 217(1), pp. 22-28.

JING, D., GUO, L., ZHAO, L., ZHANG, X., LIU, H., LI, M., SHEN, S., LIU, G., HU, X., ZHANG, X., ZHANG, K., MA, L., GUO, P., 2010. Efficient solar hydrogen production by photocatalytic water splitting: From fundamental study to pilot demonstration. *International Journal of Hydrogen Energy,* 35(13), pp. 7087-7097.

JING, D., LIU, H., ZHANG, X., ZHAO, L., GUO, L., 2009. Photocatalytic hydrogen production under direct solar light in a CPC based solar reactor: Reactor design and preliminary results. *Energy Conversion and Management,* 50(12), pp. 2919-2926.

JOSSET, S., HAJIESMAILI, S., BEGIN, D., EDOUARD, D., PHAM-HUU, C., LETT, M., KELLER, N., KELLER, V., 2010. UV-A photocatalytic treatment of Legionella pneumophila bacteria contaminated airflows through three-dimensional solid foam structured photocatalytic reactors. *Journal of hazardous materials,* 175(1–3), pp. 372-381.

KANADE, K.G., BAEG, J., KALE, B.B., MI LEE, S., MOON, S., KONG, K., 2007. Rose-red color oxynitride : A visible light photocatalyst to hydrogen production. *International Journal of Hydrogen Energy,* 32(18), pp. 4678-4684.

KANECO, S., KURIMOTO, H., OHTA, K., MIZUNO, T., SAJI, A., 1997. Photocatalytic reduction of CO2 using TiO2 powders in liquid CO2 medium. *Journal of Photochemistry and Photobiology A: Chemistry,* 109(1), pp. 59-63.

KANECO, S., KURIMOTO, H., SHIMIZU, Y., OHTA, K., MIZUNO, T., 1999. Photocatalytic reduction of CO2 using TiO2 powders in supercritical fluid CO2. *Energy,* 24(1), pp. 21-30.

KANG, M., 2003. Synthesis of Fe/TiO2 photocatalyst with nanometer size by solvothermal method and the effect of H2O addition on structural stability and photodecomposition of methanol. *Journal of Molecular Catalysis A: Chemical,* 197(1-2), pp. 173-183

KASANEN, J., SALSTELA, J., SUVANTO, M., PAKKANEN, T.T., 2011. Photocatalytic degradation of methylene blue in water solution by multilayer TiO2 coating on HDPE. *Applied Surface Science,* 258(5), pp. 1738-1743.

KATO, H., ASAKURA, H., KUDO, A., 2003. Highly efficient water splitting into H2 and O2 over lanthanum-doped NaTaO3 photocatalysts with high crystallinity and surface nanostructure. *Journal of American Chemists Society,* 10, pp. 3082-3089

KHAN, M.M.T., CHATTERJEE, D, KRISHNARATNAM, M., BALA, M., Photosensitized reduction of N_2 by $RuII(bipy)_3^{2+}$ adsorbed on the surface of $Pt/TiO_2/RuO_2$ semiconductor particulate system containing RuIII-EDTA complex and L-ascorbic acid. *Journal of Molecular Catalysis* 72: 13-18 (1992).

KHAN, Z., QURESHI, M., 2012. Tantalum doped BaZrO3 for efficient photocatalytic hydrogen generation by water splitting. *Catalysis Communications,* 28(0), pp. 82-85

KIM, J.Y., KIM, C.S., CHANG, H.K., KIM, T.O., 2011. Synthesis and characterization of N-doped TiO2/ZrO2 visible light photocatalysts. *Advanced Powder Technology,* 22(3), pp. 443-448.

KOCA, A., ŞAHIN, M., 2002. Photocatalytic hydrogen production by direct sun light from sulfide/sulfite solution. *International Journal of Hydrogen Energy,* 27(4), pp. 363-367

KOČÍ, K., MATĚJKA, V., KOVÁŘ, P., LACNÝ, Z., OBALOVÁ, L., 2011. Comparison of the pure TiO2 and kaolinite/TiO2 composite as catalyst for CO2 photocatalytic reduction. *Catalysis Today,* 161(1), pp. 105-109.

KOČÍ, K., MATĚJŮ, K., OBALOVÁ, L., KREJČÍKOVÁ, S., LACNÝ, Z., PLACHÁ, D., ČAPEK, L., HOSPODKOVÁ, A., ŠOLCOVÁ, O., 2010. Effect of silver doping on the TiO2 for photocatalytic reduction of CO2. *Applied Catalysis B: Environmental,* 96(3–4), pp. 239-244.

KOČÍ, K., OBALOVÁ, L., MATĚJOVÁ, L., PLACHÁ, D., LACNÝ, Z., JIRKOVSKÝ, J., ŠOLCOVÁ, O., 2009. Effect of TiO2 particle size on the photocatalytic reduction of CO2. *Applied Catalysis B: Environmental,* 89(3–4), pp. 494-502.

KOČÍ, K., RELI, M., KOZÁK, O., LACNÝ, Z., PLACHÁ, D., PRAUS, P., OBALOVÁ, L., 2011. Influence of reactor geometry on the yield of CO2 photocatalytic reduction. *Catalysis Today,* 176(1), pp. 212-214.

KOHNO, Y., HAYASHI, H., TAKENAKA, S., TANAKA*, T., FUNABIKI, T., YOSHIDA, S., 1999. Photo-enhanced reduction of carbon dioxide with hydrogen over Rh/TiO2. *Journal of Photochemistry and Photobiology A: Chemistry,* 126(1–3), pp. 117-123.

KOMAI, Y., OKITSU, K., NISHIMURA, R., OHTSU, N., MIYAMOTO, G., FURUHARA, T., SEMBOSHI, S., MIZUKOSHI, Y., MASAHASHI, N., 2011. Visible light response of nitrogen and sulfur co-doped TiO2 photocatalysts fabricated by anodic oxidation. *Catalysis Today,* 164(1), pp. 399-403.

KUO, H.P., WU, C.T., HSU, R.C., 2009. Continuous reduction of toluene vapors from the contaminated gas stream in a fluidised bed photoreactor. *Powder Technology,* 195(1), pp. 50-56.

LEE, D., CHEN, H., CHEN, Y., 2012. Photocatalytic reduction of carbon dioxide with water using InNbO4 catalyst with NiO and Co3O4 cocatalysts. *Journal of Physics and Chemistry of Solids.*

LEE, D., KIM, S., CHO, I., KIM, S., KIM, S., 2004. Photocatalytic oxidation of microcystin-LR in afluidized bed reactor having TiO$_2$-coated activated carbon. *Separation and Purification Technology,* 34(1-3), pp. 59-66.

LEE, J., LEE, J., 2003. *Review of advances in biological CO$_2$ mitigation technology.* The Korean Society for Biotechnology and Bioengineering.

LEE, J.H., NAM, W., KANG, M., HAN, G.Y., YOON, K.J., KIM, M., OGINO, K., MIYATA, S., CHOUNG, S., 2003. Design of two types of fluidized photo reactors and their photo-catalytic performances for degradation of methyl orange. *Applied Catalysis A: General,* 244(1), pp. 49-57.

LEE, S-K, MILLS, A, 2003. Novel photochemistry of *leuco*-Methylene Blue. *Chemistry Communications,* , pp. 2366-2

LEFFLER, B., *Stainless: Stainless steels and their property.*

LEGGETT, L.M.W., BALL, D.A., 2012. The implication for climate change and peak fossil fuel of the continuation of the current trend in wind and solar energy production. *Energy Policy,* 41(0), pp. 610-617

LI PUMA, G., YUE, L.P., 2001. The modeling of a fountain photocatalytic reactor with a parabolic profile. *Chemical Engineering Science,* 56, pp. 721-726

LI PUMA, G., YUE, P.L., 1999. Enhanced Photocatalysis in a Pilot Laminar Falling Film Slurry Reactor. *Industrial and Engineering Chemistry Research,* 38, pp. 3246-3254

LI, K., MARTIN, D., TANG, J., 2011. Conversion of Solar Energy to Fuels by Inorganic Heterogeneous Systems. *Chinese Journal of Catalysis,* 32(6), pp. 879-890

LI, W., LI, J., WANG, X., CHEN, Q., 2012. Preparation and water-splitting photocatalytic behavior of S-doped WO3. *Applied Surface Science,* (0)

LI, X., LIU, H., LUO, D., LI, J., HUANG, Y., LI, H., FANG, Y., XU, Y., ZHU, L., 2012. Adsorption of CO2 on heterostructure CdS(Bi2S3)/TiO2 nanotube photocatalysts and their photocatalytic activities in the reduction of CO2 to methanol under visible light irradiation. *Chemical Engineering Journal,* 180(0), pp. 151-158.

LI, X., PAN, H., LI, W., ZHUANG, Z., 2012. Photocatalytic reduction of CO2 to methane over HNb3O8 nanobelts. *Applied Catalysis A: General,* 413–414(0), pp. 103-108.

LI, X., ZHUANG, Z., LI, W., PAN, H., 2012. Photocatalytic reduction of CO2 over noble metal-loaded and nitrogen-doped mesoporous TiO2. *Applied Catalysis A: General,* 429–430(0), pp. 31-38.

LI, Y., WANG, W., ZHAN, Z., WOO, M., WU, C., BISWAS, P., 2010. Photocatalytic reduction of CO2 with H2O on mesoporous silica supported Cu/TiO2 catalysts. *Applied Catalysis B: Environmental,* 100(1–2), pp. 386-392.

LI, Y., WU, J., HUANG, Y., HUANG, M., LIN, J., 2009. Photocatalytic water splitting on new layered perovskite A2.33Sr0.67Nb5O14.335 (A = K, H). *International Journal of Hydrogen Energy,* 34(19), pp. 7927-7933.

LIANG, H.C., LI, X.Z., NOWOTNY, J., 2010. Photocatalytic Properties of TiO2 Nanotubes. *Solid State Phenomena,* 162, pp. 295-328

LIAO, C., HUANG, C., WU, J.C.S., 2012. Novel dual-layer photoelectrode prepared by RF magnetron sputtering for photocatalytic water splitting. *International Journal of Hydrogen Energy,* 37(16), pp. 11632-11639

LIM, T.H., KIM, S.D., 2005. Photocatalytic degradation of trichloroethylene (TCE) over TiO2/silica gel in a circulating fluidized bed (CFB) photoreactor. *Chemical Engineering and Processing: Process Intensification,* 44(2), pp. 327-334

LIM, T.H., 2000. Photocatalytic decomposition of NO by TiO2 particles. *Journal of Photochemistry and Photobiology A: Chemistry,* 134(3), pp. 209-217

LIN, H., CHANG, Y., 2010. Photocatalytic water splitting for hydrogen production on Au/KTiNbO5. *International Journal of Hydrogen Energy,* 35(16), pp. 8463-8471

LING, C.M., MOHAMED, A.R., BHATIA, S., 2004. Performance of photocatalytic reactors using immobilized TiO2 film for the degradation of phenol and methylene blue dye present in water stream. *Chemosphere,* 57(7), pp. 547-554.

LINKOUS, C.A., MINGO, T.E., MURADOV, N.Z., 1994. Aspects of solar hydrogen production from hydrogen sulfide using semiconductor particulates. *International Journal of Hydrogen Energy,* 19(3), pp. 203-208

LINKOUS, C.A., MURADOV, N.Z., RAMSER, S.N., 1995. Consideration of reactor design for solar hydrogen production from hydrogen sulfide using semiconductor particulates. *International Journal of Hydrogen Energy,* 20(9), pp. 701-709

LIU, B., TORIMOTO, T., YONEYAMA, H., 1998. Photocatalytic reduction of CO2 using surface-modified CdS photocatalysts in organic solvents. *Journal of Photochemistry and Photobiology A: Chemistry,* 113(1), pp. 93-97

LIU, G., HOIVIK, N., WANG, K., JAKOBSEN, H., 2012. Engineering TiO2 nanomaterials for CO2 conversion/solar fuels. *Solar Energy Materials and Solar Cells,* 105(0), pp. 53-68.

LIU, S., SYU, H., 2012. One-step fabrication of N-doped mesoporous TiO2 nanoparticles by self-assembly for photocatalytic water splitting under visible light. *Applied Energy,* (0),

LIU, W., JI, M., CHEN, S., 2011. Preparation, characterization and activity evaluation of Ag2Mo4O13 photocatalyst. *Journal of hazardous materials,* 186(2-3), pp. 2001-2008

LIU, Z., SHEN, S., GUO, L., 2012. Study on photocatalytic performance for hydrogen evolution over CdS/M-MCM-41 (M = Zr, Ti) composite photocatalysts under visible light illumination. *International Journal of Hydrogen Energy,* 37(1), pp. 816-821

LO, C., HUANG, C., LIAO, C., WU, J.C.S., 2010. Novel twin reactor for separate evolution of hydrogen and oxygen in photocatalytic water splitting. *International Journal of Hydrogen Energy,* 35(4), pp. 1523-1529.

LO, C., HUNG, C., YUAN, C., WU, J., 2007. Photoreduction of carbon dioxide with H2 and H2O over TiO2 and ZrO2 in a circulated photocatalytic reactor. *Solar Energy Materials and Solar Cells,* 91(19), pp. 1765-1774.

MAEDA, K., 2011. Photocatalytic water splitting using semiconductor particles: History and recent developments. *Journal of Photochemistry and Photobiology C: Photochemistry Reviews,* 12(4), pp. 237-268

MAHMOODI, N.M., ARAMI, M., LIMAEE, N.Y., 2006. Photocatalytic degradation of triazinic ring-containing azo dye (Reactive Red 198) by using immobilized TiO2 photoreactor: Bench scale study. *Journal of hazardous materials,* 133(1–3), pp. 113-118

MAJI, S.K., DUTTA, A.K., SRIVASTAVA, D.N., PAUL, P., MONDAL, A., ADHIKARY, B., 2011. Effective photocatalytic degradation of organic pollutant by ZnS nanocrystals synthesized via thermal decomposition of single-source precursor. *Polyhedron,* 30(15), pp. 2493-2498.

MAJI, S.K., MUKHERJEE, N., MONDAL, A., ADHIKARY, B., 2012. Synthesis, characterization and photocatalytic activity of α-Fe2O3 nanoparticles. *Polyhedron,* 33(1), pp. 145-149.

MALATO, S., BLANCO, J., VIDAL, A., RICHTER, C., 2002. Photocatalysis with solar energy at a pilot-plant scale: an overview. *Applied Catalysis B: Environmental,* 37(1), pp. 1-15.

MAO, J., PENG, T., ZHANG, X., LI, K., ZAN, L., 2012. Selective methanol production from photocatalytic reduction of CO2 on BiVO4 under visible light irradiation. *Catalysis Communications,* 28(0), pp. 38-41.

MASCOLO, G., COMPARELLI, R., CURRI, M.L., LOVECCHIO, G., LOPEZ, A., AGOSTIANO, A., 2007. Photocatalytic degradation of methyl red by TiO2: Comparison of the efficiency of immobilized nanoparticles versus conventional suspended catalyst. *Journal of hazardous materials,* 142(1–2), pp. 130-137.

MCCULLAGH, C., ROBERTSON, P.K.J., ADAMS, M., POLLARD, P.M., MOHAMMED, A., 2010. Development of a slurry continuous flow reactor for photocatalytic treatment of industrial waste water. *Journal of Photochemistry and Photobiology A: Chemistry,* 211(1), pp. 42-46.

MCCULLAGH, C., SKILLEN, N., ADAMS, M., ROBERTSON, P.K.J., 2011. Photocatalytic Reactors for Remediation: A Review. *Journal of Chemical Technology and Biotechnology,* 86(8), pp. 1002-1017.

MEHRVAR, M., ANDERSON, W.A., MOO-YOUNG, M., 2002. Preliminary analysis of a tellerette packed-bed photocatalytic reactor. *Advances in Environmental Research,* 6(4), pp. 411-418.

MELGHIT, K., AL-RABANIAH, S.S., 2006. Photodegradation of Congo red under sunlight catalysed by nanorod rutile TiO2. *Journal of Photochemistry and Photobiology A: Chemistry,* 184(3), pp. 331-334

MELGHIT, K., AL-RUBAEI, M.S., AL-AMRI, I., 2006. Photodegradation enhancement of Congo red aqueous solution using a mixture of SnO2·xH2O gel/ZnO powder. *Journal of Photochemistry and Photobiology A: Chemistry,* 181(2–3), pp. 137-141

MENG, N.C., JIN, B., ZHU, H.Y., CHOW, C.W.K., SAINT, C., 2009. Application of H-titanate nanofibers for degradation of Congo Red in an annular slurry photoreactor. *Chemical Engineering Journal,* 150, pp. 49-54.

MIDILLI, A., DINCER, I., 2008. Hydrogen as a renewable and sustainable solution in reducing global fossil fuel consumption. *International Journal of Hydrogen Energy,* 33(16), pp. 4209-4222

MIKKELSEN, M., JORGENSEN, M., KREBS, F.C., 2009. *The teraton challenge. A review of fixation and transformation of carbon dioxide.* - The Royal Society of Chemistry.

MILLS, A, WANG, J., 1999. Photobleeching of methylene blue sensitised by TiO_2: an ambiguous system? *Journal of Photochemistry and Photobiology A: Chemistry,* 127, pp. 123-11

MILLS, A., LE HUNTE, S., 1997. An overview of semiconductor photocatalysis. *Journal of Photochemistry and Photobiology A: Chemistry,* 108(1), pp. 1-35

MILLS, A., 2012. An overview of the methylene blue ISO test for assessing the activities of photocatalytic films. *Applied Catalysis B: Environmental,* (0),

MILLS, A., HILL, G., BHOPAL, S., PARKIN, I.P., O'NEILL, S.A., 2003. Thick titanium dioxide films for semiconductor photocatalysis. *Journal of Photochemistry and Photobiology A: Chemistry,* 160, pp. 185-194.

MIN, Y., ZHANG, K., CHEN, Y., ZHANG, Y., 2011. Synthesis of novel visible light responding vanadate/TiO2 heterostructure photocatalysts for application of organic pollutants. *Chemical Engineering Journal,* 175(0), pp. 76-83.

MINERO, C., PELIZZETTI, E., MALATO, S., BLANCO, J., 1993. Large solar plant photocatalytic water decontamination: Degradation of pentachlorophenol. *Chemosphere,* 26(12), pp. 2103-2119.

MIZUKOSHI, Y., MAKISE, Y., SHUTO, T., HU, J., TOMINAGA, A., SHIRONITA, S., TANABE, S., 2007. Immobilization of noble metal nanoparticles on the surface of TiO2 by the sonochemical method: Photocatalytic production of hydrogen from an aqueous solution of ethanol. *Ultrasonics sonochemistry,* 14(3), pp. 387-392.

MORI, K., YAMASHITA, H., ANPO, M., 2012. Photocatalytic reduction of CO2 with H2O on various titanium oxide photocatalysts. *Royal Society of Chemistry Advances,* 2(8), pp. 3165-3172

MOUNIRA., M., 1996. Mitigation of CO2 greenhouse effect. Combined disposal and utilisation by photocatalysis. *Energy Conversion and Management,* 37(6–8), pp. 1345-1350

MUKHERJEE, P.S., RAY, A.K., 1999. Major Challenges in the desgn of large scale photocatalytic reactors for water treatment. *Chemical Engineering Technology,* 22(3), pp. 253-260.

NADA M. DIMITRIJEVIC, BAIJU K. VIJAYAN, OLEG G. POLUEKTOV, TIJANA RAJH, KIMBERLY A. GRAY, HAIYING HE,, PETER ZAPOL, 2011. Role of Water and Carbonates in Photocatalytic Transformation of CO2 to CH4 on Titania. *Journal of The American Chemical Society,* 133, pp. 3964-3971

NAKATA, K., FUJISHIMA, A., 2012. TiO2 photocatalysis: Design and applications. *Journal of Photochemistry and Photobiology C: Photochemistry Reviews,* 13(3), pp. 169-189

NAM, W., KIM, J., HAN, G., 2002. Photocatalytic oxidation of methyl orange in a three-phase fluidized bed reactor. *Chemosphere,* 47(9), pp. 1019-1024

NATARAJAN, K., NATARAJAN, T.S., BAJAJ, H.C., TAYADE, R.J., 2011. Photocatalytic reactor based on UV-LED/TiO2 coated quartz tube for degradation of dyes. *Chemical Engineering Journal,* 178(0), pp. 40-49.

NELSON, R.J., FLAKKER, C.L., MUGGLI, D.S., 2007. Photocatalytic oxidation of methanol using titania-based fluidized beds. *Applied Catalysis B: Environmental,* 69(3-4), pp. 189-195

NGUYEN, T-V, WU, J.C.S., 2008. Photoreduction of CO2 to fuels under sunlight using optical-fiber reactor. *Solar Energy Materials and Solar Cells* 92: 864-872.

NOGUEIRA, R.F.P., JARDIM, W.F., 1996. TiO2-fixed-bed reactors for water decontamination using solar light. *Solar Energy,* 56(5), pp. 471-477

OCHUMA, I.J., FISHWICK, R.P., WOOD, J., WINTERBOTTOM, J.M., 2007. Photocatalytic oxidation of 2,4,6-trichlorophenol in water using a cocurrent downflow contactor reactor (CDCR). *Journal of hazardous materials,* 144, pp. 627-633.

OHTANI, B., IWAI, K., NISHIMOTO, S., SATO, S., 1997. Role of platinum deposits on titanium (IV) oxide particles:structural and kinetic analyses of photocatalytic reaction in aqueous alcohol and amino acids solutions. *Journal of Physical Chemistry B,* 101, pp. 3349-3359.

OLIWENSTEIN, L., 2011. The Prodigal Sun. *Engineering and Science,* Spring/Summer, p. 32-35

OROZCO, S.L., ARANCIBIA-BULNES, C.A., SUÁREZ-PARRA, R., 2009. Radiation absorption and degradation of an azo dye in a hybrid photocatalytic reactor. *Chemical Engineering Science,* 64, pp. 2173-2185

OWEN, N.A., INDERWILDI, O.R., KING, D.A., 2010. The status of conventional world oil reserves—Hype or cause for concern? *Energy Policy,* 38(8), pp. 4743-4749.

PAZ, Y., 2012. Application of TiO_2 photocatalysis for air treatment: Patents' Overview. *Applied Catalysis B: Environmental,* 99(3-4), pp. 448-460

PECKNER, D., BERNSTEIN, I.M., 1977. *Handbook of Stainless Steels.* New York: McGraw-Hill Book Company.

PEILL, N., HOFFMANN, M., 1995. Development and Optimisation of TiO_2-Coated Fiber-Optic Cable Reactor: Photocatalytic Degradation of 4-Chlorophenol. *Environ. Sci. Techno.,* 29, pp. 2974-7

PHONTHAMMACHAI, N., GULARI, E., JAMIESON, A.M., WONGKASEMJIT, S., 2006. Photocatalytic membrane of a novel high surface area TiO2 synthesised

from titanium triisopropanolamine precursor. *Applied Organometallic Chemistry,* 20(8), pp. 499-504.

POURAHMAD, A., SOHRABNEZHAD, S., KASHEFIAN, E., 2010. AgBr/nanoAlMCM-41 visible light photocatalyst for degradation of methylene blue dye. *Spectrochimica Acta Part A: Molecular and Biomolecular Spectroscopy,* 77(5), pp. 1108-1114

QIN, X., JING, L., TIAN, G., QU, Y., FENG, Y., 2009. Enhanced photocatalytic activity for degrading Rhodamine B solution of commercial Degussa P25 TiO2 and its mechanisms. *Journal of hazardous materials,* 172(2–3), pp. 1168-1174.

RANDRON, C., IRVINE, J.T.S., ROBERTSON, P.K.J., 2008. Synthesis of Visible-Light-Activated Yellow Amorphous TiO$_2$ Photocatalyst. *International Journal of Photoenergy,* , pp. 1-6.

RASHED, M.N., EL-AMIN, A.A., 2007. Photocatalytic degradation of methyl orange in aqueous TiO2 under different solar irradiation sources. *International Journal of Physical Sciences,* 2(3), pp. 73-81

RAY, A.K., BEENACKERS, A.A.C.M., American Institute of Chemical Engineers. Novel swirl-flow reactor for kinetic studies of semiconductor photo-catalysis. *Applied Chemical Engi,* 43(10), pp. 2571-2578.

REILLY, K., TAGHIPOUR, F., WILKINSON, D.P., 2012. Photocatalytic Hydrogen Production in a UV-irradiated Fluidized Bed Reactor. *Energy Procedia,* 29(0), pp. 513-521

RIZZO, L., KOCH, J., BELGIORNO, V., ANDERSON, M.A., 2006. Removal of methylene blue in a photocatalytic reactor using polymethylmethacrylate supported TiO2 nanofilm. *Presented at the 9th Environmental Science and Technology Symposium*.

ROBERTSON, P.K.J., 1996. Semiconductor photocatalysis: an environmentally acceptable alternative production technique and effluent treatment process. *Journal of Cleaner Production,* 4(3-4), pp. 203-212

ROSAS-BARRERA, K.L., ROPERO-VEGA, J.L., PEDRAZA-AVELLA, J.A., NIÑO-GOMEZ, M.E., PEDRAZA-ROSAS, J.E., LAVERDE-CATAÑO, D.A., 2011. Photocatalytic degradation of methyl orange using Bi2MNbO7 (M = Al, Fe, Ga, In) semiconductor films on stainless steel. *Catalysis Today,* 166(1), pp. 135-139.

SAKKAS, V.A., ISLAM, M.A., STALIKAS, C., ALBANIS, T.A., 2010. Photocatalytic degradation using design of experiments: A review and example of the Congo red degradation. *Journal of hazardous materials,* 175(1–3), pp. 33-44.

SALU, O.A., ADAMS, M., ROBERTSON, P.K.J., WONG, L.S., MCCULLAGH, C., 2011. Remediation of oily wastewater from an interceptor tank using novel photocatalytic drum reactor. *Desalination and Water Treatment,* 26(1-3), pp. 87-91.

SANGCHAY, W., SIKONG, L., KOOPTARNOND, K., 2012. Comparison of photocatalytic reaction of commercial P25 and synthetic TiO2-AgCl nanoparticles. *Procedia Engineering,* 32(0), pp. 590-596

SANSIVIERO, M.T.C., DOS SANTOS, D.S., JOB, A.E., AROCA, R.F., 2011. Layer by layer TiO2 thin films and photodegradation of Congo red. *Journal of Photochemistry and Photobiology A: Chemistry,* 220(1), pp. 20-24.

SATO, S., NAKAMURA, R., ABE, S., 2005. Visible-light sensitization of TiO2 photocatalysts by wet-method N doping. *Applied Catalysis A: General,* 284(1–2), pp. 131-137

SCZECHOWSKI, J.G., KOVAL, C.A., NOBLE, R.D., 1995. A Taylor vortex reactor for heterogeneous photocatalysis. *Chemical Engineering Science,* 50, pp. 3163-3173.

SEKINE, I., OKANO, C., 1989. Corrosion Behavior of Mild Steel and Ferritic Stainless Steels in Oxalic Acid Solution. *Corrosion Science,* 45(11), pp. 924-932

SERPONE, N., EMELINE, V., 2002. Suggested terms and definitions in photocatalysis and radiocatalysis. *International Journal of Photoenergy,* 4.

SHAFIEE, S., TOPAL, E., 2009. When will fossil fuel reserves be diminished? *Energy Policy,* 37(1), pp. 181-189.

SHAFIEE, S., TOPAL, E., 2010. A long-term view of worldwide fossil fuel prices. *Applied Energy,* 87(3), pp. 988-1000

SHANG, J., LI, W., ZHU, Y., 2003. Structure and photocatalytic characteristics of TiO2 film photocatalyst coated on stainless steel webnet. *Journal of Molecular Catalysis A: Chemical,* 202(1–2), pp. 187-195

SHIFU, C., WEI, Z., WEI, L., HUAYE, Z., XIAOLING, Y., YINGHAO, C., 2009. Preparation, characterization and activity evaluation of p–n junction photocatalyst p-CaFe2O4/n-Ag3VO4 under visible light irradiation. *Journal of hazardous materials,* 172(2–3), pp. 1415-1423.

SI, C., ZHOU, J., GAO, H., LIU, G., 2012. Photocatalytic degradation of formaldehyde in a fluidized bed with sound-magnetic assistance. *Advanced Powder Technology,* (0),.

SKOOG, A.D., HOLLER, F.J., CROUCH, S.R., 2007. *Principles of Instrumental Analysis.* 6th edn. Canada: Thomson Brooks/Cole.

SOLOMON, S., QIN, D., MANNING, M., CHEN, Z., MARQUIS, M., AVERYT, K.B., TIGNOR, M., MILLER, H.L., 2007. *IPCC, 2007: Climate Change 2007: The Physical Science Basis. Contribution of Working Group I to the Fourth Assessment Report of the Intergovernmental Panel on Climate Change.* Cambridge, United Kingdom and New York, USA: Cambridge University Press.

SON, Y.H., JEON, M.K., BAN, J.Y., KANG, M., CHOUNG, S.J., 2005. Application ofthree-phase fluidised photocatalytic system for decomposition of acetic acid andd ammonnia. *Journal of Industrial Engineering Chemistry,* 11(6), pp. 938-944.

SREETHAWONG, T., YOSHIKAWA, S., 2006. Enhanced photocatalytic hydrogen evolution over Pt supported on mesoporous prepared by single-step sol–gel process with surfactant template. *International Journal of Hydrogen Energy,* 31(6), pp. 786-796

TAGA, Y., 2009. Titanium oxide based visible light photocatalysts: Materials design and applications. *Thin Solid Films,* 517(10), pp. 3167-3172.

Taqui Khan MM, Chatterjee D, Bala M, Photocatalytic reduction of N2 to NH 3 sensitized by the [RuIII-ethylenediaminetetraacetate-2,2'-bipyridyl]- complex in a Pt-TiO2 semiconductor particulate system. *Journal of Photochemistry and Photobiology A: Chemistry* 67: 349-352 (1992).

TAYLOR, C.E., NOCETI, R.P., 2000. New developments in the photocatalytic conversion of methane to methanol. *Catalysis Today,* 55(3), pp. 259-267

TAYLOR, C.E., 2003. Methane conversion via photocatalytic reactions. *Catalysis Today,* 84(1-2), pp. 9-15

TERAMURA, K., OKUOKA, S., TSUNEOKA, H., SHISHIDO, T., TANAKA, T., 2010. Photocatalytic reduction of CO2 using H2 as reductant over ATaO3 photocatalysts (A = Li, Na, K). *Applied Catalysis B: Environmental,* 96(3–4), pp. 565-568.

TERAMURA, K., TSUNEOKA, H., SHISHIDO, T., TANAKA, T., 2008. Effect of H2 gas as a reductant on photoreduction of CO2 over a Ga2O3 photocatalyst. *Chemical Physics Letters,* 467(1–3), pp. 191-194.

TSYDENOV, D.E., PARMON, V.N., VORONTSOV, A.V., 2012. Toward the design of asymmetric photocatalytic membranes for hydrogen production: Preparation of TiO2-based membranes and their properties. *International Journal of Hydrogen Energy,* 37(15), pp. 11046-11060

UNER, D., OYMAK, M.M., 2012. On the mechanism of photocatalytic CO2 reduction with water in the gas phase. *Catalysis Today,* 181(1), pp. 82-88.

USUBHARANTANA, P., MCMARTIN, D., VEAWAB, A., TONTIWACHWUTHIKUL, P., 2006. Photocatalytic Process for CO2 Emission Reduction from Industrial Flue Gas Streams. *Industrial and Engineering Chemistry Research,* 45, pp. 2558-2568.

USUI, N., IKENOUCHI, M., 1997. The biological CO2 fixation and utilization project by RITE(1) — Highly-effective photobioreactor system —. *Energy Conversion and Management,* 38, Supplement(0), pp. S487-S492

UZUNOVA-BUJNOVA, M., TODOROVSKA, R., DIMITROV, D., TODOROVSKY, D., 2008. Lanthanide-doped titanium dioxide layers as photocatalysts. *Applied Surface Science,* 254(22), pp. 7296-7302.

VAN WELL, M., DILLERT, R.H.G., BAHNEMANN, D.W., BENZ, V.W., MUELLER, M.A., 1997. A Novel Nonconcentrating Reactor for Solar Water Detoxification. *Journal of Solar Energy Engineering,* 119, pp. 114-119.

VARGHESE, O.K., PAULOSE, M., LATEMPA, T.J., GRIMES, C.A., 2009. High-rate Solar Photocatalytic Conversion of CO2 and Water Vapour to Hydrocarbon Fuels. *Nano Letters,* 9(2), pp. 731-737.

VELLA, G., IMOBERDORF, G.E., SCLAFANI, A., CASSANO, A.E., ALFANO, O.M., RIZZUTI, L., 2010. Modeling of a TiO2-coated quartz wool packed bed photocatalytic reactor. *Applied Catalysis B: Environmental,* 96(3–4), pp. 399-407.

VORONSTOV, A.V., SAVONOV, E.N., SMIRNIOTIS, P.G., 2000. Vibrofluidised and fixed-bed photocatalytic reactors: case of gaseous acetone photooxidation. *Chemical Engineering Science,* 55(21), pp. 5089-5098.

WAHI, R.K., YU, W.W., LIU, Y., MEJIA, M.L., FALKNER, J.C., NOLTE, W., COLVIN, V.L., 2005. Photodegradation of Congo Red catalyzed by nanosized TiO2. *Journal of Molecular Catalysis A: Chemical,* 242(1–2), pp. 48-56.

WANG, E., ZHENG, Q., XU, S., LI, D., 2011. Treatment of Methyl Orange by Photocatalysis Floating Bed. *Procedia Environmental Sciences,* 10, Part B(0), pp. 1136-1140.

WANG, F., MIN, S., HAN, Y., FENG, L., 2010. Visible-light-induced photocatalytic degradation of methylene blue with polyaniline-sensitized composite photocatalysts. *Superlattices and Microstructures,* 48(2), pp. 170-180.

WANG, Q., AN, N., CHEN, W., WANG, R., WANG, F., LEI, Z., SHANGGUAN, W., 2012. Photocatalytic water splitting into hydrogen and research on synergistic of Bi/Sm with solid solution of Bi–Sm–V photocatalyst. *International Journal of Hydrogen Energy,* 37(17), pp. 12886-12892.

WANG, T., YANG, L., DU, X., YANG, Y., 2013. Numerical investigation on CO2 photocatalytic reduction in optical fiber monolith reactor. *Energy Conversion and Management,* 65(0), pp. 299-307.

WARD, J.D., MOHR, S.H., MYERS, B.R., NEL, W.P., 2012. High estimates of supply constrained emissions scenarios for long-term climate risk assessment. *Energy Policy,* (0),.

WEI, Y., LI, J., HUANG, Y., HUANG, M., LIN, J., WU, J., 2009. Photocatalytic water splitting with In-doped H2LaNb2O7 composite oxide semiconductors. *Solar Energy Materials and Solar Cells,* 93(8), pp. 1176-1181.

WIERSMA, B.J., 2004. *Corrosion Mechanisms and Rates for Carbon Steel and Stainless Steel Materials Exposed to Oxalic Acid Solutions.* USA: U.S. Department of Energy.

WIERSMA, B.J., 2004. *Hydrogen Generation During the Corrosion of Carbon Steel in Oxalic Acid.* (WSRC-TR-2004-00109). USA: The U.S. Department of Energy.

WIERSMA, B.J., MICKALONIS, J.I., BEAM, D.C., POIRIER, M.R., HERMAN, D.T., FINK, S.D., PAREIZS, J.M., FONDEUR, F.F., *In-situ Monitoring of Corrosion during a Laboratory Simulation of Oxalic Acid Chemical Cleaning.* USA: U.S. Department of Energy.

WOOD, F.M., 2008. *The Photocatalytic Destruction of Volatile Organic Compounds Generated by The Oil and Gas Industry.* Doctor of Philosophy thesis, Robert Gordon University.

WU, J.C.S., 2009. Photocatalytic Reduction of Greenhouse Gas CO2 to Fuel. *Catalysis Surveys from Asia,* 13, pp. 30-40

WU, J.C.S., LIN, H., LAI, C., 2005. Photo reduction of CO2 to methanol using optical-fiber photoreactor. *Applied Catalysis A: General,* 296(2), pp. 194-200

WU, Y., YUAN, H., JIANG, X., WEI, G., LI, C., DONG, W., 2012. Photocatalytic degradation of 4-tert-octylphenol in a spiral photoreactor system. *Journal of Environmental Sciences,* 24(9), pp. 1679-1685.

YAN, S.C., WANG, Z.Q., LI, Z.S., ZOU, Z.G., 2009. Photocatalytic activities for water splitting of La-doped-NaTaO3 fabricated by microwave synthesis. *Solid State Ionics,* 180(32–35), pp. 1539-1542.

YANG, C., VERNIMMEN, J., MEYNEN, V., COOL, P., MUL, G., 2011. Mechanistic study of hydrocarbon formation in photocatalytic CO2 reduction over Ti-SBA-15. *Journal of Catalysis,* 284(1), pp. 1-8.

YANG, J., YAN, H., WANG, X., WEN, F., WANG, Z., FAN, D., SHI, J., LI, C., 2012. Roles of cocatalysts in Pt–PdS/CdS with exceptionally high quantum efficiency for photocatalytic hydrogen production. *Journal of Catalysis,* 290(0), pp. 151-157.

YAO, G., WANG, F., WANG, X., GUI, K., 2010. Magnetic field effects on selective catalytic reduction of NO by NH3 over Fe2O3 catalyst in a magnetically fluidized bed. *Energy,* 35(5), pp. 2295-2300.

YU, S., HUANG, C., LIAO, C., WU, J.C.S., CHANG, S., CHEN, K., 2011. A novel membrane reactor for separating hydrogen and oxygen in photocatalytic water splitting. *Journal of Membrane Science,* 382(1–2), pp. 291-299.

YULIATI, L., YOSHIDA, H., 2008. Photocatalytic conversion of methane. *Chemical Society Reviews,* 37(8), pp. 1592-1602

ZHANG, H., LI, Y., ZHANG, H., WANG, H., 2008. *Materials Letters,* 62, pp. 2729-2732.

ZHANG, S., CHEN, L., LIU, H., GUO, W., YANG, Y., GUO, Y., HUO, M., 2012. Design of H3PW12O40/TiO2 and Ag/H3PW12O40/TiO2 film-coated optical fiber photoreactor for the degradation of aqueous rhodamine B and 4-nitrophenol under simulated sunlight irradiation. *Chemical Engineering Journal,* 200–202(0), pp. 300-309.

ZHANG, W., ZHANG, J., CHEN, Z., WANG, T., 2009. Photocatalytic degradation of methylene blue by ZnGa2O4 thin films. *Catalysis Communications,* 10(13), pp. 1781-1785.

ZHANG, Y., WAN, J., KE, Y., 2010. A novel approach of preparing TiO2 films at low temperature and its application in photocatalytic degradation of methyl orange. *Journal of hazardous materials,* 177(1–3), pp. 750-754

ZHANG, Z., ANDERSON, W.A., MOO-YOUNG, M., 2004. Experimental analysis of a corrugated plate photocatalytic reactor. *Chemical Engineering Journal,* 99(2), pp. 145-152

ZHANG, Z., WU, H., YUAN, Y., FANG, Y., JIN, L., 2012. Development of a novel capillary array photocatalytic reactor and application for degradation of azo dye. *Chemical Engineering Journal,* 184(0), pp. 9-15.

ZHENG, X., WEI, L., ZHANG, Z., JIANG, Q., WEI, Y., XIE, B., WEI, M., 2009. Research on photocatalytic H2 production from acetic acid solution by Pt/TiO2 nanoparticles under UV irradiation. *International Journal of Hydrogen Energy,* 34(22), pp. 9033-9041.

ZHU, H., JIANG, R., FU, Y., GUAN, Y., YAO, J., XIAO, L., ZENG, G., 2012. Effective photocatalytic decolorization of methyl orange utilizing TiO2/ZnO/chitosan nanocomposite films under simulated solar irradiation. *Desalination,* 286(0), pp. 41-48.

ZHU, H., JIANG, R., XIAO, L., CHANG, Y., GUAN, Y., LI, X., ZENG, G., 2009. Photocatalytic decolorization and degradation of Congo Red on innovative crosslinked chitosan/nano-CdS composite catalyst under visible light irradiation. *Journal of hazardous materials,* 169(1–3), pp. 933-940.

Appendix I
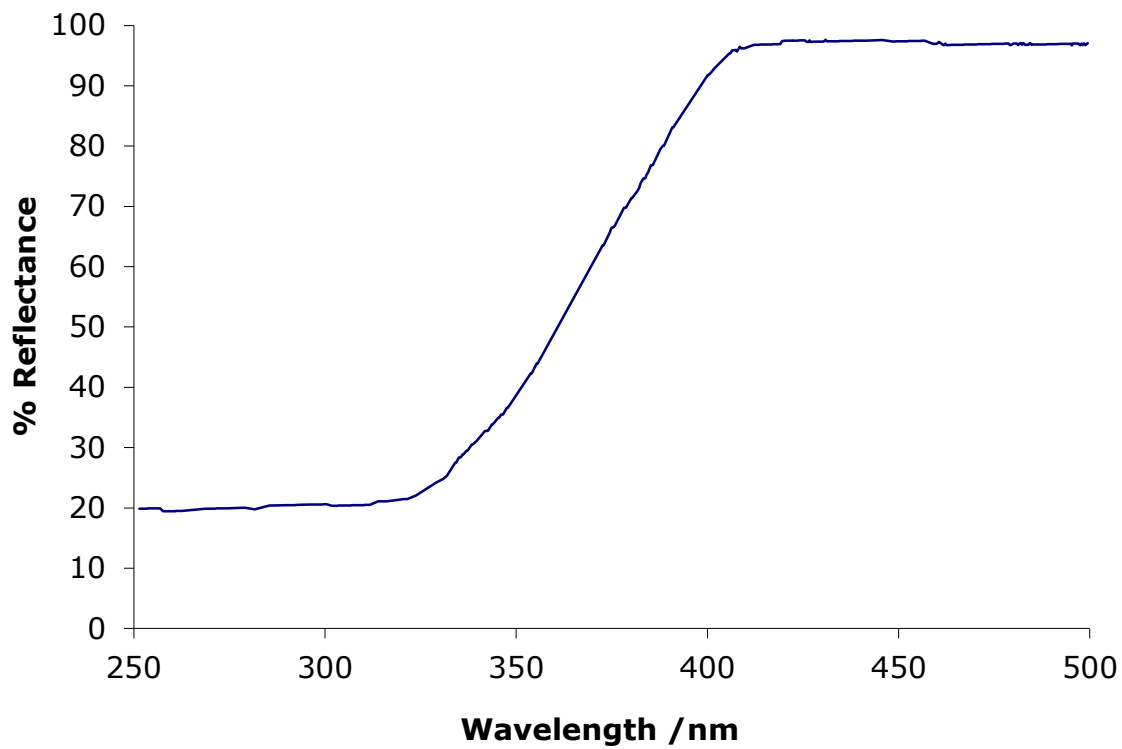
Diffuse reflectance spectra of P25 TiO₂
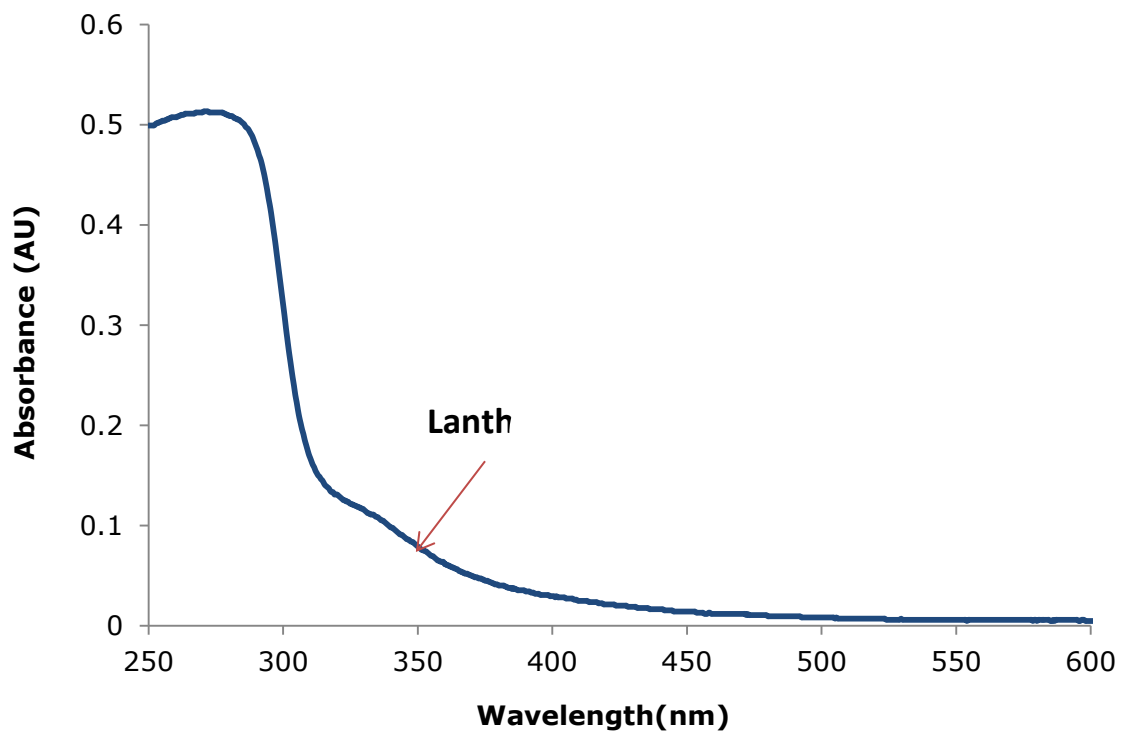
Diffuse reflectance spectra of NaTaO₃.La supplied by colleagues at CalTech
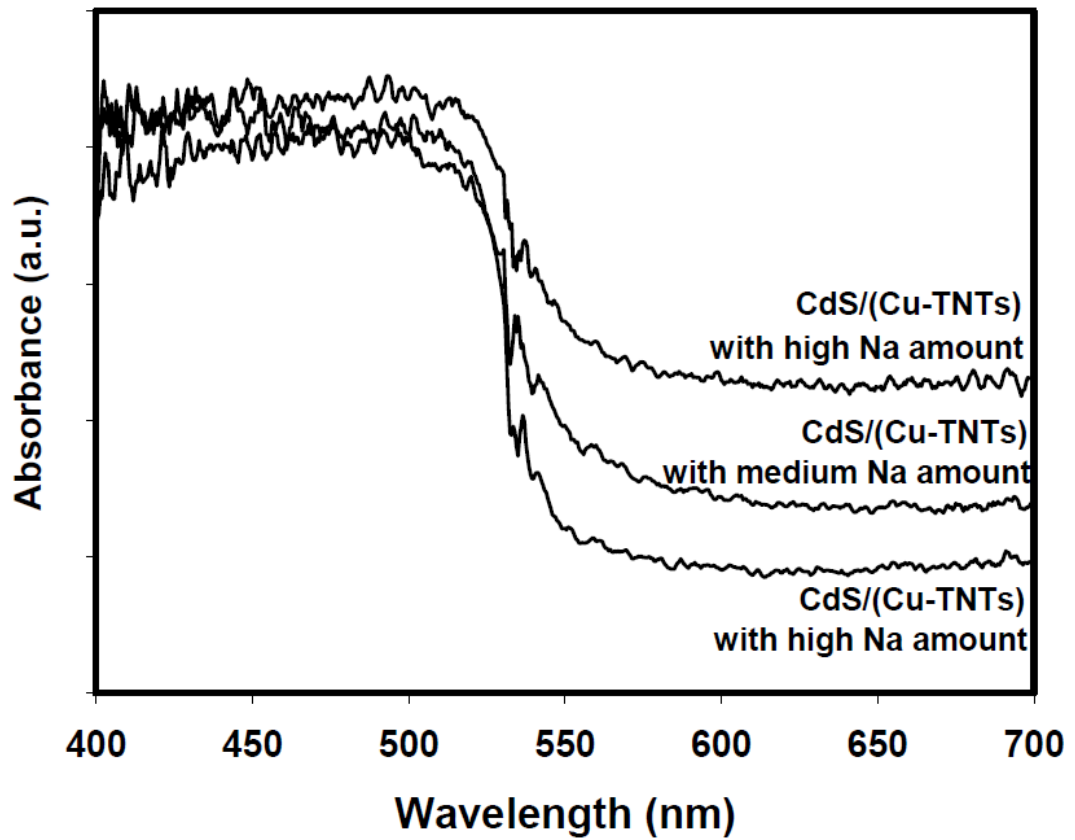
Diffuse reflectance spectra of Cu-TNT-CdS samples supplied by colleagues at CalTech
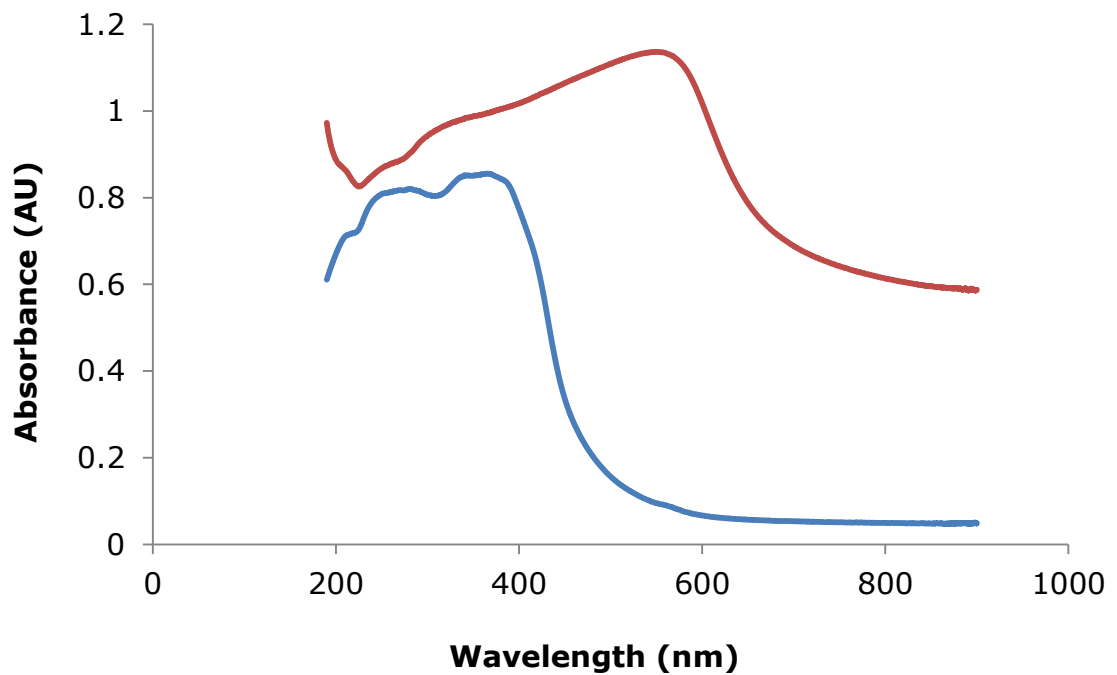
Diffuse reflectance spectra of C₃N₄ (blue) and Sr₀.₉₇NbO₃ (red) samples supplied by colleagues at the University of St. Andrews
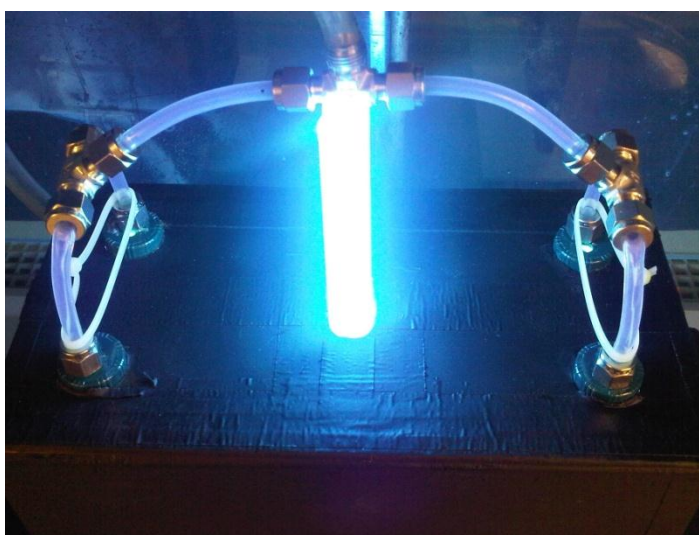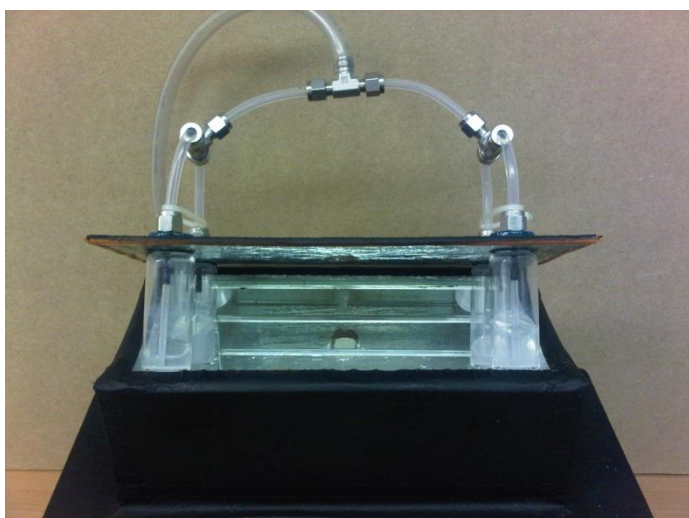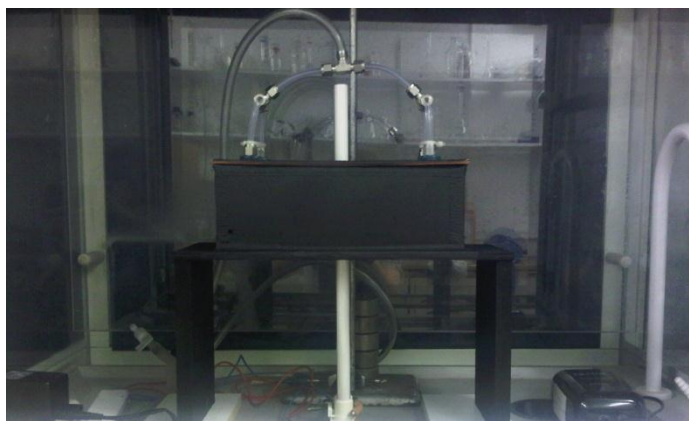
Images of MCPR displaying the general geometry of the unit, reaction vessels and illumination
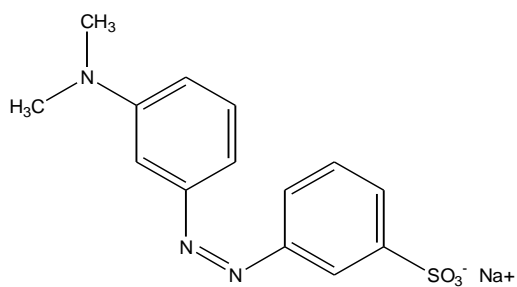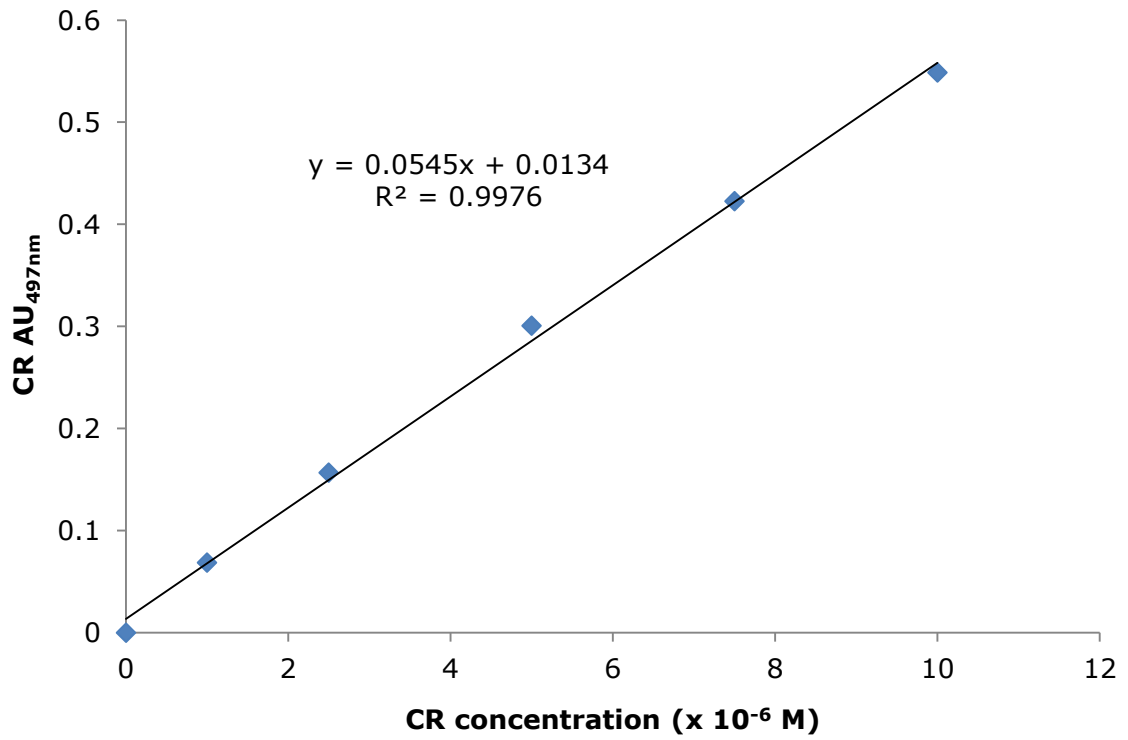
MO structure
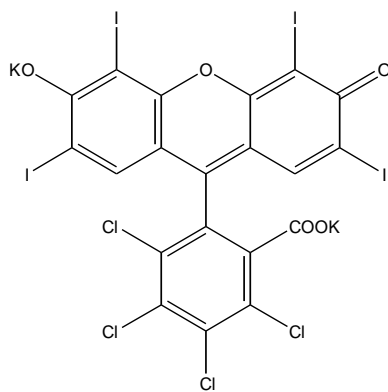
RB structure

CR structure

$y = 0.2574x + 0.0127$
$R^2 = 0.9999$
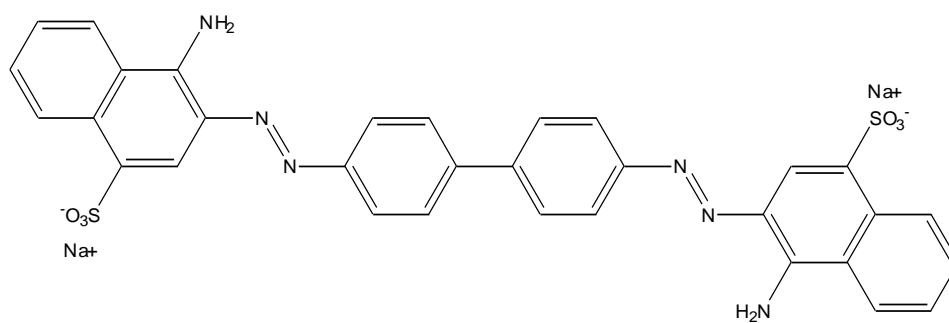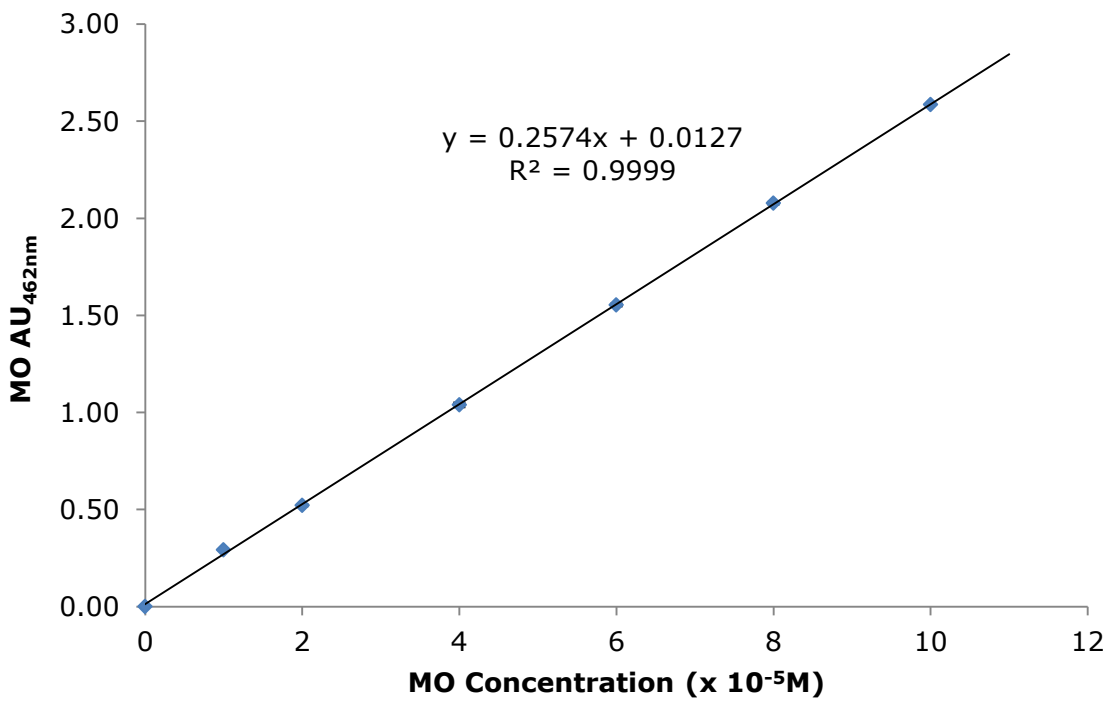
Calibration graph of known MO concentrations measured at 462 nm

$y = 0.0714x - 0.006$
$R^2 = 0.9998$
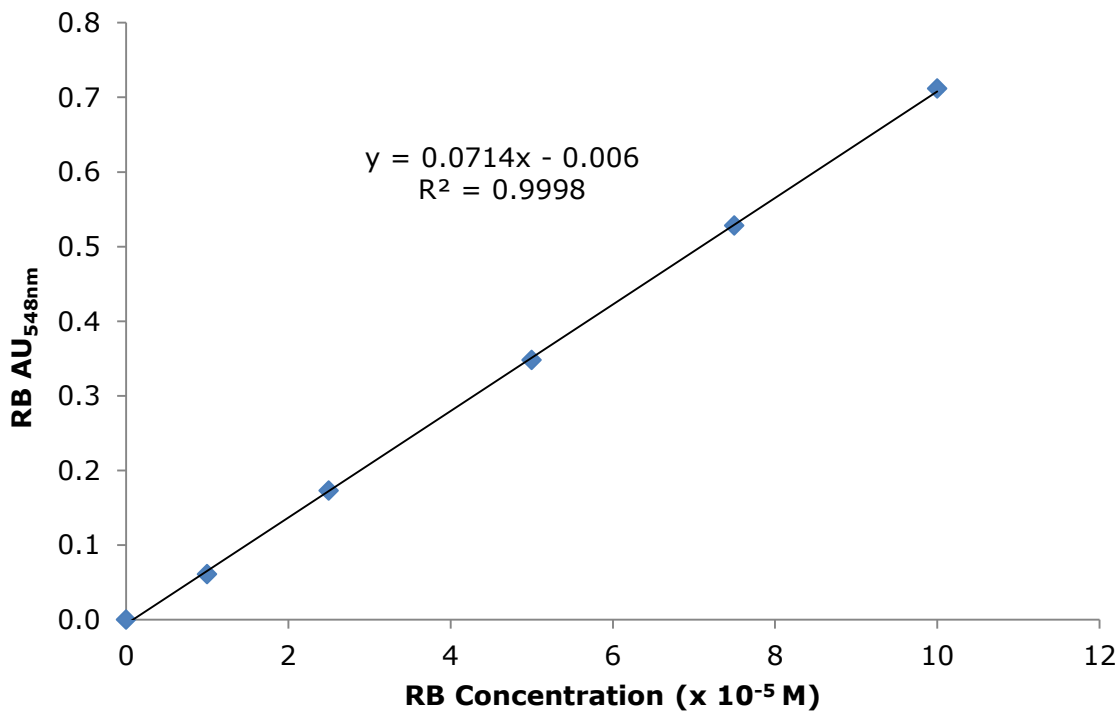
Calibration graph of known RB concentrations measured at 548 nm

Calibration graph of known CR concentrations measured at 497 nm
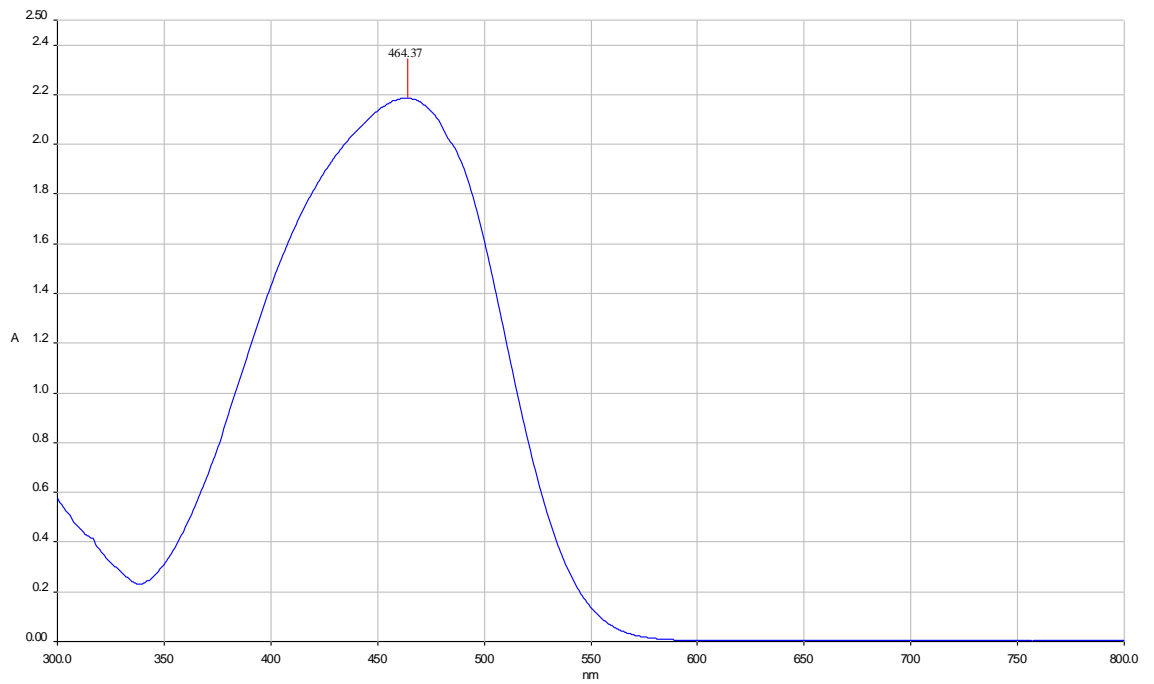
UV-Vis spectra of MO
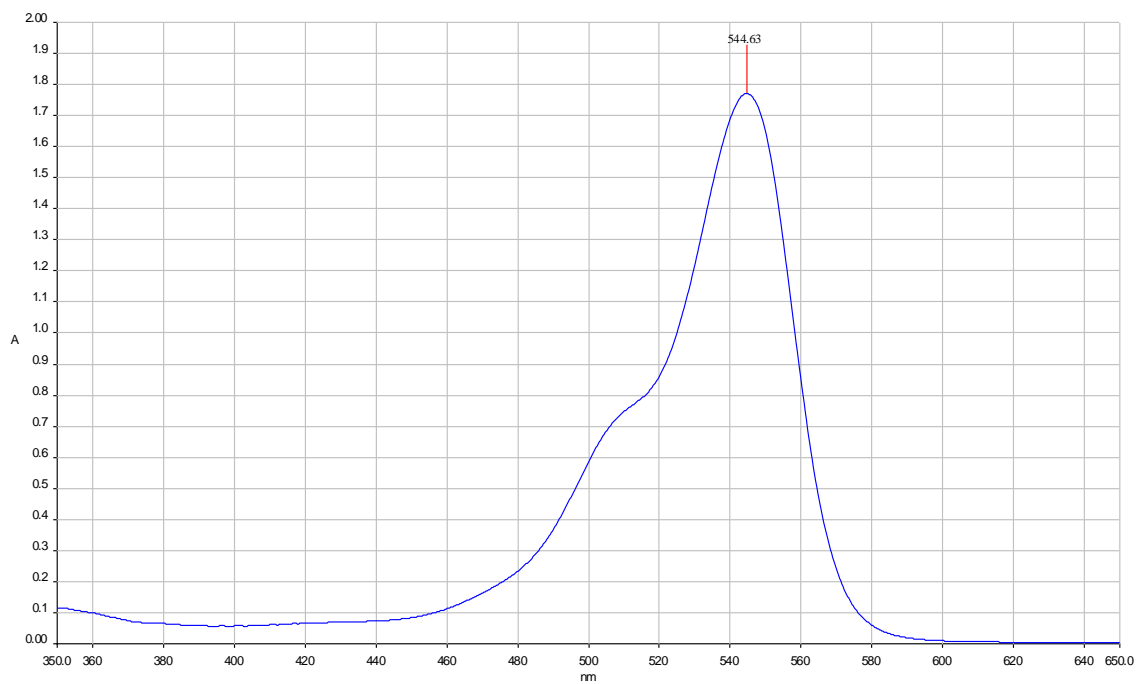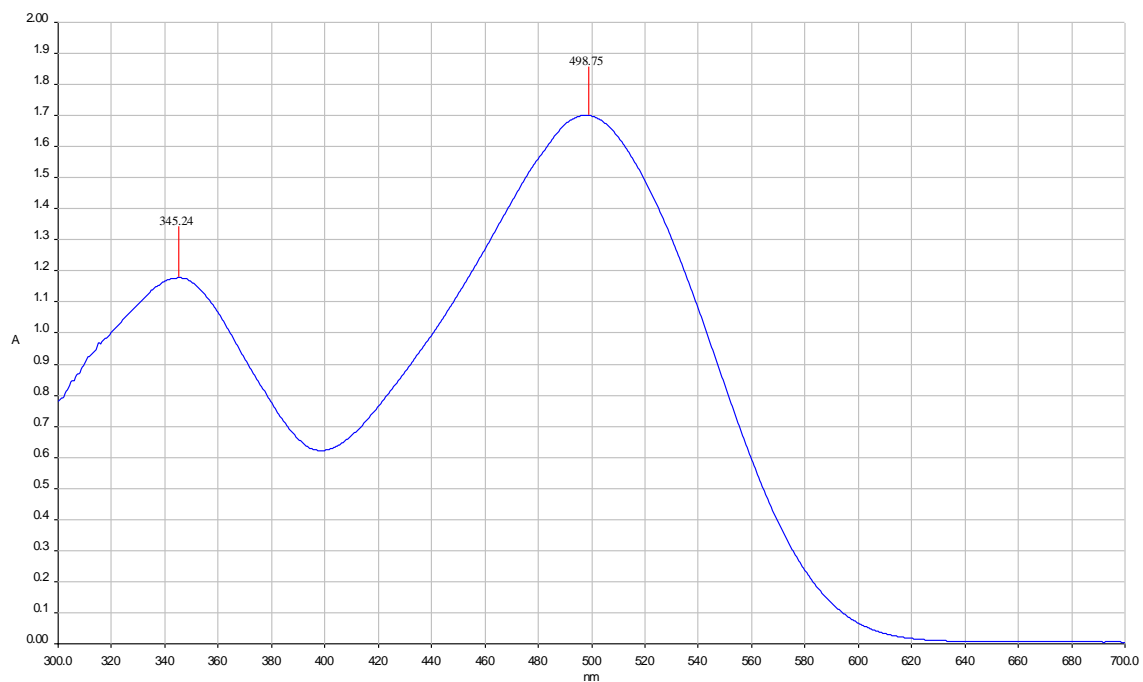
UV-Vis spectra of RB

UV-Vis spectra of CR
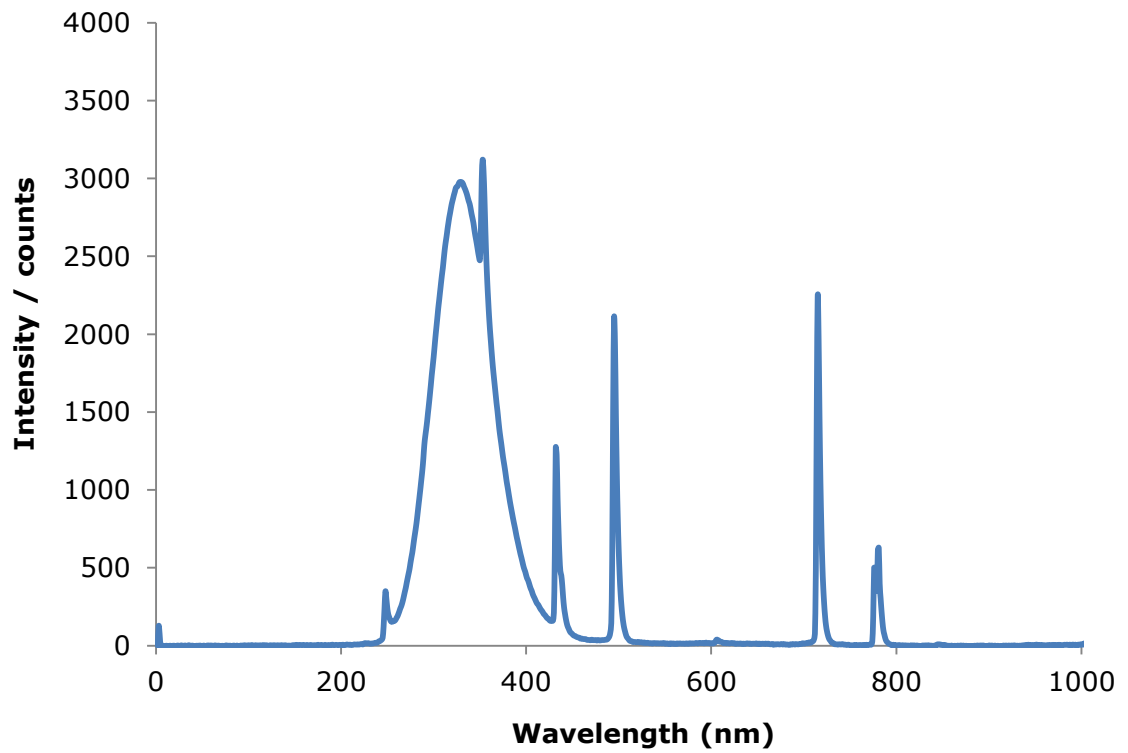
Spectral output of Philips 36 W UV lamp
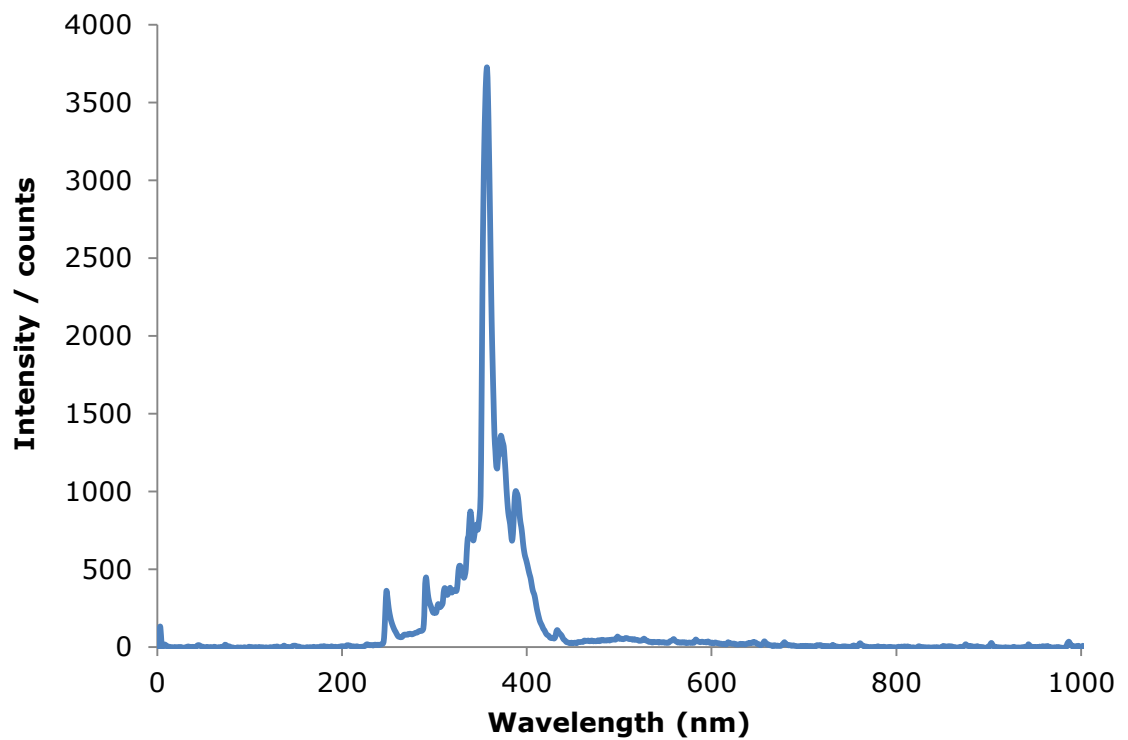
Spectral output of Dr. Hönle 500 W UV lamp
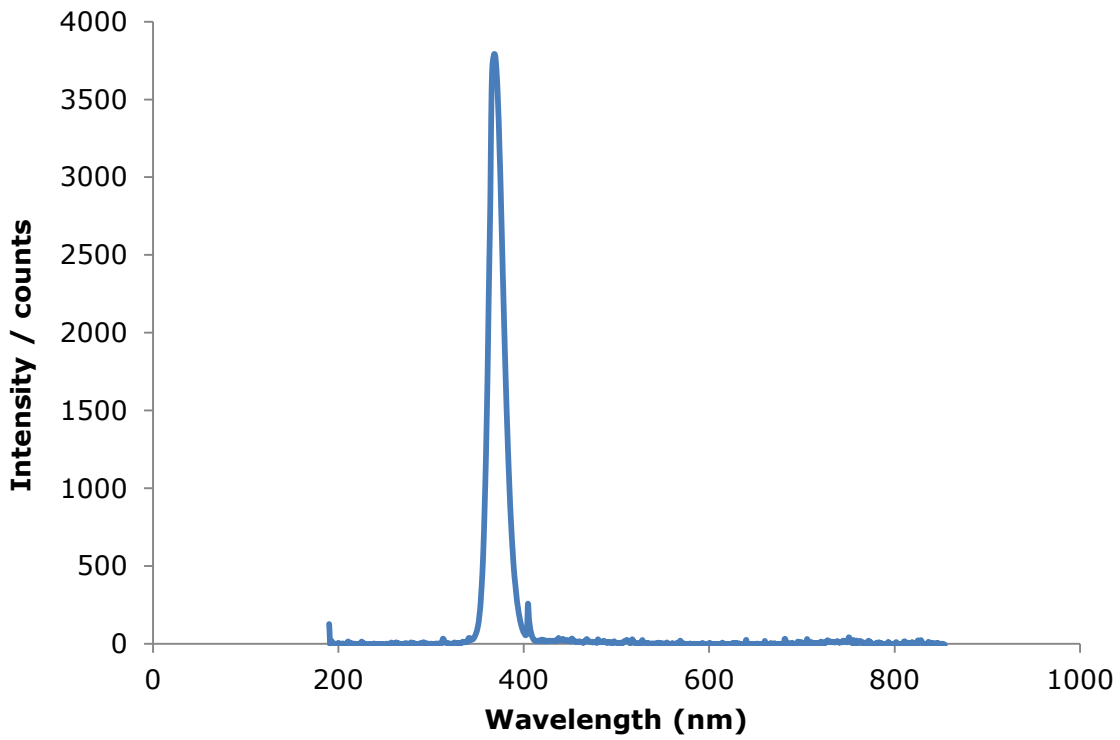
Spectral output of half moon structured 49 W UV lamp
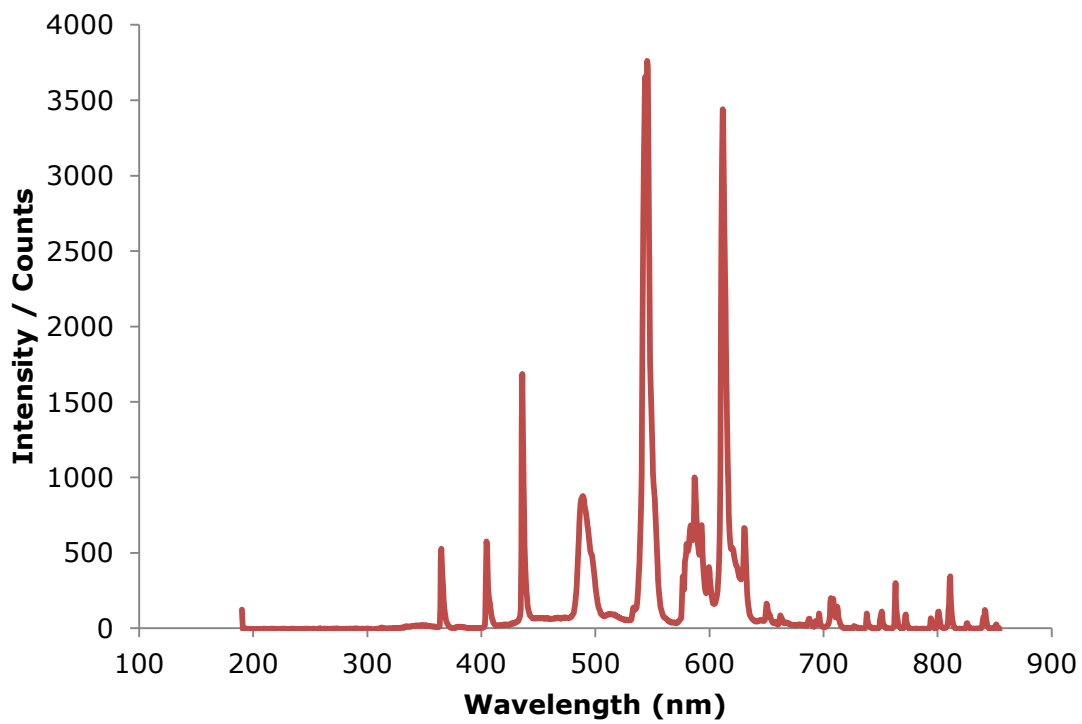
Emission spectrum for Visible Lamp (red)
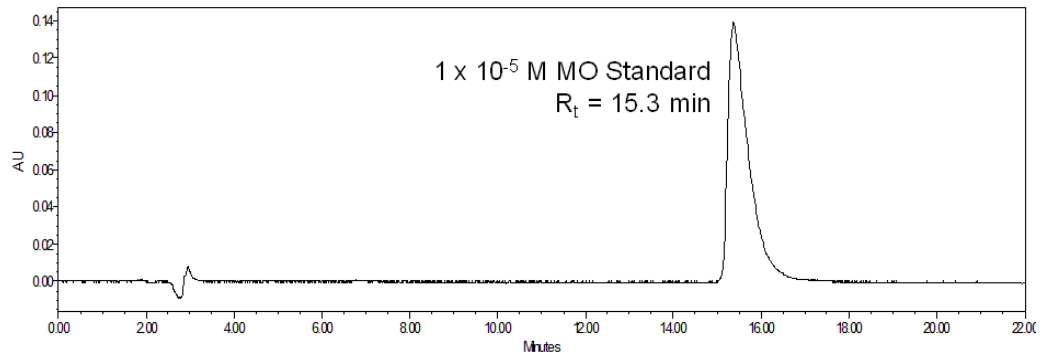
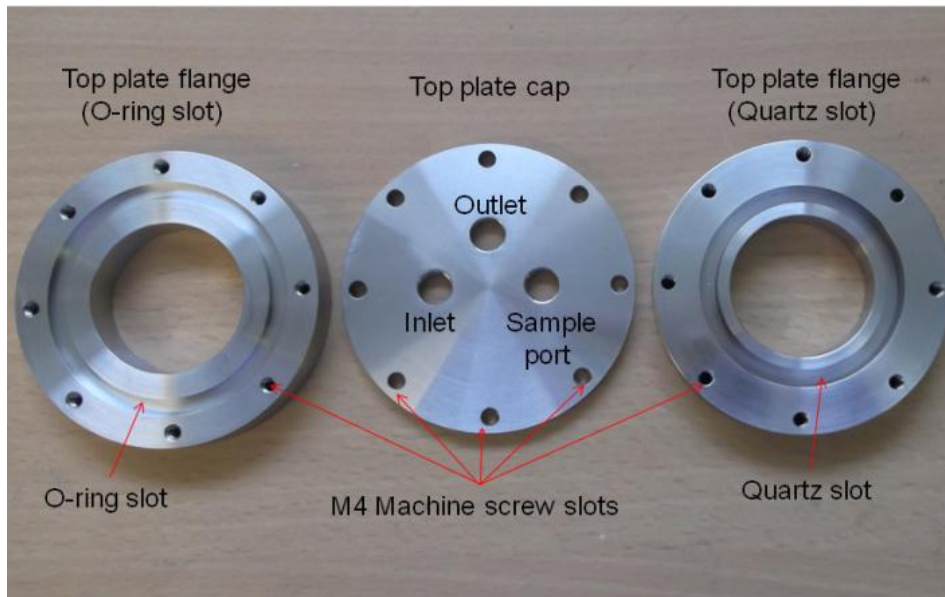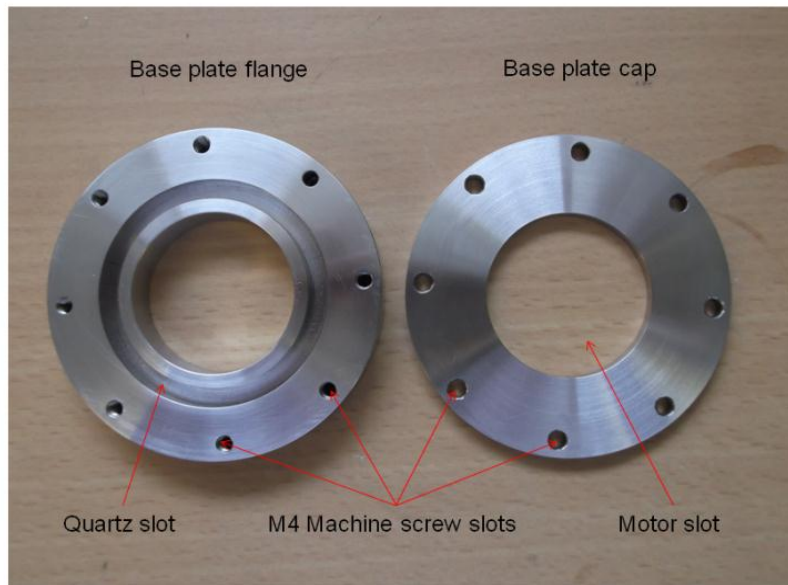*HPLC Chromatogram of Standard MO Sample where R_t is retention time (min)*

a.
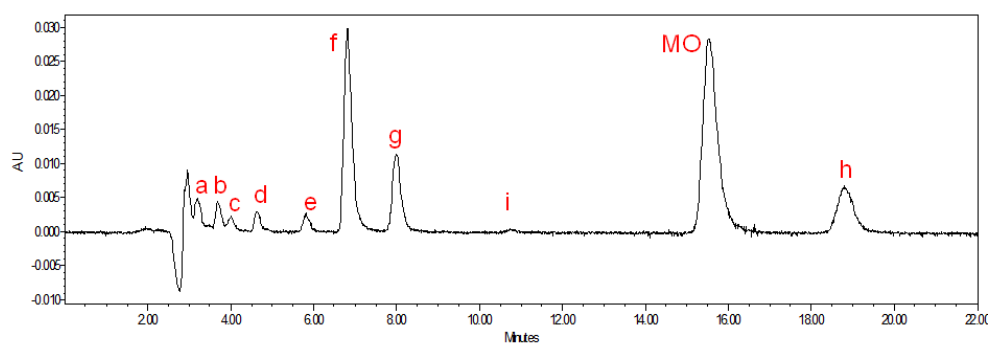
b.
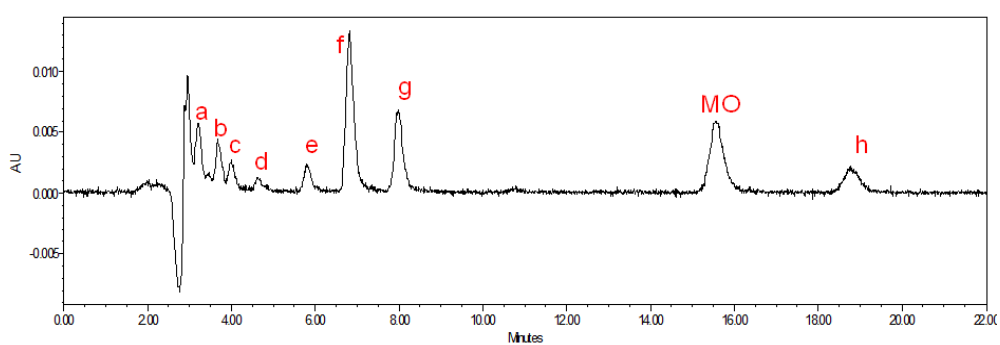
c.

d.
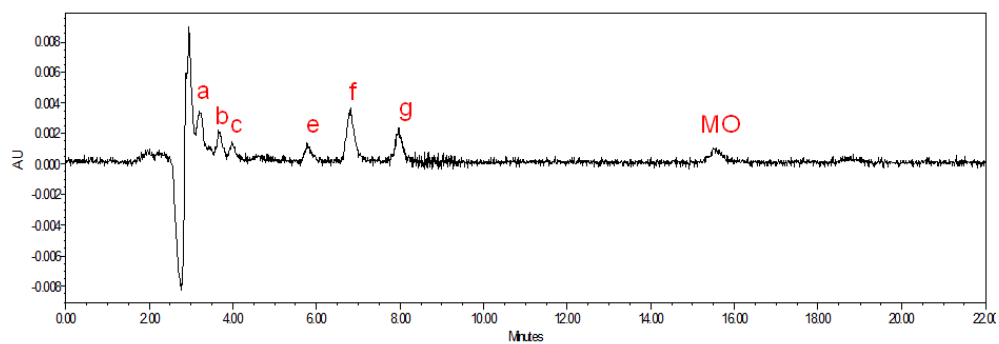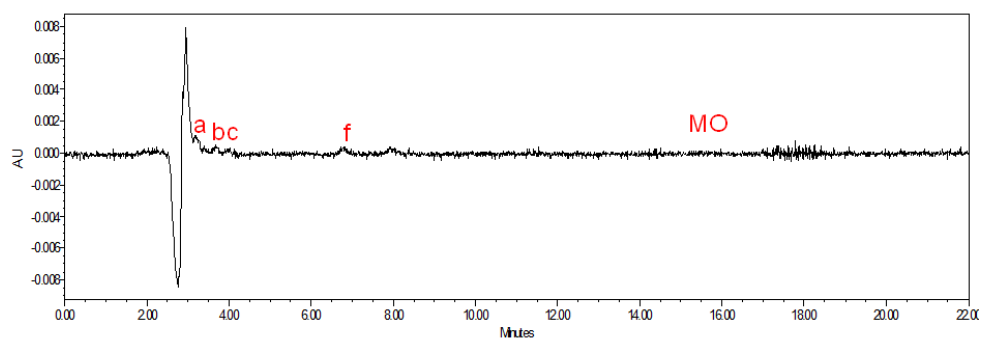
HPLC chromatogram of samples exposed to (a) 10 (b) 20 (c) 30 and (d) 40 min of UV illumination
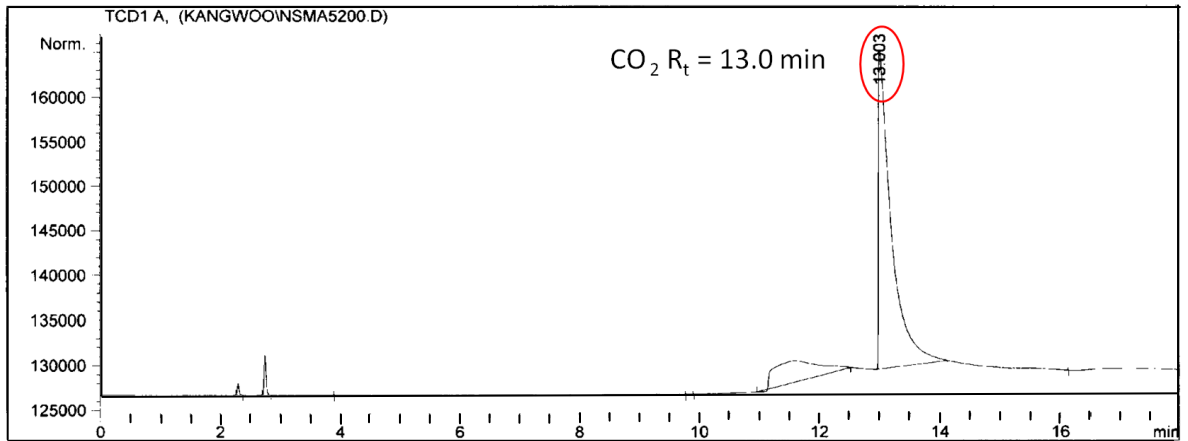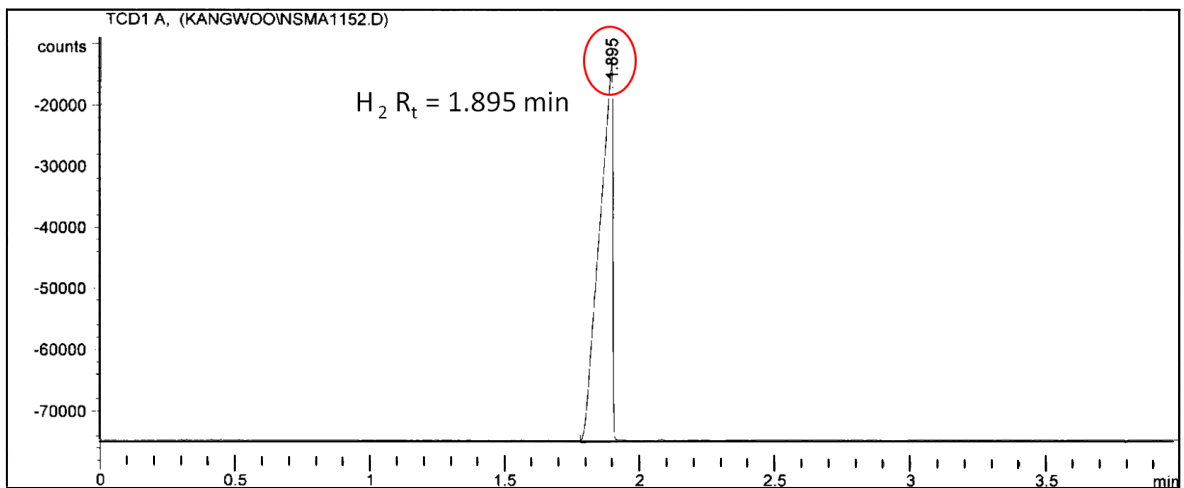
Image of top plate flange and cap

Image of base plate flange and cap

*Images of George Ellery Hale solar telescope displaying the exterior
and interior mirrors which guide light down the illumination shaft.*

GC chromatogram of standard CO$_2$ sample

GC Chromatogram of standard H$_2$ sample (CalTech)